THE PHYSICAL REVIEW

VOLUME 86 Second Series NUMBER

APRIL 1, 1952

Published for the

AMERICAN PHYSICAL SOCIETY

by the

AMERICAN INSTITUTE OF PHYSICS

Lancaster, Pa., and New York, N. Y.

Information for Contributors

Manuscripts

Send manuscripts to S. A. Goudsmit, Brookhaven National Laboratory, Upton, Long Island, New York.

Each article submitted will in general consist of (a) textual material, i.e., all material which is to be set in type, and (b) drawings or photographs from which zinc etchings or copper halftones will be made. Textual material will consist of an abstract, the body of the paper, tabular material, references, and figure captions. All of this material must be in English, typewritten (except mathematical expressions) double spaced with wide margins (for editorial instructions to the printer) on a durable, white paper, preferably letter size. The original copy, not the carbon, should be submitted.

For general style, spellings, abbreviations, and form, recent issues of this journal should be consulted.

The prime requisite is that the copy shall be clear to the typesetter, who is neither a physicist nor a mathematician.

Abstracts

An abstract must accompany each article. It should be adequate as an index and as a summary. As an index, it should give all subjects, major and minor, concerning which new information is presented. As a summary it should give the conclusions of the article and all numerical results of general interest.

Mathematical Expressions

All but the simplest mathematical expressions should be carefully printed in by hand. Be sure to distinguish between capital and small letters. Indicate clearly superscripts and subscripts by inverted carets and carets, respectively. Avoid complicated superscripts and subscripts. Avoid repetition of a complicated expression by representing it by some convenient symbol. Identify in the margin Greek letters and unusual symbols. Use fractional exponents instead of root signs. Use the solidus (/) for fractions wherever its use will save vertical space.

References

References should appear as footnotes, numbered consecutively, and arranged thus:

[1] A. B. Smith, Phys. Rev. 62, 852 (1932).
[2] H. Lamb, *Hydrodynamics* (Cambridge University Press, Teddington, England, 1960), sixth edition, pp. 573, 645.

Tables

All but the simplest tabular material should be organized in tabular form rather than as a part of the running text. Tables may be typewritten on sheets separate from the running text with indications in the margin of the running text where the table is to be inserted. Each table must have a caption which will make the data in the table intelligible without reference to the text. Avoid complicated column headings; if necessary, use symbols which are explained in the table caption.

Figures

Wherever possible figures should be planned for the width of a column of the *Physical Review* (3 inches). A convenient reduction ratio is about 2:1 or 3:1. The original drawings or photographs should therefore be in general about 6 to 9 inches wide and the lettering and symbols should be large enough on the original that when reduced they shall not be less than about $\frac{1}{16}$ in. (~1.5 mm). If the reduction is 3:1, the original lettering should be not less than $\frac{1}{16}$ in. high.

The process of making zinc etchings or copper halftones is a black and white photographic one. Therefore line drawings must be in *india ink* on white paper or tracing cloth. Coordinate paper is not desirable but if used must be blue lined and the coordinate lines which are to show must be inked over.

Photographs should have maximum black and white contrast.

Plan figures to use space efficiently. Avoid wasting space, particularly at the top or bottom.

Identify on the black or other suitable place each original drawing or photograph with the author's name and the figure number. Figures should be numbered consecutively and their approximate position indicated in the margin of the running text. Figure captions should be typed and included with the manuscript (not as part of the figure).

Avoid round and oval photographs.

Alterations

Take great care that each manuscript is typographically accurate. A limited number of alterations in proof are unavoidable, but the cost of making extensive alterations after the article has been set in type will be charged to the author.

Proof and all correspondence concerning papers in the process of publication should be addressed to the Publication Manager, American Institute of Physics, 57 East 55 Street, New York 22, New York.

THE PHYSICAL REVIEW

A journal of experimental and theoretical physics established by E. L. Nichols in 1893

VOLUME 86

Second Series

APRIL 1–JUNE 15, 1952

Published for the

AMERICAN PHYSICAL SOCIETY

by the

AMERICAN INSTITUTE OF PHYSICS

Incorporated

THE PHYSICAL REVIEW

A journal of experimental and theoretical physics established by E. L. Nichols in 1893

Published by the American Institute of Physics for the

AMERICAN PHYSICAL SOCIETY

Officers

President

J. H. VAN VLECK
Harvard University
Cambridge, Massachusetts

Vice-President

ENRICO FERMI
Institute for Nuclear Studies
University of Chicago
Chicago 37, Illinois

Secretary

K. K. DARROW
Bell Telephone Laboratories
Office:
Columbia University
New York 27, New York

Treasurer

G. B. PEGRAM
Columbia University
New York 27, New York

Local Secretary for the Pacific Coast

J. KAPLAN
University of California at Los Angeles
Los Angeles, California

Managing Editor

S. A. GOUDSMIT
Brookhaven National Laboratory
Upton, Long Island
New York

BOARD OF EDITORS

Editor

S. A. GOUDSMIT

Assistant Editor

S. PASTERNACK

Associate Editors

HARVEY BROOKS
R. F. CHRISTY
C. L. CRITCHFIELD
M. DEUTSCH
T. H. JOHNSON
BRUNO ROSSI
M. GOLDHABER
R. HOFSTADTER
A. W. LAWSON
A. PAIS
R. SERBER
C. H. TOWNES
W. P. ALLIS
F. G. BRICKWEDDE
W. B. FRETTER
CONYERS HERRING
H. W. LEVERENZ
ARNOLD NORDSIECK

Manuscripts for publication should be submitted to S. A. GOUDSMIT, Brookhaven National Laboratory, Upton, Long Island, New York. The authors' institutions are requested to pay a publication charge of **$8** per page which, if honored, entitles them to 100 free reprints. Instructions will be sent with galley proofs.

Proof and all correspondence concerning papers in the process of publication should be addressed to the Publication Manager, American Institute of Physics, 57 East 55 Street, New York 22, New York.

Subscription Price

United States and Canada **$25.00**
Elsewhere **$27.00**

Back Numbers [1]

Yearly back number rate when complete year is available:
Prior to 1949: **$20.00**
Thereafter: **$27.00**
Single copies: **$2.00** each, prior to July, 1929;
$1.00 each, July, 1929–December, 1941;
$2.00 each, January, 1942–December, 1946;
$1.00 each, January, 1947–December, 1948;
$1.25 each, thereafter.
General index, 1893–1920: **$4.00.**

Subscriptions, renewals, and orders for back numbers should be addressed to the American Institute of Physics, 57 East 55 Street, New York 22, New York.

Changes of address in the case of members of the American Physical Society should be addressed to the Treasurer; in the case of other subscribers to the American Institute of Physics.

[1] For Series 1 inquire of Physics Department, Cornell University, Ithaca, New York.

The Physical Review is published semi-monthly at Prince and Lemon Streets, Lancaster, Pennsylvania.

Entered as second-class matter March 6, 1947, at the Post Office at Lancaster, Pennsylvania, under the Act of March 3, 1879.

Acceptance for mailing at special rate of postage provided for in paragraph (d-2), section 34.40, P. L. & R. of 1948, authorized January 27, 1933.

THE
PHYSICAL REVIEW

A journal of experimental and theoretical physics established by E. L. Nichols in 1893

SECOND SERIES, VOL. 86, NO. 1 APRIL 1, 1952

Forward Scattering of Light by a Coulomb Field

F. ROHRLICH* AND R. L. GLUCKSTERN†
Laboratory of Nuclear Studies, Cornell University, Ithaca, New York
(Received October 25, 1951)

The complex scattering amplitude for the scattering of light by a Coulomb field (Delbrück scattering) in the forward direction is calculated exactly by two methods. First, the Feynman method is used and necessitates very tedious and complicated calculations. Then, the method of analytical continuation is applied to the pair production cross section and yields the same result much more easily. An exact analytical expression is obtained for the dispersive and absorptive parts of the amplitude. The result is plotted as a function of energy. The low energy limit agrees with previous calculations for this limit by Kemmer and Ludwig.

INTRODUCTION

ONE of the most interesting predictions made by quantum electrodynamics is the scattering of light by light.[1] This effect is in contradiction to the classical Maxwell equations which, because of their linearity, cannot account for it. Weisskopf[2] has shown that a nonlinear correction to the Maxwell equations will do justice to the phenomenon.

Experimental verification of this effect proved impossible because of its extremely small size in a crossed beam experiment. Considerably more fruitful is the idea of observing this process in a modified form in which light is scattered by a static electromagnetic field. The strong Coulomb fields of heavy nuclei seem by far the best targets. The occurrence of the scattering of light by a Coulomb field was first suggested by Delbrück,[3] and the effect is often referred to as Delbrück scattering. But until recently the effect remained of academic value only.

A few years ago renewed interest in the problem came from the new formulations of quantum electrodynamics. The only two observable processes involving closed electron loops in the Feynman diagrams are the polarization of the vacuum and the scattering of light by light. The former was verified experimentally beyond any doubt by the well-known Lamb-Retherford experiment on the level shift of the hydrogen atom and is of second order.

The Delbrück effect can be regarded as a photon self-energy effect in a Coulomb field. A method based on this view point could actually be used to calculate the process. But there seem to be no essential advantages in the method.

Very recent experiments by Wilson[4] in this laboratory seem to confirm the existence of the Delbrück effect. However, more complete calculations will be necessary for a quantitative analysis of these observations.

The foregoing remarks and the recent great improvements in calculating technique may justify the following very long and tedious calculations. Earlier investigations by Achieser and Pomerantschuk[5] and by Kemmer and Ludwig[6] yielded results which will be confirmed and augmented in this work and in a paper by Bethe and Rohrlich[7] immediately following this paper.

Finally, the present work shows and confirms a successful application of the extremely elegant method of

* Now at Palmer Physical Laboratory, Princeton University, Princeton, New Jersey.
† Now at Sloane Physics Laboratory, Yale University, New Haven, Connecticut.

[1] O. Halpern, Phys. Rev. **44**, 855 (1933); H. Euler and B. Kockel, Naturwiss. **23**, 246 (1935); H. Euler, Ann. Phys. **26**, 398 (1936); R. Karplus and M. Neuman, Phys. Rev. **80**, 380 (1950) and **83**, 776 (1951).

[2] V. Weisskopf, Kgl. Danske Videnskab. Selskab Mat.-fys. Medd. **XIV**, No. 6 (1936).

[3] M. Delbrück, Z. Physik **84**, 144 (1933).

[4] R. R. Wilson, private communication.

[5] A. Achieser and I. Pomerantschuk, Physik. Z. Sowjetunion **11**, 478 (1937).

[6] N. Kemmer, Helv. Phys. Acta **10**, 112 (1937); N. Kemmer and G. Ludwig, Helv. Phys. Acta **10**, 182 (1937).

[7] H. A. Bethe and F. Rohrlich, Phys. Rev. **86**, 10 (1951).

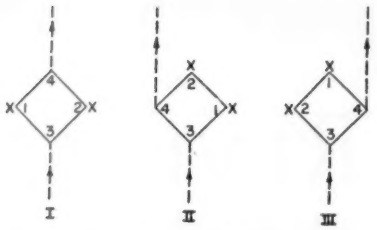

FIG. 1. Feynman diagrams for Delbrück scattering.

analytic continuation which was first suggested in a paper by Jost, Luttinger, and Slotnick,[8] on the basis of unpublished work by Wheeler and Toll.

Before turning to the actual calculations we note first that Delbrück scattering to first order in the external field vanishes identically because of Furry's theorem.[9] In carrying the calculation to second order in the Coulomb field, one finds soon that the manifold integrals involved cannot be expressed in terms of known functions and that a numerical solution is in general extremely impracticable. Valid approximations for intermediate angles also seem extremely obscure. We decided, therefore, to restrict ourselves first to forward scattering. This will enable us to carry out the calculation exactly and to express the final result in closed form. Also, we will be able to use the method of analytic continuation. Finally, we expect to provide a basis for calculations at other angles.

In the following we shall first give the Feynman method (method A). This is a very straightforward calculation, but extremely complicated and tedious in its actual performance. It seems to us that a brief sketch of this method and the essential technical points used should be sufficient. The analytic continuation method (method B) is given in much greater detail, since it is not so well known and is very much simpler than the other method. In B we assume the total pair production cross section as known and use a well-known theorem of optics to write down directly the absorptive (imaginary) part of the Delbrück scattering amplitude in the forward direction. The analyticity of the scattering matrix is then used to find the dispersive (real) part of this amplitude.

The final section contains a discussion of the results[10] and a comparison with earlier work.

Method A

The three different Feynman diagrams to be considered are shown in Fig. 1. The crosses stand for the action of the static potential

$$V(r)=Ze/r=(Ze/2\pi^2)\int e^{i\mathbf{q}\cdot\mathbf{r}}d_3q/\mathbf{q}^2. \tag{1}$$

In the usual notation[11] the first diagram yields the following integral in a well-known manner,

$$A_4^{\mu}(\mathbf{q}_1)A_4^{\nu}(\mathbf{q}_2)\int\frac{\mathrm{Tr}[\gamma_\mu(i\mathfrak{p}-m)\gamma_4(i\mathfrak{p}-i\mathfrak{q}_1-m)\gamma_\nu(i\mathfrak{p}-i\mathfrak{q}_1-i\mathfrak{k}'-m)\gamma_4(i\mathfrak{p}+i\mathfrak{k}-m)]d_4p}{(p^2+m^2)[(p-q_1)^2+m^2][(p-q_1-k')^2+m^2][(p+k)^2+m^2]}, \tag{2}$$

where μ and ν are the directions of polarization of the incoming and outgoing waves, $k=(\mathbf{k}, i\omega)$ and $k'=(-\mathbf{k}, -i\omega)$ are the corresponding wave number four-vectors, and $q_1=(\mathbf{q}_1, 0)$ and $q_2=(\mathbf{q}_2, 0)$ are the momentum transfers of the two actions of the potential. $A_4(\mathbf{q})=iV(\mathbf{q})$ is the Fourier transform of the Coulomb potential, Eq. (1). The expression (2) must still be integrated over $\mathbf{q}_1$ and $\mathbf{q}_2$, but reduces to the threefold integral over $\mathbf{q}_1$ only because of momentum conservation. The result is—apart from constants—the required scattering amplitude which depends on the polarizations, the energy $|\mathbf{k}|=|\mathbf{k}'|=\omega$ and the scattering angle $\vartheta=\cos^{-1}(\mathbf{k}\cdot\mathbf{k}'/\omega^2)$.

It will be convenient to use natural units ($\hbar=c=m=1$) and the following variables:

$$\begin{aligned} 2\mathbf{Q}&=\mathbf{q}_2-\mathbf{q}_1, \quad Q=(\mathbf{Q}, 0)\\ 2\mathbf{P}&=\mathbf{k}'-\mathbf{k}, \quad P=(\mathbf{P}, 0)\\ 2\mathbf{K}&=\mathbf{k}'+\mathbf{k}, \quad K=(\mathbf{K}, i\omega), \end{aligned} \tag{3}$$

which satisfy

$$\mathbf{K}\cdot\mathbf{P}=0, \quad \mathbf{K}^2+\mathbf{P}^2=\omega^2.$$

If we now restrict ourselves to forward scattering, we have $\mathbf{P}=0$, $\mathbf{K}=\mathbf{k}=\mathbf{k}'$. The scattering of an unpolarized beam is, in this case, equal to the scattering of a linearly polarized beam in the plane perpendicular to its polarization. No change of the direction of polarization can occur for forward scattering. Therefore, the traces can be easily carried out.

The method of integration over p is well known[12] and need not be given here. It introduces the auxiliary variables x, y, z. There result three kinds of terms which will be called $M_I^{(0)}$, $M_I^{(2)}$, and $M_I^{(4)}$. With the proper

[8] Jost, Luttinger, and Slotnick, Phys. Rev. **80**, 189 (1950).
[9] See F. J. Dyson, Phys. Rev. **75**, 486, 1736 (1949).

[10] Most of the results obtained in this paper were reported at the Washington meeting of the American Physical Society; see Phys. Rev. **83**, 218 (1951). Unfortunately, the numerical values quoted there for a_1 are in error. The corrected values are shown in Table I of the present paper.

[11] $x=(x_1, x_2, x_3, x_4)=(\mathbf{r}, x_4)=(x, y, z, i\tilde{t})$; $\mathfrak{p}=\Sigma\gamma_\mu p_\mu$; $d_4x=dxdydzd\tilde{t}$; $c=1$.

[12] See R. P. Feynman, Phys. Rev. **76**, 769 (1949). In order to assure gauge invariance, regulators can be used. The condition $\Sigma c_i=0$ is sufficient in this case.

constants, the contribution of the first diagram to the forward scattering amplitude (in units of $(\alpha Z)^2 r_0$) is

$$a_I(\omega,0)=\int (M_I^{(0)}+M_I^{(2)}+M_I^{(4)})d_5Q/\mathbf{Q}^4, \tag{4}$$

$$M_I^{(0)}=\int_0^1 dx\int_0^x dy\int_0^y dz P_I^{(0)}\Big/ b_I^2,$$

$$M_I^{(2)}=\int_0^1 dx\int_0^x dy\int_0^y dz P_I^{(2)}\Big/ b_I, \tag{5}$$

$$M_I^{(4)}=\int_0^1 dx\int_0^x dy\int_0^y dz P_I^{(4)}\ln b_I,$$

$$b_I=1+2\mathbf{K}\cdot\mathbf{Q}(z+y(y-x-z))+\mathbf{Q}^2y(1-y). \tag{6}$$

$P_I^{(0)}$, $P_I^{(2)}$, and $P_I^{(4)}$ are essentially the traces which multiply the 0th, 2nd, and 4th power of $\not{p}$ in the expression (2). They are linear combinations of ω^2, $\mathbf{Q}^2$, $\mathbf{K}\cdot\mathbf{Q}$, $(\mathbf{e}\cdot\mathbf{Q})^2$, $\mathbf{Q}^4$, $(\mathbf{K}\cdot\mathbf{Q})^2$, $\omega^2\mathbf{Q}^2$, $\omega^2(\mathbf{K}\cdot\mathbf{Q})$, $\mathbf{Q}^2(\mathbf{K}\cdot\mathbf{Q})$, and $\omega^2(\mathbf{e}\cdot\mathbf{Q})^2$; the coefficients are polynomials of up to fourth order in x, y, and z. $\mathbf{e}$ is a unit vector in the direction of polarization.

This whole procedure has to be repeated for the diagrams II and III of Fig. 1. The results are completely analogous to (4), (5), and (6).

The integrals in (5) deserve special attention. As was pointed out by several authors,[9,12] the method of integration over p actually implies that the singularities on the real p_0 axis, i.e., $p_0=\pm(\mathbf{p}^2+m^2)^{\frac{1}{2}}$ are moved slightly into the upper (or lower) half-planes. In other words, the path of integration around the singularities has to be properly taken into account. It contributes a purely imaginary term to be added to the principle part of the integral. If we restrict the integration first to the principle parts, the result will be the diffractive or real part, a_1, of the scattering amplitude. The absorptive or imaginary part, a_2, is found best by assuming the electron mass to have a small negative imaginary part. The integrals in (4) are now well defined, since the expression (5) for b_I should be augmented by a term $-i\epsilon$, where ϵ is eventually taken in the limit zero.

From here on the calculation is quite straightforward, but extremely complex and tedious, even though the specialization to $\vartheta=0$ simplifies the task considerably.

The integration over the three auxiliary variables x, y, and z can be reduced to a double integral by a judicious change of variables, having b_I, b_{II}, and b_{III} independent of one of the three new variables, and maintaining a simple region of integration. For example the sequence of variable changes required for b_I is

Variable			Region of integration	
x	y	z	$\int_0^1 dx\int_0^x dy\int_0^y dz$	(7a)
$u=1-x$	$v=y$	$w=y-z$	$\int_0^1 dv\int_0^{1-v} du\int_0^v dw$	(7b)
$u=(1-v)\zeta$	$v=v$	$w=v\xi$	$\int_0^1 v(1-v)dv\int_0^1 d\zeta\int_0^1 d\xi$	(7c)
$\zeta=\zeta$	$v=v$	$\eta=\xi-\zeta$	$\int_0^1 v(1-v)dv\int_0^1 d\eta\int_0^{1-\eta} d\zeta$ $+\int_0^1 v(1-v)dv\int_{-1}^0 d\eta\int_{-\eta}^1 d\zeta.$	(7d)

At this stage we have

$$b_I=1+v(1-v)[\mathbf{Q}^2-2\mathbf{K}\cdot\mathbf{Q}\eta]. \tag{8a}$$

In the second term of the last step, (7d), let $\eta\rightarrow-\eta$ and $\mathbf{Q}\rightarrow-\mathbf{Q}$ simultaneously, leaving b_I unchanged and the region of integration becomes

$$\int_0^1 v(1-v)dv\int_0^1 d\eta\left(\int_0^{1-\eta} d\zeta_1+\int_\eta^1 d\zeta_2\right). \tag{9a}$$

If we finally let

$$Y=1-\eta,\quad \zeta_2=1-\zeta_3, \tag{7e}$$

we obtain

$$b_I=1+v(1-v)(\mathbf{Q}^2-2\mathbf{K}\cdot\mathbf{Q}+2\mathbf{K}\cdot\mathbf{Q}Y), \tag{8b}$$

with the region of integration

$$\int_0^1 v(1-v)dv\int_0^1 dY\left(\int_0^Y d\zeta_1+\int_0^Y d\zeta_3\right). \tag{9b}$$

The regions of integration for the two terms are now the same, but the integrand in the second term of Eq. (9b) must include the changes $\mathbf{Q}\rightarrow-\mathbf{Q}$, $\eta\rightarrow-\eta$, and $\zeta\rightarrow1-\zeta$ before combination with the integrand in the first term.

Similar changes bring the integrals in II and III into the same form,[13] allowing complete combination of all integrand polynomials. In all cases the ζ integration is trivial, and the required integrals reduce to the following

[13] Note that the integrals for diagrams II and III of Fig. 1 differ only in the sign of $\mathbf{Q}$, since each integral is equal to its Hermitian adjoints.

general forms

$$\int_0^1 v^m dv \int_0^1 Y^n dY \ln b_I \quad m=1,2 \qquad n=1 \quad (10a)$$

$$\int_0^1 v^m dv \int_0^1 Y^n dY \Big/ b_I \quad m=1,2,3,4 \qquad n=1,2,3 \quad (10b)$$

$$\int_0^1 v^m dv \int_0^1 Y^n dY \Big/ b_I^2 \quad m=1,2,3,4,5,6 \quad n=1,2,3,4 \quad (10c)$$

with b_I given by Eq. (8b). The Y integration is straightforward, though complicated, and leads to algebraic forms in v as well as a logarithmic term. The algebraic terms can once again be integrated without difficulty, and in most cases the logarithmic term can be integrated by parts. The one integral which is not straightforward is

$$\tfrac{1}{2}L_a = \int_0^1 \frac{dv}{v} \ln[1+av(1-v)] \qquad (11)$$

which is most easily performed by differentiating with respect to a.

$$\frac{\tfrac{1}{2}dL_a}{da} = \int_0^1 \frac{(1-v)dv}{1+av(1-v)} = \frac{1}{\sqrt{a}(a+4)^{\frac{1}{2}}} \ln\left[\frac{(4+a)^{\frac{1}{2}}+\sqrt{a}}{(4+a)^{\frac{1}{2}}-\sqrt{a}}\right]. \qquad (12)$$

Very fortunately, the factor $1/[a(a+4)]^{\frac{1}{2}}$ is the derivative of the logarithmic term so that we have

$$L_a = \left[\ln\left(\frac{[4+a]^{\frac{1}{2}}+\sqrt{a}}{[4+a]^{\frac{1}{2}}-\sqrt{a}}\right)\right]^2. \qquad (13)$$

The constant in the integrations over a is evaluated in the limit $a=0$ and vanishes.

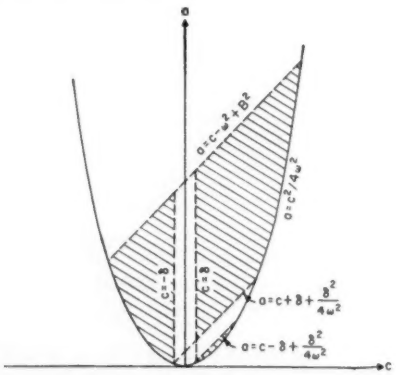

FIG. 2. Region for the a–c-integration.

At this point the quantity $(\mathbf{e}\cdot\mathbf{Q})^2$ is averaged over polarizations giving

$$\langle(\mathbf{e}\cdot\mathbf{Q})^2\rangle_{\text{av}} = \tfrac{1}{2}\mathbf{Q}^2 \sin^2\theta_{KQ} = \tfrac{1}{2}(\mathbf{Q}^2+(\mathbf{K}\cdot\mathbf{Q})^2/\omega^2).$$

The result of the Y and v integrations can be written as

$$a(\omega,0) = \int [L_a f_1(a_1c)+L_b f_2(b_1c)+T_a f_3(a_1c) + T_b f_4(b_1c)+f_5(a_1c)]d_3Q/Q^4, \qquad (14)$$

where L_a is given by Eq. (13),

$$T_a = \frac{(4+a)^{\frac{1}{2}}}{\sqrt{a}} \ln\left[\frac{(4+a)^{\frac{1}{2}}+\sqrt{a}}{(4+a)^{\frac{1}{2}}-\sqrt{a}}\right], \qquad (15)$$

$$a = b+c = \mathbf{Q}^2, \qquad (16a)$$

$$b = \mathbf{Q}^2 - 2\mathbf{K}\cdot\mathbf{Q}, \qquad (16b)$$

$$c = 2\mathbf{K}\cdot\mathbf{Q}, \qquad (16c)$$

and the f_i are algebraic functions of a, b, c (separable into simple polynomials and quotients, i.e., $1/c$, a^2/c^3, b^2/c^4, $1/c(a+4)$, etc.).

The d_3Q integration reduces to the double integral $\int \mathbf{Q}^2 dQ \int d(\mathbf{Q}\cdot\mathbf{K}/QK)$ because of the azimuthal symmetry of zero angle scattering. $\mathbf{Q}\cdot\mathbf{K}/QK$ is the cosine of the angle of $\mathbf{Q}$ referred to the polar direction $\mathbf{K}$. The terms in (14) separate readily into some terms expressed as functions of a and c, and others expressed as functions of b and c. If the integrand is expressed in terms of a and c the region of integration is

$$\int_0^\infty \frac{da}{4\omega} \int_{-2\omega\sqrt{a}}^{2\omega\sqrt{a}} dc, \qquad (17)$$

whereas if the integrand is in terms of b and c the region may be obtained by substituting $a=b+c$ in (17):

$$\int_0^\infty \frac{da}{4\omega} \int_{-2\omega\sqrt{a}}^{2\omega\sqrt{a}} dc = \int_{-\infty}^\infty \frac{dc}{4\omega} \int_{c^2/4\omega^2}^\infty da = \int_{-\infty}^\infty \frac{dc}{4\omega} \int_{c^2/4\omega^2-c}^\infty db = \int_{-\omega^2}^\infty \frac{db}{4\omega} \int_{2\omega^2-2\omega(\omega^2+b)^{\frac{1}{2}}}^{2\omega^2+2\omega(\omega^2+b)^{\frac{1}{2}}} dc. \qquad (18)$$

The required integrations are therefore

$$\int_0^\infty \frac{da}{4\omega a^2} L_a \int_{-2\omega\sqrt{a}}^{2\omega\sqrt{a}} dc f_1(a_1c) + \int_0^\infty \frac{da}{4\omega a^2} T_a \int_{-2\omega\sqrt{a}}^{2\omega\sqrt{a}} dc f_3(a_1c) + \int_0^\infty \frac{da}{4\omega a^2} \int_{-2\omega\sqrt{a}}^{2\omega\sqrt{a}} dc f_5(a_1c), \qquad (19)$$

and

$$\int_0^\infty \frac{zdz}{2\omega} L_{z^2-\omega^2} \int_{2\omega^2-2\omega z}^{2\omega^2+2\omega z} \frac{dc}{(c+z^2-\omega^2)^2} f_2(z^2-\omega^2, c)$$
$$+\int_0^\infty \frac{zdz}{2\omega} T_{z^2-\omega^2} \int_{2\omega^2-2\omega z}^{2\omega^2+2\omega z} \frac{dc}{c+z^2-\omega^2} f_1(z^2-\omega^2, c), \quad (20)$$

where $z^2=\omega^2+b$. Since we have arranged to do integrations over a and b (or z) last in (19) and (20), respectively, the c-integration (over simple but lengthy algebraic forms) offers no problem.

However, we have created a new problem for ourselves by the separation of (14) into (19) and (20) for integration purposes. Although (14) in its entirety is convergent (and integrable) throughout the range of integration, neither (19) nor (20) is convergent. Poles have been introduced at

$$a=0 \text{ and } \infty, \quad b=0 \text{ and } \infty, \quad \text{and} \quad c=0.$$

They have been brought in by the separation and appear in the f's as well as in the result of the c integration. We have used a consistent pair of cutoffs, δ and B as shown in Figs. 2 and 3, to make (19) and (20) finite. The integrations in each case are carried out over the shaded region only, each integration having to be broken up into several "pieces." Of course, after the evaluation of (19) and (20) in the limit $\delta\to 0$, $B\to\infty$, the cut-off dependent terms must and do vanish.

After the c-integration in (19) has been performed, there remain the integrations over a of the form

$$\int da L_a/a^n, \quad \int da T_a/a^n, \quad (21)$$

and of other less complicated forms which can be readily evaluated. The two forms in (21) may be evaluated for $n\neq 1$ ($n=1$ does not occur) by integration by parts.

After the c-integration in (20), it becomes convenient to express the final integration once again in terms of b, and many of the resulting forms are the same as in (21). With the aid of several contour integrations in the upper (or lower) half b plane the forms may all be expressed in terms of the following four functions:

$$C_1(p)=\mathrm{Re}\int_0^{1/p} \frac{\sin^{-1}x}{x}\cosh^{-1}\frac{1}{px}dx, \quad (22a)$$

$$D_1(p)=\mathrm{Re}\int_0^{1/p} \frac{\cosh^{-1}(1/px)}{(1-x^2)^{\frac{1}{2}}}dx, \quad (22b)$$

$$E_1(p)=\mathrm{Re}\int_0^{1/p} \left(\frac{1-p^2x^2}{1-x^2}\right)^{\frac{1}{2}}dx, \quad (22c)$$

$$F_1(p)=\mathrm{Re}\int_0^{1/p} \frac{dx}{[(1-x^2)(1-p^2x^2)]^{\frac{1}{2}}}. \quad (22d)$$

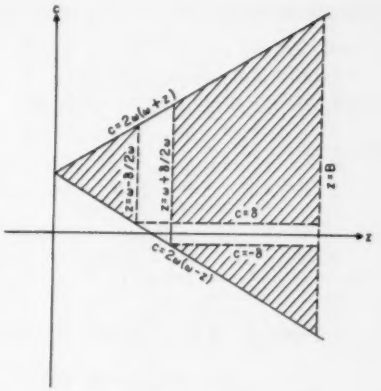

FIG. 3. Region for the b-c-integration.

The result of the combination of all terms gives for the real part of the matrix element.

$$a_1(\omega,0)=(p/\pi)(2C_1(p)-D_1(p))$$
$$+(1/27\pi p)[(109+64p^2)E_1(p)$$
$$-(67+6p^2)(1-p^2)F_1(p)]-p^2/9-9/4, \quad (23)$$

where $p=2/\omega$, and $a(\omega,0)=a_1(\omega,0)+ia_2(\omega,0)$.

The imaginary part of the matrix element arises from the b-integration alone and only from the L_b and T_b terms. These two functions defined in (13) and (15) are real for $b>-4$ and complex for $b<-4$. Since the b-integration goes from $-\omega^2$ to $+\infty$, there will be no imaginary contribution for $\omega\leqslant 2$, but there will be one for $\omega>2$, the contribution coming directly from the range $-\omega^2\leqslant b\leqslant -4$. The complete expressions for L_a and T_a are

$$L_a=2\lim_{\epsilon\to 0}\int_0^1 \ln(1-i\epsilon+az(1-z))dz/z$$
$$=(2\sinh^{-1}\tfrac{1}{2}\sqrt{a})^2 \quad (a\geqslant 0) \quad (24)$$
$$=-(2\sin^{-1}\tfrac{1}{2}\sqrt{-a})^2 \quad (-4\leqslant a\leqslant 0)$$
$$=(2\cosh^{-1}\tfrac{1}{2}\sqrt{-a})^2-\pi^2-4\pi i\cosh^{-1}\tfrac{1}{2}\sqrt{-a} \quad (a\leqslant -4)$$

$$T_a=2\lim_{\epsilon\to 0}\int_0^1 dz\ln(1-i\epsilon+az(1-z))$$
$$=2(1+4/a)^{\frac{1}{2}}\sinh^{-1}\tfrac{1}{2}\sqrt{a} \quad (a\geqslant 0) \quad (25)$$
$$=2(-1-4/a)^{\frac{1}{2}}\sin^{-1}\tfrac{1}{2}\sqrt{-a} \quad (-4\leqslant a\leqslant 0)$$
$$=(1+4/a)^{\frac{1}{2}}(2\cosh^{-1}\tfrac{1}{2}\sqrt{-a}-i\pi) \quad (a\leqslant -4).$$

To obtain the imaginary part we start with the b-integration in Eq. (18) between the limits $-\omega^2$ and -4. There are, therefore, no cut-off considerations to complicate the algebra. The integrations otherwise proceed

as before and the result is

$$a_2(\omega, 0)=0 \quad (\omega\leqslant 2)$$
$$=(p/\pi)[2C_2(p)-D_2(p)]-(1/27\pi p)$$
$$\times[(109+64p^2)E_2(p)-(67+6p^2)(1-p^2)F_2(p)], \quad (\omega>2) \quad (26)$$

where

$$C_2(p)=\int_1^{1/p}\frac{\cosh^{-1}x}{x}\cosh^{-1}\frac{1}{px}dx, \quad (27a)$$

$$D_2(p)=\int_1^{1/p}\frac{\cosh^{-1}(1/px)}{(x^2-1)^{\frac{1}{2}}}dx, \quad (27b)$$

$$E_2(p)=\int_1^{1/p}\left(\frac{1-p^2x^2}{x^2-1}\right)^{\frac{1}{2}}dx, \quad (27c)$$

$$F_2(p)=\int_1^{1/p}\frac{dx}{[(x^2-1)(1-p^2x^2)]^{\frac{1}{2}}}, \quad (27d)$$

Comparison of Eqs. (23) and (26) shows that the real and imaginary parts are identical in form except for the last two terms of a_1, which are missing in a_2. Similarly, the functions C_1 and C_2, etc., are closely related.

For actual calculations the functions C and D can easily be expanded in power series, whereas the functions E_1, E_2, and F_1, F_2, can be expressed in terms of the complete elliptic integrals of the first and second kind, $F(x)$ and $E(x)$. We have

$$E_1(p)=E(p) \quad (p\leqslant 1),$$
$$=pE(1/p)+(1/p-p)F(1/p) \quad (p\geqslant 1),$$
$$F_1(p)=F(p) \quad (p\leqslant 1),$$
$$=(1/p)F(1/p) \quad (p\geqslant 1),$$
$$E_2(p)=F[(1-p^2)^{\frac{1}{2}}]-E[(1-p^2)^{\frac{1}{2}}] \quad (p\leqslant 1),$$
$$F_2(p)=F[(1-p^2)^{\frac{1}{2}}] \quad (p\leqslant 1).$$

The power series expansions break down near $p=1$ where one has to proceed numerically. In particular one finds

$$C_1(1)=1.62876, \quad (28a)$$

$$D_1(1)=1.83193. \quad (28b)$$

$D_1(1)$ is twice Catalan's constant.[14]

Method B

Consider Cauchy's theorem for an analytic function

$$w(z)=\frac{1}{2\pi i}\oint\frac{w(\zeta)d\zeta}{\zeta-z}.$$

Let z be on the real axis, $z=x$, and assume that w is regular in the upper half-plane. We can choose the path of integration to follow the real axis from $-R$ to $+R$ with a small half-circle in the positive direction around the point x, and to close in a large half-circle R over the upper half-plane of the complex variable $\zeta=\xi+i\eta$. We thus find

$$w(x)=\frac{1}{2\pi i}\mathrm{P}\int_{-R}^{R}\frac{w(\xi)d\xi}{\xi-x}+\tfrac{1}{2}w(x)+\frac{1}{2\pi i}\int_R\frac{w(\zeta)}{\zeta}d\zeta, \quad (29)$$

where in the last integral x has been neglected. We further assume that $w(\zeta)/\zeta$ is regular at $\zeta=0$, so that

$$\int_R\frac{w(\zeta)}{\zeta}d\zeta=-\int_{-R}^{R}\frac{w(\xi)}{\xi}d\xi.$$

We separate $w(\xi)$ into its real and imaginary part and find from Eq. (29) and the last equation in the limit $R\to\infty$,

$$u(\xi)=\frac{x}{\pi}\mathrm{P}\int_{-\infty}^{\infty}\frac{v(\xi)d\xi}{\xi(\xi-x)}, \quad (30a)$$

$$v(\xi)=\frac{-x}{\pi}\mathrm{P}\int_{-\infty}^{\infty}\frac{u(\xi)d\xi}{\xi(\xi-x)}. \quad (30b)$$

The complex scattering amplitude $a(\omega, 0)=a_1(\omega, 0)+ia_2(\omega, 0)$ satisfies the assumptions[15] made about $w(\xi)$ when ξ is identified with the energy ω.

A well-known theorem of optics[16] relates the total absorption cross section $\sigma_{\mathrm{abs}}(\omega)$ and the forward scattering amplitude $a(\omega, 0)$

$$\sigma_{\mathrm{abs}}(\omega)=4\pi\lambda\,\mathrm{Im}a(\omega, 0)=2\pi pa_2(\omega, 0). \quad (31)$$

The absorption process that corresponds to the elastic scattering of light by a Coulomb field is pair production. The total pair production cross section is well known. We will use the analytical form obtained by Jost, Luttinger, and Slotnick.[17]

In our notation we therefore find without calculation

$$a_2(\omega, 0)=0 \quad (\omega\leqslant 2)$$
$$=(p/\pi)[2C_2(p)-D_2(p)]$$
$$+(1/27p\pi)[-(109+64p^2)E(\{1-p^2\}^{\frac{1}{2}})$$
$$+(42+125p^2+6p^4)F(\{1-p^2\}^{\frac{1}{2}})] \quad (\omega\geqslant 2). \quad (32)$$

Making use of the fact that $\sigma_{\mathrm{abs}}(\omega)$ is an even function of ω we find from Eq. (30a)

$$a_1(\omega, 0)=(\omega^2/4\pi^2)\mathrm{P}\int_{-\infty}^{\infty}\frac{\sigma_{\mathrm{abs}}(\omega')d\omega'}{\omega'(\omega'-\omega)} \quad (33a)$$

$$=(\omega^2/2\pi^2)\mathrm{P}\int_2^{\infty}\frac{\sigma_{\mathrm{abs}}(\omega')d\omega'}{\omega'^2-\omega^2} \quad (33b)$$

$$=\frac{1}{\pi^2}\mathrm{P}\int_0^1\frac{\sigma_{\mathrm{abs}}(p')dp'}{p^2-p'^2}. \quad (33c)$$

[14] See E. Jahnke and F. Emde, *Tables of Functions* (Dover Publications, Inc., New York, 1943), p. 80.

[15] See also the remarks at the end of this paper.

[16] Recently, a very general proof was given by M. Lax, Phys. Rev. **78**, 306 (1950). Further references may be found in this paper.

[17] See reference 8. Two misprints in their paper should be noted: in Eq. (56) the sign of $82a^3/3$ and in Eq. (57) the sign of $2F_1(\alpha)$ are wrong.

Although the functions C_2, D_2, E, and F are quite complicated, the integration indicated in Eq. (33c) can be carried out without serious difficulties and the result can be found in terms of a closed expression.

In the remainder of this section we will briefly indicate how this integration can be carried out.

The integral containing the function $C_2(p)$ is

$$\mathrm{P}\int_0^1 \frac{p'^2 C_2(p')dp'}{p^2-p'^2}$$

$$=\mathrm{P}\int_0^1\left(-1+\frac{p^2}{p^2-p'^2}\right)dp'\int_1^{1/p}\frac{\cosh^{-1}x}{x}\cosh^{-1}\frac{1}{p'x}dx$$

$$=\mathrm{P}\int_0^1\frac{dy}{y}\cosh^{-1}\frac{1}{y}\int_0^y\left(-1+\frac{p^2}{p^2-p'^2}\right)\cosh^{-1}\frac{y}{p'}dp',$$

where we used $y=p'x$ and interchanged the order of the integration. An elementary integration yields for the first term $-\pi^2/4$. The second term becomes by partial integration

$$p^2\mathrm{P}\int_0^1\frac{dy}{y}\cosh^{-1}\frac{1}{y}\int_0^y\frac{dp'}{p^2-p'^2}\cosh^{-1}\frac{y}{p'}$$

$$=\frac{p}{2}\int_0^1 dy\cosh^{-1}\frac{1}{y}\int_0^y\ln\left|\frac{p+p'}{p-p'}\right|\frac{dp'}{p'(y^2-p'^2)^{\frac{1}{2}}}$$

$$=\frac{p}{2}\pi\int_0^1\frac{dy}{y}\cosh^{-1}\frac{1}{y}\,\mathrm{Re}\sin^{-1}\frac{y}{p}.$$

Here, we made use of the equality[18]

$$\mathrm{Re}\int_0^1\ln\frac{1+ax}{1-ax}\frac{dx}{x(1-x^2)^{\frac{1}{2}}}=\pi\,\mathrm{Re}\sin^{-1}a. \qquad (34)$$

Combining these results we find

$$\mathrm{P}\int_0^1\frac{p'^2C_2(p')dp'}{p^2-p'^2}=-\frac{\pi^2}{4}+\tfrac{1}{2}\pi pC_1(p), \qquad (35)$$

where $C_1(p)$ is identical with the function defined in (22a) as it resulted in method A.

The term in $D_2(p)$ of Eq. (33c) is treated similarly:

$$\mathrm{P}\int_0^1\frac{p'^2D_2(p')dp'}{p^2-p'^2}$$

$$=\mathrm{P}\int_0^1\left(-1+\frac{p^2}{p^2-p'^2}\right)dp'\int_1^{1/p}\frac{\cosh^{-1}(1/p'x)}{(x^2-1)^{\frac{1}{2}}}dx.$$

The first term gives $-\pi^2/4$ as before; the second term is

$$\mathrm{P}\int_0^1\frac{p^2dp'}{p^2-p'^2}\int_{p'}^1\frac{\cosh^{-1}(1/y)}{(y^2-p'^2)^{\frac{1}{2}}}dy$$

$$=\mathrm{P}\int_0^1\cosh^{-1}\frac{1}{y}dy\int_0^y\frac{p^2dp'}{(p^2-p'^2)(y^2-p'^2)^{\frac{1}{2}}}$$

$$=\frac{\pi p}{2}\,\mathrm{Re}\int_0^1\cosh^{-1}\frac{1}{y}\frac{dy}{(p^2-y^2)^{\frac{1}{2}}}$$

$$=\frac{p\pi}{2}\,\mathrm{Re}\int_0^{1/p}\frac{dx}{(1-x^2)^{\frac{1}{2}}}\cosh^{-1}\frac{1}{px}dx.$$

The result for the term in D_2 is therefore

$$\mathrm{P}\int_0^1\frac{p'^2D_2(p')dp'}{p^2-p'^2}=-\frac{\pi^2}{4}+\tfrac{1}{2}\pi pD_1(p), \qquad (36)$$

where $D_1(p)$ is identical with the function defined in Eq. (22b).

The integration of the terms of Eq. (33c) which involve complex elliptic integrals of the first and second kind may be done as follows:[19]

$$\int_0^1 F[(1-p^2)^{\frac{1}{2}}]dp$$

$$=\int_0^1\frac{dx}{(1-x^2)^{\frac{1}{2}}}\int_0^1\frac{dp}{(1-x^2+p^2x^2)^{\frac{1}{2}}}$$

$$=\int_0^1\frac{dx}{x(1-x^2)^{\frac{1}{2}}}\tan^{-1}x=\frac{\pi^2}{4}, \qquad (37)$$

$$\int_0^1 p^2F[(1-p^2)^{\frac{1}{2}}]dp=\tfrac{1}{2}\int_0^1\frac{dx}{x}\frac{1}{(1-x^2)^{\frac{1}{2}}}$$

$$\times\left[\tanh^{-1}x+\frac{1}{x}\left(1-\frac{\tan^{-1}x}{x}\right)\right]$$

$$=\tfrac{1}{2}(\pi^2/4-\pi^2/8)=\pi^2/16, \qquad (38)$$

$$\int_0^1\frac{F[(1-p'^2)^{\frac{1}{2}}]}{p^2-p'^2}dp'$$

$$=\frac{1}{2p}\,\mathrm{Re}\int_0^1\frac{dx}{(1-x^2)^{\frac{1}{2}}}\frac{1}{(1-(1-p^2)x^2)^{\frac{1}{2}}}$$

$$\times\ln\frac{1+p^{-1}(1-(1-p^2)x^2)^{\frac{1}{2}}}{1-p^{-1}(1-(1-p^2)x^2)^{\frac{1}{2}}}$$

$$=\frac{\pi}{2p}\,\mathrm{Re}F\left(p,\sin^{-1}\frac{1}{p}\right)=\frac{\pi}{2p}F_1(p). \qquad (39)$$

[18] D. Bierens de Haan, *Nouvelles Tables d'Integrales Definies* (Stechert, New York, 1939), Table 122 (2).

[19] See reference 18, Table 122, (10).

The last integration can again be found in Bierens de Haan.[20]

In a similar way one finds

$$\int_0^1 E[(1-p^2)^{\frac{1}{2}}]dp=\pi^2/8, \tag{40}$$

$$\int_0^1 \frac{E[(1-p'^2)^{\frac{1}{2}}]}{p^2-p'^2}dp'$$

$$=-\int_0^1 \frac{x^2dx}{(1-x^2)^{\frac{1}{2}}}\int_0^1 \frac{dp'}{(1-x^2+p'^2x^2)^{\frac{1}{2}}}$$

$$+\int_0^1 \frac{1-x^2+p^2x^2}{(1-x^2)^{\frac{1}{2}}}dx\cdot \mathrm{P}\int_0^1 \frac{dx}{(p^2-p'^2)(1-x^2+p'^2x^2)^{\frac{1}{2}}}$$

$$=-\frac{\pi}{2}+\frac{1}{2p}\,\mathrm{Re}\int_0^1 dx\left(\frac{1-x^2+p^2x^2}{1-x^2}\right)^{\frac{1}{2}}$$

$$\times\ln\frac{1+p^{-1}(1-x^2+p^2x^2)^{\frac{1}{2}}}{1-p^{-1}(1-x^2+p^2x^2)^{\frac{1}{2}}}.$$

We can use the identity

$$\mathrm{Re}\int_0^1 dx\left(\frac{1-r^2x^2}{1-x^2}\right)^{\frac{1}{2}}\ln\frac{1+q(1-r^2x^2)^{\frac{1}{2}}}{1-q(1-r^2x^2)^{\frac{1}{2}}}$$

$$\equiv\mathrm{Re}\frac{\pi}{q}\int_0^1\frac{dx}{x^2}\left[\frac{1}{(1-q^2x^2)^{\frac{1}{2}}[1-(1-r^2)q^2x^2]^{\frac{1}{2}}}-1\right],$$

and find with $y=1/x$

$$-\frac{\pi}{2}+\frac{\pi}{2}\,\mathrm{Re}\int_0^1\frac{dx}{x^2}\left(\frac{p}{[(1-x^2)(p^2-x^2)]^{\frac{1}{2}}}-1\right)$$

$$=-\frac{\pi}{2}+\frac{\pi}{2}\,\mathrm{Re}\left(\frac{1}{2}\int_{-\infty}^{\infty}-\frac{1}{2}\int_{-1}^{1}\right)$$

$$\times dy\left(\frac{py^2}{[(y^2-1)(p^2y^2-1)]^{\frac{1}{2}}}-1\right)$$

$$=-\frac{\pi}{2}-\frac{\pi}{2}\,\mathrm{Re}\int_0^1 dy\left(\frac{py^2}{-[(1-y^2)(1-p^2y^2)]^{\frac{1}{2}}}-1\right),$$

since the first integral vanishes. Thus[21]

$$\mathrm{P}\int_0^1\frac{E[(1-p'^2)^{\frac{1}{2}}]}{p^2-p'^2}dp'=\frac{\pi}{2p}[F_1(p)-E_1(p)], \tag{41}$$

where F_1 and E_1 are identical with the functions defined in (22c and d).

It is easily seen that the real part of the forward scattering amplitude, $a_1(\omega, 0)$ as defined by (33c), (31), and (32), can be written with the aid of our intermediate results [Eqs. (35) to (41)], in terms of C_1, D_1, E_1, and F_1, as defined by (22). The final result is identical with the result in Eq. (23) of method A. It is easily seen that Eqs. (26) and (32) are also identical.

TABLE I. The forward scattering amplitude $a(\omega, 0)=a_1(\omega, 0)+ia_2(\omega, 0)$ in units of $(\alpha Z)^2r_0$ and the forward differential cross section in lead for some characteristic energy values.

Energy (Mev)	$a_1(\omega, 0)$	$a_2(\omega, 0)$	$d\sigma(\omega, 0)/d\Omega$ for Pb
0.411	0.0205	0	0.00428 mb/sterad
1.33	0.241	0.0058	0.591 mb/sterad
2.62	0.912	0.265	9.18 mb/sterad
17.6	11.87	14.5	3.57 b/sterad
200	150	395	1.82 kb/sterad

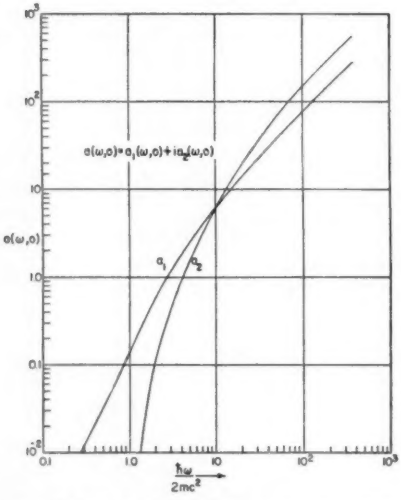

FIG. 4. Delbrück scattering amplitude for forward scattering in units of $(\alpha Z)^2r_0$ as a function of energy.

DISCUSSION OF RESULTS

The dispersive and absorptive parts of the forward scattering amplitude are plotted *versus* energy in Fig. 4. Up to about 10 Mev the dispersive part dominates, whereas for higher energies the absorptive part is the larger of the two and dominates by orders of magnitude for very high energies. The divergence of the scattering amplitudes for very high energies is not surprising; the vacuum is an infinite source of pairs, and their production is limited only by the available energy. Compared with known phenomena involving an index of refraction, the vacuum has its "resonance" at $\omega=\infty$, such that there is no change of sign of the refractive index, and a_1 is positive throughout.

The differential Delbrück scattering cross section per unit solid angle, $d\sigma(\omega, 0)/d\Omega$ for $\vartheta=0$ is

$$d\sigma(\omega, 0)/d\Omega=|a_1(\omega, 0)+ia_2(\omega, 0)|^2(\alpha Z)^4r_0^2, \tag{42}$$

[20] See reference 18, Table 122 (15).

[21] See reference 18, Table 12 (9).

since our scattering amplitude is given in units of $(\alpha Z)^2 r_0$ where r_0 is the classical electron radius.

In the high energy limit one finds easily

$$a_1(\omega, 0) = 7\omega/18 \qquad (\omega \gg 1), \qquad (43a)$$

$$a_2(\omega, 0) = (7\omega/9\pi) \ln(2\omega) \quad (\omega \gg 1). \qquad (43b)$$

The latter is obviously in agreement with $\omega/4\pi$ times the high energy limit of the total pair production cross section.

Near the pair production threshold, $\omega = 2$, the absorption part is

$$a_2(\omega, 0) = \tfrac{1}{3}(1-2/\omega)^{\frac{3}{2}} \quad (\omega \gtrsim 2), \qquad (44)$$

which vanishes, of course, at the threshold.

In the low energy limit the Delbrück scattering amplitude becomes

$$a(\omega, 0) = a_1(\omega, 0) = (73/72)(\omega^2/32). \qquad (45)$$

This function is plotted in Fig. 5 together with the exact expression. The close agreement shows that nearly up to the pair production cross section Delbrück scattering is qualitatively almost entirely classical dipole scattering, the cross section being proportional to ω^4. The classical aspect is seen in the fact that the amplitude is independent of Planck's constant. Abandoning natural units for a moment, we find for the low energy limit

$$d\sigma(\omega, 0)/d\Omega = (73/72)^2(1/32)^2(\hbar\omega/mc^2)^4(\alpha Z)^4 r_0^2$$
$$= (73/72)^2(1/32)^2(\omega/c)^4 Z^4 (e^2/mc^2)^6. \qquad (45')$$

The only calculation in the literature on forward Delbrück scattering is a low energy limit by Kemmer and Ludwig.[6] Their work corresponds exactly to the calculations of Euler[1] on the scattering of light by light. They assume an arbitrary potential, which must fall off fast enough, however; therefore, they do not carry out the Q integration indicated in our Eq. (14). Taking the limit in this integral we find

$$a(\omega, 0) = (11/135) 32\pi\omega^2 \int dQ$$

in agreement with Kemmer and Ludwig.

A few characteristic numerical values for forward scattering are listed in Table I.

Experiments on the elastic scattering of light by heavy elements necessarily yield cross sections which are the result of interference of the following three phenomena: Thomson scattering by the nucleus, Rayleigh scattering by the electrons (primarily K-electrons, unless the energies are very low), and Delbrück scattering by the nuclear Coulomb field. All three

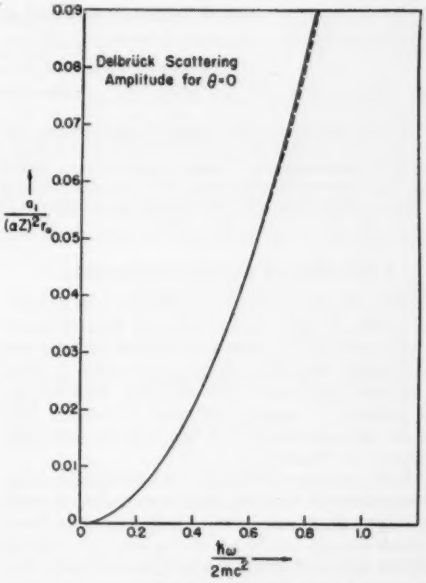

FIG. 5. Low energy limit of the Delbrück scattering amplitude (dashed line) compared with the exact curve (solid line).

effects are coherent. Since both Rayleigh and Delbrück scattering have complex scattering amplitudes—the photoeffect being the absorptive process associated with Rayleigh scattering—an analysis of these experiments cannot be made until the differential cross sections of these processes are known quantitatively.

In conclusion, we draw attention to the very elegant method of analytic continuation. Its applicability, however, needs further study. We assumed here that $a(\omega)$ fulfills all the conditions imposed on $w(\zeta)$. On the other hand, the validity of the assumption that $w(\zeta)/\zeta$ is regular at $\zeta = 0$ is guaranteed by gauge invariance for all processes involving real photons.

An application other than the one given here is, for example, the calculation of the elastic Rayleigh scattering for zero angle from the photoelectric absorption cross section. Also, convergence arguments may be used to infer from dispersion integrals like Eq. (33) an upper limit on the high energy behavior of the absorption process. Finally, Eq. (30b) can be used to infer the absorption cross section from the dispersive forward scattering.

Small Angle Scattering of Light by a Coulomb Field

H. A. BETHE AND F. ROHRLICH*
Laboratory of Nuclear Studies, Cornell University, Ithaca, New York
(Received December 5, 1951)

The angular distribution for small angles and the total cross section for Delbrück scattering (the elastic scattering of γ-rays by the Coulomb field of heavy nuclei) are calculated approximately. The method is a combination of an impact parameter and an analytic continuation method. It is valid for energies $\hbar\omega$ large compared to the electron rest energy mc^2. Curves are given for the shapes of the dispersive and absorptive parts of the differential cross section, valid for angles of order $mc^2/\hbar\omega$ or less.

I. METHOD OF IMPACT PARAMETERS

THE preceding paper[1] dealt with the forward scattering of light by the Coulomb field of heavy nuclei. Unfortunately, these results do not permit direct experimental verification. Exact calculations at other angles meet with considerable difficulty. However, recent preliminary experiments[2] seem to indicate that data for the scattering of high energy γ-rays into small angles can be obtained.

It is the purpose of this paper to calculate the shape and magnitude of the differential cross section for small angles in an approximation valid for high energies. Since at these energies nearly all of the incident wave is scattered into very small angles, this calculation will also give us an estimate of the total cross section. Achieser and Pomerantschuk pursued the same aim in a very complicated calculation.[3] Their results will be compared with ours in the last section of this paper.

We start our discussion from the well-known scattering formula of quantum mechanics which we apply to high energy γ-rays. The scattered amplitude in direction θ is

$$f(\theta)=-\tfrac{1}{2}i\lambda\sum_l(2l+1)(c_le^{2i\delta_l}-1)P_l(\cos\theta), \quad (1)$$

where λ is the wavelength of the γ-ray divided by 2π, δ_l is the phase shift for angular momentum l, and c_l is the absolute value of the amplitude of the outgoing radial wave l. If only scattering could occur, c_l would be equal to unity and (1) would reduce to the ordinary Rayleigh formula. Since the γ-rays can also be absorbed, forming electron pairs, c_l is less than 1, in fact,

$$1-c_l^2=\gamma_l \quad (2)$$

gives the probability of absorption for γ-rays of angular momentum l. If we succeed in calculating $f(\theta)$ from (1), its absolute square will give the differential cross section for potential scattering of γ-rays.

We shall first use the fact that the absorption probabilities γ_l and the phase shifts δ_l are small, of order $e^2/\hbar c$ or less [see Eq. (18), below]. Then we may write

$$-i(c_le^{2i\delta_l}-1)\equiv\alpha_l+i\beta_l, \quad (3)$$

$$\alpha_l\approx 2\delta_l, \quad (3a)$$

$$\beta_l=1-c_l\approx\tfrac{1}{2}\gamma_l. \quad (3b)$$

Next we note that an extremely large number of terms l contribute to the sum in (1), the number being of the order of a/λ where a is the radius of the atom. (For 100-Mev γ-rays, this is about 10,000 terms.) Therefore the sum in (1) may be replaced by an integral over the impact parameter,

$$b=\lambda l, \quad (4)$$

and the spherical harmonics may be replaced by their asymptotic expression for large l and small θ,

$$P_l(\theta)\approx J_0(l\theta)=J_0(bs), \quad (5)$$

where

$$s=\theta/\lambda=k\theta \quad (5a)$$

is the momentum change of the γ-ray, $k=1/\lambda$ is the wave number. Then the scattered amplitude will depend on the frequency ω and on s, and we may write

$$f(\theta)=a_1(s,\omega)+ia_2(s,\omega), \quad (6)$$

$$a_1(s,\omega)=k\int bdb\alpha(b,\omega)J_0(bs), \quad (7a)$$

$$a_2(s,\omega)=k\int bdb\beta(b,\omega)J_0(bs), \quad (7b)$$

where the quantities α and β are given in Eqs. (3a, b) and are now regarded as functions of the impact parameter b (and ω).

The quantity $\gamma(b,\omega)=2\beta(b,\omega)$ is the probability of pair production by a wave packet of γ-rays of frequency ω, traversing an atom at a distance b from the nucleus. This is a well-defined physical quantity which can in principle be obtained from the theory of pair production. We shall show in Sec. III how this may be done, while in Sec. II we shall give a simple approximation for γ. In any case, the total cross section for pair production may be written

$$\sigma_{\text{pair}}(\omega)=2\pi\int bdb\gamma(b,\omega), \quad (8)$$

* Now at Palmer Physical Laboratory, Princeton University, Princeton, New Jersey.
[1] F. Rohrlich and R. Gluckstern, Phys. Rev. **86**, 1 (1952).
[2] R. R. Wilson, private communication.
[3] A. Achieser and I. Pomerantschuk, Physik. Z. Sowjetunion **11**, 478 (1937).

so that γ is related to the partial pair cross section for impact parameter b.

There is no such simple physical meaning for the phase shift δ, and hence for $\alpha(b, \omega)$. However, we shall obtain α by the principle of analytic continuation which was already used successfully in the preceding paper. In fact, we shall assume that $\alpha(b, \omega)+i\beta(b, \omega)$ for fixed b, is an analytic function of ω. Then, from the theory of analytic continuation,

$$\alpha(b, \omega)=\frac{\omega}{\pi}\mathrm{P}\int_{-\infty}^{\infty}\frac{\beta(b, \omega')d\omega'}{(\omega'-\omega)\omega'}, \tag{9}$$

where P denotes the principal part.

Physically, our assumption means that we regard a *part* of the atom, *viz.*, the cylindrical ring between b and $b+db$, by itself as a dispersive medium for γ-rays. Rays of any frequency may be absorbed or scattered by this ring, and its refractive index may be obtained from the absorption coefficient by the usual formula of dispersion theory which is identical with (9). That it is possible to consider this ring independently of the rest of the atom depends on the possibility of constructing wave packets of γ-rays which only hit the ring but not (appreciably) the rest of the atom. For the validity of (9) it is necessary that such wave packets can be constructed for all frequencies ω' for which the absorption probability $2\beta(b, \omega')$ is appreciable. Here the particular properties of the pair production cross section are very helpful: $\sigma_{\text{pair}}(\omega)$ and hence $\gamma(b\,\omega)$ for all b are zero for $\omega<2mc^2$ and still small for frequencies slightly greater than $2mc^2$. Hence our wave packets need to be constructed only for wavelengths small compared to the Compton wavelength. But it is well known that wave packets can be constructed which define the position to about one wavelength. Therefore, if we permit the width of the ring db to be a Compton wavelength or larger, the wave packets can be constructed for all relevant values of ω'. But the pair production arises equally from all impact parameters b between the Compton wavelength and the atomic radius, and therefore a definition of the impact parameter to a Compton wavelength is sufficient.[4]

In order to use the formula (9), we must decide how β behaves for negative frequencies. But it was shown in the preceding paper that $a_2(s=0, \omega)$ is an odd function of ω. Since $k=\omega/c$, it then follows from (7b) that $\beta(b, \omega)$ is an even function of ω. This gives

$$\alpha(b, \omega)=\frac{\omega}{\pi}\mathrm{P}\int_{0}^{\infty}\beta(b, \omega')\left(\frac{1}{\omega'-\omega}+\frac{1}{\omega'+\omega}\right)\frac{d\omega'}{\omega'}. \tag{10}$$

In this way, we have expressed the amplitude of the potential (Delbrück) scattering of γ-rays, $f(\theta)$, in terms of the probability (partial cross section) for pair production as a function of frequency and impact parameter. The differential cross section for Delbrück scattering is of course

$$d\sigma_{\text{scatt}}/d\Omega=|f(\theta)|^2=a_1^2(\omega, s)+a_2^2(\omega, s). \tag{11}$$

II. CALCULATION USING A SIMPLE ASSUMPTION

We must now determine the absorption probability $\gamma(b, \omega)$. It was shown by Bethe[5] that the total pair production cross section can be written as an integral over the momentum transfer to the nucleus q, namely,

$$\sigma_{\text{pair}}=\int_{0}^{\infty}(dq/q)\varphi(q), \tag{12}$$

where $\varphi(q)$ is constant between

$$q_{\min}=1/a \text{ or } 1/kb \text{ (whichever is larger)}$$

and

$$q_{\max}=1/b_0. \tag{13}$$

Here

$$b_0=\hbar/mc \tag{13a}$$

is the Compton wavelength and a is the radius of the Fermi atom. For $q<q_{\min}$ and $q>q_{\max}$, φ falls off fairly rapidly.

The momentum given to the nucleus is approximately related to the impact parameter by $q=1/b$. Thus we find approximately

$$\sigma_{\text{pair}}=A\int_{b_0}^{1/q_{\min}}db/b, \tag{14}$$

where A is a constant. In the case of no screening, the upper limit in (14) is kb_0^2 and

$$\sigma_{\text{pair}}=A\ln kb_0=A\ln(\hbar\omega/mc^2). \tag{15}$$

Comparison with the known pair cross section[6] shows that

$$A=(28/9)\bar{\phi} \quad \text{where} \quad \bar{\phi}=Z^2r_0^2/137 \tag{15a}$$

is Heitler's cross-section unit. On the other hand, σ_{pair} may be written in terms of β, using (2) and (3):

$$\sigma_{\text{pair}}(\omega)=2\pi\int bdb2\beta(b, \omega). \tag{16}$$

Comparison with (14) gives in the case of no screening

$$\begin{aligned}&\beta=A/4\pi b^2\equiv C/b^2 \quad \text{if} \quad b_0<b<b_{\max}=kb_0^2,\\ &\beta=0 \quad\qquad\qquad\ \text{if} \quad b>kb_0^2=(\hbar\omega/mc^2)b_0.\end{aligned} \tag{17}$$

In the case of screening, kb_0^2 is replaced by a, the atomic radius. For $b<b_0$, (14) would give $\beta=0$ but it is more accurate to take

$$\beta=C/b_0^2. \tag{17a}$$

[4] It is necessary for this argument to use the impact parameter b, not the angular momentum l. It would be impossible to construct a physical region of the atom (dispersive ring) which would correspond to the same l for all λ.

[5] H. A. Bethe, Proc. Cambridge Phil. Soc. **30**, 524 (1934).

[6] See W. Heitler, *Quantum Theory of Radiation* (Oxford University Press, London, 1945). Note that the additive constants are here included in the logarithm.

The coefficient

$$C=A/4\pi=(7/9\pi)\bar{\phi}. \tag{17b}$$

Thus the maximum pair production probability, for $b<b_0$, is

$$\gamma=2\beta=(14/9\pi)(Z^2r_0^2/137b_0^2)=(14/9\pi)(Z^2/137^2), \tag{18}$$

which is 1/600 for uranium. This justifies our assumption in Eq. (2) that γ is small.

For a given b we may consider β as a function of ω and obtain for $b_0<b<a$:

$$\begin{aligned}\beta&=C/b^2 \quad \text{if} \quad \omega>\omega_{\min}(b)\\ \beta&=0 \quad\ \ \text{if} \quad \omega<\omega_{\min}(b),\end{aligned} \tag{19}$$

where

$$\omega_{\min}(b)=ck_{\min}(b); \quad k_{\min}(b)=b/b_0^2. \tag{19a}$$

Further,

$$\beta=0 \quad \text{for} \quad b>a, \quad \text{any } \omega \tag{19b}$$

$$\beta=C/b_0^2 \quad \text{for} \quad b<b_0, \quad \omega>c/b_0. \tag{19c}$$

Equation (19) may now be used to obtain α by the analytic continuation formula (10); this gives

$$\alpha(b,\omega)=\frac{C}{\pi b^2}\ln\frac{\omega+\omega_{\min}(b)}{|\omega-\omega_{\min}(b)|} \tag{20}$$

$$=\frac{C}{\pi b^2}\ln\frac{k+b/b_0^2}{|k-b/b_0^2|} \quad \text{for} \quad b_0<b<a, \tag{20a}$$

$$\alpha=0 \quad \text{for} \quad b>a,$$

and b is to be replaced by b_0 in (20) for $b<b_0$.

We can now insert α and β into (7) to calculate the amplitudes for a given scattering angle. Putting $b/b_0=t$ and $sb_0=x$, we find from (7b) and (19)

$$a_2(s,\omega)=Ck\left[\int_0^1 tdtJ_0(xt)+\int_1^\infty (dt/t)J_0(xt)\right]. \tag{21}$$

The upper limit of the integral has been put equal to ∞, whereas the correct limit would be, according to (17),

$$\begin{aligned}t_{\max}&=kb_0 \quad \text{(no screening)},\\ t_{\max}&=a/b_0 \quad \text{(screening)}.\end{aligned}$$

This would make a difference only for very small $x(<1/t_{\max})$ and thus for very small scattering angles:

$$\begin{aligned}\theta&=1/(kb_0)^2 \quad \text{(no screening)},\\ \theta&=1/ka \quad\ \ \text{(screening)}.\end{aligned}$$

However, the correct $t_{\max}$ would have to be used to obtain the scattering in the forward direction for comparison with the preceding paper.

The first integral is $J_1(x)/x$, whereas the second integral cannot be written in closed form. Since x is small we can expand in a power series and find

$$\int_x^\infty \frac{du}{u}J_0(u)=\text{const}-\ln x+\frac{x^2}{8}-\frac{x^4}{2^8}+\frac{x^6}{2^9\cdot 3^2}-\cdots. \tag{21a}$$

The constant occurring here is found by considering the case of very small x,

$$\begin{aligned}\int_x^\infty \frac{du}{u}J_0(u)&=\frac{2}{\pi}\int_0^{\pi/2}d\phi\int_x^\infty\frac{du}{u}\cos(u\cos\phi)\\ &=(2/\pi)\int_0^{\pi/2}d\phi\ \mathrm{Ci}(x\cos\phi)\\ &=-(2/\pi)\int_0^{\pi/2}d\phi\ \ln(\gamma x\cos\phi)=\ln(2/\gamma x).\end{aligned} \tag{22}$$

The constant is therefore $\ln(2/\gamma)=0.116$ and we have the result

$$a_2(s,\omega)=Ck\left(\ln\frac{2}{\gamma}-\ln x+\tfrac{1}{2}+\frac{x^2}{16}-\frac{x^4}{2^8\cdot 3}+\frac{x^6}{2^{11}\cdot 3^2}-\cdots\right)\equiv CkF_2(x). \tag{23}$$

We now turn to the evaluation of $a_1(s,\omega)$. Using (20) and inserting $\omega_{\min}$ from (19) we get

$$a_1(s,\omega)=\frac{Ck}{\pi}\left[\int_0^1 tdtJ_0(xt)\ln\frac{kb_0+t}{|kb_0-t|}+\int_1^\infty\frac{dt}{t}J_0(xt)\ln\frac{kb_0+t}{|kb_0-t|}\right]. \tag{24}$$

For $\hbar\omega\gg mc^2$ the logarithm can be approximated by $2t/kb_0$ and

$$\begin{aligned}a_1(s,\omega)&=(C/\pi b_0)\left[(2/x)\int_0^\infty J_0(u)du+2\int_0^x J_0(u)du(u^2x^{-3}-x^{-1})\right]\\ &=\frac{C}{\pi b_0}\left(\frac{2}{x}-\frac{4}{3}+\frac{x^2}{3\cdot 5}-\frac{x^4}{2^4\cdot 5\cdot 7}+\cdots\right)\\ &\equiv(C/b_0)F_1(x).\end{aligned} \tag{25}$$

The total cross section is

$$\sigma=2\pi\int_0^\pi |a_1(\theta)+ia_2(\theta)|^2\sin\theta d\theta\equiv\sigma_1+\sigma_2. \tag{26}$$

From the preceding results we find with

$$x=kb_0\theta=(\hbar\omega/mc^2)\theta, \tag{26a}$$

$$\sigma_1=2\pi(C/b_0)^2(mc^2/\hbar\omega)^2\int_0^\infty F_1^2(x)xdx,$$

$$\sigma_2=2\pi(C/b_0)^2\int_0^\infty F_2^2(x)xdx. \tag{27}$$

Obviously, σ_2 is by far larger than σ_1. The integral occuring in σ_2 can be evaluated, using the definition (21) and the orthogonality relation of the Bessel functions

$$\int xdxJ_0(xt)J_0(xt')=t^{-1}\delta(t'-t). \tag{27a}$$

This yields

$$\int F_2^2xdx=\int_0^1 tdt+\int_1^\infty dt/t^3=1. \tag{28}$$

In the case of σ_1, an approximate evaluation is elementary, *viz.*,

$$\int F_1^2xdx=(2/\pi)^2\int_{x_1}^\infty xdx/x^2=4\pi^{-2}\ln(1/x_1), \tag{28a}$$

where x_1 is the smallest value of x for which (21) is valid, *viz.*, $x_1=b_0/a$ for complete screening and $x_1=1/kb_0$ without screening. Therefore we get, using (17b),

$$\sigma_2=2\pi C^2/b_0^2=(98/81\pi)(\bar{\phi}^2/b_0^2)$$
$$=0.385(\alpha Z)^4r_0^2, \tag{29a}$$

$$\sigma_1=3\pi^{-3}(mc^2/\hbar\omega)^2\sigma_2\ln(\hbar\omega/mc^2)$$
without screening, (29b)

$$=3\pi^{-2}(mc^2/\hbar\omega)^2\sigma_2\ln(a/b_0) \text{ complete screening.} \tag{29c}$$

The numerical factor in (29a) should not be taken too seriously because the integral in (28) depends appreciably on the region $t<1$ for which our theory is only approximate. Likewise, in (29b, c) an unknown constant should be added to the logarithms.

Within the range of validity of these formulas, i.e., for $\hbar\omega\gg mc^2$, the total cross section is almost entirely the result of the "absorptive" part of the scattering amplitude a_2. The ratio of the potential scattering to the pair production cross section is, from (15) and (17b):

$$\frac{\sigma_2}{\sigma_{\text{pair}}}=\frac{C}{2b_0^2\log}=\frac{7\alpha(Z\alpha)^2}{18\pi\log}=\frac{0.124\alpha(Z\alpha)^2}{\log}, \tag{30}$$

where log is the logarithm in the pair production cross section, Eq. (15).

III. THEORY OF THE IMPACT PARAMETER METHOD

We shall now give a more accurate mathematical theory of the impact parameter method which we have used, and we shall show how the scattered amplitudes $a_2(s,\omega)$ could, at least in principle, be calculated exactly.

For this purpose, we construct a γ-ray wave packet traversing the atom at a distance b from the nucleus by setting

$$\psi=(2\pi)^{-1}v^{-\frac{1}{2}}\int\exp[i(\mathbf{k}_0+\mathbf{u})\cdot\mathbf{r}]\varphi(\mathbf{u})du_xdu_y, \tag{31}$$

where φ may for instance be chosen as

$$\varphi\equiv\exp(-i\mathbf{u}\cdot\mathbf{b})\chi(u)=\alpha\pi^{-\frac{1}{2}}\exp[-i\mathbf{u}\cdot\mathbf{b}-\tfrac{1}{2}\alpha^2u^2]. \tag{32}$$

The wave vector $\mathbf{k}_0$ is fixed, the added wave vector $\mathbf{u}$ is assumed perpendicular to $\mathbf{k}_0$ which is taken in the z-direction. Evaluation of (31) gives

$$\psi=(\pi v)^{-\frac{1}{2}}\alpha^{-1}\exp[i\mathbf{k}_0\cdot\mathbf{r}-(\boldsymbol{\varrho}-\mathbf{b})^2/2\alpha^2] \tag{33}$$

where $\boldsymbol{\varrho}$ is the component of $\mathbf{r}$ in the xy-plane. Thus ψ is indeed confined to impact parameters near $\mathbf{b}$, within an accuracy α. Further, the magnitude of the wave vector $\mathbf{k}_0+\mathbf{u}$ is essentially the same as that of k_0 provided α is not too small; e.g., the choice $\alpha=b_0$ will make $\mathbf{k}_0+\mathbf{u}$ differ from k_0 only by an amount of relative order $(mc^2/\hbar\omega)^2$.

Generally, φ is assumed normalized,

$$\int|\varphi(u)|^2du_xdu_y=\int|\chi(u)|^2du_xdu_y=1, \tag{34}$$

so that ψ is normalized to one particle incident per unit time. If then the pair production probability is calculated per unit time, as usual, this will give directly the probability $\gamma(b,\omega)$ used in Sec. I.

Consider now the matrix element for the production of a pair of electrons of momenta $\mathbf{p}_+$, $\mathbf{p}_-$ such that

$$E_++E_-=k_0. \tag{35}$$

Let us denote this matrix element by

$$M(\mathbf{k},\mathbf{p}_+,\mathbf{p}_-,\mu,\sigma_+,\sigma_-). \tag{36}$$

It is a function of the quantum $\mathbf{k}$, and its polarization μ, of the spins of the two electrons σ_+, σ_- and, of course, of their momenta. Then the matrix element for producing the same electrons by the wave packet (31) is

$$N=(2\pi)^{-1}$$
$$\times\int du_xdu_y\varphi(u)M(\mathbf{k}_0+\mathbf{u},\mathbf{p}_+,\mathbf{p}_-,\mu,\sigma_+,\sigma_-). \tag{37}$$

To get the total pair production probability 2β for the wave packet (31), $|N|^2$ must be summed over σ_+ and σ_-, averaged over μ, and integrated over the directions of $\mathbf{p}_+$ and $\mathbf{p}_-$ and finally over the magnitude of one of them. This defines the $\beta(b,\omega)$ used in Sec. I in terms of mathematical operations which can all be carried out.

To get any further, let us introduce the vectors

$$\mathbf{q}_0=\mathbf{p}_+ +\mathbf{p}_- -\mathbf{k}_0 \tag{38}$$

and

$$\mathbf{w}=(\mathbf{p}_+ -\mathbf{p}_-)_\perp, \tag{38a}$$

where $\perp$ denotes the component in the plane perpendicular to $\mathbf{k}_0$. It is easily seen that also $\mathbf{q}_0$ is nearly in this plane.[5] Then, if the magnitude of $\mathbf{p}_+$ [and hence also $\mathbf{p}_-$ from (35)] is given, $\mathbf{q}_0$ and $\mathbf{w}$ determine the vectors $\mathbf{p}_+$ and $\mathbf{p}_-$. The matrix element in (37) may then be written

$$M(\mathbf{q}_0-\mathbf{u},\ \mathbf{w},\ \text{spins}), \tag{39}$$

and $\mathbf{w}$ is independent of $\mathbf{u}$. It is worth noting[5] that the actual differential cross section and matrix element depend most strongly on $(\mathbf{q}_0-\mathbf{u})$ and less on $\mathbf{w}$.

The pair production probability for our wave packet is now

$$2\beta=(2\pi)^{-2}\int dE_+ \sum_{\text{spin}} \times\int d^2\mathbf{u}d^2\mathbf{u}'d^2\mathbf{w}d^2\mathbf{q}_0\varphi(\mathbf{u})\varphi^*(\mathbf{u}') \times M(\mathbf{q}_0-\mathbf{u},\ \mathbf{w},\ \text{spin})M^*(\mathbf{q}_0-\mathbf{u}',\ \mathbf{w},\ \text{spin}), \tag{40}$$

where $d^2\mathbf{u}$ denotes integration over $du_x du_y$. Equation (40) could be evaluated, but it is easier to go directly to the scattered amplitude given in (7b), which becomes

$$a_2(s)=(2\pi)^{-1}k\int d^2\mathbf{b}\,\exp(i\mathbf{b}\cdot\mathbf{s})\beta(\mathbf{b})$$

$$=\tfrac{1}{2}k(2\pi)^{-3}\int dE_+\sum_{\text{spin}}\int d^2\mathbf{b}d^2\mathbf{u}d^2\mathbf{u}'d^2\mathbf{w}d^2\mathbf{q}_0 \times\exp(i\mathbf{b}\cdot\mathbf{s})\varphi(\mathbf{u})\varphi^*(\mathbf{u}') \times M(\mathbf{q}_0-\mathbf{u},\mathbf{w},\text{spin})M^*(\mathbf{q}_0-\mathbf{u}',\mathbf{w},\text{spin}). \tag{41}$$

Remembering now (32), the factors containing b can be integrated:

$$\int d^2b\,\exp[i\mathbf{b}\cdot(\mathbf{s}+\mathbf{u}'-\mathbf{u})]=(2\pi)^2\delta(\mathbf{s}+\mathbf{u}'-\mathbf{u}). \tag{42}$$

The integration over $\mathbf{u}'$ can then be carried out. At the same time, we introduce

$$\mathbf{q}=\mathbf{q}_0-\tfrac{1}{2}(\mathbf{u}+\mathbf{u}'); \tag{43}$$

then we have

$$a_2(s)=(k/4\pi)\int dE_+\sum_{\text{spin}} \times\int d^2\mathbf{u}d^2\mathbf{w}d^2\mathbf{q}\chi(\mathbf{u})\chi(\mathbf{u}-\mathbf{s}) \times M(\mathbf{q}-\tfrac{1}{2}\mathbf{s},\ \mathbf{w},\ \text{spin})M^*(\mathbf{q}+\tfrac{1}{2}\mathbf{s},\ \mathbf{w},\ \text{spin}). \tag{44}$$

All reference to the auxiliary variable u has now been eliminated from the matrix elements M. The integral over $\mathbf{u}$ is elementary but can be further simplified by assuming that α in (32) is very small. This means very sharp definition of the γ-ray beam in space, and is indeed a necessary assumption if the first line of Eq. (41) is to hold exactly: if α were larger, the various wave packets (31) for different b would not be sufficiently orthogonal. Assuming α small, we can put $\chi(\mathbf{u}-\mathbf{s})=\chi(\mathbf{u})$ and the u-integral reduces to the normalization integral (34). Thus we get the final result

$$a_2(s)=(k/4\pi)\int dE_+\sum_{\text{spin}} \times\int d^2\mathbf{q}d^2\mathbf{w}M(\mathbf{q}-\tfrac{1}{2}\mathbf{s},\ \mathbf{w},\ \text{spin}) \times M^*(\mathbf{q}+\tfrac{1}{2}\mathbf{s},\ \mathbf{w},\ \text{spin}), \tag{45}$$

which is entirely independent of the original wave packet assumption. For $s=0$ we get simply

$$a_2(0)=(k/4\pi)\sigma_{\text{pair}}, \tag{46}$$

which was already used in the preceding paper.

Equation (45) could again be evaluated exactly, and $a_1(s)$ could then be obtained by analytic continuation. We shall here be content with the following rough calculation. The matrix element $M(q_1, w, \text{spin})$ is, for any important w and spin, found to be about inversely proportional to q_1 provided $q_{\min}<q_1<q_{\max}$ as defined in (13), and decreases more rapidly (as q_1^{-2}) for $q>q_{\max}=1/b_0$. Indeed, if this is assumed, the contribution to the pair cross section from a given q turns out to be proportional to

$$d^2\mathbf{q}\,|M(q,w,\text{spin})|^2\sim qdq/q^2 \tag{46a}$$

as it should be according to (12). Then we can integrate (45) over all variables except q and obtain approximately

$$a_2(s)=Bk\int_{q_{\min}}^{q_{\max}}\frac{d^2\mathbf{q}}{|\mathbf{q}-\tfrac{1}{2}\mathbf{s}|\,|\mathbf{q}+\tfrac{1}{2}\mathbf{s}|} =Bk\int\frac{qdqd\phi}{[(q^2+\tfrac{1}{4}s^2)^2-q^2s^2\cos^2\phi]^{\frac{1}{2}}}, \tag{47}$$

where B is a constant and k the wave number. Now if $q_{\min}\ll s\ll q_{\max}$, the integral over ϕ gives a result of order $1/s^2$ for $q<s$, and of order $1/q^2$ for $q>s$. Hence

$$a_2(s)\sim k\left[\int_0^s\frac{qdq}{s^2}+\int_s^{1/b_0}\frac{qdq}{q^2}\right]=k\left[\ln\frac{1}{b_0 s}+\tfrac{1}{2}\right], \tag{48}$$

in agreement with Eq. (23). This justifies the assumptions made in the simple theory of Sec. II.

IV. DISCUSSION OF THE RESULTS

The angular distribution of the dispersive and absorptive amplitude is given by $F_1(x)$ and $F_2(x)$ of Eqs. (25) and (23), respectively. The shape of the differential cross section is plotted in Fig. 1 as a function of $x=sb_0=(\hbar\omega/mc^2)\theta$.

For very small angles, $\theta<\lambda\!\!\!^{-}/b_{\max}=(mc^2/\hbar\omega)b_0/b_{\max}$ with $b_{\max}$ given by (17), these functions do not give the correct angular distribution, since large impact parameters were incorrectly treated by extending the integral in (21) to infinity. This could easily be remedied if desired, and even screening could be included. In the limit of zero momentum transfer $x=0$, and if $t_{\max}=kb_0$ is inserted as the upper limit in (21), the results of the preceding paper[1] are approximately recovered.

At large angles, $\theta\gg mc^2/\hbar\omega$, Eqs. (25) and (23) will not be accurate because then the main contribution comes from small impact parameters $b<b_0$ and Eq. (17a) is not a good approximation. For the "absorptive" part $a_2(s)$, the method of Sec. III would still give correct results as long as θ is small compared with one radian. However, for the dispersive part this will not work because for the small b which are now important, the pair production starts at low energy and thus at wavelengths $\lambda\!\!\!^{-}$ comparable to b; therefore the uncertainty principle will prevent definition of the impact parameter for frequencies ω' which contribute materially to the analytic-continuation integral (10), and a_1 cannot be reliably calculated. On the other hand, this does not make much difference for the scattering because a_1 is very small compared to a_2 which is calculable.

The differential cross section is determined essentially by F_2^2 in Fig. 1, because it was shown in (29), (25) that the dispersive part F_1^2 is relatively unimportant. As is seen from Fig. 1, F_2^2 increases substantially with decreasing x, namely by about a factor 20 between $x=1$ and $x=0.1$; according to Eq. (23), F_2^2 is proportional to $(\log 1/x)^2$. This increase is in contrast to the angular distribution of the pair electrons produced by the γ-ray which is essentially constant for $x<1$, i.e., for angles less than $mc^2/\hbar\omega$.

In Fig. 1, we have also plotted for comparison the diffraction scattering from a black sphere. The radius of this sphere was arbitrarily chosen as $7b_0$ because the part of the atom responsible for pair production and potential scattering extends from b_0 to the atomic radius, and $7b_0$ may be a reasonable average. The black-sphere scattering is then $(J_1(7x)/7x)^2$; the coefficient 40 in the figure was also chosen arbitrarily. It is seen from Fig. 1 that F_2^2 agrees with the black-sphere curve reasonably well in the mean, but that F_2^2 is higher both at very small and at large x. This is understandable because the scattering is really not from a black sphere of definite radius but from a "gray" sphere with opacity varying with radius; at small x, the outer parts of the atom become effective and increase the scattering because of the large radii involved; at large x, where a

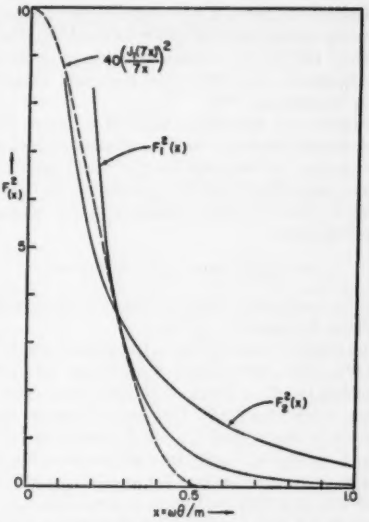

FIG. 1. Shape factor $F^2(x)$ of the angular distribution. The subscripts 1 and 2 refer to the dispersive and absorptive parts, respectively. For comparison the diffraction from a black sphere of radius $7b_0$ is plotted on arbitrary scale; it is $40[J_1(7x)/7x]^2$.

sphere of radius $7b_0$ would give very little scattering because of interference, the particularly black region near b_0 still gives appreciable scattering.

The dispersive scattering F_1^2 falls off still more rapidly with increasing θ than F_2^2. This is because, for any impact parameter b, the dispersive amplitude a_1 is largely determined by the ratio $\omega_{\min}(b)/\omega$ where $\omega_{\min}(b)$ is the frequency at which γ-rays passing at impact parameter b begin to produce pairs appreciably. The larger this ratio $\omega_{\min}(b)/\omega$ (as long as it is less than unity), the greater will be the dispersive effect; since $\omega_{\min}(b)$ is proportional to b according to Eq. (19a), the larger b give a greater dispersive effect as can be seen from (20); but the larger b will contribute to the scattering only at the smallest angles.

The energy dependence of the scattered amplitudes at a given finite s is

$$a_1(s)\sim\text{const}, \quad a_2(s)\sim\omega \quad \text{if} \quad \hbar\omega\gg mc^2, \tag{49}$$

whereas at zero momentum transfer the preceding paper[1] gives the result

$$a_1(0)\sim\omega, \quad a_2(0)\sim\omega\ln\omega. \tag{50}$$

This is without screening; with screening this will be replaced by

$$a_1(0)\sim\omega_0, \quad a_2(0)\sim\omega\ln\omega_0, \tag{51}$$

where $\omega_0=\omega_{\min}(a)$ [see Eq. (19a)], with a the atomic radius. The energy dependence of (51) is the same as that of (49), but that of (50) is not. This is because in

the absence of screening, the step increase of a_1, a_2 with decreasing x will continue down to $x_1=b_0/b_{\max}(\omega)$, see Eq. (17), and will then flatten out; this, in combination with the angular dependence just discussed, will give the energy dependence (50).

Achieser and Pomerantschuk,[3] in a rather complicated paper, calculated only the dispersive part of the cross section. In the high energy limit, they find an angular dependence $1/\theta^2$ in agreement with our result $F_1^2\sim 1/x^2$. Also the total dispersive cross section obtained by them,

$$\sigma_1=\beta(\alpha Z)^4(mc^2/\hbar\omega)^2r_0^2\ln(\hbar\omega/mc^2) \qquad (52)$$

with β an unknown numerical factor, agrees with our result for this quantity, (29b).

The absolute value of the total cross section is given by (29a) which gives about 6 millibarns for uranium. According to (30), its ratio to the pair production cross section is about 1/8000. This factor is made up of a factor α, a factor $(\alpha Z)^2$, a small numerical factor of about $\frac{1}{4}$, and 1/log. Except for energies above about 10^{10} ev, the total cross section for potential scattering is much less than that for Compton scattering.

This is different for the differential cross section, because of the large forward maximum. According to (23), (17b), the differential cross section per unit solid angle is

$$\sigma(\theta)=(7/9\pi)^2(Z\alpha)^4r_0^2(\hbar\omega/mc^2)^2F_2^2(x) \qquad (53)$$

which, for uranium, is

$$\sigma(\theta)=1.0(\hbar\omega/mc^2)^2F_2^2(x) \text{ millibarns/steradian.}$$

For 300 Mev and $x=0.1$, corresponding to $\theta=0.01°$, this gives 3000 barns per steradian. For the Compton effect, the differential cross section is Zr_0^2 in the forward direction, independent of energy; this is 7 barns/steradian for uranium. Rayleigh scattering is $Z^2r_0^2$ in the exact forward direction, and much less for $x=0.1$ which represents a large angle for Rayleigh scattering. Therefore scattering of γ-rays at such high energies and small angles represents mainly potential scattering.

For the experimental observation, the main requirements are excellent collimation and elimination of all electrons from pair production and of the secondary γ-rays emitted by these electrons. The latter can best be done by using the different angular distribution. Unfortunately, since the scattering is mainly absorptive, its observation at high energy would not reveal anything about vacuum polarization, but would merely test the theory of the spatial distribution of pair production inside the atom.

Scattering and Absorption of Pi-Mesons in Carbon*

H. BYFIELD, J. KESSLER, AND L. M. LEDERMAN
Columbia University, New York, New York

(Received December 3, 1951)

The interactions of positive and negative pi-mesons of 62 Mev with carbon nuclei were studied in a magnet cloud chamber, using the external beams of the Nevis cyclotron. A Coulomb-nuclear interference is observed in the elastic scattering. This establishes that the nuclear potential is attractive for mesons. Nuclear cross sections obtained are $\sigma_{\text{abs}}=181\pm22$ mb, $\sigma_{\text{el}>}=148\pm30$ mb. A complex square well model for the nucleus is considered.

I. EXPERIMENTAL PROCEDURE

A DETAILED investigation has been made of the scattering and absorption of positive and negative pi-mesons in carbon nuclei. To accomplish this, a 16-inch cloud chamber, working in a magnetic field of 5000 gauss, was exposed to the 70-Mev meson beams of the Nevis cyclotron. The chamber was expanded once per minute, and at optimum supersaturation the cyclotron was pulsed. Figure 1 represents a typical photograph of the meson beam, in which, however, two interactions are observed. The scattering plate has a thickness of 2.14 g/cm^2. Momenta of incident and emerging particles are determined with an average precision of 10 percent, which includes measurement errors as well as multiple scattering and turbulence effects. The latter contributions are determined from zero field photographs which are taken every tenth expansion. The momentum measurements are performed on stereoscopic reprojections by comparing the tracks with curves drawn on Lucite templates. The templates are also used to extrapolate the tracks to the origin of the event in the carbon plate. All energies are then corrected for the ionization loss in the carbon.

About 4000 photographs were scanned in reprojection for interactions, flux tracks, and π-μ decays in the gas. A total of 500 carbon events was recorded with approximately equal numbers of positive and negative mesons in the interval 62 ± 10 Mev (interaction energy). These included stars, inelastic scatterings and elastic scatterings greater than 9°. Corrections to the data include the following: (1) Beam contaminations were determined for cloud-chamber geometry as in previous experiments[1] to be 12 ± 3 percent electrons in the π^- beam, less than 2 percent positrons in the π^+ beam; 8 ± 3 percent mu-mesons in both beams.[2] A correction was made for the number of electrons which stop in the plate because of radiative collisions. (2) The finite thickness of the plate leads to the necessity of recognizing "stoppings" as an important part of the interaction. These may be due to stars with low energy and fast neutron prongs, or prongs emitted at ~90°. Also, inelastically scattered mesons or elastic scatters through ~90° or out of the illumination would appear as stops. The latter is by far the most serious source of error and is avoided by restricting the region of acceptance for these events to a central fraction of the illuminated depth. A correction is then made to the elastic scattering, using the observed angular distribution and the total solid angle lost to the scattered meson. The thickness of the plate also obscures the distinction between strongly inelastic scatterings and stars. Thus, the inelastic cross section quoted is actually a lower limit.

II. EXPERIMENTAL RESULTS

The results are presented in Table I and in Figs. 2 and 3.[3] The errors quoted in the table include statistics, beam uncertainties and, where necessary, estimates of the errors in corrections. The elastic scattering results are integrated from 20° because, as is seen from Figs. 2 and 3, the rise is so rapid below 20° that small uncertainties in the lower limit would severely affect the cross sections. The inelastic scatterings that have been observed were defined by an energy change of at least 15 Mev. This definition was imposed by the energy resolution, and hence it is recognized that a part of the "elastic" cross section may actually be due to incoherent scattering. The average energy of the inelastically scattered π^- mesons is 22 Mev; of the π^+ mesons, 30 Mev.

The absorption of the π^+ mesons exhibit an interesting feature which is illustrated by the star in Fig. 1.[4] The two emergent fast protons bear an angular relation to the incident meson and to one another, which is consistent with the reaction $\pi^+ + d \rightarrow p + p$. If we consider angular agreement within 10° as establishing a correlation, the fraction of observed stars which exhibit this correlation is 12 ± 4 percent. This corresponds to a cross section of 19 mb, and within the poor statistics available the proton angular distribution is isotropic.

* This program was jointly sponsored by the ONR and AEC.

[1] Lederman, Booth, Byfield, and Kessler, Phys. Rev. **83**, 685 (1951).

[2] The μ^+ contamination of the π^+ beam is assumed equal to the μ^- contamination of the π^- beam.

[3] The total cross sections are to be compared with the results of a similar experiment by A. Shapiro [Phys. Rev. **84**, 1063 (1951)], in which the mean interaction energy was 45 Mev.

[4] Similar events in emulsions were discussed by G. Bernardini, International Conference, Chicago, September, 1951. See also, Bernardini and Levy, Phys. Rev. **84**, 610 (1951).

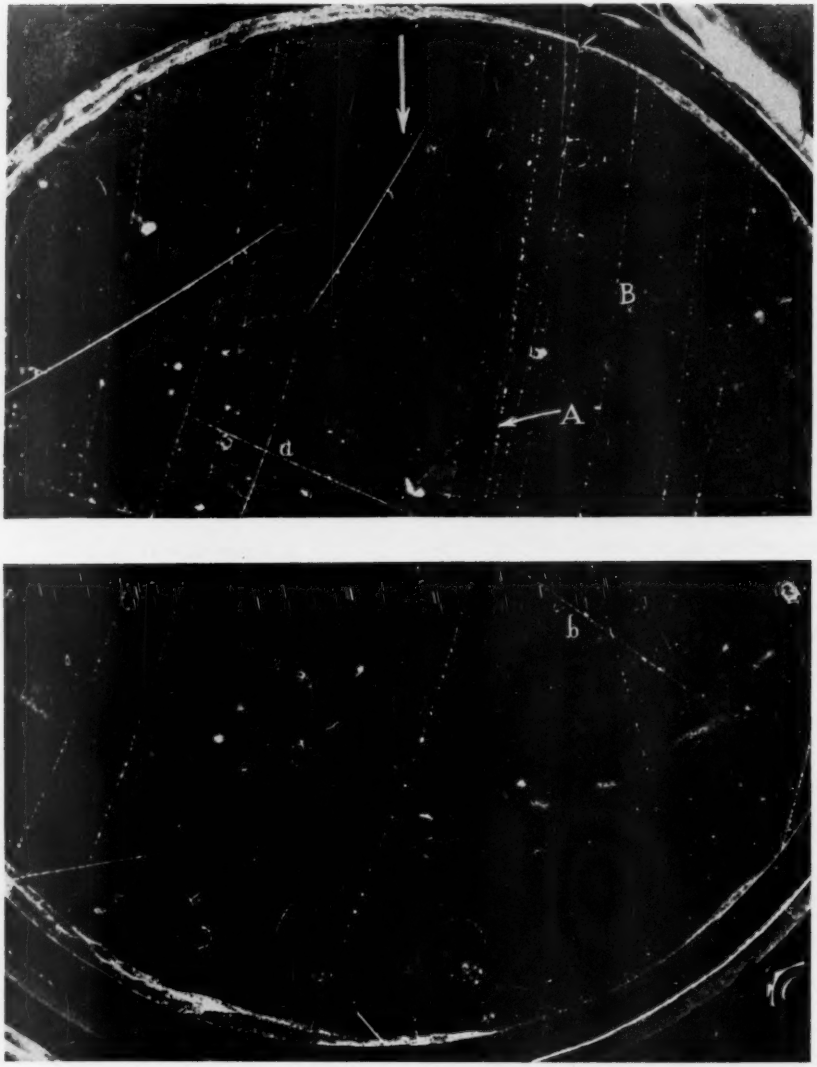

FIG. 1. 70-Mev π^+ meson beam photograph. Meson A yields a 2 proton star, prongs a and b. Meson B elastically scatters through an angle of 32°.

III. DISCUSSION

The general nature of the angular distributions strongly suggests a Coulomb interference effect. If this is true, the interference term and, in fact, practically all Coulomb contributions are eliminated by forming:

$$\sigma_{\text{nucl}}=\tfrac{1}{2}(\sigma_{\pi^+}+\sigma_{\pi^-})-\sigma_{\text{Coul}} \quad (1)$$

where σ_{Coul} is the Rutherford scattering, modified by the appropriate nuclear charge distribution. The result of the above procedure for a uniform distribution of charge is presented in Fig. 4. The total cross section for nuclear elastic scattering obtained is 148±30 mb. The pure nuclear data of Fig. 4 plus the absorption cross

sections of Table I provide a test of nuclear models for pi-meson interactions.

Following the transparency theory,[5] the pi-meson in the nucleus may be thought to experience a potential which is capable of scattering, absorbing, and reflecting the meson wave. To investigate this model without neglecting any of the possible optical processes ($kR=2.5$), a partial wave solution of the Schrödinger equation was sought, in which the scattering potential is taken of the form $V_n+i\sigma_n$.[6] These parameters, plus the nuclear radius, were required to account for the total elastic scattering cross section (148 mb) and the total absorption cross section (average of π^+ and π^- results, 181 mb). For a nuclear radius of $1.47\times10^{-13}A^{\frac{1}{3}}$, the parameters which were found to fit the data are $V_n=18$ Mev, and $\sigma_n=9$ Mev. These results correspond to an argument of the inside solutions of $k'R=2.95+0.20i$ and, consequently, to a mean free path in nuclear matter of 8.3×10^{-13} cm.[7] To see if these results are consistent with the large charge dependence effect exhibited by the data, a Born approximation

TABLE I. Pion-carbon cross sections in millibarns, cloud chamber.

	Stars Protons >40 Mev				Elastic scattering		Inelastic scattering
	0	1	2	Total	20–180°	65–180°	$\Delta E>15$ Mev
π^-	110	34	4	148±18	165±15	63	46±10
π^+	34	77	42	153±22	89±10	38	15±8

calculation was carried out for the potential

$$V=\pm Ze^2/r, \quad r>R$$
$$V=\pm Ze^2/2R(3-r^2/R^2)-V_n+i\sigma_n, \quad r<R \tag{2}$$

corresponding to a uniform charge distribution over the region of the nucleus. The result is plotted in Fig. 5. The lack of good agreement is not surprising in view of the crudeness of the approximation. However, the results indicate that a Coulomb interference is, in fact, being observed. It is noted that the interference is a quite sensitive test of the nuclear parameters acting upon the meson. In fact, the observation of the interference immediately limits both the real and imaginary well depths to $\lesssim30$ Mev. With these limitations, the nuclear parameters obtained for the model become unique. The angular distribution predicted by the square well model has the general shape of Fig. 4 but falls more slowly from the forward peak and fails by a factor of 8 to give the large backward scattering

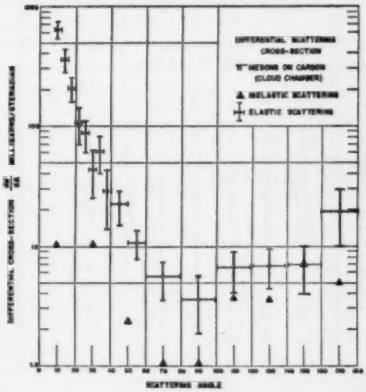

FIG. 2. Differential elastic and inelastic scattering of negative pions on carbon.

observed. A partial suppression of the odd angular momentum phase shifts would produce agreement with experiment, but the physical interpretation of V_n would then become even more difficult.

An immediate result of the Coulomb interference is that the potential experienced by the meson in carbon is proved to be attractive. This is in disagreement with Schiff's[8] formulation of nonlinear meson theory, in which the nonlinearity corresponds to a point-contact repulsion between mesons. Another result of the Coulomb contribution is that the π^- to π^+ ratio of total absorption cross sections (sum of star and inelastic scattering) should (for ~60-Mev mesons) go as: $(HV_c(R)/E/(1-V_c(R)/E)$. This ratio for carbon is 1.08, in fair agreement with the experiment. The

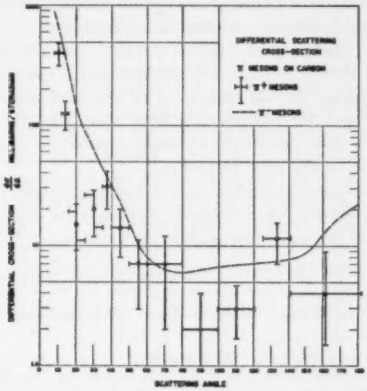

FIG. 3. Differential elastic scattering of positive ions in carbon. The dotted curve reproduces the negative cross section.

[5] Fernbach, Serber, and Taylor, Phys. Rev. **75**, 1352 (1949).

[6] The meson mass in the Schrödinger equation is replaced by the total energy.

[7] The results here given differ from those calculated for the same model by a WKB approximation [H. A. Bethe and R. R. Wilson, Phys. Rev. **83**, 690 (1951)], chiefly in that we obtain the same opacity with a much longer mean free path, which is a sensitive function of the real well depth. The exact solution has also been studied independently by J. Steinberger (private communication).

[8] L. I. Schiff, Phys. Rev. **84**, 1 (1951).

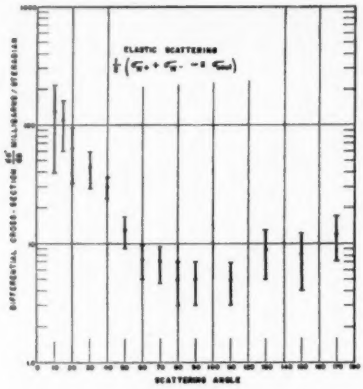

FIG. 4. Differential elastic scattering cross section for pions on carbon obtained by averaging the π^+ and π^- results and subtracting the contribution of a uniformly charged sphere (Born approximation).

Coulomb barrier (2.6 Mev) must also account for a decreased number of inelastically scattered π^+ mesons, although the observed effect appears still to be too large. Poor statistics and ambiguity caused by the thickness of the plate leave this point still uncertain.

The good correlation double-proton stars observed with π^+ mesons are interesting in view of the two nucleon models for meson absorption.[9,10] The assumption is made that pairs of nucleons, inside the nucleus, retain their interaction property of meson absorption as exhibited in the elementary process: $\pi^+ + d \rightarrow 2p$.[11] The probability that neither recoiling nucleon suffers a collision in escaping from the carbon nucleus, when averaged over all possible absorption position, is ~ 0.22. For this (classical) calculation, the mean free path for 90-Mev neutrons in nuclear matters was employed.[5] Thus, the 12 percent of observed proton pair stars corresponds to ~ 60 percent of all the stars observed. Allowing for a contribution from absorption by n-n pairs, it is seen that the two-nucleon model can account for most of the π^+ absorptions.[12]

The assumption that bound nucleons retain their meson interaction properties implies that we may separate the mean free path in nuclear matter:

$$\lambda^{-1} = 0.120 \times 10^{13} \text{ cm}^{-1} = \lambda^{-1}(\text{scatt}) + \lambda^{-1}(\text{star}).$$

Then, in terms of elementary cross sections, the simplest considerations suggest

$$\lambda(\text{star}) = (4/3)\pi R^3 / Z\sigma_a^* \qquad (3)$$

where σ_a^* is the cross section per proton for absorption in the nucleus. Brueckner, Serber, and Watson[10] have set $\sigma_a^* = \Gamma\sigma(\pi^+ + d)$ where $\sigma(\pi^+ + d)$ is the observed[11] cross section and Γ measures the degree of two-nucleon correlation in nuclear structure. Similarly, one may investigate

$$\lambda(\text{scatt}) = \frac{(4/3)\pi R^3}{\frac{1}{2}\gamma A[\sigma(\pi^+ + p) + \sigma(\pi^- + p)]}, \qquad (4)$$

where $\sigma(\pi^{\pm} + p)$ is assumed equal to $\sigma(\pi^{\mp} + n)$. γ measures the alteration in the free cross sections produced by the binding. This would include the Pauli principle[13] and the effect of the change in relative energy of the meson-nucleon system.[14] If it is assumed that the inelastic scatterings observed in carbon are due to meson-nucleon collisions,[15] then $\lambda(\text{scatt})$ may be obtained from the data on π^- mesons. The probability of subsequent absorptions of the scattered meson is estimated[16] as 0.2, and this leads to $\lambda(\text{scatt})/\lambda(\text{star}) \lesssim 2.9$

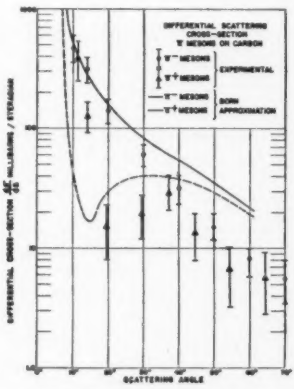

FIG. 5. Differential elastic scattering of positive and negative mesons on carbon computed from the Born approximation. The nuclear well depths are $V = 18$ Mev, $\sigma = 9$ Mev. The charge distribution is taken as uniform over a sphere of radius $1.47 \times 10^{-13} A^{\frac{1}{3}}$ cm.

[9] S. Tamor, Phys. Rev. **77**, 412 (1950).
[10] Brueckner, Serber, and Watson, Phys. Rev. **84**, 258 (1951).
[11] Durbin, Loar, and Steinberger, Phys. Rev. **83**, 646, **84**, 581 (1951); Clark, Roberts, and Wilson, Phys. Rev. **83**, 649 (1951).
[12] Occasional stars are observed, both in emulsions and in this cloud-chamber experiment, of a single proton with almost all of the meson energy (~ 200 Mev).
[13] M. H. Johnson, Phys. Rev. **83**, 510 (1951).
[14] Nagle, Anderson, Fermi, Long, and Martin, Bull. Am. Phys. Soc. **27**, No. 1, 28 (1952).
[15] This is in contrast to the conclusions drawn from the strongly inelastic scatterings observed in emulsions: Bernardini, Booth, and Lederman, Phys. Rev. **83**, 1277 (1951). The probability of two successive scatterings is now seen not to be negligible.
[16] The probability of subsequent absorptions of the scattered meson depends on the longer mean free path at reduced energy (Bernardini, Booth, and Lederman, Phys. Rev. **83**, 1075 (1951)); Isaacs, Sachs, and Steinberger, Phys. Rev. **85**, 803 (1951). Although an exact phase shift treatment of the model is preferable, this quantity was here obtained entirely via the "particle" picture [see Eq. (6), reference 10].

where the inequality reflects the experimental uncertainty discussed in Sec. I. Using this ratio, Eq. (3) yields $\Gamma \lesssim 3.3$. Equation (4) yields

$$\gamma[\sigma(\pi^+ + p) + \sigma(\pi^- + p)] \gtrsim 8 \text{ mb}.$$

For meson energy losses greater than 15 Mev, γ is estimated to be of the order of 1. The non-charge exchange scattering of pions on protons has not yet been measured, but should, when compared with improved data of the above kind, indicate whether the binding effects are as simple as has been here assumed.[17]

The authors wish to acknowledge the contributions and encouragement of Professors G. Bernardini and E. T. Booth to this experiment. We were also stimulated and assisted by conversations with Professors Rainwater, Serber and Steinberger, and Drs. S. Epstein, T. A. Green, and D. C. Peaslee.

[17] If the charge exchange contribution is small, the results of Isaacs, Sachs, and Steinberger give $\sigma(\pi^+ + p) + \sigma(\pi^- + p) = 45$ mb. This would imply that neglected interference effects add up destructively in carbon.

PHYSICAL REVIEW VOLUME 86, NUMBER 1 APRIL 1, 1952

Spontaneous Fission*

EMILIO SEGRÈ
University of California, Los Alamos Scientific Laboratory, Los Alamos, New Mexico
(Received July 17, 1951)

This paper summarizes part of the work on spontaneous nuclear fission performed at Los Alamos before 1945. The experimental technique used to detect spontaneous fission in the heavy alpha-active elements has been described, and the decay constants for spontaneous fission observed in a number of substances have been listed. The number of neutrons emitted per spontaneous fission of U^{238} has also been measured and found to be 2.2 ± 0.2.

HISTORICAL

THE first attempt to discover spontaneous fission in uranium was made by Libby,[1] who, however, failed to detect it on account of the smallness of effect. In 1940, Petrzhak and Flerov,[2] using more sensitive methods, discovered spontaneous fission in uranium and gave some rough estimates of the spontaneous fission decay constant of this substance. Subsequently, extensive experimental work on the subject has been performed by several investigators and will be quoted in the various sections of this article.

Bohr and Wheeler[3] have given a theory of the effect based on the usual ideas of penetration of potential barriers.

On this project spontaneous fission has been studied for the past several years in an effort to obtain a complete picture of the phenomenon. For this purpose the spontaneous fission decay constants λ have been measured for separated isotopes of the heavy elements wherever possible. Moreover, the number ν of neutrons emitted per fission has been measured wherever feasible, and other characteristics of the spontaneous fission process have been studied. This report summarizes part of the spontaneous work done at Los Alamos up to January 1, 1946. A chronological record of the work is contained in the Los Alamos reports. The experiments were conducted mainly by O. Chamberlain, G. Farwell, J. Jungerman, E. Segrè, and C. Wiegand.

EXPERIMENTAL TECHNIQUES

The experiments directed to the measurement of λ consisted in principle of putting a certain amount of the material to be investigated in ionization chambers connected to linear amplifiers, and counting the fission pulses. The material was deposited on platinum disks as a thin layer.[4]

In all these experiments one of the main difficulties is offered by the alpha-activity of the samples. As a matter of fact, this often limits the amount of a substance that can be studied at one time in an ionization chamber. The reason for this is that the fissions are recognized from the large size pulses that they give in the ionization chambers. Now the pulses generated by single alphas are from 10 to 20 times smaller; however, if the alpha-emission is very strong, fluctuations in the alpha-activity background may simulate large pulses and cause spurious fission counts to be recorded.

Qualitatively, these fluctuations will be roughly proportional to the square root of the number of alphas emitted during the "resolving time" of the apparatus. Attempts have been made to obtain a more quantitative picture of this effect by developing a suitable theory, but the phenomena that give rise to spurious pulses are too complex to be analyzed in a really satisfactory way,

* This paper is based on work performed under the auspices of the Manhattan District and was reported more fully in a classified Los Alamos document issued in 1945.
[1] W. F. Libby, Phys. Rev. **55**, 1269 (1939).
[2] K. A. Petrzhak and G. N. Flerov, Compt. Rend. Acad. Sci. U.S.S.R. **28**, 500 (1940); J. Phys. U.S.S.R. **3**, 275 (1940).
[3] N. Bohr and J. Wheeler, Phys. Rev. **56**, 426 (1940).
[4] Most of the samples were prepared by D. Hufford, Mary Miller, J. Miskel, and R. Potter.

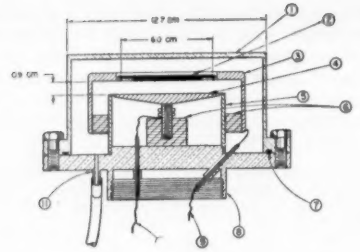

FIG. 1. Argon chamber. 1—Brass cover; 2—mounting sample; 3—sample holder and high tension electrode; 4—collecting electrode; 5—guard ring; 6—polystyrene insulating supports; 7—rubber gaskets; 8—threaded collar fastens chamber to amplifier chassis; 9—high tension lead (platinum glass seal waxed in place); 10—grid lead; 11—gas outlet.

and we shall limit ourselves to the statement above and to some experimental results to be given later.

It is clear, however, that it is desirable to have a high resolving power in the apparatus. The limitations to this may come from the collection time of electrons in the chamber and from the frequency response or rise time of the amplifier. For the chamber, electron collection with its high velocity is imperative. The chambers were filled with tank argon,[5] and special precautions had to be taken to avoid the presence of traces of organic vapors with their poisoning effects on the electron collection.

Two models of chambers were used. They are drawn in Figs. 1 and 2. The large chambers (Fig. 2) were used for material of low specific activity (U^{235}, U^{238}, Th) for which it is possible to use many milligrams of a substance without troubles due to the alpha-activity. This requires large surfaces for the samples in order to preserve their thinness. The small chambers were used for the more active substances (Fig. 1).

The amplifiers used must have high resolving power and good stability in gain. They must be absolutely free from disturbances such as high tension sparks, surges in the power supplies, etc.; for this reason we have used battery operated units shielded in large metal boxes. The wiring diagram of one of these amplifiers is given in Fig. 3.

The pulses of the amplifier were registered on an impulse meter and could also be fed through a pulse lengthener to an Esterline-Angus recorder (Fig. 4). The recording affords a useful check on the behavior of the apparatus and was made periodically on all units.

The Esterline-Angus recording was also used to check that the fission pulses obey the Poisson distribution law. How well this occurs is shown in Fig. 5, where we have reported the distribution of 141 uranium fissions.

Special precautions have to be taken also to shield substances that undergo neutron fission from neutrons due to cosmic rays. In the Los Alamos experiments, a shield of B_2O_3, 7.4 grams per square centimeter thick, was used. This means 2.7 grams per square centimeter of boron, which should cut down all the effects due to slow neutrons originating in cosmic rays by more than a factor of 10. It may be added that such a shield cuts off substantially all neutrons below 200 electron volts of energy.

In order to determine the spontaneous fission decay constant λ for the various substances, it is essential to know the amount effectively counted in each sample. This is done for most substances by subjecting the chamber containing the sample to be calibrated to a constant neutron flux produced by a Ra+Be source and counting the fissions obtained.[6] Without changing the source or the geometry we then replace the sample to be calibrated with a standard sample containing a known amount of substance and deposited in such a way as to be sure that it is thin for fission fragments. The amount of substance in the standard multiplied by the ratio of the fission rates of the unknown to the standard then gives the effective amount contained in the sample. After this calibration, a curve giving the observed fission rate *versus* the gain of the amplifier may be taken in order to estimate the size of the errors that may be introduced by small gain changes. Figure 6 shows one of these plateau curves.

During operation the gain of each unit was checked every one or two days with a pulse generator (wiring diagram, Fig. 7). Also, for long periods, polonium samples having alpha-activities larger than the samples investigated were substituted for the latter in the ionization chambers in order to check that no spurious counts would be registered. The samples were also periodically rotated among the units available.

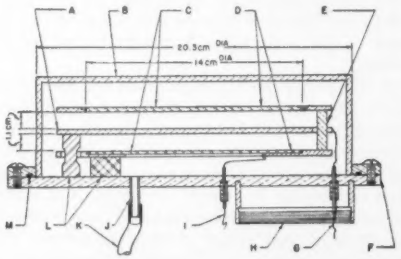

FIG. 2. Double deck nitrogen chamber. *A*—Collecting electrode; *B*—brass cover; *C*—sample holders and high tension electrodes; *D*—mounted samples; *E*—brass supports; *F*—brass base plate; *G*—grid lead; *H*—threaded collar fastens chamber to amplifier chassis; *I*—high tension lead (platinum glass seal waxed in place); *J*—gas outlet; *K*—rubber hose and clamp; *L*—polystyrene insulating supports; *M*—rubber gasket.

[5] Linde Company, incandescent lamp grade. The purity of this argon is 99.5 percent or better, the remainder being nitrogen. Special precautions are taken to remove all oxygen.

[6] The details of this experimental procedure are due to G. Farwell (private communication, available in report LA, 490).

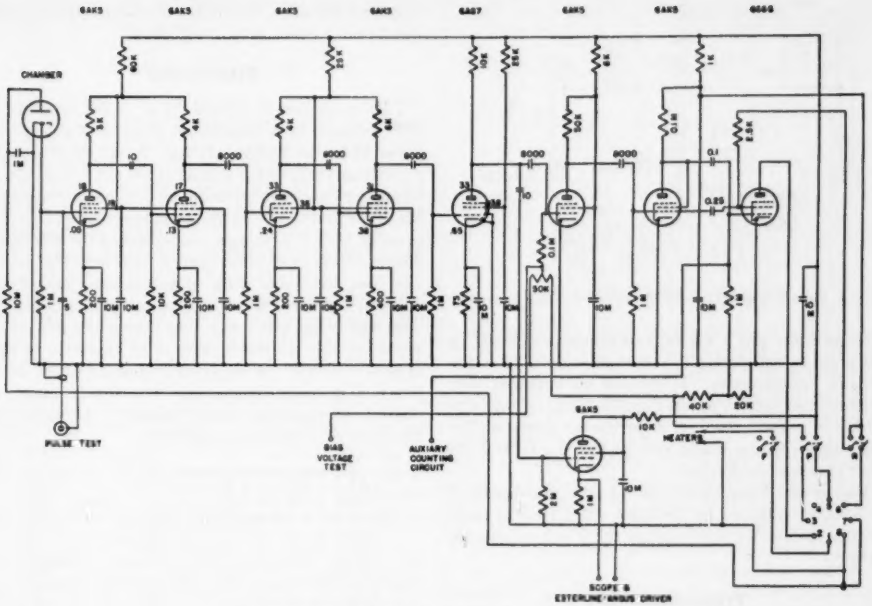

FIG. 3. Fast rise time battery amplifier.

SPONTANEOUS FISSION OF THE VARIOUS NUCLEI

The single substances investigated will now be discussed.

Radium 226

This substance was investigated by West.[7] He found an upper limit of 0.6 fission per gram per second for its spontaneous fission decay constant.

Ionium (Th^{230})

A sample of ionium extracted by Dr. Fontana from uranium ores was kindly put at our disposal by Dr. Hamilton. In this sample the Th/Io ratio is 3.4. The plates were prepared as thin layers by evaporation of a solution on platinum disks and the amount of ionium was calculated from the alpha-activity assuming a half-life of ionium of 8.3×10^4 years. The plates had a diameter of 4 centimeters and contained approximately 1 milligram of ionium each. They were observed for about 1300 hours total, corresponding to 1.45 gram hours of observation. Two fissions occurred in that time; however, they may well be due to the thorium in the sample. Indeed, one would expect (see below) in 5 gram hours of observation on thorium about 0.8 fission.

We conclude that 3.8×10^{-4} fission per gram per second is the upper limit for the spontaneous fission of ionium.

Thorium (Th^{232})

The large chambers were used for the investigation of this substance. The material used was thorium nitrate (C. P. Baker) which was ignited to ThO_2 and deposited as a thick layer using a small amount of collodion binder. The effective amount was determined by comparing the fast neutron fission of the sample with that of a thin layer of ThO_2 in the same chamber and source geometry. The thorium did not undergo any special treatment and hence was not radioactively pure. It is clear, however, that the concentration of thorium family products present in the sample is exceedingly small. In each pair of disks used in the large chambers there were approximately 0.25 gram of thorium effective. In the Los Alamos experiments 178 fissions in 1202-gram hours of observation were counted. This gives 4.1×10^{-5} fission per gram per second.

There is a small cosmic-ray effect even for fast neutron fissions in thorium, but this is practically negligible. As a matter of fact, we can estimate that the cosmic-ray effect will be less than 10^{-6} fission per gram per second.

Since the thorium spontaneous fission is so small, the question of its possible causation by impurities has to be considered. Of these, only ordinary uranium can be

[7] D. West *et al.*, private communication available also as report MP-P-18.

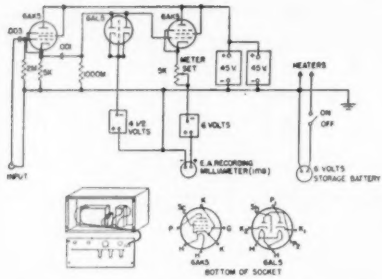

FIG. 4. Pulse lengthener to feed the Esterline Angus recorder.

of importance and a special experiment was made on this point by subjecting the thorium samples to a slow neutron bombardment. It showed an apparent slow neutron cross section of less than 10^{-27} cm^2; if this were all due to natural uranium impurity the corresponding spontaneous fission would still be less than 0.1 of the effect observed in thorium.

Maurer and Pose[8] have reported some measurements on neutron emission by thorium, attributed to spontaneous fission. We shall discuss them in a subsequent section.

Protoactinium 231

The material used for the samples was obtained from Dr. Agruss. The samples were electrolytically deposited on platinum, and the amount was determined by alpha-counting assuming a half-life of 3.2×10^4 years. Two samples were used: one of 140×10^{-6} gram, which was observed for 1119 hours and gave one fission; and one of 490×10^{-6} gram, which gave 10 fissions in 1129 hours. From these data we conclude that protoactinium gives 5×10^{-3} fission per gram per second. Again, this is probably an upper limit. From data on thermal irradiations of this same material, we know that it contains less than

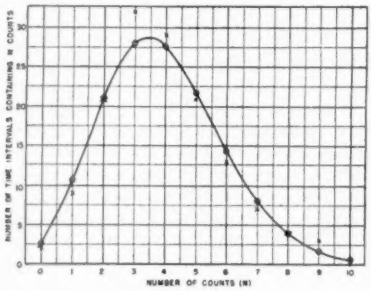

FIG. 5. Time distribution of uranium spontaneous fission. Circles, Poisson distribution; crosses, observed numbers.

[8] W. Maurer and H. Pose, Z. Physik **121**, 285 (1943).

2 percent uranium. The effect of this impurity on the spontaneous fission rate is negligible.

Uranium 232

This substance is formed by a $(d,2n)$ reaction on Th^{232} followed by a beta-decay. The material used was prepared by the Berkeley Group. It was evaporated on a platinum disk, and it had an alpha-activity of 6×10^6 disintegration per minute due to U^{232}. Assuming a half-life of 30 years for U^{232}, the sample contains 5.3×10^{-8} gram of U^{232}. The sample was observed for 950 hours, during which time three fissions occurred. The sample was also irradiated with slow neutrons and fission counted in order to find its content of ordinary uranium. This was found to be such that during the time of observation only 0.2 fission were to be expected. In spite of this, in view of the long period of observation, during which a spurious fission may conceivably occur, we consider the apparent decay constant of 16 fissions per gram per second as an upper limit.

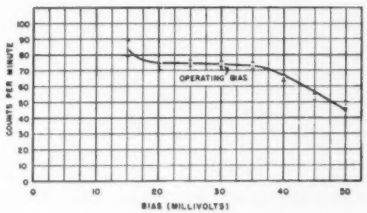

FIG. 6. Fission bias curve.

Uranium 233

This substance is formed by a (d,p) or an (n,γ) reaction on Th^{232} followed by 2 beta-emissions. Its half-life is 1.63×10^5 years.[9] Several samples were examined in the small chambers. The material was obtained by (n,γ) on Th in the Clinton pile and prepared in the Metallurgical Laboratory in Chicago. It was electroplated on platinum foils. It was observed so as to accumulate 1.35-gram hours during which one fission occurred. This fission may be explained by the U^{238} content of the sample. This result gives a decay constant smaller than 2×10^{-4} fission per gram per second.

Uranium 234

A sample of U^{234} was obtained on loan from Dr. Latimer in Berkeley. The material was prepared by extraction of UX_1 from uranium and subsequent decay of this substance. It contained a little over 10^{-5} gram effective of U^{234} as measured by its alpha-activity. We observed it for 3300 hours without observing any spontaneous fissions, from which we conclude that the

[9] Measured by G. A. Linenberger; private communication available in LAMS-256.

spontaneous decay constant is smaller than 9×10^{-3} fission per gram per second.

Uranium 235 and 238

These isotopes which occur in natural uranium could not be separated quantitatively from each other, and the observations were always performed on mixtures containing all three of the natural uranium isotopes. However, the compositions of the mixtures could be changed by using materials enriched by the electromagnetic method.

In these experiments large chambers of the second type were used.

If we call λ_x, λ_y, λ_z, the spontaneous fission decay constants of U^{238}, U^{235}, U^{234} in fission per gram per second, we find the counting rate c_i in a given sample is

$$c_i = x_i\lambda_x + y_i\lambda_y + z_i\lambda_z, \tag{1}$$

where x_i, y_i, z_i are the grams of U^{238}, U^{235}, U^{234} in that sample. Practically, the term $z_i\lambda_z$ turns out always to be negligible compared with the other two because, as stated above, λ_z is small and also z_i is generally small. By observing the counting rate in samples of different known isotopic composition, we can solve the equations for λ_x and λ_y.

We shall now describe in detail an example of these measurements. In this run three samples were used, one of ordinary uranium and two of enriched material. The isotopic composition of these materials is

$$U^{238}:U^{235}:U^{234} = 141:1:0.00725$$

in mass and

$$U^{238}:U^{235}:U^{234} = 0.334:1:0.00588$$

in mass, respectively. The isotopic analysis was checked for the enriched material by mass spectrograph and by a method of analysis[10] involving the measurement of the mass, alpha-activity, and fission cross section of the material. The samples were electroplated on platinum disks 13 centimeters in diameter and 0.01 centimeter thick and ignited to U_3O_8. The total mass of uranium was determined by direct weighing, and the mass of U^{235} by measuring the fissions occurring in a slow neutron flux. From these measurements we find that the ordinary uranium sample contains (in two plates) 38.50 milligrams of U and the two enriched samples used contain 42.95 milligrams and 36.60 milligrams of enriched material, respectively.

The normal sample gave 310 fissions in 381 hours. The enriched samples gave 101 fissions in 395 hours and 133 fissions in 558 hours. These raw data have to be corrected for the efficiency of the chamber. This is done by taking a curve of the fission rate with a constant neutron source *versus* bias of the amplifier and extrapolating to zero bias and then correcting further this result to take into account, theoretically, that some

[10] J. W. Kennedy and E. Segrè, Report MDDC-973.

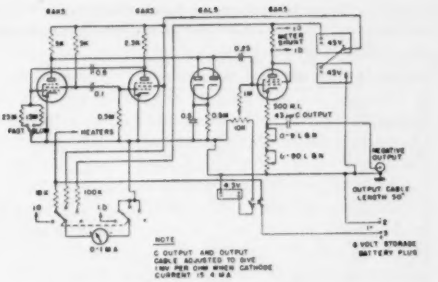

FIG. 7. Fast rise time pulse generator.

fission fragments cannot escape from the layer because of the finite thickness of the same. The first correction is 6 percent, the second is 3 percent. With these corrections we find, e.g., that normal material gives 310 fissions/13.39 g×hr = 23.2 or 6.43×10^{-3} fission per gram per second.

Similarly, enriched material gives 1.91×10^{-3} fission/g sec. Introducing these numbers into Eq. (1) and solving, we obtain $\lambda_x = 6.48\times10^{-3}$ fission/g sec and $\lambda_y = 0.40\times10^{-3}$ fission/g sec; $\lambda_z Z$ can be neglected.

The errors in these values come from statistical error in counting, for which we use the square root of the number of counts; error in the absolute mass of the foil (2 percent) and in the counting efficiency (2 percent); and error in the isotopic composition (2 percent in the ratio of U^{235} to U^{238}).

Calling R the ratio of U^{238} to U^{235} in the enriched sample and using standard formulas of the theory of errors, one finds, neglecting some small terms:

$$(\Delta\lambda_x)^2 = (1/m_1)^2(\Delta c_1)^2 + (c_1/m_1^2)^2(\Delta m_1)^2, \tag{2}$$

$$(\Delta\lambda_y)^2 + \{c_1R/m_1^2\}^2(\Delta m_1)^2 + \{c_2(R+1)/m_2^2\}^2(\Delta m_2)^2 + (R/m_1)^2(\Delta c_1)^2 + \{(R+1)/m_2\}^2(\Delta c_2)^2 + \{c_1/m_1 - c_2/m_2\}^2(\Delta R)^2 \tag{3}$$

in which m_1 is the effective mass of the sample of normal material, m_2 is the effective mass of the sample of enriched material, and c_1 and c_2 their counting rates in counts per hour.

In the run we are considering we had $m_1 = 0.0350$ g, $\Delta m_1 = 0.0010$; $m_2 = 0.0350$ g, $\Delta m_2 = 0.0010$; $c_1 = 0.814$ c/hr, $\Delta c_1 = 0.046$; $c_2 = 0.240$ c/hr, $\Delta c_2 = 0.016$; $R = 0.334$, $\Delta R = 0.007$. With these data, substituting in (2) and

TABLE I. Spontaneous fission constants of U isotopes.

Date	$\lambda_x\times10^3$	$\Delta\lambda_x\times10^3$	$\lambda_y\times10^3$	$\Delta\lambda_y\times10^3$
1943–44	6.67	0.41	0.3	1.3
December, 1944 and January, 1945	6.48	0.41	0.40	0.23
February–March, 1945	7.55	0.41	0.38	0.23
Average	6.90	0.24	0.38	0.17

TABLE II. Spontaneous fission constants.

Element	A	Fissions observed	Hours of observations	g hr of observation	λ in fissions/g sec
Ra	226	2			(<0.6)
Th(Io)	230	2	1326	1.45	$<3.8\times10^{-4}$
Th	232	178	6300	1202	4.2×10^{-6}
Pa	231	11	2200	0.62	5×10^{-3}
U	232	3	950	5×10^{-5}	16
U	233	1	1050	1.35	$<2\times10^{-4}$
U	234	0	3370	3.4×10^{-2}	$<9\times10^{-3}$
U	235				$(3.0\pm1.7)\times10^{-4}$
U	238				$(6.90\pm0.24)\times10^{-3}$
Np	237	6	1480	1.11	$\leq1.4\times10^{-3}$
Np	239	0	146	2.5×10^{-3}	<11
Pu	238	144	833	19×10^{-6}	2.14×10^{3}
Pu	239	12	~10,000	0.33	1.0×10^{-3}
95	241	3	2700	1.6×10^{-5}	(46)

(3), we obtain

$$\lambda_s=(6.48\pm0.41)\times10^{-3}\text{ fission/g sec},$$

$$\lambda_y=(0.40\pm0.23)\times10^{-3}\text{ fission/g sec}.$$

Several series of measurements were made, and the results are summarized in Table I. In the final result we have to make another correction to take into account a residual effect of cosmic rays on the apparent spontaneous fission of U^{225}, and our present best figures are

$$\lambda_x=(6.90\pm0.24)\times10^{-3}\text{ fission/g sec},$$

$$\lambda_y=(0.30\pm0.17)\times10^{-3}\text{ fission/g sec}.$$

It would be possible to improve these measurements for U^{235} using almost pure U^{235} for the samples.

Neptunium 237

This isotope is formed by beta-decay of the 7-day U^{237}, which in turn is obtained by an n-$2n$ reaction on U^{238}. Its half-life is 2.2×10^{6} years.

The samples investigated were prepared in the pile and were supplied to Los Alamos by the Metallurgical Laboratory in Chicago. An early investigation with a sample of 8×10^{-5} gram protracted so as to accumulate 127×10^{-3} gram hour of observation gave only 1 fission. Later, with 3 stronger samples (about 8×10^{-4}), we accumulated 1.113 gram hours of observation with 6 fissions recorded. This would give 1.4×10^{-3} fission per gram per second.

The effect of a possible small contamination of plutonium or uranium in the sample is negligible as tested by slow neutron irradiation; however, it is better to consider 1.4×10^{-3} fission per gram per second rather as an upper limit because it is difficult to be absolutely sure of the genuineness of the few fission pulses observed over 1482 hours of counting.

Neptunium 239

A sample of this material was prepared by J. Miskel from depleted uranium irradiated in the water boiler. The sample was purified from fission products, uranium, and plutonium and deposited on a platinum disk by evaporation. Its mass was determined by the growth of the alpha-activity of plutonium 239 in an aliquot. Approximately 0.45×10^{-6} gram were present initially and the sample was observed for 146 hours during which time no spontaneous fissions occurred. Taking into account the decay of the Np^{239}, we find that the gram hours of observation were approximately 2.5×10^{-5}. From this we conclude that 11 fissions per gram per second is the upper limit for the spontaneous fission of Np^{239}.

Plutonium 238

This substance is prepared by a $(d,2n)$ reaction[11] on U^{238}, and it has a half-life of about 60 years.

The sample used was kindly supplied by the Metallurgical Laboratory in Chicago, and had been accidentally contaminated with Pu^{239} in such a way that the ratio of the alpha-activity of Pu^{238} to that of Pu^{239} was 0.895. This was determined with differential alpha-range apparatus.

The Pu^{238} was mounted by evaporation on platinum disks and the effective amount present was measured by observing the slow neutron fission of the contaminant plutonium 239, and using the ratio of the alpha-activities quoted above. In each of our three samples we had approximately 10^{-5} gram of Pu^{239} and 2×10^{-8} gram of Pu^{238} effective. The samples were observed for a total of 830 hours, corresponding to 18.8×10^{-6} gram hour for Pu^{238} and 8.6×10^{-3} gram hour for Pu^{239}. 144 fissions were counted. From this we deduce a spontaneous fission decay constant of 2.1×10^{3} fissions per gram per second. The possible contribution of other Pu isotopes to spontaneous fission is negligible, being at the most of the order of 1 percent of the total observed.

Plutonium 239

Plutonium 239 was investigated for spontaneous fission soon after its discovery and no fissions were detected during about 5×10^{-4} gram hour of observation.[12] This study was pursued with the increasing amounts of plutonium that became available at successive dates. The samples were deposited on platinum disks by evaporation, electrolytically, or by painting. The effective amount present was generally determined by comparison with a thin standard, in a constant slow neutron flux. The thin standard was in turn alpha-counted. A half-life for Pu^{239} of 24,300 years was used.

The early material produced in the Berkeley cyclotron gave 12 fissions in observations extending over about 10,000 hours, and this corresponds to 0.010 fission per gram per second.

[11] G. T. Seaborg and A. C. Wahl, National Nuclear Energy Series, Vol. 14B, paper 1.4; for the mass assignment see Kennedy, Perlman, Segrè, and Wahl, paper 1.9.

[12] J. W. Kennedy and A. C. Wahl, private communication.

95^{241}

A sample of this material borrowed from the Metallurgical Laboratory in Chicago was examined. In this sample 95^{241} was mixed with a relatively large amount of lanthanum. Three plates were made, each containing about 7×10^{-9} gram of 95^{241}. This weight is deduced from the alpha-activity assuming a half-life of 40 years. The samples were observed for a total of 2700 hours, corresponding to 1.8×10^{-5} gram hour. Three fissions were registered. We consider the resulting number, 46 fissions per gram per second, an upper limit for the spontaneous fission constant of this material.

SUMMARY

Table II summarizes all the data accumulated up to the present time on spontaneous fission decay constants. In column 1 the chemical symbol of the element is given; in column 2, its atomic mass A; in column 3, the total number of fissions observed in all samples; in column 4, the total number of hours over which the observations have extended. This information is important because it is clear that the possibility of spurious fissions is proportional to the duration of the observations. Column 5 gives the gram hours of observation summed over all samples. Column 6 gives the spontaneous fission constant λ in fissions per gram per second, whenever it is known, with its probable error.

The expression $<t$ means that if one fission had been observed instead of none, that would be the calculated spontaneous fission constant; this means that one has the probability $1/e$ that the spontaneous fission decay constant is larger than t. More generally, it can be shown that if there have been no spontaneous fissions in a time t, the probability that the decay constant is smaller than $1/\tau$ is $e^{-t/\tau}$.

Sometimes it is convenient to use the "half-life for spontaneous fission," i.e., the half-life of a nuclear species that would obtain if the only decay possibility were spontaneous fission. This quantity is connected with the fissions per gram per second by the relation

$$T=1.32\times10^{16}/\lambda A,$$

where T is given in years, λ in fissions per gram per second, and A is the atomic mass.

The probability λ' that a given atom undergoes spontaneous fission in one second is

$$\lambda'=1.66\times10^{-24}A\lambda \text{ (λ in fissions/g sec).}$$

In addition to the data given in Table II, it is clear from our blank runs that brass undergoes spontaneous fission at a rate $<10^{-9}$ fission per gram per second.

NEUTRON EMISSION IN SPONTANEOUS FISSION

A most interesting question is to find the number ν of neutrons emitted, on the average, per fission. This number is well known for slow neutron induced fission in U^{235} and Pu^{239}, and it is clearly desirable to know it also for spontaneous fission.

Neutrons emitted spontaneously by natural uranium were detected by Fermi and others in the early Columbia experiments on the pile in 1941. Once a pile with an appreciable multiplication was set up, it was observed that even with all sources removed, the neutron density in the pile was quite appreciable. This density was attributed to the spontaneous emission of neutrons by the uranium and by measuring it with indium detectors and by comparing it with the density produced by sources emitting a known number of neutrons, it was possible to determine the number of neutrons emitted spontaneously by uranium. In this way it was found that about 1.5×10^{-2} neutron per gram per second were emitted by ordinary uranium.[13]

The spontaneously emitted neutrons were also detected by Scharff-Goldhaber and Klaiber.[14] These authors obtained about 1.75×10^{-2} neutron per gram per second of an energy above 800 kev.

Pose[15] measured the neutron emission of ordinary uranium and of thorium. His results have to be corrected because he assumes that 1 millicurie Rn+Be emits 15,000 neutrons per second. If one uses the figure 11,000 which is the best estimate available, based upon 13,000 neutrons per second for 1 millicurie Ra+Be, one obtains for uranium an emission of 1.54×10^{-2} neutrons per gram per second and for thorium 0.24×10^{-3} neutrons per gram per second. The latter figure is in all probability in error because, combined with the known spontaneous fission constant of thorium, it would give $\nu(\text{Th})=5.7$, which seems higher than is likely.

Hanson[16] has also measured the neutron emission from a uranium sphere with a long boron counter and found $(1.6\pm0.1)\times10^{-2}$ neutron per gram per second. Other measurements made at the Clinton pile gave a value of 1.5×10^{-2}, and we think that the present best value for the spontaneous neutron emission of uranium is 1.5×10^{-2} neutron per gram per second. It is believed that this value is accurate to about 10 percent, not including possible errors in the calibration of primary neutron standards. Since the calibration of such standards, however, enters in practically all neutron measurements in the same way, errors in the calibration cancel in relative measurements.

From this value of the neutron emission and from the spontaneous fission constant given previously, we find $\nu(28)=2.2\pm0.3$.

THEORY OF SPONTANEOUS FISSION

Several attempts have been made to explain spontaneous fission by a mechanism similar to that invoked by Gamow in the theory of alpha-disintegration.

---

[13] E. Fermi, private communication.
[14] G. Scharff-Goldhaber and G. S. Klaiber, private communication later published in Phys. Rev. **70**, 229 (1946).
[15] H. Pose, Z. Physik **121**, 293 (1943).
[16] A. O. Hanson, private communication and LA-276.

TABLE III. Comparison of experimental and calculated spontaneous fission constants.

	λ'_{exp}	Flügge λ'	Turner λ'	Photofission threshold Mev
Io	$<1.5\times10^{-25}$	1.2×10^{-24}		
Th^{232}	1.6×10^{-26}	1.2×10^{-26}		5.40
Pa^{231}	2.0×10^{-24}	1.1×10^{-21}		
U^{233}	$<10^{-25}$		8×10^{-20}	5.18
U^{234}	$<3.3\times10^{-24}$	1.1×10^{-20}	6.6×10^{-21}	
U^{235}	$(1.1\pm0.7)\times10^{-25}$	1.1×10^{-21}	1.1×10^{-21}	5.31
U^{238}	2.7×10^{-24}	1.2×10^{-24}	2.7×10^{-24}	5.08
Np^{237}	$<5.4\times10^{-25}$		1.2×10^{-19}	
Pu^{238}	8.4×10^{-19}		6.8×10^{-17}	
Pu^{239}	4.0×10^{-24}	1.2×10^{-17}	8.2×10^{-18}	5.31
95^{241}	$(<2\times10^{-20})$		7.4×10^{-16}	

Bohr and Wheeler,[17] in their fundamental paper on fission, give a calculation of the spontaneous fission probability by assuming that a nucleus comes about 10^{21} times per second into the optimum configuration for fission and that the transparency of the barrier is given by

$$\exp[-(2\pi/h)(2ME_f)^{\frac{1}{2}}\alpha], \tag{4}$$

in which E_f is the photofission threshold for the nucleus in question, M the mass of the nucleus, and α a length of the order of magnitude of the nuclear radius. They emphasize, however, that this estimate can give only the order of magnitude of the transparency, i.e., of the exponent in the expression of the lifetime.

Attempts have been made by S. Flügge[18] and L. Turner[19] to make more precise evaluations of the spontaneous fission constant using the formula of Bohr and Wheeler and an expression for E_f given by the same authors; but they have not been successful, as shown by the following table in which we report the spontaneous fission probabilities in sec^{-1} calculated by these authors, and the experimental results. In the case of the numbers given by Turner the probabilities have been so normalized as to give the correct value for U^{238}.

The weakness of the expression (4) given above for a precise calculation of the spontaneous fission constant is borne out even more by the experimental values for the photofission threshold reported by Koch, McEllinney, and Gasteiger[20] and given in column 4 of Table III.

How much the nuclear spin present in the odd isotopes may affect the transparency of the barrier is an open question.

An attempt to measured directly the transparency of the fission barrier, a little below the top, has been made along the following lines: Np^{237} and Pa^{231} have a neutron fission threshold of about 400 kev. A slow neutron capture hence excites the compound nucleus to about 400 kev below the threshold. Preliminary experiments by G. Farwell and M. Kahn give 0.1 barn as an upper limit for the fission cross section at thermal energy for both substances.

Now σ_f/σ_τ, the ratio of the fission cross section to the capture cross section, can be expressed as

$$\sigma_f/\sigma_\tau=\nu\tau/\Gamma_\tau,$$

in which ν is the number of times per second in which the nucleus comes into a configuration most favorable to fission, τ is the transparency of the barrier, and Γ_τ is the probability per unit time that the compound nucleus loses its excitation by gamma-ray emission.

For a slow neutron fissioner like U^{235} we know that σ_f/σ_τ a few units. On the other hand, for these nuclei τ is supposed to be about one. We conclude from this that ν/Γ_τ is of the order of a few units, say 5.

For Np^{237}, since the capture cross section for thermal neutrons is about 100 barns, we find that σ_τ/σ_f is at least 1000; hence

$$\sigma_f/\sigma_\tau\sim10^{-3}=5\tau, \quad \text{or} \quad \tau\simeq2\times10^{-4},$$

where we have assumed for ν/Γ_τ the value 5 as for other heavy nuclei. Protoactinium, with a capture cross section of about 300 barns, gives a similar result.

It must be remembered that this value of the transparency is very crude and probably represents an upper limit, because all experimental errors in the determination of the slow neutron fission cross sections of Np^{237} and Pa^{231} tend to make them appear too large.

[17] N. Bohr and J. Wheeler, Phys. Rev. **56**, 426 (1939).
[18] S. Flügge, Z. Physik **121**, 294 (1943).
[19] L. Turner, Revs. Modern Phys. **17**, 292 (1945).
[20] Koch, McEllinney, and Gasteiger, private communication, later published in Phys. Rev. **77**, 329 (1950).

Nuclear Elastic Scattering of High Energy Protons*

R. E. RICHARDSON,† W. P. BALL, C. E. LEITH, JR., AND B. J. MOYER
Radiation Laboratory, Department of Physics, University of California, Berkeley, California

(Received October 10, 1951)

The differential elastic scattering cross sections of carbon, magnesium, aluminum, silicon, sulfur, copper, silver, tantalum, wolfram, lead, and bismuth for 340-Mev protons are measured as a function of the angle of scattering. The source of the 340-Mev protons is the external scattered deflected proton beam of the Berkeley 184-inch synchrocyclotron. The scattered protons are detected by a triple coincidence scintillation counter telescope whose detection threshold is set by copper energy attenuators placed between the last two transstilbene scintillators.

The observed angular distributions are similar to the pattern observed in Fraunhofer diffraction of plane electromagnetic waves by an opaque disk. The details of the diffraction patterns indicate that the nuclei appear partially transparent to the 340-Mev protons.

The observed patterns are found to be consistent with those predicted from elastic scattering of 83-Mev neutrons, indicating that the Coulomb forces are only important in changing the patterns at very small angles.

An attempt is made to observe spin-dependent variations in the patterns from neighboring nuclei whose moments are known to differ appreciably. Within the statistics and resolution of the experiment no appreciable variations are detected.

I. INTRODUCTION

A. Previous Diffraction Experiments

WITHIN certain energy limits elastic scattering of high energy nucleons by nuclei is analogous to optical Fraunhofer diffraction, considering the nucleus as the scattering obstacle and using the DeBroglie wavelength ($\lambda=\hbar/p$) of the high energy nucleons as the incident wavelength.

Amaldi *et al.*[1] have observed the angular distribution of 14-Mev neutrons scattered from Pb nuclei, using neutrons produced by the D+Li reaction. The neutrons had a DeBroglie wavelength of 7.5×10^{-13} cm and were nearly monoenergetic, making them useful for seeking diffraction effects in heavy nuclei. The angular distribution observed had a strong forward peak, with a minimum at about 25° and a small secondary maximum near 40°. Assuming that the Pb nucleus behaved as an opaque sphere, they deduced from the position of the minimum that the radius of the Pb nucleus was about 1×10^{-12} cm.

Using the 90-Mev neutron beam of the 184-inch synchrocyclotron, Bratenahl, Fernbach, Hildebrand, Leith, and Moyer[2] have investigated the diffraction of neutrons by Be, C, Al, Cu, Ag, and Pb. The minima in their patterns were obscured by the energy spread of the neutron beam, which is produced by stripping of 190-Mev deuterons in a one-half inch thick Be target placed in the circulating deuteron beam.[3] The differential scattering cross sections were observed to be not zero in the region of expected secondary maxima for the heavier elements. Their results at the center of the forward peaks were well described by the opaque nucleus picture, but at larger angles the predictions of the transparent nucleus theory of Fernbach, Serber, and Taylor[4] gave a better fit to the experimental points.[5]

Transparency of a spherical nucleus should alter the shape of the diffraction pattern by increasing the intensity in the region of the minima, decreasing the intensities of the secondary maxima, and causing the entire pattern to broaden slightly corresponding to a slight decrease in radius.

The present experiment makes use of higher energy and better energy resolution, thus providing a better test of the nuclear model. The differential cross sections may be integrated and compared with the total neutron cross sections of DeJuren,[6] and of DeJuren and Moyer.[7] Because of the Rutherford scattering, the proton curves to be integrated must be corrected at small angles in order to compare with neutron results (see Sec. V, B).

B. Wavelength of Particles in Present Experiment

Bratenahl *et al.* consider the energy distribution of their neutron beam and the energy dependence of their detection efficiency to arrive at an effective energy of 83 Mev for their particles, giving a DeBroglie wavelength of 3.05×10^{-13} cm. The wavelength of the 340-Mev protons used in the present experiment is 1.43×10^{-13} cm. This shorter wavelength causes the diffraction patterns to be more concentrated in the forward direction, making intensities higher and thus more easily observable above background. The narrowing makes necessary the use of instruments of high angular resolu-

* This work has been performed under the auspices of the AEC.
† Now at Project Lincoln, M.I.T., Cambridge, Massachusetts.
[1] Amaldi, Bocciarelli, Cacciapuoti, and Trabacchi, Nuovo cimento **3**, 15, 203 (1946).
[2] Bratenahl, Fernbach, Hildebrand, Leith, and Moyer, Phys. Rev. **77**, 597–605 (1950).
[3] R. Serber, Phys. Rev. **72**, 1008 (1947).
[4] Fernbach, Serber, and Taylor, Phys. Rev. **75**, 1352 (1949).
[5] It has recently been pointed out by S. Pasternack and H. S. Snyder, Phys. Rev. **80**, 921 (1951), that the calculational method may introduce some error into the theoretical curves.
[6] James DeJuren, Phys. Rev. **80**, 27 (1950).
[7] J. DeJuren and B. J. Moyer, Phys. Rev. **81**, 919 (1951).

tion in order to detect the details of the diffraction pattern.

Protons provide certain distinct advantages over neutrons in such an experiment, namely: (1) a monoenergetic incident beam, (2) exclusion of inelastically scattered particles more easily accomplished by range selection, and (3) detection efficiency essentially unity.

There are a few disadvantages related to the proton charge. Rutherford scattering distorts the diffraction patterns at small angles; but for the energy and scattering thicknesses here employed, this is completely negligible in the region of the detail of interest. Furthermore, the multiple scattering in the target and air path affect angular resolution, and energy loss in the target must be considered.

C. Nuclear Eccentricities

If the shape of the nucleus is ellipsoidal rather than spherical, and if the nuclei are randomly oriented in the scattering target, the diffraction pattern may be expected to be altered in much the same way as the alteration due to nuclear transparency. Since the nuclear electric quadrupole moment is related to the departure from spherical symmetry, the results of experiments of this type might be used to set upper limits upon the electric quadrupole moments of the nuclei measured. In order to separate the transparency effects from the quadrupole moment effects, the diffraction pattern of a nucleus known to have a high spin is compared with those of its neighbors having spins of zero or one-half. Simple calculation shows that upper limits inferred from experiments of the accuracy here presented would be far larger than the values of eccentricity usually quoted, and greatly improved accuracy would be required to yield any useful information of this sort.

II. THEORY

A. Coulomb Correction

The exact solution of the wave equation involving both Coulomb and nuclear force fields is in a series of confluent hypergeometric functions. Since the bombarding energy in this experiment is much higher than the Coulomb barrier energies of the nuclei involved, the effects of the Coulomb field will be neglected as a first approximation. Therefore the theory will be given for the neutron case, with corrections which should come out of the exact solution indicated.

B. Neutron Solution in Partial Waves[8]

The wave function for the scattered neutron wave, which is obtained by subtracting the expression for the unperturbed incident plane wave from the solution for the case in which the scattering nucleus is present, may be represented asymptotically at large distance r from the scattering center, and at an angle θ from the direction of the incident beam by

$$\Psi_{\text{scatt}} \simeq \frac{e^{ikr}}{2ikr} \sum_{l=0}^{\infty} (2l+1)(e^{2i\delta_l}-1)P_l(\cos\theta), \qquad (1)$$

where δ_l is determined by matching the solution of the wave equation in the field-free region to that within the boundaries of the scattering potential. If there is no absorption in the scattering nucleus, δ_l is a real number measuring the phase shift between the lth partial wave in the diverging components of the wave function with scatterer present and the corresponding lth component of the unperturbed plane wave. In the case in which absorption is also present, δ_l is a complex number

$$\delta_l = \alpha_l + i\beta_l, \qquad (2)$$

where β_l is the exponent determining the absorption of the lth partial wave.

The lth partial wave may be associated with particles in the beam which provide an angular momentum of $l\hbar$ with respect to the center of mass of the system, which is practically the center of mass of the scattering nucleus. Since the wavelength of the incident particles is appreciably smaller than the nuclear radius, it makes sense to speak of the particle colliding within the area represented by the cross section of the nucleus. If the impact parameter is b, the angular momentum is

$$pb = l\hbar, \text{ from which } l = pb/\hbar = b/\lambda = kb. \qquad (3)$$

For the Pb nucleus, values of l up to nearly $l=40$ should be considered for 340-Mev particles, since the largest value of impact parameter at which nuclear forces can be felt is equal to R, the nuclear radius. Particles passing at larger distances should be unaffected, so that no components of the scattered beam should arise from $l>kR$.

The corresponding solution for the proton case would contain, besides δ_l, an additional phase shift[9]

$$\epsilon_l = \eta_l - \nu \ln 2kr, \qquad (4)$$

where ν depends upon the charges, masses, and relative velocities of the interacting proton and nucleus, and η_l is the argument of a Γ function which depends upon ν and l. Thus the method of partial waves is not strictly applicable to the proton case, but gives an asymptotic solution independent of r only for force fields of finite range. The higher values of l which would be introduced by the Coulomb field give contributions to the cross section only at extremely small angles.

In the opaque nucleus theory it is considered that all particles which strike the nucleus are "absorbed," i.e., removed from the high energy beam by inelastic processes. In this case β_l will be infinite for $0 \leq l \leq kR$,

[8] The method of solution in partial waves was originated by J. W. Strutt (Lord Rayleigh), and presented in Proc. London Math. Soc. (1) **IV**, 253 (1873), as a method of solution for optical problems. Its application to nuclear physics is presented in most standard texts on wave mechanics. [See for example, Leonard I. Schiff, *Quantum Mechanics* (McGraw-Hill Book Company, Inc., New York, 1949), pp. 103–121.]

[9] See reference 8, p. 119.

and zero for l greater than kR; and α_l is zero for $l>kR$. Thus for the perfectly absorbing sphere the scattered wave, Eq. (1), becomes

$$\Psi_{\text{scatt}}\simeq-\frac{e^{ikr}}{2ikr}\sum_{l=0}^{l<kR}(2l+1)P_l(\cos\theta). \tag{5}$$

It is interesting to note that these components of the scattered wave are just the corresponding outgoing components of the unperturbed plane wave shifted in phase by 180°. This is equivalent to removing these outgoing components from the total wave field, which is just what would be expected from a perfectly absorbing sphere and is an example of Babinet's principle from physical optics.

The differential scattering cross section per unit solid angle, which is just the square of the amplitude of the scattered wave multiplied by r^2, is seen to be

$$\frac{d\sigma}{d\Omega}(\theta)=\frac{1}{4k^2}\Big[\sum_{l=0}^{l<kR}(2l+1)P_l(\cos\theta)\Big]^2. \tag{6}$$

This distribution may be reduced to the optical Fraunhofer diffraction pattern of plane light waves of wavelength $\lambda=2\pi/k$ incident upon an opaque disk of radius $R'=R+1/k$, which is usually given for small angles as

$$\frac{d\sigma}{d\Omega}(\theta)=k^2(R')^4\left[\frac{J_1(2kR'\sin\tfrac{1}{2}\theta)}{2kR'\sin\tfrac{1}{2}\theta}\right]^2, \tag{7}$$

where J_1 is a first-order Bessel function.

If there is not complete absorption of those particles which strike the nucleus, the problem is one of diffraction of the incident wave by a sphere of material characterized by an index of refraction and an absorption coefficient. The index of refraction is due to the fact that the magnitude of the propagation vector may change within the nucleus because of the nuclear potential well. The absorption coefficient arises from interaction of the incident particle with individual nucleons in the nucleus, which is postulated to be the method of removing particles from the beam by giving rise to inelastic scattering. The absorption coefficient used by Fernbach, Serber, and Taylor[4] is just the numerical density of nucleons in the nucleus multiplied by the nucleon-nucleon scattering cross sections obtained from n-p and p-p scattering experiments and modified to allow for the suppression of small momentum transfers in the nucleus due to the Pauli exclusion principle. They obtain for a spherical scatterer with a nonreflecting surface

$$\Psi_{\text{scatt}}\simeq\frac{e^{ikr}}{2ikr}\sum_{l=0}^{l+\frac{1}{2}<kR}(2l+1)[e^{(-K+2ik_1)s_l}-1]P_l(\cos\theta), \tag{8}$$

where k_1 is the change in propagation constant upon entering the nucleus, K is the absorption coefficient

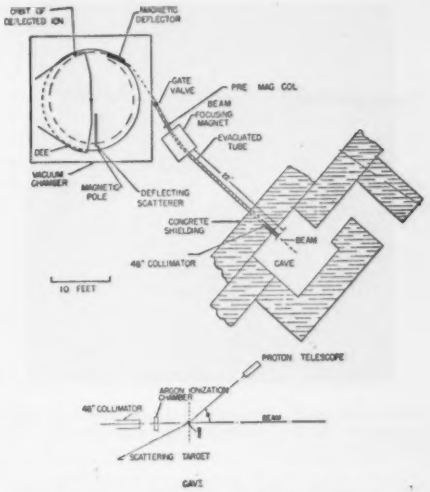

FIG. 1. General arrangement of the experiment.

given by

$$K=(3/4\pi R^3)[Z\sigma_{np}'+(A-Z)\sigma_{nn}'] \tag{9}$$

and s_l is essentially the path length, within the nucleus, of the particle having angular momentum equal to $l\hbar$:

$$s_l=[k^2R^2-(l+\tfrac{1}{2})^2]^{\frac{1}{2}}/k. \tag{10}$$

The criterion for nonreflection is that the potential must not change appreciably within one wavelength.

The cross sections σ_{np}' and σ_{nn}' in Eq. (9) are the effective n-p and n-n scattering cross sections for collisions with nucleons in nuclei. In the case of proton diffraction they are replaced by σ_{pp}' and σ_{np}', respectively. The numerical values to be employed are obtained from known values of σ_{pp} and σ_{np} in free particle collisions, modified by effects of the Pauli principle.

III. EXPERIMENTAL PROCEDURE

A. General Method

In Fig. 1 is shown a diagram of the experimental layout. The collimated external proton beam of the 184-inch synchrocyclotron beam is monitored by an argon-filled ionization chamber whose collected charge is integrated electronically. The scatterer is a thin sheet of material with a cross-sectional area considerably greater than the beam area, and the scattered protons are detected by a triple-coincidence scintillation counter proton telescope which is shielded from particles which may scatter from the mouth of the collimator or from the ionization chamber. The number of incident protons is determined by the charge collected by the ionization chamber, and the number of protons scattered at an

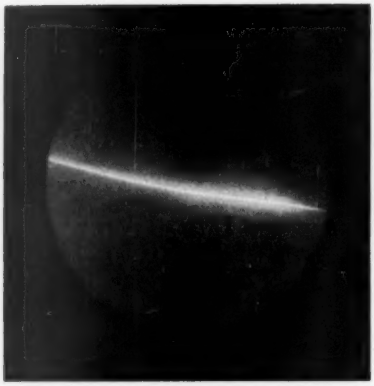

FIG. 2. Autograph of the scattered deflected beam, showing the line character. Made by exposing an x-ray film in the direct beam, positive print, actual size.

angle θ into the solid angle offered by the telescope is determined by the number of counts from the telescope. These two numbers may be used to determine the differential scattering cross section, as is shown in Sec. V.

B. Source of the Proton Beam

When a thin scatterer is placed in the full energy circulating proton beam of the 184-inch synchrocyclotron some of the protons are multiply scattered at such an angle that they enter the magnetic deflecting channel[10] and are removed from the main vacuum chamber into an evacuated tube which carries them through an opening in the main concrete shielding into a separate shielded enclosure usually referred to as the "cave," as shown in Fig. 1. The duration of the scattered beam pulse is about 20 μsec with a usual repetition rate of about 60 per second. The energy of the protons which are accepted is determined by the path in the magnetic deflecting channel and by the path through the beam focusing magnet which directs them down the straight portion of the evacuated tube into the cave. The energy of this beam is known from the curvature in the magnetic field, and has also been measured as described below to have a range in Cu of 93.7 g/cm^2 which corresponds to an energy of approximately 340 Mev. The energy may vary by a few Mev from one day to another due to slight differences in the setting up of the deflecting system, but the variation is certainly not more than ± 1 percent.

C. Collimation

The beam is collimated to the proper size consistent with the angular resolution desired by means of a 48-inch long brass plug which is inserted into the evacuated tube where it passes through the 15-foot concrete shielding. For most of the runs, the collimator used had an inside diameter of $\frac{1}{4}$ inch and was tapered toward the outer end to a diameter of $\frac{3}{4}$ inch in order to decrease the probability of multiple scattering from the collimator back into the beam. This gives a beam at the scatterer of approximately $\frac{5}{8}$-inch diameter. For the high angular resolution runs, the circular collimator in the shielding was replaced by a rectangular collimator in order that the scattered beam might appear to come from a line source instead of a circular source, thus increasing the angular resolution without at the same time introducing too much of a decrease in counting rate.

During the course of this experiment it was discovered that when the premagnet collimator (see Fig. 1) is wide open the cross section of the beam as it enters the cave is concentrated mainly in a line about $\frac{1}{32}$ inch broad and tilted at an angle of about 13° to the horizontal, as shown in Fig. 2. The rectangular collimator used was $\frac{3}{16}$ in.$\times\frac{3}{4}$ in. When it was used, so tilted as to line up with the beam cross section, to replace the $\frac{1}{2}$-inch diameter circular collimator, the counting rate was not appreciably changed.

D. Setting of the Scatterer

In order that all of the protons elastically scattered into the telescope at any given angle will have traversed the same path length and thus have lost the same amount of energy by ionization in the target, the scatterer is not placed perpendicular to the beam, but is inclined to the perpendicular at half the angle by which the telescope is inclined to the beam.

E. Counting Rate, Background, Accidentals

The triple coincidence counting rate is kept to about one count per beam pulse by controlling the beam intensity. At this counting rate, the number of accidental triple coincidences is negligible, as determined by observing the counting rate as a function of beam intensity. The counting rates in the individual photomultipliers are much higher than this. They are, in fact, sometimes so high that the mechanical registers of the scalers cannot follow them. Since the coincidence unit has a short resolving time, better than the scalers by nearly a factor of a hundred, this high individual counting rate is not objectionable.

After each datum run, a run is made under the same conditions except that the scattering target is removed to determine background. The background is considered in determining the magnitude of the effect as well as in determining the statistical accuracy of the points. The background is comparable to the true counting rate near and after the first minima of the diffraction patterns, necessitating the making of long datum runs and long background runs in order to obtain points of statistical significance in this region.

[10] C. E. Leith, Phys. Rev. **78**, 89 (1950).

In order to eliminate any slowly varying instrumental errors such as voltage drift from apparently changing the shape of the diffraction pattern, the datum points are not taken for the angles in numerical order, but are taken at angles much farther apart than the spacing desired in the final points, with the intermediate points taken later.

F. Detection Threshold and Absorption by the Energy Attenuators

In order to determine the detection efficiency of the proton telescope and to set the detection threshold, the telescope was placed in the direct beam with no scatterer present, and the counting rate was measured as a function of the thickness of Cu energy attenuator present. For this run, the beam intensity was so low that the argon ionization chamber could not be used as a monitor. Therefore, the double coincidence counts of the first two scintillators, which are before the energy attenuator, were used as a monitor. Because of the thickness of the scintillators and their holders, the curve could not be continued to zero thickness. The curve is shown in Fig. 3, and it is seen that the curve may be extrapolated to a ratio of unity from a thickness corresponding to the Cu equivalent of the scintillators and their dural holders. The curve is seen to cut off at an equivalent thickness of 93.7 g/cm² of Cu (mean range), which corresponds to 340 Mev on the curves of Aron, Hoffman, and Williams.[11] The extrapolated range is 95.5 g/cm². Bakker and Segrè[12] have measured the extrapolated range of the electrostatically deflected proton beam to be 93.7 g/cm². Mather[13] has independently determined the energy of the electrostatically deflected beam by means of the Čerenkov radiation in dense glass. He finds the energy to vary from 339 Mev to 341 Mev, depending upon the setting up of the deflecting system. Taking this as a correct value and comparing the range with that of Bakker and Segrè, it is found that the energy of scattered deflected beam may be as high as 344 Mev. It is expected that the scattered deflected beam may have a slightly higher energy than the electrostatically deflected beam, since its orbit must expand to a slightly greater radius than that at which the electrostatic deflector operates. Bakker and Segrè indicate that the curves of Aron *et al.* give an energy which is slightly too low due to the fact that they used too high an ionization potential in their calculations. Since the ionization potential enters into the energy loss equation in a logarithmic term, the error is expected to be small, and the discrepancy between the range-energy curves and the measurements of Mather may be considered to be due to this error.

For most of the data an energy threshold of 330 Mev was employed, while for some of the early runs the value was 315 Mev. The detection efficiency, which is determined by reading the ratio corresponding to the thickness of energy attenuator used in the experiment, varies from 48 percent to 56 percent in the various runs, but is constant within a given run. In determining the energy threshold, the energy loss of the protons due to ionization in the target must be added to the ionization loss in the counters and energy attenuator; so in the case of a 330-Mev threshold the total copper equivalent of the path to the center of the last crystal was 87.0 g/cm². The decrease in energy due to center-of-mass motion must also be considered, but is negligible except for the lightest target elements used. The decrease in the number of protons due to inelastic scattering in the target of particles which have been elastically scattered is negligible.

G. Lining Up the Scattering Frame

The detection angle is determined by setting the pointer of the telescope arm at a particular marker on the calibrated angular scale of the scattering frame. The 0° line is aligned with the proton beam in the following manner:

After the cyclotron has been tuned up and a satisfactory beam has been obtained in the cave, x-ray films are exposed in the beam at the front and rear of the cave. The developed films show darkened spots where the beam has passed through them. The centers of these

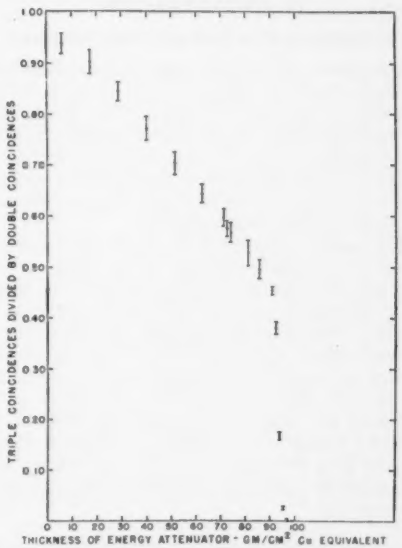

FIG. 3. Energy attenuator effect at zero degrees. The mean range of the beam is 93.7 g/cm² of Cu. The extrapolated range is 95.5 g/cm² of Cu. Particles are lost in the attenuator both by absorption and by scattering out.

[11] Aron, Hoffman, and Williams, Atomic Energy Commission Unclassified Report No. 663 (1949).
[12] C. J. Bakker and E. Segrè, Phys. Rev. **81**, 489 (1951).
[13] R. L. Mather, Phys. Rev. **84**, 181 (1951).

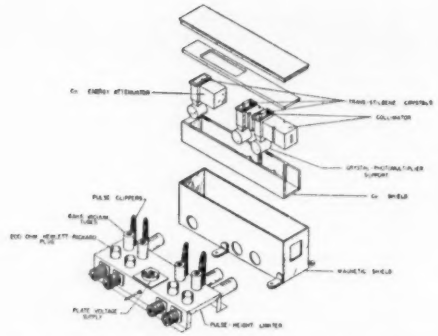

FIG. 4. The proton telescope, showing copper shielding and iron shielding. The energy attenuator is seen before the last crystal holder. The collimating opening may be seen at the front of the telescope. The chassis to the left of the telescope contains pulse-shaping circuits which limit and clip the pulses.

spots are used to stretch a string through the cave in the position occupied by the beam center. Fiducial marks at the front and rear of the scattering frame are then aligned with respect to this string, after which the string is removed, and a film is exposed at the scatterer position as a check on the alignment. With reasonable care, it is possible to align the frame to within a small fraction of a degree.

IV. INSTRUMENTATION

A. Ionization Chamber and Beam Integrator

The proton beam is monitored with an argon-filled ionization chamber operated at a pressure of 92-cm Hg and with a sensitive thickness of 2.002 inches. The multiplication factor of the chamber has been measured by comparison with a Faraday cage and found to be 1095 ± 15 for 340-Mev protons. The chamber is operated at a voltage high enough so that there is no detectable ion recombination before collection.

The charge collected by the ionization chamber is stored in a standard capacitor whose voltage is continuously recorded upon moving paper tape by means of a Speedomax recorder fed from a feedback dc amplifier. The amplifier maintains its input grid at ground potential so that the leakage in the signal cable leading to the capacitor is negligible and the capacitance of the cable does not have to be considered in determining the total charge collected in terms of the recorded voltage. The recording circuit automatically recycles after attaining a predetermined voltage, and automatically calibrates itself periodically against a standard cell.

B. Scatterers

The C, Al, Cu, Ni, and Pb scattering targets were machined from stock materials. The Ta and W targets were cut from stock foil. The S, Si, and Mg targets are pellets which were compressed from powdered stocks. The Si targets contain a small amount of hydrocarbon binder. The Bi targets were cast. After forming, the targets were weighed on chemical balances and their dimensions measured with micrometer calipers. The weights and dimensions thus determined are used in the calculations. The densities were also calculated and compared with known densities to rule out the possibilities of "blow-holes" or voids.

C. Energy Attenuators

The energy attenuators are two-inch square slabs of Cu machined from stock materials. They were weighed and measured in the same manner as were the scattering targets. Their densities were found to agree with the known density.

D. Proton Telescope

The scattered protons are detected by a triple-coincidence scintillation counter telescope consisting of three trans-stilbene crystals each viewed by a 1P21 electron photomultiplier tube. The signals from the photomultipliers are amplified, clipped, limited, and fed to the coincidence circuit. It is necessary to limit the amplitude of the pulses since the background includes a great number of inelastically scattered protons which are going slowly in the first two crystals, thus giving pulses very much larger than those due to the elastically

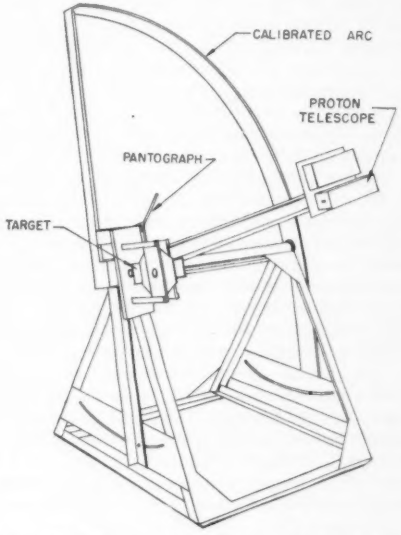

FIG. 5. The tilting proton scattering frame which makes use of the line character of the beam to increase angular resolution without much sacrifice of counting rate.

scattered particles. These large pulses are apt to "feed through" the coincidence circuit unless all the pulses are limited to some standard height. The coincidence circuit is found to work most efficiently when all the pulses are of the order of two volts in amplitude.

The various double coincidence counting rates are measured as a monitor of the operation of the equipment.

Angular resolution of the telescope is determined by the opening in a one-inch thick Cu collimating block placed between the first and second phosphors. This thickness is sufficient so that any particle missing the opening will not be counted in the last crystal.

In order to decrease the individual counting rates the entire telescope is enclosed in a $\frac{1}{4}$-inch thick Cu box to keep out the general background of "slow" particles which exists in the cave. In front of the first crystal is placed a three-inch long Cu block having in it a hole of the same size as the hole in the collimating block. It has been determined that the presence of this block appreciably decreases the single counting rates of the first and second phosphors by keeping out randomly directed particles.

The first and second phosphors are made only slightly larger than the opening in the collimating block since the ambient background counting rate is dependent upon the whole volume of the scintillators, while only the portion offered to the collimator is effective in giving true counts. The last crystal is made approximately an inch and a half square in order to count a large portion of the protons which are multiply scattered in the energy attenuating Cu blocks.

The stray magnetic field in the cave due to the cyclotron magnet is about 20 gauss. Since photomultipliers may be affected by this field, the entire telescope, except for an entrance hole, is enclosed in a magnetic shield of one-eighth inch thick mild steel with a $\frac{1}{4}$-inch thick lid. The proton telescope is shown in Fig. 4.

E. Scattering Frame

The scattering frame is shown in Fig. 5. It is so constructed that the plane in which the measurements are made may be set perpendicular to the "line source" which the beam produces as it strikes the scatterer. The scattering targets are mounted upon a remotely controlled hexagonal wheel allowing several targets to be run at the same scattering angle without necessitating a shutdown of the cyclotron in order to enter the cave. Pilot lights at the control station indicate which target is in the scattering position at any time.

The proton telescope is clamped to a rigid Dural channel which keeps it pointed at the scatterer. This arm is pivoted upon the shaft which supports the scatterer wheel. The four-inch by $\frac{3}{8}$-inch Dural plate which makes up the circular arc of the frame is calibrated at one degree intervals, and the arm, which carries a vernier calibrated in tenths of a degree, may be clamped to the circular arc at any angle.

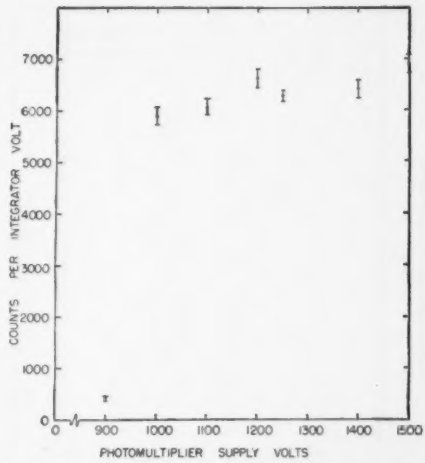

FIG. 6. Typical voltage plateau for the detecting system with 340-Mev protons incident.

In order that the target will always be set at half the angle at which the telescope is set, the scatterer support is connected to the telescope arm by means of an equal-arm pantograph, which insures bisection of the angle.

F. Coincidence Circuit

The coincidence circuit used in this experiment is a Rossi type quadruple coincidence circuit using a crystal diode as a diode clamp in the plate circuit, and a crystal diode signal expander circuit in the output. It was designed and constructed at this laboratory by R. Madey and B. Ragent for use in meson experiments, and is very similar to one devised by Garwin.[14] In order to use this as a triple coincidence circuit, the signal from one of the photomultipliers is split and fed into two different channels of the coincidence circuit. The resolving time is approximately 2×10^{-8} second. The signals from the photomultipliers, after shaping, are amplified by Hewlett-Packard type 460-A distributed amplifiers before being fed to the coincidence circuit, and the coincidence output is fed through a linear amplifier to a scaler.

In order to insure that all of the protons scattered into the telescope are counted, a check is made of counting rate as a function of the photomultiplier tube supply voltage. As the voltage is increased it is expected that more of the weak pulses will be made large enough to cause counts. At excessively high tube voltages, the thermal noise level is expected to be so high as to give accidental coincidences. In Fig. 6 is shown a typical plot of triple coincidence counts per unit integrated beam as a function of tube voltage. It is seen that there is a very

[14] R. L. Garwin, Rev. Sci. Instr. **21**, 569 (1950).

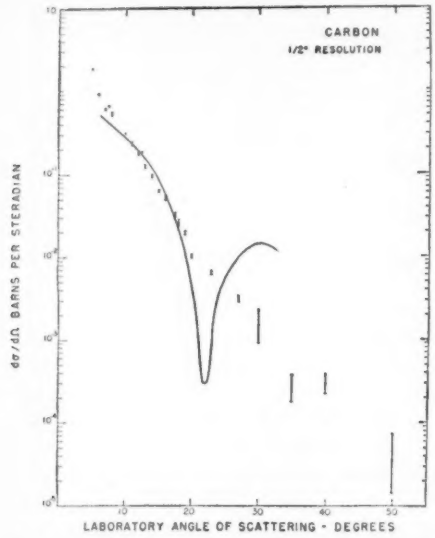

FIG. 7. Differential elastic scattering cross section as a function of angle for 340-Mev protons on C. The curve is the prediction of the transparent nucleus theory, modified for the effect of the finite angular resolution.

broad plateau in which all of the protons are being counted, but accidental coincidences are negligible.

V. CALCULATIONS

A. Differential Scattering Cross Section

If the cross section does not vary appreciably over the angular region accepted by the telescope, at a given nominal angle, the number of true counts expected in the proton telescope when n protons are incident is given by

$$K(\theta)=NnT_a(d\sigma/d\Omega)\Delta\Omega, \qquad (11)$$

where N is the number of scattering nuclei per square centimeter; n is the number of incident protons, which is measured by the ionization chamber, with known multiplication factor; T_a is the transmission factor of the energy attenuator and telescope, which is varied from 0.48 to 0.56 for the various runs; $\Delta\Omega$ is the solid angle subtended by the proton telescope; and $d\sigma/d\Omega$ is the differential elastic scattering cross section. It must be noted that N varies as $(\cos\frac{1}{2}\theta)^{-1}$ since the target is turned through $\frac{1}{2}\theta$. Solution for $d\sigma/d\Omega$ yields the values presented in Sec. VI.

The true counting rate is determined from the actual data by subtracting the background counts per integrator volt from the actual counts per integrator volt recorded during a datum run. The statistical deviation due to the counting statistics is the square root of the sum of the squares of the individual deviations of actual and background counts per volt.

B. Total Cross Section for Elastic Scattering

The total elastic scattering cross section is found by integrating the differential cross section over all angles. While the measurements do not give a true picture of nuclear scattering at very small angles, due to Coulomb effects, the total solid angle included in these angles is very small. As an approximation for the integration, the differential cross-section curve is made to approach the zero degree axis in the same manner as would be inferred from the 83-Mev neutron results of Bratenahl *et al.*[3] The contributions at angles larger than those measured will be less than 1 percent.

C. Angular Resolution

The angular resolution is determined by the geometry of the detection system and by the thickness of the scattering target. The size of the beam at the target, which determines the effective size of the source which the telescope sees, and the size of the opening in the telescope collimating block are so chosen that the maximum deviation from the nominal scattering angle at which a proton may be scattered and still be detected is equal to the nominal angular resolution. The angular deviation at which the intensity falls to half-maximum is somewhat smaller than this. The angular spread due to multiple Coulomb scattering in the target is Gaussian, with the thicknesses of the targets so chosen that the

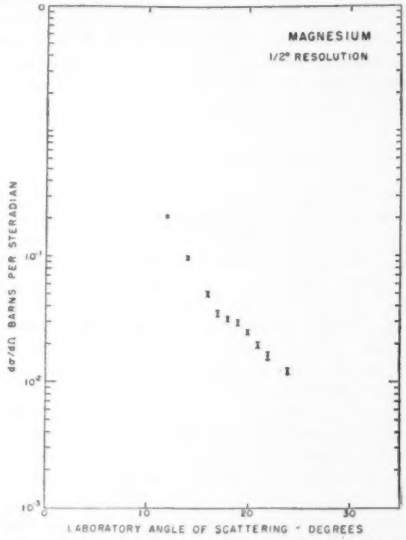

FIG. 8. Differential elastic scattering cross section as a function of angle for 340-Mev protons on Mg.

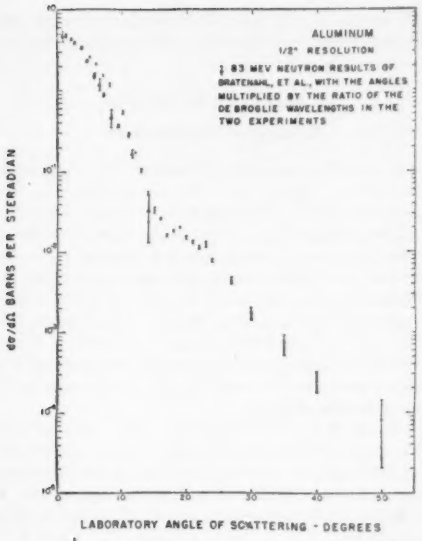
ALUMINUM
1/2° RESOLUTION
83 MEV NEUTRON RESULTS OF
BRATENAHL, ET AL., WITH THE ANGLES
MULTIPLIED BY THE RATIO OF THE
DE BROGLIE WAVELENGTHS IN THE
TWO EXPERIMENTS
dσ/dΩ BARNS PER STERADIAN
LABORATORY ANGLE OF SCATTERING - DEGREES

FIG. 9. Differential elastic scattering cross section as a function of angle for 340-Mev protons on Al.

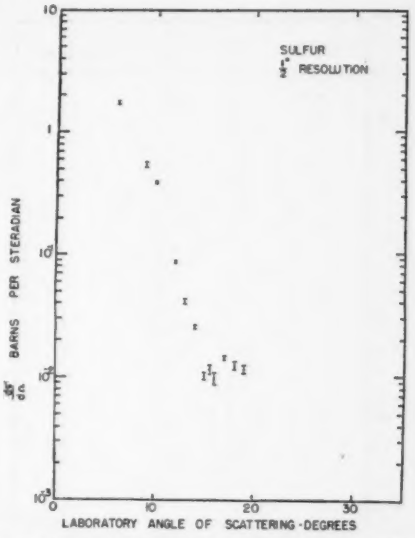

FIG. 11. Differential elastic scattering cross section as a function of angle for 340-Mev protons on S.

half-width at half-maximum is equal to the nominal angular resolution. The angular divergence of the incident beam is negligible in the determination of angular resolution, due to the long path from the cyclotron to the cave.

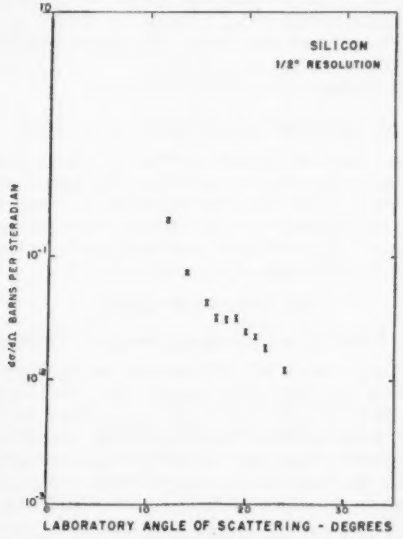

FIG. 10. Differential elastic scattering cross section as a function of angle for 340-Mev protons on Si.

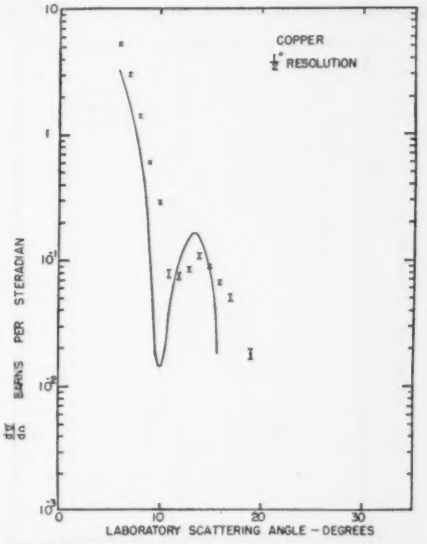

FIG. 12. Differential elastic scattering cross section as a function of angle for 340-Mev protons on Cu. The curve is the prediction of the transparent nucleus theory, modified for the effect of the finite angular resolution.

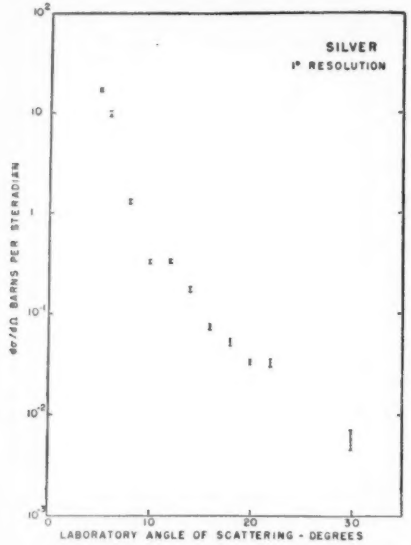

FIG. 13. Differential elastic scattering cross section as a function of angle for 340-Mev protons on Ag.

The total air path of the protons from the exit of the evacuated tube to the telescope is two meters. The root-mean-square displacement of 340-Mev protons in this path length is 1.8 mm. This displacement at the telescope would correspond to an angular spread of approximately $\pm 0.1°$.

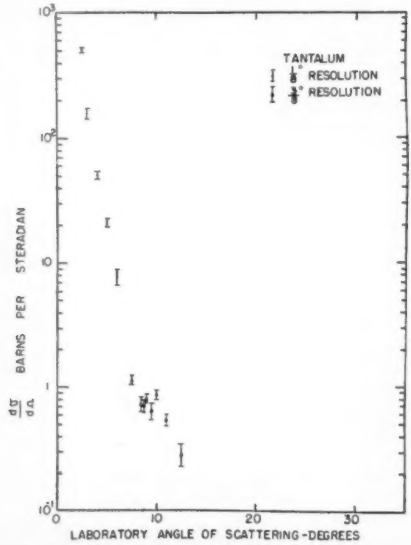

FIG. 14. Differential elastic scattering cross section as a function of angle for 340-Mev protons on Ta.

VI. RESULTS AND CURVES[15]

A. Angular Distributions

The data for the angular distributions for the elements measured are plotted in Figs. 7 through 17. The differential elastic scattering cross section in barns per steradian is shown as a function of the angle of scattering in the laboratory system, which is equivalent to the center-of-mass system except for large angles where the difference is a few degrees for light elements. The center-of-mass angle is larger than the laboratory angle by 3.5° at 50° for C. The difference is only 1.6° for Al at 50°. It is correspondingly smaller for the heavier elements. The errors shown are the usual standard deviations based upon counting statistics.

Because of the large variation of the cross sections with angle, the cross-section scale is made logarithmic. It is interesting to note that the ratio of the differential cross section of C at 5° to that at 50° is about 60,000. It should be noted that the data are not all plotted with the same scales.

The curves shown are the predictions of the transparent nucleus theory, modified for the effect of finite angular resolution. On the Al curve, the datum points of Bratenahl *et al.* have been plotted, with the angle multiplied by 0.469, which is the ratio of the wavelengths in the two experiments.

In Fig. 18 the positions of the maxima and minima of the measured diffraction patterns are plotted as a function of atomic mass number. The apparent tendency of the lower mass points to lie above an $A^{\frac{1}{3}}$ curve is to be expected from transparent nucleus concepts.

B. Total Elastic Scattering Cross Sections

The total cross sections for "nuclear" elastic scattering are found by continuing the curves toward zero degrees in the same shape as was found in the neutron case by Bratenahl *et al.* The resulting curves are then integrated to determine the total elastic scattering cross sections. The results are tabulated in Table I.

VII. SOURCES OF ERROR

A. Detection of Inelastically Scattered Particles

Cladis, Hadley, and Moyer[16] are investigating the protons scattered by nucleon-nucleon collisions when 340-Mev protons impinge upon various target nuclei. The description of this type of scattering is fairly well supplied by simple two-body collision considerations in which the target nucleon has an initial momentum characteristic of a particle in a nucleus. This simple

[15] Preliminary results have been given by Richardson, Ball, Leith, and Moyer, Phys. Rev. **83**, 859 (1951).
[16] Cladis, Hadley, and Moyer, Phys. Rev. **81**, 649 (1951).

picture is of course only an approximation in view of the requirements imposed by the final state of the residual nuclear system and over-all conservation of energy.

In the small-angle region this process will contribute some protons with energies above the threshold of the proton telescope. Their number is, however, sufficiently small as to be insignificant in data of the accuracy here presented, except possibly in the case of carbon in the vicinity of 5°–10°.

In this connection it should be mentioned that some of the early runs were made with a 315-Mev threshold, and their results were not significantly different from those made with the 330-Mev threshold.

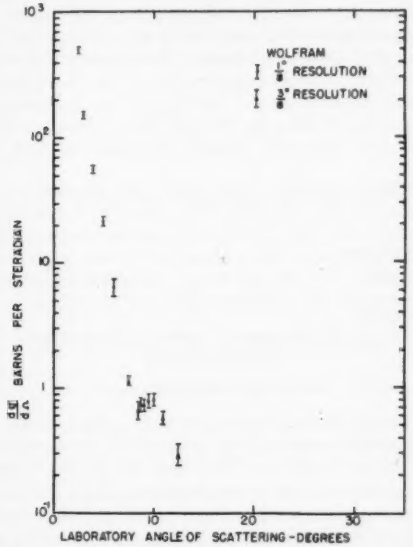

FIG. 15. Differential elastic scattering cross section as a function of angle for 340-Mev protons on W.

B. Energy Threshold

It is not possible to determine exactly the detection threshold of the apparatus because of straggling in the energy attenuator. For convenience, the same energy attenuator is used in most of the runs having the same angular resolution. The energy loss in the scatterers, which were chosen so as to have multiple scattering angles appropriate to the angular resolution desired, varied by a few Mev. This means that the detection threshold was not exactly the same for all elements, but the variation was so small as to be unimportant. The same energy attenuator was used for all angles. Since the correction for center-of-mass motion is small, the variation of energy of elastically scattered protons with angle is relatively unimportant. As an extreme example, the

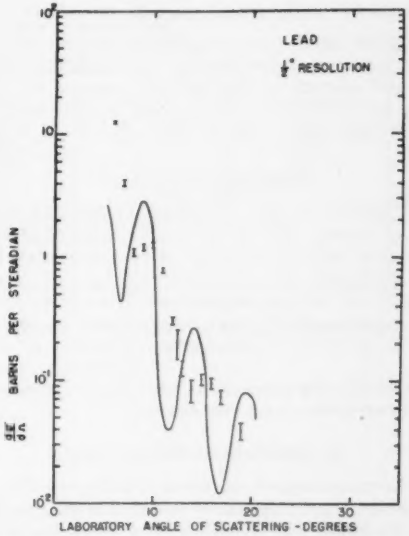

FIG. 16. Differential elastic scattering cross section as a function of angle for 340-Mev protons on Pb. The curve is the prediction of the transparent nucleus theory, modified for the effect of the finite angular resolution.

energy decrease due to center-of-mass correction is only about 5 Mev for C at 30°. Nearly all of the datum points

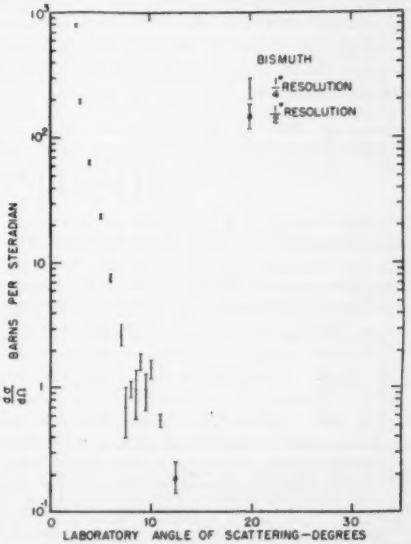

FIG. 17. Differential elastic scattering cross section as a function of angle for 340-Mev protons on Bi.

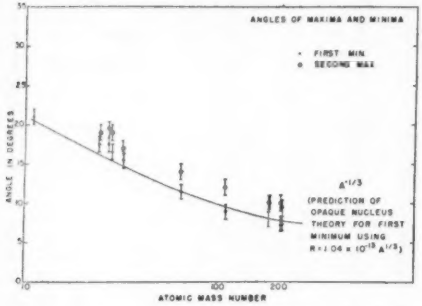
ANGLES OF MAXIMA AND MINIMA
FIRST MIN.
SECOND MAX.
ANGLE IN DEGREES
ATOMIC MASS NUMBER
A^1/3
(PREDICTION OF OPAQUE NUCLEUS THEORY FOR FIRST MINIMUM USING R=1.04 × 10^-13 A^1/3)

FIG. 18. Angles of maxima and minima plotted *vs* atomic mass number.

included in this paper are at smaller angles than this, where the effect is not even this large.

C. Double Scattering in Target

An uncertainty not yet considered is the possibility of a proton experiencing two wide-angle scattering events in the target. The probability for a double scattering into an angle θ is proportional to the product of the probability of scattering into an angle α and that for scattering into β, where $\theta=\alpha+\beta$. This is negligible for the thin targets and for the angles considered.

D. Rutherford Scattering into Large Angles

Williams[17] has considered relativistic Coulomb scattering and has corrected for the finite size of the nucleus, considering the charge to be uniformly distributed throughout the nucleus. He obtains for the differential scattering cross section

$$\frac{d\sigma}{d\Omega}(\theta)=\left[\frac{Ze^2}{2M\beta^2c^2\gamma}\right]^2\frac{1}{\sin^4\frac{1}{2}\theta}\frac{1}{\left[1+\left(\frac{b}{\lambda}\sin\frac{1}{2}\theta\right)^2\right]^2} \quad (12)$$

where all symbols have their usual meaning, with M being the reduced mass. This formula gives cross sections of 6.7×10^{-25} cm² and 7.9×10^{-26} cm² at 6° and 8°, respectively, from Pb. These cross sections are down by a factor of about thirty from the values measured in this experiment. For C at 10° the factor is greater than one hundred.

Gatha[18] is at present undertaking the solution of the wave equation including both the Coulomb and nuclear effects and considering transparency. His preliminary results indicate that the Coulomb effect should be important only up to about 2° for C and 6° for Pb.

It is interesting to set an approximate upper limit upon the angle at which a proton may scatter by single Rutherford scattering. The maximum sidewise momentum which the proton may acquire in the collision is proportional to the square root of the Coulomb barrier energy of the struck nucleus. The square root of the ratio of the barrier energy to that of the total kinetic energy (incident energy) will then give an approximate upper limit to the angle. For 340-Mev protons incident upon Pb, this angle is about 12°, while for C it is about 5°.

The angular distribution of multiply Coulomb scattered particles is Gaussian. The probability for multiple Coulomb scattering into an angle greater than twice the half-width at half-maximum of the Gaussian is less than the probability for single Rutherford scattering into the same angle, which has been shown to be negligible.[17]

TABLE I. Total cross sections for "nuclear" elastic scattering.[a]

Element	Cross section (barns)
C	0.098
Al	0.201
Cu	0.515
Ag	0.884
Pb	0.934

[a] No errors are indicated, since the value is very sensitive to the method of continuing the differential cross sections toward zero degrees. In some cases, the use of the datum points at very small angles instead of neglecting the Coulomb scattering by continuing the curves to match the corresponding neutron data would change the cross section by a factor of 2 or 3. The value shown is in each case less than the upper limit set by the work of DeJuren (see reference 6) and DeJuren and Moyer (see reference 7) for 270-Mev neutrons.

VIII. CONCLUSIONS AND COMPARISON WITH THEORY

A. Angular Distributions

The angular distributions are seen to give evidence of diffraction as expected, except for C. It is even possible to suspect a minimum for C near 20°, but the datum points are not close enough together to make the minimum certain. Since the transparent nucleus theory considers a model in which the nucleus is a sphere with an index of refraction, the model probably does not hold for such a light nucleus with its small number of nucleons. The results of this experiment indicate that C appears quite "open" to the 340-Mev protons.

The relative heights of the secondary maxima of succeeding orders agree favorably with diffraction theory for Pb in which two secondary maxima have been observed. The minima appear at slightly larger angles than in the theoretical curves, indicating that the nuclei are probably even more transparent than assumed in the transparent nucleus theory.

The 83-Mev neutron results may be matched by a nuclear radius given by $R=1.39\times10^{-13}A^{\frac{1}{3}}$ cm. If the nuclear radii are calculated by Eq. (7), using the positions of the first minima found in this experiment, it is found that the radii of opaque nuclei which would give

[17] E. J. Williams, Proc. Roy. Soc. (London) **169A**, 531 (1939).

[18] K. M. Gatha, private communication.

minima at those positions would be given by a coefficient which varies from 0.84 for C to 1.13 for Pb. This is again an indication of nuclear transparency.

B. Total Cross Sections for Elastic Scattering

The total cross sections for nuclear scattering, omitting the Coulomb part, were determined by counting squares on a curve of cross section per unit angle $d\sigma/d\theta = 2\pi \sin\theta d\sigma/d\Omega$, plotted as a function of angle. Although the total solid angle offered at large angles is much greater than that at small angles, the cross sections fall off rapidly enough that the contribution for angles greater than 30° is negligible in all cases. The results of the integration are consistent with the neutron results in that they fall always below the upper limits for elastic scattering indicated by the neutron experiments.

C. Nuclear Eccentricities

The high spin nuclei show no statistically important differences from their zero-spin neighbors, except that the Al minimum appears slightly sharper, but the resolution is such that nuclear eccentricities would need to be much larger than currently held values to be discernible.

IX. ACKNOWLEDGMENTS

The authors wish to express their gratitude to Professor E. O. Lawrence for his kind interest in the progress of this work. They also wish to thank the cyclotron crew and especially Mr. J. L. MacMullen for their assistance in the investigation of the structure of the emergent proton beam. Dr. S. Fernbach and Dr. K. M. Gatha have been very helpful in discussions of the theoretical aspects.

PHYSICAL REVIEW VOLUME 86, NUMBER 1 APRIL 1, 1952

Nuclear Photodissociation by High Energy Synchrotron Gamma-Rays*

SEISHI KIKUCHI
Cornell University, Ithaca, New York
(Received October 15, 1951)

The stars and single proton tracks produced in photographic emulsions exposed to a beam of high energy synchrotron gamma-rays have been analyzed. The maximum energy of the bremsstrahlung spectrum was varied between 150 and 300 Mev. The following subjects were studied: 1. the cross section for star production as a function of the excitation energy; 2. the energy distribution of the protons from stars as well as single protons; 3. the angular distribution of star protons as well as single protons; and, 4. the relative number of stars associated with a meson coming out.

The cross section for the nuclear photoevents increases with increasing energy above the meson threshold. There seem to be two sorts of processes taking place in competition with each other. One is the so called free meson effect; namely, a free meson is produced inside the nucleus by the interaction of a photon with a nucleon and is then absorbed in the same nucleus. The other effect is a process in which a photon is absorbed directly by a group of nuclear particles without emitting a real meson. Evidence for the free meson effect is seen in the fact that the angular distribution of star protons of energy between 20 and 60 Mev in the case of 300-Mev excitation shows a strong forward peak. Evidence for the existence of the direct absorption of photons comes from the fact that the angular distribution of star protons of high energy, say about 100 Mev, shows a forward asymmetry.

The cross section for direct absorption is much larger than expected from Levinger's theory of nuclear photodissociation. The cross section should be at least of the same order of magnitude as the free meson effect.

I. INTRODUCTION

NOT much is known about the photodissociation of nuclei by gamma-rays whose quantum energy is above the threshold of photomeson production. The cross section for (γ,n), (γ,p), $(\gamma,2n)$, (γ,np), $\cdots$ reactions has been studied up to about 100 Mev, and the results show that the cross sections reach their maximum somewhere below 50 Mev and then decrease gradually to a very small value, which is not yet exactly measured. The purpose of the present experiment is to investigate the nuclear photodissociation when the energy of the photon exceeds the meson threshold, by studying the stars and the single proton tracks produced in a photographic emulsion exposed directly to a beam of high energy synchrotron gamma-rays.

It is expected that above the meson threshold stars will be produced by the emission and subsequent absorption of mesons in the same nucleus. Actually, it was found that the probability for star production begins to increase as the energy of the photon exceeds the meson threshold.[1] The problem is whether or not this effect can be explained in terms of the so called free meson effect alone. The present results indicate not only the existence of the free meson effect but the existence of another effect whose cross section is comparable with the free meson effect.

The production of high energy protons from any target irradiated by high energy gamma-rays has been reported, and their energy distribution and angular

* This work has been supported by the ONR.

[1] R. D. Miller, Phys. Rev. **82**, 260 (1951); S. Kikuchi, Phys. Rev. **81**, 1060 (1951).

TABLE I. Relative number of events produced in a photographic emulsion at different excitation energies.

Excitation energy in Mev	150	200	250	300	300–150
Single protons { <20 Mev	200±50			170±20	−30±60
Single protons { >20 Mev	35± 5			47± 8	12± 9
2-prong stars {positive	16± 2			47± 6	32± 7
2-prong stars {probable	9± 2			46± 7	37± 7
3-or-more-prong stars	25± 3	36±4	86±12	100	75± 3
Meson-associated stars	0			5± 2	5± 2

distribution have been studied.[2] It is expected that by the study of individual nuclear photoevents in photographic emulsions the origin of these so called photoprotons will be made clear. The advantage of the use of the photographic emulsion method lies more in the clarification of the qualitative side of the phenomenon rather than the quantitative side. In the present work a greater effort was made to take advantage of this circumstance than to get accurate values.

II. EXPERIMENTAL PROCEDURE

The photographic emulsions used were both Ilford C2 and G5. The thicknesses of emulsion used were 200, 300, and 600 microns. At the earlier stage of the work, emulsions were exposed to an uncollimated beam of synchrotron bremsstrahlung gamma-rays, 3.6 meters from the synchrotron target. Later, they were exposed to a beam in the large vacuum chamber of the pair spectrometer at about 6 meters from the synchrotron target. The electron contamination of the beam was swept away by the magnetic field of the pair spectrometer, and a pure gamma-ray beam hit the plates which were set uncovered, emulsion side facing the beam. For thick G5 emulsion this procedure helped very much to get rid of blackening due to the electron contamination of the beam. In the case of G5 emulsion there were many secondary electron tracks starting in the emulsion. Most of them were parallel to the beam and did not prevent us from finding or measuring the prongs which were not parallel to the beam. When the emulsion surface is perpendicular to the beam, the secondary electrons travel normally to the surface and the disturbance is the least.

In the case of 200-micron emulsion the maximum radiation one can give to the G5 emulsion was about 5×10^8 Q,[3] distributed uniformly over the area of a 1 in. $\times$3 in. plate. In the case of 600-micron emulsion the limit was one third of this amount. In the case of C2 emulsion about ten times more radiation can be given than in the case of G5 emulsion of the same thickness.

[2] C. Levinthal and A. Silverman, Phys. Rev. **82**, 822 (1951); D. Walker, Phys. Rev. **81**, 654 (1951); J. C. Keck, Ph.D. thesis, Cornell University (1951).

[3] Q, the number of equivalent quanta, is a quantity defined by

$$Q = \frac{\text{total flux of gamma-rays}}{\text{maximum energy of bremsstrahlung spectrum}},$$

and is used conveniently in dealing with the bremsstrahlung gamma-rays. See references 5 and 6.

The processing of the plates was done according to the method developed by Occhialini[4] and others using amidol. In some cases of C2 emulsion, hydroquinone developer was used instead of amidol. It was necessary to underdevelop the plates in order to measure the energy of protons between 20 and 60 Mev by the gap density measurement. The uniformity of the development for 200-micron emulsion was very satisfactory. In the case of 600-micron emulsion there was a slight depth dependence in the degree of development.

III. THE RELATIVE FREQUENCY OF APPEARANCE OF DIFFERENT SORTS OF EVENTS

The nuclear photoevents analyzed were as follows:

1. Stars. In this note a star means an event such that more than two visible prongs start from a point in the emulsion. Prongs shorter than 3 microns were regarded as recoils of the residual nucleus and were not counted as prongs. The stars are classified according to the number of prongs.

2. Single prongs. This means a visible prong starting in the emulsion without association with any other visible prongs. A single prong might be a proton, deuteron, triton, alpha-particle, or meson. Some of them might be associated with neutron prongs, which are not visible. Among the single prongs only the proton prongs were analyzed. The single meson prongs were mostly light, and it was hard to obtain reliable statistics from them.

3. Meson-associated stars. This means a kind of star from which a meson comes out. If the meson is of low energy and is stopped in the emulsion, it often forms a sort of double star.

Table I shows the relative frequency with which different sorts of events were observed at different excitation energies. All the figures were taken from data obtained with G5 emulsion. In the case of 300- and 150-Mev excitation, most of the data was taken from 600-micron emulsion. In the other cases 200-micron emulsions were used. Though nothing has been said yet about the energy measurement of the protons, part of the classification of events in Table I is made according to the energy of the protons.

The numbers for the cases of different excitation energies are normalized to the same number of equivalent quanta, using the data given in the next section. The number of 3-or-more-prong stars in the case of 300-Mev excitation was taken as a standard.

There was an ambiguity about the number of two-prong stars, as such a star was easily confused with a single track suffering a large angle scattering. The use of 600-micron thick emulsion diminished this ambiguity considerably, compared with the case of 200-micron emulsion. There are still an equal number of doubtful cases and positive cases.

[4] Dilworth, Occhialini, and Vermaesen, Bulletin Du Centre De Physique Nucleaire De L'Universite De Bruxelles, No. 13a, Fevrier (1950).

The knowledge of the number of single protons in proportion to the number of stars is important in connection with the discussion of the mechanism of star production and also in connection with the relation of the present results to the results of other workers on photoprotons observed by counter experiments. To eliminate the doubt which might arise from the fact that a single proton starting in the emulsion is a rather inconspicuous event, so that the number given might be too small, the efficiency of the scanning was checked by scanning a part of the area twice. On the average the efficiency for single protons was about 80 percent, whereas that for stars was 92 percent. The figures given in Table I have not been corrected for this factor.

The method by which the percentage of meson-associated stars was determined will be mentioned in Sec. VII.

As the numbers are normalized to equal Q, the difference of the corresponding numbers at two different excitation energies indicates to a good approximation the contribution of the photons whose energies lie between the corresponding excitation energies.[5] Thus the last column of Table I shows the contribution of photons of energy above 150 Mev contained in the bremsstrahlung spectrum of maximum energy 300 Mev. It is worthwhile to note that a good fraction of the single protons in the 300-Mev case is due to photons of energy below 150 Mev. We will refer to this point again in Sec. VI.

IV. THE EXCITATION CURVE FOR STAR PRODUCTION

The experiment described in this section was carried out at a fairly early stage of the work, where only C2 emulsions had been used. The 200-micron C2 emulsions were exposed directly to the beam of synchrotron bremsstrahlung gamma-rays of maximum energy 150, 200, 250, and 300 Mev, and the numbers of stars produced in the emulsions were compared. The intensity of the beam at different excitation energies was calibrated by the intensity of radioactivity induced in a carbon plate exposed to the beam simultaneously with the emulsion, by the reaction $C^{12}(\gamma,n)C^{11}$. This means that the beam intensity was normalized to the same intensity at the resonance energy of the $C^{12}(\gamma,n)C^{11}$ reaction, which lies at about 25 Mev. The cross section in terms of equivalent quanta Q should be,[6] to a good approximation, proportional to the number of stars produced in the emulsion per standard intensity of the C^{11} activity. In every case the emulsion and the carbon plate were exposed to the beam for three minutes. The counting of the activity, started 5 minutes after the exposure was finished, was done with a commercial Geiger counter in standard geometry for 7 minutes. It was checked in advance that the activity in this time interval was due to C^{11}. The actual number of counts was 400 to 700 in 7 minutes, while the background count was about 140 in 7 minutes.

TABLE II. The cross section per Q for the production of stars of three or more prongs.

Excitation energy in Mev	150	200	250	300
Cross section per Q, arb. units	1.95±0.18	2.55±0.19	5.63±0.56	6.04±0.41
Cross section per Q, corrected	2.05±0.20	3.00±0.22	7.20±0.72	8.15±0.57
Absolute cross section per $Q\times10^{27}$ cm²	1.5 ±0.4	2.2 ±0.2	5.4 ±0.5	6.1 ±0.4

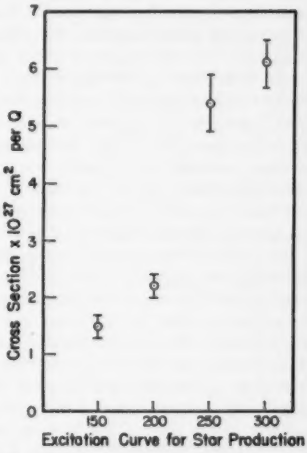

FIG. 1. Excitation curve for star production.

In counting the stars there was the ambiguity about the two-prong stars, as already mentioned. Only those events were counted as two-prong stars when it was certain that they were different particles because of the difference in the grain density of the two prongs or because of the increase in grain density of both prongs along the track as the distance from the common point increases.

[5] It is a special character of the bremsstrahlung spectrum that, if the spectra obtained at two different excitation energies E_1 and E_2 ($E_1<E_2$) are normalized to the same number of Q, they coincide approximately with each other in the region below E_1.

[6] The cross section in terms of Q, $\sigma_Q(E)$, at the excitation energy E is defined by $\sigma_Q(E)=n/(N\times Q)$, where Q is the number of equivalent quanta corresponding to the flux which went through the area in which n events were found, and N is the number of atoms per unit area of emulsion. To get the cross section per photon, we have to take the difference, $\sigma_Q(E+dE)-\sigma_Q(E)$, and divide it by the number of photons between E and $E+dE$ for unit Q. If we use the approximation that the spectrum is given by $W(E)=Q_0/E$ for $E<E_{max}$ and 0 for $E>E_{max}$, where $W(E)dE$ is the number of photons between E and $E+dE$ and Q_0 is a constant, Q is equal to Q_0, as is easily shown. In this case the cross section per photon $\sigma(E)$ is simply given by

$$\sigma(E)=Ed\sigma_Q(E)/dE.$$

The error caused by the fact that the C2 emulsion is not sensitive to high energy protons was estimated in the following way. First the sensitivity of the individual emulsion was determined by finding out how far the proton tracks could be followed from the end of their range. The C2 emulsion is supposed to be sensitive to protons up to the energy of 60 Mev. But in the present case they were processed rather lightly by the hydroquinone developer using the dry method, and it was determined that the emulsion was sensitive up to 30 Mev. Thus, knowing the sensitivity of C2, one can figure out from the actual prong spectrum and energy spectrum obtained by analyzing the stars in G5 emulsion, what the prong spectrum should be like and how many stars are overlooked when C2 emulsion was used. A careful study on about 300 stars obtained in 600-micron G5 emulsion showed that the prong spectrum is somewhat distorted in C2 emulsion and that the correction to be applied to the total number of the stars is about (35±5) percent in the case of 300-Mev excitation. In the case of 150-Mev excitation the number of the protons above 30 Mev is relatively small compared to the case of 300-Mev excitation, and the same consideration showed that the correction should be (5±3) percent.

The results are shown in Table II. The first row shows the figures proportional to the number of stars for the standard intensity of C^{11} activity before the correction for the insensitivity of the C2 emulsion. The second row shows the values after this correction. The amount of correction for the cases of 200 and 250 Mev was determined simply by linear interpolation. The ratio of the number of stars per Q produced in the emulsion at 300-Mev and 150-Mev excitation is 4.0±0.5 after the correction and 3.1±0.1 before the correction. The other method of determining this ratio is to determine the number of low energy single protons in proportion to the number of stars. The low energy protons, say below 20 Mev, starting in the emulsion would be due to gamma-rays of low energy through the reactions (γ,p), (γ,np), and so on. Therefore one can use the number of low energy single protons as a measure of Q values; and the ratio of the number of stars to the number of single protons of low energy gives the cross section per Q. Taking into account only those single protons and stars which start in the middle 400 microns of the 600-micron emulsion, the ratio can be determined fairly certainly. In the present case, the protons of energy below 20 Mev were counted, and the result was 4.5±1.6 for the ratio. Owing to the rather small number counted, the error is fairly large. But the value is in better agreement with the corrected value from Table II than with the value before the correction.

TABLE III. The energy distribution of star protons and single protons. The cross section is expressed in microbarns per Mev per Q.

Energy in Mev	300-Mev excitation Star	300-Mev excitation Single	150-Mev excitation Star	150-Mev excitation Single
20– 30	150±20	155±32	36±6	135±17
30– 40	89±17	75±22	17±4	54±11
40– 50	70±15	80±23	5±2	20± 6
50– 60	64±14	34±15	6±2	15± 6
60– 80	15± 4	7± 5	0	2± 1
80–100	10± 3	7± 5	1±1	2± 1
100–120	12± 4	7± 5	1±1	3± 2
120–140	8± 3	0	0	0
140–160	7± 3	0	0	0

The cross section as a function of excitation energy is plotted in Fig. 1. The value of the ordinate indicates the absolute cross section (see next section). The cross section seems to rise fairly steeply above 150 Mev. The trend is similar to the excitation curve for photomeson production. One might argue that the steep rise of the curve does not necessarily show the rapid rise of the cross section of photonuclear interaction itself. It might come from the fact that the energy of the nucleon or group of nucleons set in motion by the primary photonuclear event increases with the increasing excitation energy and therefore the probability that these particles produce a star by collision with another nucleon, inside the nucleus, increases rapidly with the excitation energy. This argument might be true if star production were a small part of all photonuclear events. However, as the figures of Table I show, the production of stars of 3 or more prongs constitutes a large part of all photonuclear events, so that the result described in this section shows definitely that the cross section for the photonuclear interaction does increase rapidly above 150 Mev.

Similar results have been obtained by Miller[1] at Berkeley. Miller used C2 emulsion and counted stars of 3 or more prongs. The relative values of the cross section at different excitation energies agree quite well with the present values before correction.

V. THE ABSOLUTE MEASUREMENT OF THE CROSS SECTION FOR STAR PRODUCTION

The absolute cross section for star production at 300-Mev excitation was determined by measuring the integrated beam intensity sent through the emulsion with the ionization chamber and current integrator calibrated with the gamma-ray pair spectrometer[7] by Keck[2] of this laboratory. 1.08×10^{8} Q was sent through a 300-micron thick G5 emulsion. Stars of 3 or more prongs were counted and the over-all average cross section σ was determined by the relation $\sigma QN=n$, where N is the sum of the number of atoms of different kinds except hydrogen per cm^2 of emulsion, and n is the total number of stars of 3 or more prongs. Since we have as yet no information about the Z-dependence of the cross section it is most reasonable to give the value of cross section in this way. As soon as we know the Z-dependence we can calculate the cross section for each element from the known data about the atomic concentration of different elements in emulsion.

[7] DeWire, Ashkin, and Beach, Phys. Rev. **83**, 505 (1951).

The value obtained for the cross section per Q for the production of 3 or more prong stars at 300-Mev excitation is $(6.1\pm0.3)\times10^{-27}$ cm². This value will be used throughout as the basis for discussion.

The absolute cross section can also be determined[1] from the experiment described in Sec. IV by determining the absolute number of C^{11} atoms produced in the carbon plate exposed simultaneously with the emulsions, together with the value of $\int\sigma(E)dE$ determined by other workers. $\sigma(E)$ is the cross section for the $C^{12}(\gamma,n)C^{11}$ reaction for photons of energy E, and the integration is carried out over the vicinity of the resonance point where $\sigma(E)$ is appreciably different from zero. The result is consistent with the present result.

Miller,[1] assuming the cross section for star production to be proportional to the mass number, obtained the value 6.5×10^{-27} cm² for the silver nucleus at 322-Mev excitation. Interpolating his excitation curve, the corresponding value at 300 Mev is 5.5×10^{-27} cm² for silver. If we calculate the average cross section as defined here from these data, we get the value 2.5×10^{-27} cm², which is smaller than our value. Miller used C2 emulsion, and three-or-more-prong stars were counted. If the sensitivity of Miller's emulsion is the same as that of our C2 emulsion, the correction to be applied is a factor of 1.5. This gives the value 3.8×10^{-27} cm². The discrepancy is still a factor of 1.6, which is too large to be ascribed to experimental error. Errors involved in the calibration of the beam might be responsible for this discrepancy.

VI. THE ENERGY DISTRIBUTION OF THE PROTON PRONGS

The energy of the protons from stars, as well as that of the single protons, were determined by measuring range, gap, or grain density, according to which one of the methods gives the most accurate value for each individual case. The analysis was carried out on 600-micron G5 emulsion exclusively. The protons or stars starting within 100 microns from either surface of the emulsion were discarded. Under these conditions the ranges of the protons remaining in the emulsion were fairly long on the average, so that a moderately accurate determination of the energy was possible. The calibration curve for the gap density as a function of energy was obtained by measuring the gap density as a function of residual range for some protons of range 5000 to 15,000 microns ending in the emulsion. The energy of protons between 20 and 60 Mev was measured mostly by this method. The gap density of a 20-Mev proton was 0.17 and that of a 60-Mev proton was 0.50. The energy of protons above 60 Mev was measured by grain counting. At 60 Mev the grain density was 100 per 100 microns. The grain density-energy curve was calibrated from some long range mesons ending in the emulsion. The longest meson track used was about 10,000 microns, whose grain density at the start corresponds to that for protons of 170 Mev. Above this energy the energy was determined roughly by extrapolation. Minimum ionization was determined by the electrons from μ-e decay and also by some high energy electrons excited by gamma-rays. It was 32 grains per 100 microns. As already mentioned, the development of the emulsion was carried out to such a degree that the determination of the energy by gap measurement was as accurate as possible for the energy region between 20 and 60 Mev.

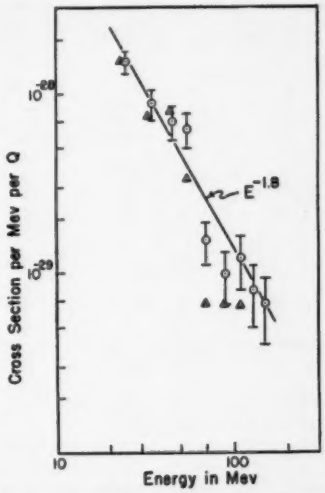

FIG. 2. Energy distribution of star protons and single protons in the case of 300-Mev excitation. The circles represent star protons and the triangles represent single protons.

The measurement was made most extensively in the case of 300-Mev excitation and less extensively in the case of 150 Mev. For other excitation energies no proton measurement was made.

There was a slight depth dependence in the degree of development. However, if we discard those prongs starting within 100 microns from either surface of the emulsion, the error caused by using the same energy gap density curve or energy-grain density curve at different depths was small enough, in so far as the higher accuracy in the definition of energy was not required. No correction arising from this circumstance was applied. Those prongs whose grain density was below 55 per 100 microns were not counted in the results. It will be shown in Sec. VII that prongs of such low grain density are mostly mesons. The results are shown in Table III.

The following conclusions can be drawn from the data shown in Table III. In the case of 300-Mev excitation, the number of single protons between 20 and 50 Mev is nearly the same as the number of star protons of the same energy range. Between 60 and 120 Mev the number of single protons is about half the

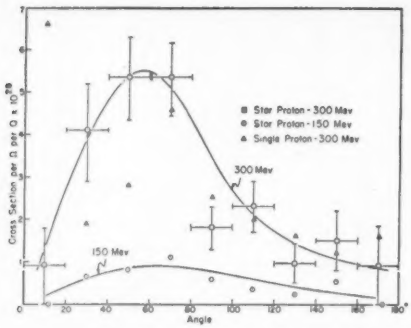

FIG. 3. Angular distribution of protons for energies between 20 and 60 Mev.

number of star protons, and above 120 Mev most of the protons are due to the stars.

Comparing the numbers at 300-Mev excitation with those at 150-Mev excitation, we see that about 75 percent of the star protons in the case of 300-Mev excitation are due to photons of energy above 150 Mev. As to the single protons, the number of protons between 20 and 30 Mev is nearly the same for 300-Mev excitation as for 150-Mev excitation, a fact which indicates that most of the single protons of this energy in the case of 300-Mev excitation are due to photons of energy below 150 Mev. Above 30 Mev the number of single protons in the case of 300-Mev excitation is twice that in the case of 150 Mev, indicating that half of the single protons observed in the case of 300-Mev excitation are due to photons of energy lower than 150 Mev.

A brief comparison of the results described in this section with the results of Levinthal and Silverman will be made here. First of all, according to the present results the photoprotons observed by Levinthal and Silverman[2] are a mixture of single and star protons. One-half of the single protons are excited by photons of energy below 150 Mev, and the rest of the single protons and most of the star protons are excited by photons of energy above 150 Mev. According to their theory the protons they observed should be due to the photons of energy much below 150 Mev.

As far as the form of the energy distribution curve is concerned, the results are in good agreement with each other. Figure 2 shows a log-log plot of the energy *versus* cross section curve in the present case. The solid line represents a function proportional to $E^{-1.8}$, where E is the energy. Levinthal and Silverman found the same distribution function, namely E^{-n}, where n is equal to 1.7 for carbon, 1.8 for copper, and 2.2 for lead. As to the absolute value of the cross section at 20 Mev, it is larger by a factor of 3 in the present case than in that of Levinthal and Silverman.

In Keck's experiment, which is concerned with much higher energy protons, mostly above 100 Mev, than in the case of Levinthal and Silverman, most of the protons seem to have come from stars. The cross section is roughly in agreement with the present results. The fact, found by Keck, that the number of protons decreases very rapidly above 150 Mev, seems to be consistent with the present result that no proton above 160 Mev was confirmed (see Sec. VIII).

VII. THE ANGULAR DISTRIBUTION OF THE PROTONS

The angular distribution of the emitted protons relative to the incident gamma-ray beam was studied by analyzing about 600 stars produced in the 600-micron G5 emulsion. The incident gamma-ray beam was sent through the emulsion at an angle of 45 degrees to the surface. The angle between the direction of emission and the incident beam was determined by measuring the dip angle of the proton track and the azimuthal angle between the proton direction and the beam direction, both projected on the emulsion surface. The shrinkage of the emulsion was taken into account. A small correction was necessary due to the distortion of the emulsion. The distortion was mostly the shearing which came from the fact that the layers near the free surface of the emulsion shrank laterally more than the bottom layers. The degree of shearing could be determined from the direction and curvature of the numerous secondary electron tracks having approximately the same direction as the incident beam. The correction due to this circumstance was 10 degrees in the worst case. In most cases it was only a few degrees.

The upper curve of Fig. 3 shows the angular distribution of protons of energy between 20 and 60 Mev coming from stars in the case of 300-Mev excitation. It shows a strong forward peak at about 50 degrees. The decrease of differential cross section below 20 degrees seems to be real. As already mentioned, about 75 percent of the protons of this group came from photons of energy above 150 Mev. To illustrate this point more clearly, the angular distribution of star protons of the same energy region in the case of 150-Mev excitation, normalized to the same Q value, is shown in the same figure without giving the error to avoid complication of the figure. The important point is that rather low energy protons, such as 20 to 60 Mev, excited by rather high energy photons, show such a

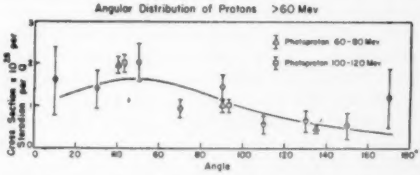

FIG. 4. Angular distribution of high energy protons in the case of 300-Mev excitation. The circles represent star protons above 60 Mev; the triangles represent photoprotons between 60–80 Mev; and the squares represent photoprotons between 100–120 Mev.

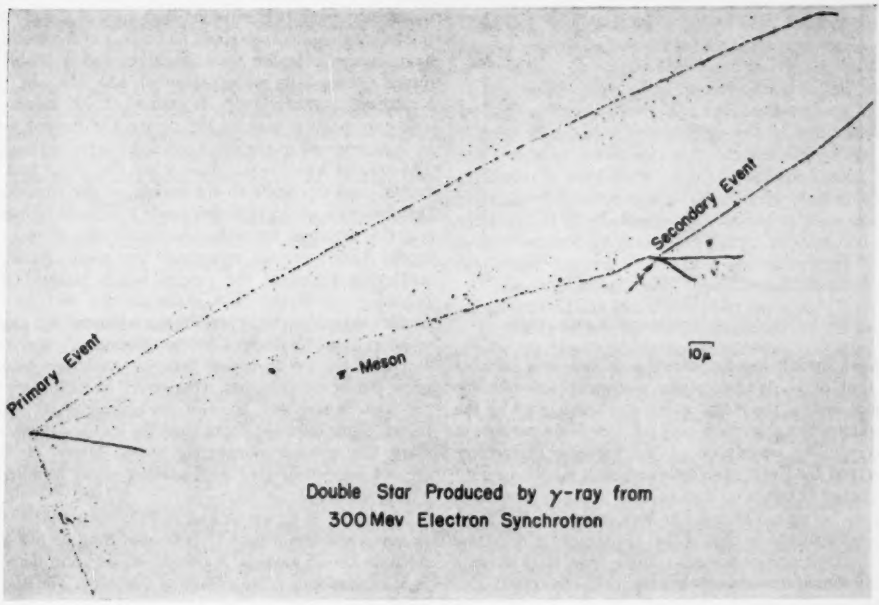

FIG. 5. A star showing production of a π-meson, which stopped in the emulsion and produced another star (Ilford C2 plate)

conspicuous forward peak. Within a fairly large statistical error, no marked difference can be observed between the angular distribution of protons of energy between 20 and 30 Mev and that of those between 30 and 60 Mev. The angular distribution of single protons of energy between 20 and 60 Mev is also shown in Fig. 3.

The angular distribution of protons from stars above 60 Mev for 300-Mev excitation is shown in Fig. 4. The prongs whose grain density was below 55 per 100 microns were not taken into account. Within fairly poor statistics one can recognize a trend towards a fairly strong forward asymmetry. It might make little sense to take an average over such a wide energy range as from 60 to 160 Mev, because it is quite possible that the angular distribution might depend strongly on the energy of the protons. To see this point more clearly, the ratio of the number of protons emitted forward ($<90°$) to the number emitted backward ($>90°$), for protons of energy between 60 and 100 Mev and between 100 and 160 Mev, is given in the following table.

Energy	60–100 Mev	100–160 Mev
Ratio	1.75 ± 0.63	2.14 ± 0.68

The differential cross section at 70 degrees averaged over 60- to 80-Mev protons is roughly 2 ± 1 microbarns per steradian per Mev per Q. Keck's value for carbon at this angle and energy is 0.75 microbarn. If, assuming the proportionality of the cross section to Z and the same angular dependence for carbon and silver, we reduce this to the average cross section for atoms constituting the emulsion, we get the value 1.5 microbarns. At this energy the number of single protons is not negligibly small compared to the star protons. Therefore Keck's value should be higher than the present value. When one considers the fairly large error stated, the results are consistent.

In connection with the interpretation of the star producing process, it is important to know the angular distribution of high energy protons. The analysis of the prongs from stars by the photographic method, as was carried out in this work, is so tedious that it is almost impracticable to get more accurate results. According to the present results, however, the number of single protons in proportion to the protons coming from stars is rather small in the high energy region. Therefore, instead of analyzing stars by using the photographic method, one can get the same information from experiments on photoprotons of high energy. Keck studied the angular distribution of photoprotons excited by 300-Mev synchrotron gamma-rays at proton energies of 100, 130, and 170 Mev. The results showed that the differential cross sections at 45°, 90°, and 135° are roughly in the ratio of 4:2:1 for 100-Mev protons. The degree of asymmetry increases with the increasing proton energy.

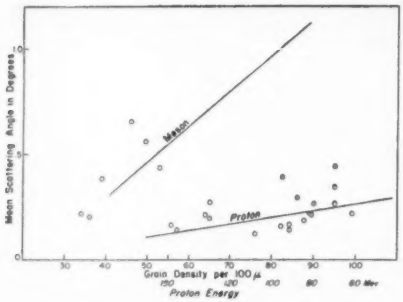

FIG. 6. The mean multiple scattering angle results.

Keck's result was confirmed by an experiment similar to that of D. Walker, using photographic emulsions placed around the target which was bombarded by the bremsstrahlung gamma-rays of 300-Mev maximum energy. The magnitude of the forward asymmetry observed by Keck was confirmed both for the protons of energy between 60 and 80 Mev and the protons of energy between 100 and 120 Mev, as shown in Fig. 4. It thus seems to be certain that the angular distribution of the high energy protons coming from stars shows a fairly strong forward asymmetry.

VIII. THE π-MESONS FROM STARS

It has been found[1] that the stars produced by gamma-rays sometimes emit a slow meson which stops in the emulsion and makes another star, or shows a π-μ decay, according as it is a π^- or a π^+. One example is shown in Fig. 5. The mesons found in this way are those of low energy, mostly below 5 Mev, and constitute only a small fraction of all mesons emitted. By extrapolating the energy spectrum obtained by Peterson, Gilbert, and White[8] down to zero energy, it is estimated that the number of mesons below 5 Mev would be roughly 0.5 percent of the total mesons. The number of stars associated with a slow meson ending in the emulsion, in proportion to the total number of stars of 3 or more prongs in the same area of emulsion, depends on the thickness of the emulsion. In the case of 600-micron emulsion there were 8 cases, compared to 1741 three-or-more-prong stars. In the case of 200-micron emulsion, the rate of observation of double stars was one case out of about 500 three-or-more-prong stars. The ratio observed in the case of 600-micron emulsion seems to be surprisingly high, because, if the mesons of energy below 5 Mev constitute only 0.5 percent of the total meson spectrum, there should be as many mesons as stars in the same area. But this was evidently not the case.

To determine the percentage of the meson-associated stars to the total number of stars the following procedure was used. It is expected that most of the meson tracks are thin, because about 80 percent of the mesons have energy of more than 20 Mev, and a 20-Mev meson corresponds to a proton of 120 Mev in its ionization power, namely 70 grains per 100 microns. The only possible way of identifying the mesons was by measurement of the mean multiple scattering angle. The trouble was the fact that when the prong had a rather large dip angle to the surface of the emulsion, the distortion of the emulsion made it difficult to carry out the multiple scattering measurement of such a track. Therefore, we measured the mean multiple scattering angles of the prongs which satisfied the following conditions: The grain density had to be smaller than 100 grains per 100 microns; the dip angle smaller than 15 degrees before processing; and the length of the prong longer than 1500 microns before going out of the emulsion. There were 26 such cases in the area where 401 three-or-more-prong stars were found. (This does not mean that the meson-associated stars are three-or-more-prong stars. Many of the mesons were associated with another prong forming a two-prong star.)

The result is shown in Fig. 6. It is clear that the 6 prongs whose grain density is smaller than 55 per 100 microns are all mesons. A proton whose grain density is 55 corresponds to an energy of 160 Mev. The above result is not surprising because the cross section for the production of such a high energy proton is exceedingly small.

We therefore assumed all prongs with grain density less than 55 to be mesons. There were 19 such prongs in the area where 401 three-or-more-prong stars were found. This means that the cross section for the production of mesons of energy above 20 Mev associated with a star is (5.0 ± 1.5) percent of the cross section for the production of stars of three or more prongs.

There were also mesons of intermediate energy, which did not end in the emulsion, but it was very easy to identify them as mesons from the wiggling of the tracks. There were 4 such cases out of the area where 1741 three-or-more-prong stars were found. Summarizing the results, the number of meson-associated stars found in a certain area of emulsion is 5.7 ± 2.0 percent of the number of three-or-more-prong stars found in the same area.

As has already been mentioned, the single meson tracks starting in the emulsion were not counted, because they are inconspicuous events and difficult to take reliable statistics about. However, we occasionally noticed a single meson starting in the emulsion without being associated with any star. Some of them were low in energy and stopped in the emulsion. Some of them were of high energy, and the identification was possible only by the mean multiple scattering angle measurement. Roughly speaking, the number of single meson tracks are of the same order of magnitude as the number of mesons associated with stars.

[8] Peterson, Gilbert, and White, Phys. Rev. **81**, 1003 (1951).

The cross section for the production of meson-associated stars is thus 6.1×10^{-27} cm² times 0.05, which is equal to 3×10^{-28} cm². The value expected from the data on the meson production is 7×10^{-28} cm² for the total cross section, assuming[8] the cross section for carbon and silver to be 4.0×10^{-28} cm² and 1.7×10^{-27} cm². Therefore, if there are twice as many single mesons as mesons from stars, which is probable, the results are consistent.

It might be worthwhile to mention here that there was one case where a slow meson came out of a star and stopped in the emulsion, decaying into what was probably a μ-meson whose range was only 200 microns.

IX. DISCUSSION OF THE RESULTS, AND CONCLUSIONS

The consistency or inconsistency of the present results with those of other workers with related problems was discussed in each section from case to case, and might be summarized as follows. In general the present results are consistent with the results of the experiments on photoprotons done by Levinthal and Silverman,[2] Walker,[3] and Keck[3] both in energy distribution and angular distribution of the protons. In the case of Levinthal and Silverman, about half of the protons seem to have come from stars excited by photons of energy above 150 Mev and the rest of the protons seem to be single protons, half of which are excited by photons of energy above 150 Mev and the rest by photons of energy below 150 Mev. In the case of Keck, where higher energy protons are concerned, most of the protons came from stars excited by photons of energy above 150 Mev. In the case of Walker the excitation energy was 200 Mev. Although no precise analysis was made in the present experiment at this excitation energy, it is clear that the origin of the protons was the same as in the other cases, with the difference that the contribution of the single protons excited by photons of energy below 150 Mev is larger than in the case of 300-Mev excitation.

For the absolute cross section, the value of Levinthal and Silverman is smaller by a factor of 3 than the present value, which is in good agreement with Keck's value. For the cross section for star production, the present value is 1.6 times larger than the value obtained by Miller[1] at Berkeley, although the relative values at different excitation energies are in close agreement with each other.

As for the interpretation of the results, the theory of Levinthal and Silverman seems to be good only for a part of the protons they observed. According to their theory the protons of energy E should be produced by photons of energy $E+25$ Mev. This means that most of the protons they observed should be due to photons of energy below 100 Mev. According to the present result, three-fourths of the protons they observed should have come from the photons of energy above 150 Mev and therefore cannot be accounted for by their theory. As will be discussed later, the free meson effect seems to be responsible for these protons.

Keck tried to explain his results mainly on the basis of Levinger's theory of photodissociation of the nuclei by high energy photons. The approximate form of the angular distribution curve fitted well with the theory, but the cross section was a few times larger than the prediction of the theory. As will be discussed below, the present result seems to show that the Levinger approximation fails to explain the production of high energy protons excited by photons of energy between 150 and 300 Mev.

There are, among others, the following three evident experimental facts which should be explained.

1. The cross section for photodissociation increases above 150 Mev, and for bremsstrahlung of maximum energy of 300 Mev, the cross section per Q is about 6.1×10^{-27} cm² plus the cross section for the production of the two- and one-prong stars. From the data given in Table I, the difference between the total cross sections at 150-Mev and 300-Mev excitation is estimated to be about 9×10^{-27} cm² per Q.

2. The angular distribution of protons of energy between 20 and 60 Mev coming from stars shows a conspicuous forward peak between 45 and 70 degrees, and 75 percent of these protons are produced by photons of energy above 150 Mev.

3. The angular distribution of star protons of energy above 60 Mev shows a fairly strong forward asymmetry.

The above-mentioned result 1 shows clearly that some kind of photonuclear process which does not occur in the low energy region begins to take place above 150 Mev. It is quite natural to consider that this is due to the free meson effect, namely the effect of production of a meson in the nucleus: Suppose the nucleons in the nucleus are free and that a photon interacts with one of them and produces a meson. The meson thus created will sometimes get out of the nucleus without interaction, but sometimes it will be absorbed in the nuclear matter before getting out. The latter case obviously results in the production of a star. Even in the former case, the chance would be large that the emitted meson form a star with the nucleon knocked out by the meson-producing process and/or with secondaries of the recoil nucleon.

According to this picture, the excitation curve for star production is nothing else but the excitation curve for photomeson production. As for the absolute value of the cross section for the star production, it is expected to be approximately equal to $\sigma_0 A$, where σ_0 is the cross section for the production of photomesons, including neutral mesons, by a nucleon and where A is the mass number.

On the other hand, experiments[9] show that the cross section for photomeson production is proportional to $\sigma_0 A^{\frac{1}{3}}$. This fact is to be explained by the absorption

[9] R. F. Mozley, Phys. Rev. **80**, 493 (1950); R. M. Littauer and D. Walker, Phys. Rev. **82**, 746 (1951).

of the meson inside the nucleus and by the Pauli exclusion principle for the recoil nucleon. The numerical value of $\sigma_0 A^{\frac{1}{3}}$ is 4.0×10^{-28} cm² for carbon[8] and 1.7×10^{-27} cm² for silver for charged mesons. Multiplying these values by $A^{\frac{1}{3}}$ and taking an average over the light and heavy atoms in the photographic emulsion, we get 3.7×10^{-27} cm². Adding the part which comes from neutral meson production, assuming that the cross section for neutral meson production is the same as for charged mesons, we get the value 5.5×10^{-27} cm² for $\sigma_0 A$. This value should be compared with the value 9×10^{-27} cm² obtained above. At present, it is not possible to say anything about the reality of the difference. The fact that the values are fairly close to each other seems to indicate the appropriateness of the assumption.

Results 2 can also be explained, at least qualitatively, on the basis of the picture used to explain result 1, if we consider that the protons of energy between 20 and 60 Mev belonging to the strong forward peak are those protons knocked out by the process in which a meson is produced. If we neglect the internal motion of the nucleons and consider them at rest, the energy of the recoil nucleon is calculated easily as a function of the angle of emission and of the photon energy, simply by applying the laws of conservation of energy and momentum. In this case protons are always ejected into the forward direction. In the case of 300-Mev bremsstrahlung there should be no protons above 20 Mev making an angle greater than 45 degrees with the incident gamma-ray beam. The energy of the protons should be a maximum at 0 degrees and should be about 70 Mev. The energy decreases as the angle of emission increases.

To predict the angular distribution exactly, we need to know the angular distribution of π-mesons emitted at the same time. The angular distribution of photomesons produced on protons by photons of energy 250 Mev has been studied by Bishop, Steinberger, and Cook.[10] According to their results the angular distribution shows a backward asymmetry and a broad maximum at 130 degrees referred to the laboratory system. The meson emitted at 130 degrees is accompanied by a recoil nucleon emitted at an angle of 20 to 35 degrees according to the energy of the photon. Anyway, the recoil nucleon should show a very steep forward asymmetry if we neglect the internal motion of the nucleons inside the nucleus.

The observed forward peak of protons is much broader than this, and moreover the angular distribution curve seems to show a decrease at very small angles. The broadening of the peak might be accounted for by the internal motion of the nucleons before the interaction and the subsequent scattering of the proton inside the nucleus. The decrease at very small angles, if it is true, seems to be hard to understand by the internal motion. Although a quantitative study of the effect of the internal motion of the nucleon on the broadening of the angular distribution is necessary before a final conclusion can be drawn, it seems reasonable to guess that the protons in question are recoil nucleons kicked out by the meson-producing reaction, because there is no other process so far known, which can explain such a conspicuous forward peak of low energy protons down to 20 Mev produced by such high energy photons.

Now, if we want to explain result 3, namely the forward asymmetry of the angular distribution of high energy protons, by the free nucleon model as in the case of 1 and 2, we meet a serious difficulty: The high energy protons, according to the free nucleon model, should be produced by the absorption of a meson inside the nucleus and, as the angular distribution of the mesons shows no sign of forward asymmetry, the protons also should be more or less isotropic in angular distribution. Such is not the case, as Fig. 4 and other experimental evidence show.

This is the point that Levinger[11] tried to explain in terms of electromagnetic photodissociation based on the theory of Schiff[12] for the photodissociation of the deuteron. The idea of Levinger is to describe the nucleus as an aggregation of "quasi-deuterons" and apply the theory of Schiff to them. According to his result the angular distribution is essentially the same as predicted by Schiff in the case of the actual deuteron, and the total cross section per photon should be equal to $1.6\times A\times\sigma_s$, where A is the mass number and σ_s is Schiff's cross section. Therefore, the dependence of the cross section on the photon energy is the same as that of Schiff's deuteron cross section, which decreases steadily with increasing photon energy.

It is interesting to examine how far the observed facts can be explained by the Levinger theory, because it might give some information indirectly about the applicability of Schiff's approximation at photon energies as high as 300 Mev. In Schiff's calculation the effect of the virtual meson field is taken into account through the nuclear force between the proton and a neutron, and the interaction of the photon with the deuteron takes place through the electric moment of the proton. The reason that this approximation is supposed to be good up to fairly high energy is that the electric dipole and quadrupole moment due to the virtual meson field almost vanish. Schiff set the limit of applicability below the photon energy of 140 Mev. Above this energy the effects of the interaction due to the magnetic moment of the virtual meson field and due to the electric moments of higher order, together with the free meson effect, might make the above-mentioned approximation invalid.

As already mentioned, the Levinger cross section is given by $1.6\times A\times\sigma_s$ per photon. Using this result, extrapolating Schiff's value of σ_s up to 300 Mev, as

[10] Bishop, Steinberger, and Cook, Phys. Rev. **80**, 291 (1950).

[11] Private communication.

[12] L. I. Schiff, Phys. Rev. **78**, 733 (1950)

Levinger did, and assuming the bremsstrahlung spectrum to be of the form Q/E, we can calculate numerically the difference between the cross section per Q for the Levinger process at 300 and 150 Mev. This difference comes out to be 3.6×10^{-28} cm².

Now it is not fair to compare this value directly with the observed cross section for the production of high energy protons, because only a fraction of the high energy protons produced by the primary process leave the nucleus retaining their energy. To avoid the ambiguity caused by the correction due to this circumstance as far as possible, let the above value, 3.6×10^{-28} cm², be compared with the corresponding cross section for star production. From Table I we see that the difference of the cross section per Q for star production including two-prong and one-prong stars at 300 Mev and 150-Mev excitation is about 9×10^{-27} cm². This is about 25 times larger than the cross section for the Levinger process. Therefore, if we assume that the Schiff-Levinger approximation is correct, most of the star-producing process should have come from the free meson effect and only about 4 percent of all the stars are due to the Levinger process. If this is so, it is difficult to understand the observed forward asymmetry of high energy protons, unless we assume that the number of high energy protons produced by each absorption of a meson is 25 times smaller than the number produced by each Levinger process, which is impossible. It is expected that there are a few more protons per elementary process in the case of the Levinger process than in the case of meson absorption. But it seems to be impossible that there will be a difference by a factor of more than 2.

Now, looking either at Fig. 5 or at the angular distribution curve obtained by Keck, it is quite natural to assume that the number of protons constituting the asymmetric part of the curve is at least the same as, and probably larger than, the number of protons belonging to the isotropic part. Therefore the process responsible for the asymmetric protons should have a cross section of at least the same order of magnitude as the process responsible for the isotropic part. This means that, besides the free meson effect, there should be another effect which gives rise to the forward asymmetry of protons and has a cross section at least ten times bigger than that predicted by the Schiff-Levinger approximation. It is understandable that in any kind of process in which more than one particle participates in the interaction with a photon, there should be a forward asymmetric distribution of protons relative to the laboratory system, because the momentum of the photon is transferred directly to the participating particles through the emission and absorption of a virtual meson.

One can consider another process which might give rise to the forward asymmetry of high energy protons, although it is somewhat hypothetical. Namely, a photon is first absorbed by a nucleon resulting in the formation of a nucleon isobar, which has been postulated by Fujimoto and Miyazawa[13] and Brueckner and Case to account for the cross section for the production of neutral mesons.[14] The lifetime of the nucleon isobar might be long enough to collide with the other nucleon before decaying into a π-meson and a normal nucleon. The result might be that the excited nucleon makes a transition to the normal state, giving a part of the energy released to the particle with which it collides. In this way the energy and momentum of the photon can be transferred to two nuclear particles without emitting a meson. The cross section for such a process should show a resonance at the energy corresponding to the energy of excitation of the nucleon. A more elaborate study of the excitation function for star production might be of interest in this connection.

In any case the study of the cross section for the photodisintegration of deuterons or alpha-particles is very important to clarify the phenomena discussed in this note. All the results obtained by the present experiment can be understood if the cross section for the photodisintegration of deuterons or alpha-particles associated with the production of high energy protons increases above the meson threshold with increasing photon energy.

In conclusion the author wishes to express his cordial thanks to Professors R. R. Wilson and H. A. Bethe for enabling the author to stay at Ithaca as well as for valuable discussions. Thanks are also due to Professor K. Greisen and Dr. S. Hayakawa for valuable discussions and to the crews of the microscope laboratory for scanning the plates.

[13] Y. Fujimoto and H. Miyazawa, Prog. Theor. Phys. **5**, 1052 (1950).
[14] K. A. Brueckner and K. M. Case, Phys. Rev. **83**, 1141 (1951).

The Nature of Work-Hardening*

J. S. KOEHLER
Department of Physics, University of Illinois, Urbana, Illinois
(Received August 8, 1951)

Two kinds of work-hardening are discussed, interaction-hardening and source-hardening. Interaction-hardening arises because a large stress must be applied to move a dislocation through a material which already contains a large number of dislocations. This paper is mainly concerned with source-hardening which occurs because the sources of easy glide become inactive. Additional glide occurs by the use of sources which act at a higher stress level. Source-hardening is the most important kind of hardening at small strains since then the dislocation density is small.

The experimental stress-strain curves obtained by Rosi and Mathewson on pure aluminum crystals can be calculated theoretically as follows: At very low temperatures one assumes that one has a distribution of "free lengths" of dislocations. The Frank-Read mechanism for the production of dislocations is used. It is also assumed in accordance with electron microscope data that generation ceases after about 500 dislocation loops have been produced. Source-hardening therefore occurs as the sources of greatest "free length" are gradually used. At finite temperatures the following modifications are introduced: The total stress is the sum of the applied stress and the stress resulting from thermal fluctuations. In addition, Brown's electron microscope data indicates that a given source produces much more glide at high temperature than at low temperature. The present theory does not predict an equation of state and does check Rosi and Mathewson's data on this topic.

Suggestions are made to explain the reason for the increased glide per source with increased temperature and to understand the way in which a source becomes inactive as a result of vacancy production.

Numerous experiments are suggested.

The major accomplishment of the paper is that it is able to show that the lamella structure found in the electron microscope pictures can be related to the mechanical properties of the metal single crystals.

I. INTRODUCTION

WE would like to describe a theory which makes it possible to understand certain aspects of work-hardening. Let us first summarize some of the available experimental data.

Rosi and Mathewson[1] have recently published resolved stress-strain curves for 99.996 percent aluminum crystals at four temperatures the lowest being 77°K. Their yield-stress data is as follows:

77°K	$\sigma_0 = 421.3$ g/mm^2
205°K	$\sigma_0 = 124.1$ g/mm^2
293°K	$\sigma_0 = 104.5$ g/mm^2
353°K	$\sigma_0 = 91.8$ g/mm^2.

Their stress-strain data extends only to about one percent strain. The curves appropriate for various temperatures are given in Fig. 1.

Brown[2] obtained electron microscope pictures on pure polycrystalline aluminum. After 15 percent extension, Brown found: at -180°C slip zones separated $\frac{1}{2}$ to 1μ each zone contains 1 to 2 lamellas; at 20°C slip zones separated 2μ each zone contains 3 to 4 lamellas; at 250°C slip zones separated 4μ each zone contains 5 to 6 lamellas. In most cases the average glide per lamella was about 2000A. The separation of the lamellas was from 200 to 800A.

Let us consider the temperature dependence of the yield stress and of the initial slope of the stress-strain curve. According to Becker[3] the probability W of a thermal stress fluctuation over a volume V which produces a total stress in excess of σ_1 is

$$W = \exp[-V(\sigma_1-\sigma)^2/2GkT], \quad (1)$$

where σ is the applied stress and G is the modulus of rigidity. If we suppose[4] that W must reach a value W_0 before glide occurs then the stress σ required for glide is

$$\sigma = \sigma_1 - [2GkT/V \log(1/W_0)]^{\frac{1}{2}} = \sigma_1 - BT^{\frac{1}{2}}. \quad (2)$$

Kuhlmann[4] has shown that Eq. (2) is in agreement with the yield stress data obtained on hexagonal metals. This relation does not fit the yield-stress data of Rosi and Mathewson given above. They fit their yield-stress data to the following relation:

$$\sigma_0 = A \exp[Q/RT] \quad (3)$$

obtaining $A = 61$ g/mm^2 and $Q = 300$ cal/g atom.

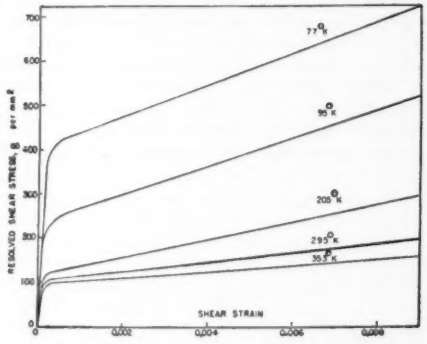

FIG. 1. The temperature dependence of the resolved stress-strain curves of pure aluminum (after Rosi and Mathewson).

* This work has been partially supported by the ONR.

[1] F. D. Rosi and C. H. Mathewson, J. Metals **188**, 1159 (1950).

[2] A. F. Brown, *Metallurgical Applications of the Electron Microscope* (The Institute of Metals, London, 1950), p. 110.

[3] R. Becker, Physik. Z. Sowjetunion **26**, 919 (1925).

[4] D. Kuhlmann, Proc. Phys. Soc. (London) **A64**, 145 (1951).

The yield-stress data of Rosi[5] on pure silver single crystals does fit relation (2). The data of Schmid and his co-workers on zinc and cadmium also fits Eq. (2). There is a further difficulty with the data of Rosi and Mathewson at very low strain. These investigators measured the temperature dependence of the Young's modulus; they found that Young's modulus increased by about a factor of two in going from 350°K to 77°K. Goens[6] measured the ratio of Young's modulus of this essentially isotropic material at 78°K to the value at 291°K; he found $E_{78}/E_{291}=1.098$. Since the low temperature data of Rosi and Mathewson appears questionable, we have fit the yield stress data at the three highest temperatures to relation (2) and used the low temperature values thus obtained for comparison with theory.

The initial slope of the stress-strain curves of aluminum and silver depends upon temperature in the following fashion:[7]

$$d\sigma/d\epsilon=(d\sigma/d\epsilon)_0\{1-CT^3\}. \qquad (4)$$

This result probably indicates that thermal fluctuations are also of importance in determining the rate of work hardening in face-centered cubic metals at high temperatures.

Figure 2 shows the variation of the initial slope of the stress-strain curve of cadmium with temperature.[8] The dependence is clearly not in agreement with that predicted by Eq. (4). The temperature dependence of the initial slope of the stress-strain curves of zinc[9] is also not given by Eq. (4). In the case of magnesium[10] the data can be fit to Eq. (4) without undue error (i.e., deviations are less than 5 percent). Since magnesium has essentially a close-packed lattice whereas zinc and cadmium do not, the data indicate that the initial slopes of the stress-strain curves of all close-packed metals vary with temperature in accordance with relation (4). If the material is not close packed, then the temperature dependence is apparently more complex.

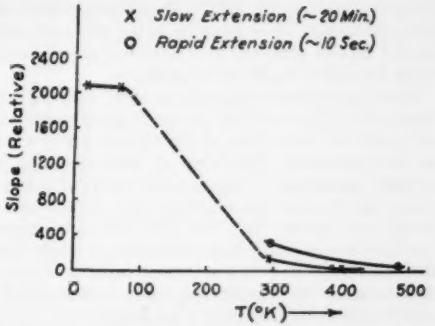

FIG. 2. The variation of the initial slope of the stress-strain curves curves of cadmium with temperature (after Schmid and Boas).

II. THEORY

A. In General

In devising theoretical explanations for the observed data it is necessary to make various assumptions. In the present paper an attempt will be made to begin with those assumptions which seem most plausible. The experimental consequences of the assumptions will then be discussed. Later, further less certain suggestions will be made to obtain a description of additional experimental results.

In the entire paper it is assumed that dislocations are generated by the Frank-Read[11] mechanism; i.e., a dislocation loop has sufficient length in the slip plane so that it bows out under an applied stress and produces dislocation rings in the slip plane as shown in Fig. 3. Since in principle the Frank-Read dislocation source is the same after the generation of a loop as it was before, any number of loops can be generated from a single source. The Frank-Read process will operate if one starts with either an edge or a screw-type dislocation; but since screw-type dislocations are not as restricted in their motion, an annealed metal probably contains more edge than screw dislocations.

It will be assumed that there are two types of work-hardening. At low strains, when the dislocation density is low, it will be assumed that a metal work-hardens because a given Frank-Read source can only produce a finite number of dislocation loops. This assumption was suggested by the fact that Brown[12] found only a finite amount of glide per slip lamella in aluminum.

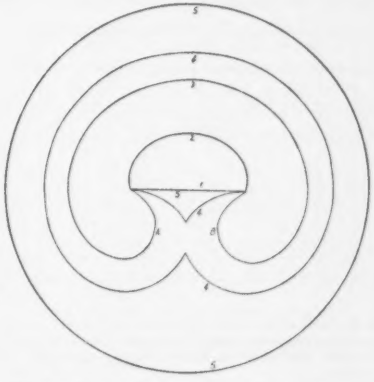

FIG. 3. Successive stages in the Frank-Read process for the generation of dislocation loops. The plane of the figure is the slip plane. The portion of the dislocation shown is anchored at its ends.

[5] F. D. Rosi, unpublished data.
[6] E. Goens, Ann. Physik Series 5, **4**, 733 (1930).
[7] See reference 1, p. 1166; see also reference 5.
[8] W. Boas and E. Schmid, Z. Physik **61**, 777 (1930).
[9] See reference 8, p. 779.
[10] E. Schmid and G. Siebel, Z. Elektrochem. **37**, 447 (1931).
[11] F. C. Frank and W. T. Read, Phys. Rev. **79**, 722 (1950).
[12] See reference 2, p. 110.

Since a given source can only produce a finite amount of glide, the sources which generate at low stress are used up and further glide can only occur by using sources which operate at higher stress levels.

When the dislocation density is large, especially in cases where glide on several intersecting slip planes has occurred, the interactions of the dislocations give rise to work-hardening. This kind of work-hardening is probably important at strains where asterism becomes noticeable (in the face-centered cubic metals above strains of a few percent). This kind of work-hardening was first considered by Taylor[13] and has recently been discussed by Mott.[14] In the present paper an attempt will be made to consider only those experiments in which interaction-hardening is not important.

B. The Low Temperature Stress-Strain Curve at Small Strains

Frank and Read estimate that a dislocation of free length l will generate if the total resolved shearing stress on it is

$$\sigma = Ga/l, \tag{5}$$

where G is the modulus of rigidity and a is the smallest distance between atoms of the lattice. If a constant driving stress is maintained, then the following consideration indicates that the expansion of a dislocation loop once started is difficult to stop. Since $E_0 = Ga^2$ is the energy per unit length of dislocation line,[15] the energy associated with a circular loop of radius r is

$$E = 2\pi r G a^2 + E'.$$

The increment of work dW done by the applied stress σ is expanding the loop from r to $r+dr$ is

$$dW = \sigma a 2\pi r dr.$$

Thus the total work done in expanding the loop to radius r is

$$W = \sigma a \pi r^2 + W'.$$

Hence the external work available goes up more rapidly than the required potential energy of the loop. The additional energy available will either be converted into kinetic energy or it will be dissipated.

Consider next the form of the low temperature stress-strain curve at small strains. The picture presented here claims that glide occurs using the sources of greatest length first. As deformation proceeds, shorter and shorter dislocations operate as sources and hence according to (5) the required stress becomes larger. Thus the form of the stress-strain curve is determined by Eq. (5), by the amount of glide which occurs on each lamella before locking, and by the distribution of the free lengths of the dislocations in the solid.

At present very little is known about the free length distribution. A distribution which seems to give reasonable results can be obtained as follows:[16] Suppose that there are N atomic lengths of dislocation line in one cubic centimeter and that along the total length of dislocation line there are n points arranged at random at which the dislocation is pinned down. The probability of finding two locking points separated by s atoms is approximately

$$P(r) = (n/N)(1-n/N)^s = c(1-c)^{l/a} \leqq c \exp[-cl/a],$$

where $c = n/N$ is the concentration of locked points along the dislocation line. The number of dislocations having lengths between l and $l+dl$ is therefore

$$N(l)dl = (Nc^2/a) \exp[-cl/a], \tag{6}$$

where the factor in front has been picked to give the proper total length of dislocation line (i.e., Na).

The low temperature stress-strain curve at small strains can now be obtained as follows: The increment $d\epsilon$ of plastic strain accomplished by using the dislocation sources having lengths between l and $l+dl$ is

$$d\epsilon = \epsilon_1 N(l)dl,$$

where ϵ_1 is the shearing strain which occurs upon using a single source. The total shearing strain accomplished by using all sources of length greater than l is

$$\epsilon = \epsilon_1 \int_l^{l_m} N(l)dl = \epsilon_1 Nc\{e^{-cl/a} - e^{-cl_m/a}\}.$$

If $\epsilon_0 = \epsilon_1 Nc \exp(-cl_m/a)$ then

$$\epsilon + \epsilon_0 = \epsilon_1 Nc e^{-cl/a}. \tag{7}$$

Solving this for l and inserting the result into Eq. (5) the resulting expression for the low temperature stress-strain curve is

$$\sigma = Gc/[\log(\epsilon_1 Nc) - \log(\epsilon+\epsilon_0)]. \tag{8}$$

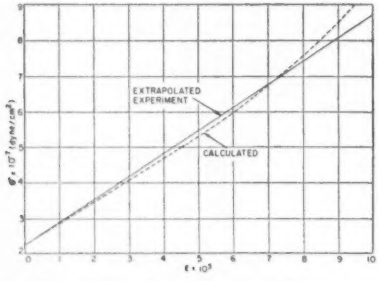

FIG. 4. Comparison of the experiment and theory at 0°K. Full line is extrapolated using stress-strain data of Rosi and Mathewson on aluminum single crystals. Dashed curve is calculated.

[13] G. I. Taylor, Proc. Roy. Soc. (London) **145**, 362 (1934).
[14] N. F. Mott, 35th Guthrie Lecture, Proc. Phys. Soc. (London) **B64**, 729 (1951).
[15] N. F. Mott and F. R. N. Nabarro, *Report of Conference on the Strength of Solids*, Phys. Soc., London (1948), p. 8.
[16] J. S. Koehler, *Imperfections in Nearly Perfect Crystals* (John Wiley and Sons, Inc., New York, to be published).

This expression can now be fit to the low temperature aluminum data.

Brown[17] found that the average amount of glide on a single lamella varied slightly with the temperature. He found

Temperature	Average slip distance
−180°C (93°K)	1600A
20°C (293°K)	2000A
250°C (523°K)	2200A

Extrapolating to 0°K, the average slip distance there is 1330A or 465 atomic distances. Hence ϵ_1, the strain resulting from the use of a single source, is 1.33×10^{-5}.

The yield stress at absolute zero is 2.3×10^7 dyne/cm^2. This figure used in Eq. (5) yields the value of 3.80×10^{-4} cm for l_m, the largest free length of dislocation line, where the low temperature value of G has been used (i.e., $G_0=3.06\times10^{11}$ dyne/cm^2).

The theoretical expression (8) has then been fitted to the experimental 0°K curve by choosing N and c. One finds that $N=0.73\times10^7$ and $c=2.30\times10^{-4}$. The resulting theoretical curve is shown in Fig. 4. The value of c indicates that the pinned down points are separated on the average by about 4300 atomic distances. Na represents the total length of dislocation line per cc in the original annealed specimen. One finds that $Na=0.21$ cm per cc. This is much smaller than the usually accepted value[18] (i.e., about 10^8 cm per cc). Fitting to the 77°K data leads to very similar results.

The cadmium stress-strain curve obtained at −253°C has been fitted in Eq. (8). The parameters which give a good fit are $l_m=4.87\times10^{-4}$ cm, $c=1.05\times10^{-4}$, $N=1.32\times10^9$. The total length of dislocation line is therefore 3.93 cm. Since data was not available giving the amount of glide per lamella, it was assumed in these calculations that the glide in cadmium per lamella at low temperature was the same number of atomic distances as that found in aluminum at low temperature (i.e., 465 atomic distances). The situation is therefore qualitatively similar for the hexagonal and the face-centered cubic metals at low temperatures. Data on the lamella structure of the hexagonal metals would be a valuable aid for further calculations. It would be especially significant if magnesium displayed such a structure and zinc and cadmium did not.

Recently in his Guthrie lecture Mott[19] has considered the way in which screw dislocations on different slip systems impede one another's motion. The net result of the crossing of a pair of such dislocations is the production of a line of vacancies joining the two. This introduces a restriction which favors the motion of edge dislocations over that of screw dislocations. Seitz[20] in his paper points out that as a result of this, glide over the entire cross section of a macroscopic specimen may require the simultaneous action of a large number of sources. Seitz estimates that for a specimen which is one square centimeter in cross section about 10^6 sources each of about one micron in length may be required to produce the slip lamella. Such an effect would increase the estimate of the length of dislocation line to a value much nearer the usually accepted figure.

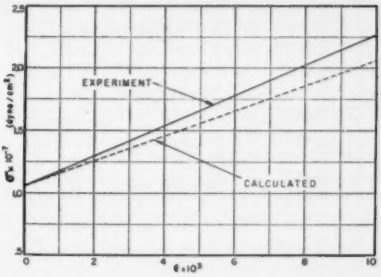

FIG. 5. Comparison of experiment and theory at room temperature. Full line is Rosi and Mathewson's data on aluminum single crystals. Theoretical curve is dashed.

C. The High Temperature Stress-Strain Curve at Small Strains

The room temperature stress-strain curve will be calculated next. This calculation is based on the low temperature theory and on Brown's information about the zone structure in aluminum at various temperatures.

Brown found that on the average each slip zone contains 1.5 lamellas at −180°C and 3.5 lamellas at room temperature. It will be assumed that each slip zone is produced by glide at a single generator. If the arguments of Mott and Seitz about the number of sources required per lamella are correct, then some revision of the above assumption will be required. The basic idea, i.e., that at high temperatures more glide is obtained for each long source used, is still admissible. The room temperature curve can therefore be calculated by modifying the low temperature calculation as follows:

1. The glide per source should be increased. In fact, the room temperature value should be $\epsilon_3=2\times10^{-4}\times3.5=7\times10^{-4}$.
2. The total stress acting to produce slip should be the sum of the applied stress and the stress arising from thermal fluctuations. The thermal stress can probably be measured by the decrease in the yield stress as the temperature is raised from 0°K to room temperature.
3. The room temperature value of G should be used.

The resulting stress-strain curve at any temperature can therefore be written as

$$\sigma=Gc/[\log(\epsilon_3Nc)-\log(\epsilon+\epsilon_4)]-FT^{\frac{1}{2}}, \qquad (9)$$

where $\epsilon_4=\epsilon_3Nc\exp[-cl_m/a]$. The expression which is subtracted takes the thermal stresses into account. Ac-

[17] See reference 2, p. 110.

[18] F. Seitz, *The Physics of Metals* (McGraw-Hill Book Company, Inc., New York, 1943), p. 93. This figure is obtained by assuming that the mosaic blocks have dislocations at their edges. See also F. Seitz and T. A. Read, J. Appl. Phys. 12, 476 (1941).

[19] See reference 14, p. 733.

[20] F. Seitz, Quarterly Supplement of Phil. Mag. (January, 1952, to be published).

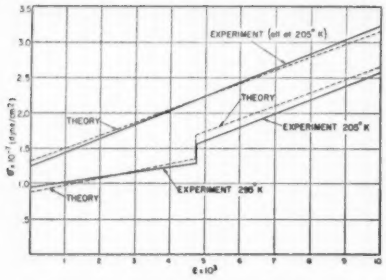

FIG. 6. Comparison of Rosi and Mathewson's equation of state data on aluminum single crystals with the present theory. Full lines are experiment. Dashed lines are calculated.

cording to our estimate, the yield stress of aluminum drops from 2.3×10^7 to 1.04×10^7 dynes/cm^2 in going from 0°K to room temperature. Inserting the other numerical constants into Eq. (9), we obtain the dashed curve shown in Fig. 5. The room temperature value of G has been used and F has been adjusted to give the required yield stress. The result is $F(293)^{\frac{1}{2}}=0.96\times10^7$ dyne/cm^2. The theoretical expression fits the experimental curve quite well. The calculated stress-strain curve at 205°K also fits the experimental curve well as we shall see later.

D. The Equation of State

If an equation of state existed for plastic flow, then the stress necessary to produce further plastic strain should be independent of the past history of the specimen; the stress required should depend only on the prior strain, the strain rate, and the temperature. Actually the experiments of Dorn, Goldberg, and Tietz[21] on polycrystals and those of Rosi and Mathewson on single crystals[22] show that the past history is important and that the plastic flow of metals cannot be described by an equation of state.

According to the views presented here, the past history is important. For example, if a specimen is strained in single slip through a strain ϵ at low temperature, the resulting state of the specimen as given by the remaining dislocation free length distribution is quite different from the result obtained by straining through ϵ at a high temperature. Qualitatively the low temperature strain uses more of the dislocation length distribution, so that if such a specimen is then warmed to the high temperature, a larger stress is required for further strain than if the prior strain had occurred at the high temperature. This prediction is in qualitative agreement with the experiments.

Rosi and Mathewson give the stress-strain curves of a single crystal pulled in tension through a strain of about one percent at 205°K and of a second crystal pulled in two stages, first at room temperature and then through the remaining strain at 205°K. The resolved stress-strain curves obtained using their data[23] are given by the full lines in Fig. 6.

The stress-strain curve which was all run at 205°K was fitted to the theory just used for the room temperature data. The glide required per source was $\epsilon_3'=1.86\times10^{-5}\times2.10=3.91\times10^{-5}$. The resulting stress-strain curve is shown dashed in Fig. 6. This figure 2.10 for the average number of glide lamellas per slip zone agrees well with Brown's electron microscope data (see Fig. 8) when it is extrapolated to 205°K.

The calculation of the stress-strain curve of a crystal which has been extended in two stages can be done as follows: Using the room temperature theory, the longest unused dislocation length l_b at the end of the room temperature strain ϵ_5 can be obtained from the equation:

$$\epsilon_3+\epsilon_4=N\epsilon_3 c\exp[-cl_b/a], \tag{10}$$

where ϵ_4 and ϵ_3 are the room temperature values of these parameters. This together with the values of G and $F(205)^{\frac{1}{2}}$ will give the stress at which the low temperature plastic strain begins [using Eq. (5)]. The remainder of the stress-strain curve is described by Eq. (9) where ϵ in the present case represents only that portion of the strain which occurs after the drop in temperature and the value of ϵ_4' to be used is

$$\epsilon_4'=\epsilon_3'Nc\exp[-cl_b/a], \tag{11}$$

where ϵ_3' is the value of ϵ_3 appropriate at 205°K. The resulting theoretical curve is shown dashed in Fig. 6. It should be mentioned that inasmuch as this particular crystal showed an abnormally low yield stress at room temperature, the theory was adjusted accordingly by using a somewhat larger l_m and a somewhat smaller c. N and the product l_mc were kept the same as before. These changes are reasaonable for a specimen of somewhat higher purity than most of those used by Rosi and Mathewson. The values used were $l_m=3.98\times10^{-4}$ cm and $c=2.296\times10^{-4}$. The theoretical results for the two stage case are shown in Fig. 6 by the lower dashed curve. The calculation should predict two things correctly, the magnitude of the increment in stress when the temperature is changed and the value of the slope at low temperature. Both quantities are reasonably well given by the theory.

If the basic ideas used in the calculations made thus far are correct, then the distribution of "free lengths" of dislocation which exists in a crystal can be obtained experimentally as follows: The number dN of glide steps produced per unit distance measured normal to the glide plane during the stress increment $d\sigma$ is measured at low temperature. This number represents the number of dislocations having length between l and $l+dl$ where the stress used and the dislocation length are associated

[21] Dorn, Goldberg, and Tietz, Trans. Am. Inst. Mining Met. Engrs. 180, 205 (1949).
[22] See reference 1, p. 1162.
[23] There exists a typographical error in Rosi and Mathewson's Table I. Crystal A should have $\sin x\cos\lambda$ equal to 0.4685.

by Eq. (5). The assumptions made above about the effect of temperature upon the strain resulting from the use of a single source can also be checked experimentally by making measurements on the number of slip zones produced per stress increment $d\sigma$ in a two stage stress-strain curve. This information together with electron microscope data on the number of glide lamellas produced per slip zone at various stresses would furnish the necessary data for the test. The data should be obtained on single crystals.

E. Interaction Hardening and Source Hardening

The present theory implies that glide on planes other than the one having the highest yield stress should occur when the resolved shearing stress on these other planes exceeds their yield stress. In the face-centered cubic and the body-centered cubic crystals which have several equivalent glide planes, this implies considerable cross slip, particularly at large strains. This glide on several intersecting slip systems leads to the entrapment of large numbers of dislocations in the specimen as a result of the interaction of the crossed dislocations with one another.[24] The entrapment makes it harder to force additional dislocations through the specimen and hence results in work-hardening. This second kind of work-hardening should probably be called interaction-hardening. The kind of hardening discussed earlier in the paper could properly be called source-hardening. Source-hardening is clearly the only kind of hardening at very small strains, whereas both are important at large strains. Rohm and Kochendorfer[25] have attempted to perform an interesting experiment in which interaction-hardening would be reduced or eliminated by constraining an aluminum crystal in such a way that glide can only occur on one slip system. They then apparently obtain no asterism and the stress-strain curve is linear. This and other evidence[4,14] indicates that interaction hardening is probably associated with asterism, deformation bands, etc.

III. FURTHER SUGGESTIONS

Certain tentative proposals will now be made to explain experimental points not thus far considered. In general, not enough data is available to decide for or against the explanations given. It is hoped that the present discussion will stimulate further decisive experimental work in this field.

A. The Increase in the Glide per Source with Temperature

The experiments of Brown and the stress-strain data both indicate that the glide per source increases with increasing temperature. Earlier in the paper it was noted that the decrease in the initial slope of the stress-strain curves of close-packed crystals is proportional to $T^{\frac{1}{2}}$. The temperature dependence of the initial slope is more complex in the case of zinc and cadmium. This behavior can be understood as follows:

After a given source has produced a large number of loops, the process of generation fails to carry through. Thermal fluctuations then produce stresses which, when acting on the portion of the dislocation that is screw type, carry a sufficient length of the dislocation into a new glide plane which is far enough from the original lamella so that a large amount of slip can occur in the new lamella (see Fig. 7 for the geometry). The separation of the lamellas in a zone is determined by the interaction force between dislocations on neighboring lamellas. The total stress must be large enough to drive the dislocations past one another. Thus[26]

$$\sigma = Ga/[8\pi(1-s)d], \tag{9}$$

where s is Poisson's ratio and d is the separation. Brown found lamella spacings from 200 to 800A after 15 percent extension. Data on polycrystalline aluminum at room temperature[27] shows that the resolved shearing stress required for 15 percent extension is 2.9×10^8 dyne/cm^2. The stress given by Eq. (9), assuming a separation of 200A, is 2.5×10^8 dyne/cm^2. At 78°K the experimental shearing stress required is about 7.1×10^8 dyne/cm^2 whereas the theoretical value, again for a spacing of 200A, is 2.9×10^8 dyne/cm^2. The present theory indicates that the spacing should be almost inversely proportional to the applied shearing stress no matter what the temperature. Further measurements on single crystals would be desirable.

The number of lamellas in a single slip zone will depend on the stress, the temperature, and the speed of deformation. Consider the temperature dependence for samples strained at the same rate. The probability W of a thermal fluctuation which produces a stress σ_1 in the cross slip system if σ is the component of the shearing stress in the cross slip system is given by Eq. (1). Since $n-1$ of the lamellas in a zone are produced by fluctuations, this number should be proportional to W. The number of lamellas per zone should, according

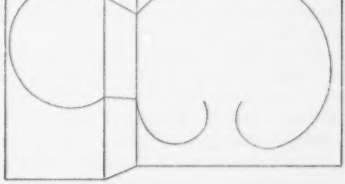

FIG. 7. Illustrating the glide produced by thermal fluctuations on slip planes near the plane of the original source.

[24] See reference 14, Sec. 8 and 10.
[25] F. Rohm and A. Kochendorfer, Z. Metallkunde 41, 265 (1950).
[26] A. H. Cottrell, *Progress in Metal Physics* (Butterworths Scientific Publications, London, 1949), Vol. I, p. 103.
[27] See reference 21, p. 219.

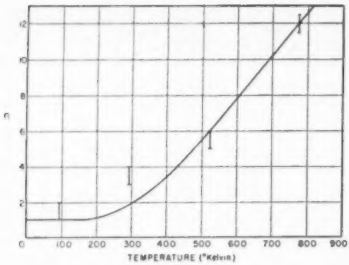

FIG. 8. The number n of glide lamellas per zone as a function of temperature. Brown's experimental values are given by the vertical lines. The solid curve is calculated.

to this theory, be compared at the same resolved shearing stress on the cross slip system at different temperatures. Brown's data is not immediately applicable because the number of lamellas per zone are compared after the same extension at the different temperatures. Nevertheless we have fitted Brown's data to an exponential. The results are shown in Fig. 8. If the above theory is correct, then a single crystal of a face-centered cubic material which has its axis nearly parallel to the [111] direction should have an abnormally large number of lamellas per zone at room temperature because the shearing stresses on the original and on the particular cross slip system having the same slip direction as the original system are nearly equal. The thermal stresses should therefore find it easy to produce the necessary cross slip. The initial slope of the stress-strain curve should also be unusually small for such a specimen.

B. The Locking of a Frank-Read Source

Brown's data[28] indicates that at all temperatures the glide per lamella ranges from 1500A to 2500A. He found that the average glide per lamella increases with temperature as follows:

−180°C	average glide = 1600A
20°C	average glide = 2000A
250°C	average glide = 2200A

The present data,[28] although not decisive, indicates that once a lamella has been formed, little, if any, further glide occurs there.

In several recent publications Seitz[29] has discussed data which indicates that moving dislocations generate vacancies. These vacancies produced in the vicinity of the glide plane may be associated with the locking process. Seitz's viewpoint is summed up by him as follows: "The generator will encounter resistance to motion as a result of vacant sites or interstitial atoms produced in the generating area only if (a) the imperfections are formed as a result of dynamical instability during motion in regions where it attains velocities comparable with the velocity of sound or (b) if vacancies and interstitials are produced in pairs in the heated annihilation zone and diffuse apart. It seems entirely feasible, however, that the limited life of a generator is determined by the fact that debris accumulates in its region of operation, particularly in the annihilation region where it attains maximum velocity." Seitz[30] explains the fact that once a generator locks, the application of larger stresses will not reactivate it, as follows: "Once a dislocation has come to rest in a region where there is a high density of vacancies, it will probably become locked into position because the vacancies in the vicinity will migrate to it and form clusters in order to relieve the local stress field in the manner suggested by Koehler in another connection."

It may be that Seitz's proposals should be extended as follows: It seems quite reasonable to suppose as Seitz did that vacancies are produced by dynamical instability at a jog in a moving dislocation. In addition, it seems plausible that the production of a vacancy or an interstitial at such a jog will be more likely to occur during the time the jog is passing an impurity, a vacancy, or an interstitial atom. The local differences in the inertial force and the binding force should make it difficult for the entire configuration to move smoothly.

It is also possible that locking occurs not so much because of debris left on the glide plane, but because after a sufficient number of jogs have been produced, the spiralling dislocation has become so ragged that the two portions in Fig. 3 which should annihilate one another no longer fit together. As a result, further generation does not occur. Such a locked annihilation center should be quite stable and should require considerable well-correlated diffusion to unlock the center.

Seitz's suggestions and the above proposals both give a qualitative explanation of the Molenaar and Aarts experiments.[31] In these experiments a polycrystalline metal wire is pulled in tension at liquid air temperature. Subsequent annealing for about ten minutes at room temperature results in an appreciable drop in the electrical resistance at liquid air temperature but no change occurs in the low temperature stress required for further extension.

If the first additional proposal made above is correct, then a small amount of lead dissolved in an aluminum crystal should produce a decrease in the amount of glide per lamella.

It must be admitted that a present the locking mechanism is not well understood.

C. Cross Slip

The theory presented in this paper implies that slip also occurs on systems which are not those associated

[28] See reference 2, p. 109.
[29] See reference 20, Part 6, Sec. I.
[30] See reference 20, Part 6, Sec. H.
[31] J. Molenaar and W. H. Aarts, Nature **166**, 690 (1950).

with the maximum shearing stress. This cross slip occurs because glide on the original slip system gradually uses up the long sources there until eventually, as the applied stress increases, the resolved shearing stress in some other slip system is large enough to induce loop generation there. The amount of glide which occurs on the cross slip lamellas will depend on whether the locking process which has stopped lamellas in the principal slip system is also at least partially effective in stopping glide on the second slip system. The present theory is consistent with the finding that during the transition from single to double slip no discontinuity is observed in the stress-strain curve of a pure metal. The treatment given in this paper implies that the glide produced by cross slip is much less than that on the primary slip system. This assumption is in accord with experiment.[22]

In conclusion, I would like to thank Dr. L. Slifken, Professor F. Seitz, and Mr. J. Marx for numerous stimulating discussions.

[22] G. I. Taylor and C. F. Elam, Proc. Roy. Soc. (London) **A102**, 643 (1923).

PHYSICAL REVIEW VOLUME 86, NUMBER 1 APRIL 1, 1952

High Energy Electron-Electron Scattering

WALTER H. BARKAS, ROBERT W. DEUTSCH, F. C. GILBERT, AND CHARLES E. VIOLET
Radiation Laboratory, Department of Physics, University of California, Berkeley, California

(Received December 10, 1951)

Eradicated electron sensitive nuclear emulsions were exposed to 200-Mev electrons at the Berkeley synchrotron. In scanning the electron tracks 427 events were observed in which the scattered electron of lower energy, or knock-on electron, had an energy greater than 30 kev. The observed differential cross section was found to agree in absolute value with Møller's theoretical cross section, although an insufficient number of high energy knock-on electrons were observed to distinguish between the Møller, relativistic Mott, and relativistic Rutherford formulas. Two pairs initiated by primary electrons and two cases in which primary electrons vanished in the emulsion were also observed in 102.6 cm of track. No heavy particle events were seen.

I. INTRODUCTION

HISTORICALLY, the electron is the best known of the fundamental particles. However, a lack of information still exists concerning its actual structure. An electron-electron scattering experiment would seem to be the ideal way to investigate the boundaries of the electron and the possibility of non-Coulomb electron-electron forces. To find deviations from a Coulomb potential, one would roughly estimate that it is necessary to have an impact parameter of the order of the classical electron radius. In order for the impact parameter to be well defined the de Broglie wavelength, λ, of the electron in the relativistic center-of-mass system must be of the order of 2.8×10^{-13} cm or less. A simple calculation shows that such a wavelength would require an energy of about 19 Bev in the laboratory system. In the present experiment 200-Mev electron primaries were used which have a de Broglie wavelength of about 10 times the classical electron radius in the relativistic center-of-mass system. Even for this wavelength, the possibility seemed to exist of observing a deviation from the Coulomb potential if the effect were strong.

The generally accepted formula giving the scattering cross section of electrons by electrons has been derived by Møller.[1] This formula in terms of the scattering angle, θ, in the relativistic center-of-mass system is the following:

$$\sigma(\theta)d\theta=\frac{(\gamma+1)\pi r_0^2\sin\theta d\theta}{\gamma^2\beta^4}\left[\csc^4\frac{\theta}{2}+\sec^4\frac{\theta}{2}-\csc^2\frac{\theta}{2}\sec^2\frac{\theta}{2}+\frac{(\gamma-1)^2}{\gamma^2}(1+4\csc^2\theta)\right], \quad (1)$$

where r_0 is the classical electron radius, $\beta=v/c$, $\gamma=1/(1-\beta^2)^{\frac{1}{2}}$, and v is the velocity of the primary electron in the laboratory system. The first two terms in the bracket correspond to the classical, relativistic Rutherford scattering formula. The third term is the quantum-mechanical exchange term. The inclusion of this term with the Rutherford formula gives the relativistic Mott formula. The fourth term represents retardation and spin interaction effects.

Equation (1) is more conveniently expressed in terms of the parameter A, defined as the ratio of kinetic energy given to the secondary or knock-on electron to the kinetic energy of the primary electron. It is not possible to distinguish between the primary and secondary electrons after collision. The knock-on electron is by definition the lower energy electron after collision. The maximum value of A is obviously 0.5. By a simple

[1] C. Møller, Z. Physik **70**, 786 (1931); C. Møller, Ann. physik. **14**, 531 (1932); K. C. Kar and C. Basu, Indian J. Phys. **18**, 223 (1944).

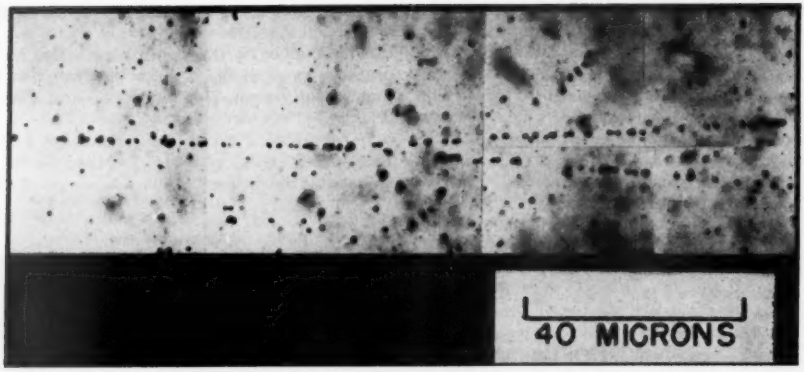

FIG. 1. Microphotograph mosaic of an electron-electron collision of large energy transfer initiated by an ~185-Mev primary electron. The angles of scatter are 9° and 2° corresponding to 32 Mev for the electron of lower energy.

transformation, as shown by Møller,[1] Eq. (1) becomes

$$\sigma(A)dA=\frac{2\pi r_0^2}{\beta^2(\gamma-1)}\left[\frac{1}{A^2(A-1)^2}-\frac{3}{A(1-A)}+\frac{(\gamma-1)^2}{\gamma^2}\left(1+\frac{1}{A(1-A)}\right)\right]dA. \quad (2)$$

The corresponding relativistic Rutherford cross section is

$$\sigma(A)dA=\frac{2\pi r_0^2}{\beta^2(\gamma-1)}\left[\frac{1}{A^2(A-1)^2}-\frac{2}{A(1-A)}\right]dA. \quad (3)$$

The relativistic Mott cross section is

$$\sigma(A)dA=\frac{2\pi r_0^2}{\beta^2(\gamma-1)}\left[\frac{1}{A^2(A-1)^2}-\frac{3}{A(1-A)}\right]dA. \quad (4)$$

Several previous experiments[2–6] have been performed to verify Møller's theory. The primary energies used in these experiments have ranged from 0.05 to only 2.64 Mev. Except for the experiment of Williams and Terroux[2] all results are in good agreement with Møller's theory. Champion,[3] Groetzinger *et al.*[6] attempted to find discrepancies between the Rutherford, Mott, and Møller formulas, Eqs. (3), (4), and (2). Champion found good agreement with the Møller equation but not with the other two equations. Groetzinger *et al.* were not able to discriminate between any of the three. However, combining their data with Champion's, they ruled out the Rutherford equation; but within statistical error they could not discriminate between the Mott and Møller equations.*

For a 200-Mev electron Eq. (2) can be approximated by the following:

$$\sigma(A)dA=\frac{2\pi r_0^2}{\beta^2(\gamma-1)}\left[\frac{1}{A^2(1-A)^2}-\frac{2}{A(1-A)}+1\right]dA. \quad (5)$$

Comparison of Eqs. (3), (4), and (5) shows that in the region of A less than 0.01 the three equations are indistinguishable. For A in the region between 0.1 to 0.5, the percentage deviation of Rutherford's cross section from Møller's cross section varies from 1 percent to 11 percent, while that of Mott's to Møller's varies from 12 percent to 56 percent. The expected number of knock-ons in photographic emulsions in the entire region from $A=0.1$ to $A=0.5$ (Fig. 1) is about one per

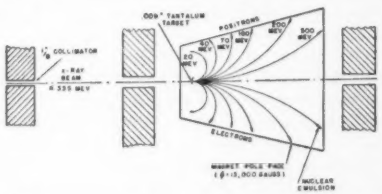

FIG. 2. Arrangement of the photographic emulsions in the magnetic field of the synchrotron pair spectrometer.

[1] E. J. Williams and F. R. Terroux, Proc. Roy. Soc. (London) **A126**, 289 (1929/1930). [Williams and Terroux were attempting to verify the theory of Thompson (J. J. Thompson, Phil. Mag. **29**, 449 (1912)). According to Hornbeck and Howell, the results of the Williams and Terroux experiment lead to cross sections which are more than twice as great as predicted from Møller's theory.]

[2] F. C. Champion, Proc. Roy. Soc. (London) **A137**, 688 (1932).

[3] G. Hornbeck and I. Howell, Proc. Am. Phil. Soc. **84**, 33 (1941).

[4] P. E. Shearing and T. E. Pardue, Proc. Am. Phil. Soc. **85**, 243 (1942).

[5] Groetzinger, Leder, Ribe, and Berger, Phys. Rev. **79**, 454 (1950).

* *Note added in proof:*—Since this paper was submitted for publication, an important new electron-electron scattering experiment employing a beam of 15.7-Mev electrons has been reported [Scott, Hanson, and Lyman, Phys. Rev. **84**, 638 (1951)]. Only a two percent deviation from Møller scattering was found. This they attribute to experimental error.

100 cm of track. Therefore one cannot hope to resolve these three equations without scanning enormous quantities of track. The scope of this experiment therefore has been limited to verifying Møller's formula for the absolute scattering cross section of 200-Mev electrons, realizing that the Rutherford and Mott formulas are equivalent to Møller's in the region where most of the data can be obtained.

II. EXPERIMENTAL PROCEDURE

The existence of electron-sensitive emulsions and a technique for eradicating accumulated background has made possible this study of high energy electron processes taking place within the nuclear emulsion. 200-micron Ilford G-5 plates were exposed to 200-Mev electrons obtained by magnetic separation in the pair spectrometer at the Berkeley synchrotron (Fig. 2). The plates were exposed so that electrons from the target entered the emulsion at a slight angle to the surface and perpendicular to the leading edge of the plate. In order to insure that only electrons which came directly from the converter were accepted, only tracks whose initial directions lay within $2\frac{1}{2}°$ of the perpendicular were scanned. This criterion included over 90 percent of all the high energy electrons entering the plate. On plates exposed with no converter in the beam the number of acceptable tracks found was less than one percent of that found on plates exposed with the converter in place.

Because of the high background of low energy electrons found in all but freshly prepared electron sensitive emulsions, it was necessary to eradicate[7] the latent image of old tracks immediately before exposure. The eradication was accomplished by storing the plates in a warm, water-saturated atmosphere for several days before use. The temperature was controlled at about 97°F by immersing a watertight box containing the plates in a thermostatically controlled water bath. The relative humidity was maintained at 10 percent by placing a wet sponge in the box with the plates. Immediately after exposure the plates were developed by a temperature cycle process[8] in order to obtain a uniform and highly sensitive development.

In order to reconstruct stereoscopically the ranges and angles of the knock-on electrons, it was necessary to measure the shrinkage factor of the emulsion. This was accomplished by passing 380-Mev alpha-particles through the undeveloped emulsion at an angle of 45° to the emulsion surface[9] and then measuring the ratio of the horizontal projection to the vertical projection of the alpha-track after development. This ratio gave the shrinkage factor directly as 2.5 ± 0.1.

[7] H. Yagoda and N. Kaplan, Phys. Rev. **73**, 634 (1948).
[8] Dilworth, Occhialini, and Vermaesen, Bull. Cen. Phys. Nuc. Brussels (1950).
[9] M. Weissbluth, University of California Radiation Laboratory Report No. 568 (1950).

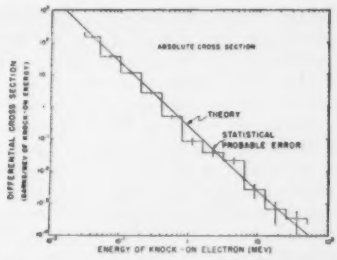

FIG. 3. Histogram of the experimental results shown with statistical probable errors. The effect of the energy resolution upon the magnitude of the absolute cross section is negligible in comparison with the statistical error.

III. METHOD OF ANALYSIS OF PLATES

The plates were scanned under ~500× magnification, and all events of interest were measured under ~2500× magnification. In these plates the grain density of a 200-Mev electron is 41.9 ± 1.0 grains per 100 μ of track. The length of primary track scanned was measured by means of the microscope stage coordinates. In order to reduce the percentage of knock-on electrons missed, each track used was scanned independently by two observers and all questionable events were examined by a third observer before a decision was reached. No track was scanned for more than 0.8 cm or beyond a detectable single scatter or a high energy electron-electron scatter. Tracks were not scanned and no event was recorded within 10μ of either surface of the emulsion. The average track length in emulsion was 0.40 cm giving an average loss due to both ionization and radiation of 30 Mev. Thus the average primary electron has a mean energy of 185 Mev. The energies of some primary electrons were measured by their multiple scattering and found to be consistent with the above calculated values.

In order to insure that no events were being missed (especially those in which the knock-on electron track was nearly vertical in the emulsion), a plot was made of the distribution of the azimuthal angles of the knock-ons about the direction of the incident electron. This distribution was found not to be significantly different from a symmetric distribution.

To determine the energy of the knock-on electron both its range and the angle between its direction and the direction of the incident electron were measured wherever possible. For very low energy knock-on electrons the angle became difficult to measure because of nuclear scattering. Therefore, the range was the principal means of determining the energy up to about 0.6 Mev.[10] Above this energy few knock-ons stayed in the emulsion, but the angle became a practical means of determining the energy. The angle, θ, is related to the knock-on kinetic energy, Q, and the incident electron

[10] B. Zajac and M. Ross, Nature **164**, 311 (1949).

kinetic energy, E, by $Q=E\cos^2\theta/[1+(E/2mc^2)\sin^2\theta]$, where mc^2 is the rest energy of the electron. For $E\sin^2\theta/2mc^2\gg1$, the knock-on energy as determined by the angle θ is nearly independent of the primary energy. For a 200-Mev primary electron this condition is met by all observed events, so we have disregarded the variation in primary energy caused by losses in the emulsion in calculating the knock-on energy. In the region where the angle and range methods of determining energy overlap, good agreement was found for the knock-on energy considering the large electron range straggle.

Knock-on electrons of energy less than 30 kev were not included in this study because of their small range (<7 μ) and because of the effect of electron binding.

IV. EXPERIMENTAL RESULTS

In Fig. 3 is shown a histogram of the results compared with the cross section as predicted by Møller. In the energy range from 30 kev to 0.1 Mev there were 182 events found in 33.4 cm of electron track. The rest of the histogram represents 245 events found in 102.6 cm of electron track. The number of electrons per cubic centimeter of emulsion was calculated to be 1.07×10^{24} from the emulsion composition given by Ilford Ltd. The effect of water absorbed in the emulsion from the atmosphere on the electron density has been measured and is negligible in this experiment.

The fact that the experimental data provides such a good fit to Møller's curve indicates that with these conditions there is no measurable deviation from a Coulomb potential for 185 ± 15 Mev electron primaries.

A similar study is being carried out using primary positrons of 200 Mev. Preliminary results[11] indicate that positron-electron scattering is similar to the electron-electron scattering in the range of knock-on energies studied here.

V. OTHER HIGH ENERGY ELECTRON PROCESSES

In the course of scanning for electron-electron collisions the following events were also noted:

In 102.6 cm of electron track two events were found in which the primary electron track divided into three tracks (Fig. 4), suggesting pair production in the field of the nucleus. By an approximate calculation[12] one would expect 1.1 pairs for this length of track.

An event was found on each of two separate plates (total path length of 102.6 cm) in which the electron track terminated in the center of the emulsion. Figure 5 is a photograph of one of the disappearances. The lengths of track before disappearance were 0.7 and 1.5 mm. The experimental arrangement and selection criteria rule out the possibility that these tracks were positrons. It is improbable that the tracks traversed an insensitive volume of the emulsion since the single grain background remains uniform and other primary tracks have no apparent change in grain density in the region of the disappearance. A short distance back on one of the disappearing electrons there is a knock-on coming off in the forward direction, confirming the assumed direction of this primary; this rules out the possibility of a Compton electron in the backward direction for this case. The fact the endings are near the center of the emulsion reduces the probability of

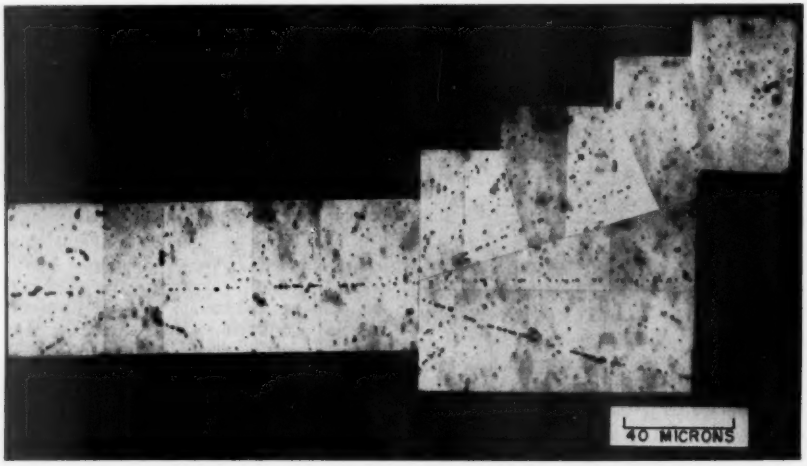

FIG. 4. Microphotograph mosaic of an electron-positron pair apparently produced in the field of a nucleus by an ~185-Mev electron.

[11] Gilbert, Violet, and Barkas, Phys. Rev. **81**, 656 (1951).
[12] Heitler, *Quantum Theory of Radiation* (Oxford University Press, New York), second edition.

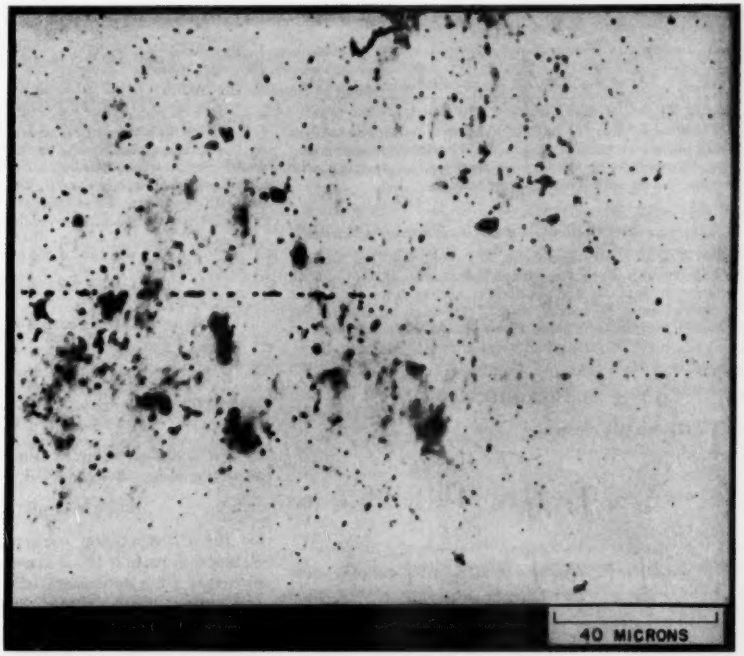

FIG. 5. Microphotograph of the disappearance of an ~185-Mev electron near the center of the emulsion.

not observing a large angle scatter out of the emulsion. The mechanism by which a high energy electron could disappear in emulsion has not been satisfactorily explained.

In scanning about 230 cm of electron track, no events were found in which protons or mesons were ejected from nuclei. Large angle nuclear scattering has been observed, but the study of such events has not been completed.

VI. ACKNOWLEDGMENTS

The emulsion method of studying electron-electron scattering was first found to be practical using fast electrons from a linear accelerator at Stanford University. Dr. G. E. Becker kindly assisted one of us (W.H.B.) in this experiment. Much of the microscope work of the preliminary experiments was done by Professor Lawrence Germain and Mrs. Edith Goodwin, and we are indebted to Mr. A. Oliver for his microphotographs and helpful advice on emulsion technique. The work was assisted greatly by the continued interest and encouragement given the film program by Professor E. O. Lawrence. We have enjoyed the invaluable cooperation of the synchrotron operating crew under the direction of Mr. George McFarland and Professor A. C. Helmholz.

First-Forbidden Beta-Decay Matrix Elements*

T. AHRENS† AND E. FEENBERG
Washington University, St. Louis, Missouri
(Received December 26, 1951)

The general theory of first-forbidden beta-transitions involves seven nuclear matrix elements in the nonrelativistic approximation. In principle the number of independent parameters can be reduced to four with the help of the relation

$$(W_f-W_i)(f|X|i)=(f|[H_0,X]|i)+(f|[H_c,X]|i)+(f|[H_r,X]|i).$$

Here W is an energy eigenvalue, X a coordinate type first-forbidden operator, H_0 the free particle Hamiltonian, H_c the Coulomb interaction, and H_r the specifically nuclear interaction. The commutators of H_0 and H_c with X are easily evaluated, but $[H_r, X]$ presents difficulties. However, the matrix elements of $[H_r, X]$ can be estimated by general physical arguments based on the semi-empirical energy surface and the validity of shell model considerations. The explicit form of H_r is not required a fortunate circumstance since H_r for complex nuclei is at present essentially unknown. These calculations determine the common proportionality factor Λ in the relations

$$\tfrac{1}{2}\Lambda\alpha Z\int \mathbf{r}/R=-i\int\boldsymbol{\alpha},$$
$$\tfrac{1}{2}\Lambda\alpha Z\int\boldsymbol{\sigma}\cdot\mathbf{r}/R=-i\int\gamma_5,$$
$$\tfrac{1}{2}\Lambda\alpha Z\int\boldsymbol{\sigma}\times\mathbf{r}/R=-\int\beta\boldsymbol{\alpha}.$$

1. INTRODUCTION

THE matrix elements[1]

$$\int\boldsymbol{\alpha},\quad\int\beta\boldsymbol{\alpha},\quad\int\gamma_5, \tag{1a}$$

$$\tfrac{1}{2}\alpha Z\int\mathbf{r}/R,\quad\tfrac{1}{2}\alpha Z\int\boldsymbol{\sigma}\cdot\mathbf{r}/R,\quad\tfrac{1}{2}\alpha Z\int\boldsymbol{\sigma}\times\mathbf{r}/R \tag{1b}$$

occur in the theory of first-forbidden transitions characterized by the selection rule $\Delta I=0,\ \pm1$ (yes).[2-4] Nonrelativistic approximations to the first three matrix elements and the association with the different covariant formulations of the beta-decay theory are shown in Table I. The designations momentum type (1a) and coordinate type (1b) are convenient to distinguish the matrix elements in the two lines of Eq. (1).

Upper limits on the squares of the matrix elements can be derived from the completeness theorem. We use the estimates

$$\langle p^2\rangle_{\text{Av}}/2M\sim 20\text{ Mev} \tag{2}$$

for the average value of the kinetic energy of the particle making the transition, and

$$\langle r^2\rangle_{\text{Av}}\sim 0.6R^2 \tag{3}$$

for the corresponding average square of the radial distance. Equation (2) is based on the single particle picture of a nucleon having binding energy of 6–8 Mev in a potential well of depth 25–30 Mev. Equation (3) follows from the assumption of uniform particle density. A small correction for a possible nonuniform particle density is unimportant in the present context. Results for the upper limits are collected in Table II.

Table II suggests that the momentum type matrix elements are dominant for small Z, while leaving open the question of which type is most important for the very largest values of Z.

It must be admitted, however, that these upper limits are too high to support strong conclusions on the relative importance of momentum and coordinate type matrix elements. Allowed favored transitions, for which $\sum_{m_f}|M|^2\sim1$, have $ft\sim3\times10^3$; first-forbidden transitions with $ft\sim10^{6-7}$ have $\sum_{m_f}|M|^2\sim10^{-3}$. Thus a factor of about 50 separates the upper limits of Table II from the mean experimental values.

TABLE I. Properties of momentum type matrix elements.

Covariant formulation	Matrix element	Nonrelativistic approximation
Polar vector	$\int\boldsymbol{\alpha}$	$-\int\mathbf{p}/Mc$
Tensor	$\int\beta\boldsymbol{\alpha}$	$-i\int\boldsymbol{\sigma}\times\mathbf{p}/Mc$
Axial vector	$\int\gamma_5$	$-\int\boldsymbol{\sigma}\cdot\mathbf{p}/Mc$

2. THEORETICAL RELATIONS BETWEEN COORDINATE AND MOMENTUM TYPE MATRIX ELEMENTS

Information on the ratios of momentum to coordinate type matrix elements is needed for an unambiguous interpretation of the experimental material. These ratios are accessible to theoretical study following a procedure suggested by a remark in reference 2. The analysis starts from the nuclear Hamiltonian[5]

* Assisted by the joint program of the ONR and AEC.
† AEC Predoctoral Fellow.
[1] α=fine structure constant, Z=atomic number of the product nucleus, R=nuclear radius with the approximate value $(e^2/2mc^2)A^{\frac{1}{3}}$. The first-forbidden pseudoscalar matrix element is not included in the present discussion. The usual statement that it is $\int\beta\gamma_5$ is misleading because this matrix element is extremely small, of the order $(p/Mc)^2$, in the nonrelativistic approximation, if the lepton covariant $\psi_e^*\beta\gamma_5\varphi_\nu$ is removed from under the integration.
[2] E. J. Konopinski and G. E. Uhlenbeck, Phys. Rev. **60**, 308 (1941).
[3] R. Marshak, Phys. Rev. **61**, 431 (1942).
[4] E. J. Konopinski, Revs. Modern Phys. **15**, 209 (1943).
[5] The isotopic spin formalism [L. Rosenfeld, *Nuclear Forces* (Interscience Publications, New York, 1948), p. 43] is used in the following calculations; i.e., the two charged states of a nucleon are described by a charge variable τ with the values $+1$ (neutron

$$H=H_0+H_c+H_\nu, \tag{4}$$

$$H_0=-c\sum \boldsymbol{\alpha}_k\cdot\mathbf{p}_k-Mc^2\sum\beta_k, \tag{5}$$

$$H_c=\frac{e^2}{8}\sum_{l\neq k}\frac{1}{r_{lk}}(1-\tau_{ks})(1-\tau_{ls}), \tag{6}$$

H_ν—specifically nuclear interactions.

The equation

$$(W_f-W_i)(f|X|i)=(f|HX-XH|i) \tag{7}$$

relates the matrix elements of $X=\sum X_kQ_k$ and the commutator of H and X.[6]

Explicitly,

$$[H_0,\sum\mathbf{r}_kQ_k]=ic\hbar\sum_k\boldsymbol{\alpha}_kQ_k$$

$$\cong(\hbar/iM)\sum_k\mathbf{p}_kQ_k, \tag{8a}$$

$$[H_0,\sum\boldsymbol{\sigma}_k\cdot\mathbf{r}_kQ_k]=-(c\hbar/i)\sum_k\{3\gamma_{ks}-2i\boldsymbol{\alpha}\cdot(\mathbf{r}\times\nabla)\}Q_k$$

$$\cong(\hbar/iM)\sum_k\boldsymbol{\sigma}_k\cdot\mathbf{p}_kQ_k$$

$$\cong-(c\hbar/i)\sum_k\gamma_{ks}Q_k, \tag{8b}$$

$$[H_0,\sum\boldsymbol{\sigma}_k\times\mathbf{r}_kQ_k]=2c\hbar\sum_k(\boldsymbol{\alpha}_k-\boldsymbol{\alpha}_k\cdot\mathbf{r}_k\nabla_k+\mathbf{r}_k\cdot\nabla_k\boldsymbol{\alpha}_k)Q_k$$

$$\cong(\hbar/iM)\sum_k\boldsymbol{\sigma}_k\times\mathbf{p}_kQ_k$$

$$\cong\hbar c\sum_k\beta_k\boldsymbol{\alpha}_kQ_k, \tag{8c}$$

$$[H_c,\sum\boldsymbol{\sigma}_k\cdot\mathbf{r}_kQ_k]=\tfrac{1}{2}e^2\sum_{l\neq k}\frac{\boldsymbol{\sigma}_l\cdot\mathbf{r}_l}{r_{lk}}(1-\tau_{ks})Q_l, \tag{9a}$$

$$[H_c,\sum\mathbf{r}_kQ_k]=\tfrac{1}{2}e^2\sum_{l\neq k}\frac{\mathbf{r}_l}{r_{lk}}(1-\tau_{ks})Q_l, \tag{9b}$$

$$[H_c,\sum\boldsymbol{\sigma}_k\times\mathbf{r}_kQ_k]=\tfrac{1}{2}e^2\sum_{l\neq k}\frac{\boldsymbol{\sigma}_l\times\mathbf{r}_l}{r_{lk}}(1-\tau_{ks})Q_l. \tag{9c}$$

The expansion theorem

$$(f|[H_c,X]|i)=\sum_{f'}(f|H_c|f')(f'|X|i)-\sum_{i'}(f|X|i')(i'|H_c|i) \tag{10}$$

suggests the approximate relation

$$(f|[H_c,X]|i)\cong[(f|H_c|f)-(i|H_c|i)](f|X|i). \tag{11}$$

state) and -1 (proton state). The functions,

$$\delta_\pm(\tau)=1,\quad \tau=\pm1$$
$$=0,\quad \tau=\mp1,$$

describe definite charge states. These functions are eigenfunctions of the isotopic spin operator τ_z: $\tau_z\delta_\pm(\tau)=\pm\delta_\pm(\tau)$.

The conventional symbol fX of Eq. (1) denotes the matrix element of the operator

$$\sum_{k=1}^{A}X_kQ_k \quad\text{or}\quad \sum_{k=1}^{A}X_kQ_k^*,$$

in which Q and Q^* are displacement operators defined by

$$Q\delta_+=\delta_- \quad Q^*\delta_-=\delta_+$$
$$Q\delta_-=0 \quad Q^*\delta_+=0.$$

[6] The symbols f and i denote final and initial states of the β-decay process while the W's are the corresponding energy eigenvalues.

TABLE II. Upper limits on the squares of the first-forbidden matrix elements.[a]

Covariant formulation	Matrix element M	Upper limit on $\sum_{m_f}\|M\|^2$
Scalar and polar vector	$\frac{1}{4}\alpha Z\int\tau/R$	$0.15(\alpha Z)^2$
Polar vector	$\int\boldsymbol{\alpha}$	0.044
Tensor and axial vector	$\frac{1}{4}\alpha Z\int\boldsymbol{\sigma}\cdot\mathbf{r}/R$	$0.15(\alpha Z)^2$
Tensor and axial vector	$\frac{1}{4}\alpha Z\int\boldsymbol{\sigma}\times\mathbf{r}/R$	$0.30(\alpha Z)^2$
Tensor	$\int\beta\boldsymbol{\alpha}$	0.088
Axial vector	$\int\gamma_5$	0.044

[a] In the last column the sum is over all values of the magnetic quantum number m_f of the final state.

Equation (11) is not likely to be greatly in error considering that the Coulomb energy difference of two neighboring isobars is large compared with nondiagonal Coulomb matrix elements; destructive interference among the neglected terms in Eq. (10) may also be a helpful factor.[7]

It is also possible that the neglected terms in Eq. (10),

$$\sum_{f'\neq f}(f|H_c|f')(f'|X|i)-\sum_{i'\neq i}(f|X|i')(i'|H_c|i), \tag{12}$$

change in a fairly random manner as regards sign and magnitude, as N and Z are varied, suggesting the possibility that Eq. (11) is accurately equivalent to Eq. (10) on the average when fluctuations are smoothed out over a range of N, Z values.

These statements are supported by a test calculation, with determinental wave functions, in which the left and right-hand members of Eq. (11) differ by less than ten percent (Appendix A). By inserting the Coulomb energies of uniformly charged spheres into the right-hand member of Eq. (11), we obtain

$$(f|[H_c,X]|i)\cong1.2e^2(Z-1)R^{-1}(f|X|i). \tag{13}$$

The matrix elements of the commutator $[H_\nu,X]$ can be estimated under special assumptions on H_ν. Conditions under which the commutator vanishes include ordinary forces (nonexchange) and zero range exchange forces. Generally speaking, such estimates have value as sample calculations, but throw no light on what actually occurs in nature.

We attempt here to evaluate the commutator without introducing an explicit form for H_ν; the calculation is based on general arguments and the semi-empirical formula for the nuclear energy surface. We use the

[7] Equations (11) and (14) involve an implicit assumption on the relative magnitudes of $(f|X|i)$, $(f'|X|i)$, and $(f|X|i')$; the situation is most favorable when

$$|(f|X|i)|\gtrsim|(f'|X|i)|$$
$$|(f|X|i')|.$$

We note also that the two-particle character of the Coulomb interaction fixes f' in Eq. (10) to the extent that it need be considered only when $\psi_{f'}$ contains a substantial component derived from configurations each differing by not more than two orbitals from corresponding configurations in ψ_f (a similar remark applies to $\psi_{i'}$ and ψ_i).

expansion theorem once more in the form expressed by Eq. (10) with H_c replaced by H_r. If nondiagonal matrix elements of H_r can be neglected the exact equation reduces to

$$(f|[H_r, X]|i) \cong [(f|H_r|f)-(i|H_r|i)](f|X|i). \quad (14)$$

The remarks in the discussion of Eq. (11) on the relative magnitude of diagonal and nondiagonal energy matrix elements, the possibility of destructive interference among the neglected terms, and a possible smoothing effect produced by averaging over a range of N, Z values all apply here in support of Eq. (14) as a useful approximation. An additional argument follows.

The terms neglected in the derivation of Eq. (14) have the form of Eq. (12) with H_r replacing H_c and require discussion only for values of f' and i' such that $(f'|X|i)$ and $(f|X|i')$ are not extremely small compared to $(f|X|i)$. Paraphrasing an earlier remark, this condition fixes f' to the extent that it enters the problem only when $\psi_{f'}$ contains a substantial component derived from configurations each differing in just one orbital from corresponding configurations in ψ_i (a similar remark applies to $\psi_{i'}$ and ψ_f). These restrictions on f' and i' hold equally well for the matrix elements of X occurring in Eq. (10).

When ψ_f is restricted as above, one can argue on physical grounds that $(f'|H_r|f)$ must be small. The argument is based on the success of shell model considerations in ordering and correlating a wide range of nuclear properties. This fact can be understood if nondiagonal matrix elements of the specifically nuclear interaction are small between states derived from configurations differing in only a few orbitals.[8] Otherwise the irregular, but strong, incidence of configuration interaction would be expected to result in many anomalous nuclear properties: anomalous, that is, from the point of view of a logically coherent shell model.

The semi-empirical energy formula contains Coulomb and symmetry terms in the form[9]

$$\tfrac{3}{5}Z(Z-1)e^2/R+u_\tau(N-Z)^2/A -(\delta/4A)\{(-1)^N+(-1)^Z\} \quad (15)$$

producing a parabolic variation of energy with $N-Z$ along an isobaric series. At the bottom of the parabola

$$\begin{aligned}\tfrac{3}{5}(e^2/R)\{Z(Z-1)-(Z-1)(Z-2)\} &= (6/5)(e^2/R)(Z-1)\\ &\cong (u_\tau/A)\{(N-Z+2)^2-(N-Z)^2\}. \quad (16)\end{aligned}$$

It is found in the treatment of the nucleus as a degenerate gas of free particles that very little of the δ-term and about 40 percent of the term in $(N-Z)^2$ comes from the kinetic energy. Accepting this result we obtain

$$\begin{aligned}(f|H_r|f)-(i|H_r|i) &\cong -0.6(u_\tau/A)\{(N-Z+2)^2-(N-Z)^2\}\\ &\quad -(\delta/2A)\{(-1)^N+(-1)^Z\}\\ &\cong -0.72(e^2/R)(Z-1)\\ &\quad -(\delta/2A)\{(-1)^N+(-1)^Z\}. \quad (17)\end{aligned}$$

Equation (7) now becomes

$$\begin{aligned}[W_i-W_f+0.48(e^2/R)(Z-1)\\ -(\delta/2A)\{(-1)^N+(-1)^Z\}](f|X|i)\\ \cong -(f|H_0X-XH_0|i). \quad (18)\end{aligned}$$

The presence of δ in Eq. (18) suggests a difference in the relation between the coordinate and momentum type matrix elements for odd and even values of A. However, the δ term simply cancels out the contribution to the energy difference from the spacing of the odd-odd and even-even parabola's and thus tends to make the general relation expressed by Eq. (18) independent of whether A is odd or even and, in the latter case, independent of whether the product nucleus is odd-odd or even-even.

Results from Eqs. (8) and (18) are summarized in the relations

$$\begin{aligned}\tfrac{1}{2}\Lambda\alpha Z\int \mathbf{r}/R &= -i\int \boldsymbol{\alpha}\\ \tfrac{1}{2}\Lambda\alpha Z\int \boldsymbol{\sigma}\cdot\mathbf{r}/R &= -i\int \gamma_5 \quad (19)\\ \tfrac{1}{2}\Lambda\alpha Z\int \boldsymbol{\sigma}\times\mathbf{r}/R &= -\int \beta\boldsymbol{\alpha},\end{aligned}$$

in which, for odd A,

$$\Lambda = 1+\frac{W_i-W_f}{mc^2}\frac{A^{\frac{1}{3}}}{Z}. \quad (20)$$

For positron emission Z is replaced by $-Z$ in Eqs. (19) and (20). This follows from the anti-Hermitian property of $i\boldsymbol{\alpha}$, $i\gamma_5$, and $\beta\boldsymbol{\alpha}$ and the fact that the roles of ψ_i and ψ_f are interchanged if the direction of the transition is reversed.

To complete the theory for applications one needs also

$$\begin{aligned}W_i-W_f &= W_0-2.5mc^2 \quad \text{(negatron emission)}\\ &= W_0+2.5mc^2 \quad \text{(positron emission)}\\ &= \Delta M+1.5mc^2 \quad (K\text{-capture}). \quad (21)\end{aligned}$$

3. DISCUSSION

In a recent publication,[10] Pursey derives relations similar to those developed in the preceding section. The procedure differs greatly in detail from that

[8] Equation (14) holds accurately for the artificial example of long-range exchange forces. In this example the solutions are eigenfunctions of H_r, all nondiagonal matrix elements of H_r vanish, and configuration interaction is completely absent. As mentioned under Eq. (13), at the opposite extreme of zero range forces $[H_r, X]$ vanishes. In this case Eq. (19) still holds, but Λ is somewhat larger than in Eq. (20).

[9] E. Feenberg, Revs. Modern Phys. **19**, 239 (1947).

[10] D. L. Pursey, Phil. Mag. **42**, 1193 (1951).

followed here since complete reliance is placed on the accuracy of single particle wave functions[11] and on the correctness of an explicit Hamiltonian operator. The assumed form of H_r is a linear combination of short-range two-particle ordinary, charge exchange, and spin-orbit coupling interactions. The contribution to Λ from the matrix element of $(f|[H_r, X]|i)$ is found to be small, in agreement with our conclusion for short-range two-particle interactions stated in the footnote following our Eq. (14). In our notation Pursey's results are equivalent to Eq. (19) with a modified value for Λ,

$$\Lambda \sim 2 + \frac{W_i - W_f}{mc^2} \frac{A^{\frac{1}{3}}}{Z}. \tag{22}$$

Our procedure with neglect of $[H_r, X]$ would yield

$$\Lambda \sim 2.4 + \frac{W_i - W_f}{mc^2} \frac{A^{\frac{1}{3}}}{Z}. \tag{23}$$

At present it is perhaps not possible to distinguish experimentally between Eq. (20) and Eqs. (22)–(23). Eventually, when the correct formulation of beta-decay theory is known down to the last coupling parameter, an experimental test should be possible.

Pursey also obtains a theoretical relation between the matrix elements of $\mathbf{r}$ and $\boldsymbol{\sigma}\times\mathbf{r}$ in the single particle approximation. Since experiment may eventually make possible a test of this relation, we give a simple non-relativistic derivation,

$$[\boldsymbol{\sigma}\cdot\mathbf{L}, \mathbf{r}] = (\hbar/i)\boldsymbol{\sigma}\times\mathbf{r} \tag{24}$$

$$(f|[\boldsymbol{\sigma}\cdot\mathbf{L}, \mathbf{r}]|i) = \hbar\{I_f(I_f+1) - I_i(I_i+1) - L_f(L_f+1) + L_i(L_i+1)\}(f|\mathbf{r}|i); \tag{25}$$

for $I_f = I_i \pm 1$, $L_f = L_i \pm 1$

$$2(I_f - L_f)(f|\mathbf{r}|i) = \mp i(f|\boldsymbol{\sigma}\times\mathbf{r}|i). \tag{26}$$

The symmetry between $\mathbf{r}$ and $\mathbf{p}$ in the definition of $\mathbf{L}$ ensures that the same analysis goes through with $\mathbf{r}$ replaced by $\mathbf{p}$ in Eqs. (24)–(26).

APPENDIX A. ESTIMATES OF THE COULOMB AND COORDINATE MATRIX ELEMENTS

We compute the coordinate and Coulomb matrix elements in the approximation of single particle orbitals. These orbitals are combined to form antisymmetrical wave functions

$$\begin{aligned}\psi_i &= (A!)^{-\frac{1}{2}}\textstyle\sum_r (-1)^{n_r} P_r u_1(1)u_2(2)\cdots u_A(A),\\ \psi_f &= (A!)^{-\frac{1}{2}}\textstyle\sum_r (-1)^{n_r} P_r v(1)u_2(2)\cdots u_A(A).\end{aligned} \tag{A1}$$

The orbitals u_k are functions of space, spin, and charge coordinates of a single nucleon. In evaluating the matrix elements we use the notation: ω_n—space and spin component of u_1; ω_p—space and spin component of v; $(1|\rho_n|2)$—neutron density matrix derived from ψ_i; the indices 1 and 2 refer to both spin and space coordinates. Also $(1|\rho_p|2)$—as above for protons; $\rho_n(\mathbf{r})$—total initial neutron density; $\rho_p(\mathbf{r})$—total initial proton density.

The general formula

$$\int\cdots\int \psi_f^*\psi_i d\tau_{34\cdots A} = \frac{1}{A(A-1)}\sum_{k=1}^{A}\{v(1)u_k(2) - v(2)u_k(1)\}^* \cdot\{u_1(1)u_k(2) - u_1(2)u_k(1)\}, \tag{A2}$$

now yields

$$\begin{aligned}A(A-1)\int\cdots\int \psi_f^* Q_1 \psi_i d\tau_{34\cdots A} &= \omega_p^*(1)\omega_n(1)(\rho_p(2)+\rho_n(2))\\ &\quad - \omega_p^*(1)\omega_n(2)(2|\rho_n|1)\\ &\quad - \tfrac{1}{2}\omega_p^*(2)\omega_n(1)(1|\rho_p|2),\end{aligned} \tag{A3}$$

$$A(A-1)\int\cdots\int \psi_f^* \tfrac{1}{2}(1-\tau_{2z}) Q_1 \psi_i d\tau_{34\cdots A} = \omega_p^*(1)\omega_n(1)\rho_p(2) - \omega_p^*(2)\omega_n(1)(1|\rho_p|2). \tag{A4}$$

Here the integration symbols in Eqs. (A3) and (A4) include a summation over the charge variables of particles 1 and 2.

In the single particle approximation the transition may be described as the transfer of a nucleon from an occupied neutron orbital u_1 to a vacant proton orbital v. This implies

$$\begin{aligned}\textstyle\sum_{m_2}\int\int\int \omega_n(2)(2|\rho_n|1)d\tau_2 &= \omega_n(1)\\ \textstyle\sum_{m_2}\int\int\int \omega_p^*(2)(1|\rho_p|2)d\tau_2 &= 0.\end{aligned} \tag{A5}$$

With the aid of Eqs. (A3) and (A5) the coordinate matrix element $(f|X|i)$ reduces to a simple integral

$$(f|\textstyle\sum X_k Q_k|i) = A(f|X_1 Q_1|i) = \sum_{m_1}\int\int\int \omega_p^*(1) X_1 \omega_n(1) d\tau_1. \tag{A6}$$

In Eq. (A4) the second term of the right-hand member is generally unimportant, particularly so when no destructive interference occurs in the first term. Consequently, we drop the second term and also, for simplicity, treat ρ_p as a constant in evaluating the

[11] Note that this involves much more than the general semi-quantitative validity of the spin-orbit shell model.

Coulomb integral. The result is

$$(f|[H_c, X]|i)=\left(f\left|\frac{e^2}{2}\sum_{l\neq k}\frac{X_l}{r_{lk}}(1-\tau_{lk})Q_l\right|i\right)=\left(f\left|A(A-1)\frac{X_1e^2}{r_{12}}\frac{1}{2}(1-\tau_{12})Q_1\right|i\right)$$

$$=\frac{3(Z-1)e^2}{4\pi R^3}\sum_{m_1}\int\cdots\int\frac{\omega_p^*(1)X_1\omega_n(1)}{r_{12}}dv_1dv_2=\frac{3(Z-1)e^2}{2R^3}\sum_{m_1}\int\int\int\int\omega_p^*(1)X_1\omega_n(1)(R^2-\tfrac{1}{5}r_1^2)dv_1. \quad \text{(A7)}$$

If now $(f|X|i)$ is comparatively large, $R^2-\frac{1}{5}r_1^2$ may be replaced safely by an approximate average value, $R^2-(1/5)R^2=(4/5)R^2$; Eq. (A7) then reduces to

$$(f|[H_c, X]|i)\cong\{6e^2(Z-1)/5R\}(f|X|i) \quad \text{(A8)}$$

in agreement with Eqs. (11) and (13).

PHYSICAL REVIEW VOLUME 86, NUMBER 1 APRIL 1, 1952

Nonlinear Meson Theory for Heavy Nuclei*

BERTRAM J. MALENKA
Department of Physics, Harvard University, Cambridge, Massachusetts

(Received December 26, 1951)

A potential well somewhat between a three-dimensional isotropic oscillator and a square well is determined by using a nonlinear meson theory for heavy nuclei in their ground states. The introduction of a phenomenological spin-orbit coupling is shown to group the energy levels obtained according to the magic numbers. Finally, it is shown that the existence of nuclear shell structure seems to imply a modification in the concept of constant nuclear density for heavy nuclei.

1. INTRODUCTION

THE failure of existing two-body interactions to account adequately for nuclear saturation and the apparent incompatibility of the observed relatively strong, short-range, two-body interaction between nucleons with the independent particle model of the nucleus, strongly suggest the possibility of many-body forces among nucleons. A detailed investigation of many-body interactions would be somewhat complicated for an exploratory calculation. However, an alternative and much simpler procedure suggests itself in the possibility of interpreting the independent particle model for a heavy nucleus in its ground state in terms of a phenomenological nonlinear meson theory.

In this paper, a sort of classical effective meson field will be determined for a heavy nucleus from a phenomenological nonlinear wave equation. In conjunction with this investigation, we will also discuss the compatibility of nuclear shells with some of our other concepts of nuclear structure.

2. AN EFFECTIVE MESON FIELD FOR A HEAVY NUCLEUS

We assume that an effective meson field for a heavy nucleus in its ground state can be characterized by a static nonlinear wave equation for a classical neutral scalar field with a time independent nucleon source density. As suggested in a previous note,[1] we assume the static wave equation to be

$$-\nabla^2\phi+\mu^2\phi+g^4(\hbar c)^{-3}\lambda\phi^3=g\rho, \quad (2.1)$$

where ρ is the nucleon density, μ the inverse meson Compton wavelength (1.4×10^{-13} cm for the π-meson) and g and λ are constants which are to be determined. Equation (2.1) is essentially the same form as that independently investigated by Schiff.[2] However, we solve this equation solely from the point of view of determining an effective meson field compatible with the independent particle model of the nucleus. As noted by Schiff,[3] the total energy associated with the meson field is

$$H=\int[\tfrac{1}{2}(\nabla\phi)^2+\tfrac{1}{2}\mu^2\phi^2+\tfrac{1}{4}g^4(\hbar c)^{-3}\lambda\phi^4-g\rho\phi]d\tau, \quad (2.2)$$

so that from Eq. (2.1)

$$H=\int[-\tfrac{1}{4}g^4(\hbar c)^{-3}\lambda\phi^4-\tfrac{1}{2}g\rho\phi]d\tau. \quad (2.3)$$

* Based on part of a thesis presented in partial fulfillment of the requirements for the degree of Doctor of Philosophy at Harvard University, November, 1951.

[1] B. J. Malenka, Phys. Rev. **85**, 686 (1952). While we make use of the form of the wave equation that was calculated in this note, we do not wish to imply that the nonlinear meson theory considered in the present paper is a consequence of vacuum polarization.

[2] L. I. Schiff, Phys. Rev. **84**, 1 (1951).

[3] See reference 2, Eqs. (12) and (14).

We also note that the proper potential energy of a nucleon in the meson field is

$$V=-g\phi. \tag{2.4}$$

The other terms in Eq. (2.2) represent the energy associated directly with the effective meson field. This identification of energy terms is quite analogous to the classical electric field, where $-g\phi$ is the potential energy of a particle of charge g in the electric field and the remaining $\frac{1}{2}(\nabla\phi)^2$ term corresponds to the volume energy associated with the field.[4] Neglecting Coulomb effects, we wish to show that the previous relations can be used to determine an independent particle potential well for neutrons or protons in a heavy nucleus.

We want to determine the effective meson field $\phi(r)$ as a function of the radial distance r from the center of a spherically symmetric heavy nucleus whose radius we take as $R=r_0A^{\frac{1}{3}}$, where, for the present, r_0 is regarded as an unspecified parameter. In accordance with our ideas, we assume that $\phi(r)$ varies quite slowly in the interior of the nucleus and that the relatively larger changes occur near the nuclear surface. Since the nuclear density appears to be roughly constant for heavy nuclei,[5] we also assume that the effective nucleon source density of Eq. (2.1) has the form

$$\begin{aligned} &\rho=\rho_0=A/(4\pi R^3/3)=(4\pi r_0^3/3)^{-1}, \quad r<R; \\ &\rho=0, \qquad\qquad\qquad\qquad\quad r>R. \end{aligned} \tag{2.5}$$

If as a first approximation ϕ_0 to $\phi(r)$ inside the nucleus, we entirely neglect the spatial variation of the meson field, then Eq. (2.1) gives

$$\mu^2\phi_0+g^4(\hbar c)^{-3}\lambda\phi_0^3=g\rho_0, \tag{2.6}$$

and if we also tentatively assume

$$\mu^2\phi_0\ll g^4(\hbar c)^{-3}\lambda\phi_0^3, \tag{2.7}$$

it follows that

$$\phi_0=\phi(0)\approx(\hbar c/g)(\rho_0/\lambda)^{\frac{1}{3}}. \tag{2.8}$$

From Eq. (2.3), it then follows that to this approximation, the effective potential energy per nucleon caused by the meson field and the nucleons is

$$H_0/A=-\tfrac{3}{4}\hbar c(\rho_0/\lambda)^{\frac{1}{3}}=-\tfrac{3}{4}\hbar c[3/(4\pi\lambda)]^{\frac{1}{3}}(1/r_0). \tag{2.9}$$

To obtain the kinetic energy of a nucleon, we use the simple Fermi-Thomas statistical model of the nucleus which gives us[6]

$$T/A=\tfrac{3}{5}[(9\pi)^{\frac{1}{3}}/8]\lambda_M^2Mc^2(1/r_0^2), \tag{2.10}$$

where λ_M is the nucleon Compton wavelength.

The value of the nuclear radius and hence of the parameter r_0 should be such that the nuclear configuration is most stable. This will be the case when the binding energy per nucleon,

$$\epsilon=-(T/A)-(H_0/A), \tag{2.11}$$

is a maximum, that is when

$$d\epsilon/dr_0=0. \tag{2.12}$$

Carrying out the differentiation, it is evident that for Eqs. (2.9) and (2.10), we obtain

$$|H_0/A|=2|T/A|, \tag{2.13}$$

so that to the approximation considered here

$$\epsilon=|T/A|. \tag{2.14}$$

We note that ϵ is a positive constant, so that the result of an effective meson field that is roughly proportional to the cube root of the nuclear density is consistent with nuclear saturation.[7] From Eq. (2.13), we can determine r_0 in terms of the constant λ and conversely the constant λ in terms of the relatively well-known value of r_0. In particular, if we take $r_0=1.5\times10^{-13}$ cm,[8] we obtain $\lambda\approx13.6$, and from Eq. (2.14), we obtain $\epsilon\approx12.6$ Mev which is about 90 percent of the volume term of 14 Mev in the empirical binding energy formula.[8]

To account for the finite size of the nucleus in determining the effective meson field, we first write Eq. (2.1) in the appropriate one-dimensional form for the spherically symmetric $\phi(r)$. In units where $\hbar=c=1$, we have

$$-d^2\phi/dr^2-(2/r)d\phi/dr+\mu^2\phi+g^4\lambda\phi^3=g\rho. \tag{2.15}$$

While we can neglect the derivatives of $\phi(r)$ in the interior of a heavy nucleus, we certainly cannot do so in the vicinity of the nuclear surface. However, in this region, we can expect the $(2/r)d\phi/dr$ term to be small compared to $d^2\phi/dr^2$, since the extent of the neighborhood of the nuclear surface in which $\phi(r)$ changes appreciably would be rather small compared to the radius of a heavy nucleus. We can then replace Eq. (2.15) by

$$-d^2\phi/dr^2+\mu^2\phi+g^4\lambda\phi^3=g\rho, \tag{2.16}$$

where for consistency, we must now require

$$d\phi/dr=0 \text{ when } r=0. \tag{2.17}$$

If we multiply Eq. (2.16) by $d\phi/dr$ and integrate, requiring that ϕ and $d\phi/dr$ vanish as r goes to infinity, we readily obtain

$$r-R=-\int_{\phi(R)}^{\phi(r)}\frac{d\phi}{[\mu^2\phi^2+\frac{1}{2}g^4\lambda\phi^4-2g\rho(\phi-\phi(R))]^{\frac{1}{2}}}. \tag{2.18}$$

[4] We may also understand Eq. (2.4) from a quantum-mechanical point of view, if we write $\rho=\sum_A\psi_A^\dagger\psi_A$ where ψ_A is the wave function for the Ath nucleon. Then a variation of the total Lagrangian with respect to $\psi_A^\dagger$ only adds the term $V\psi_A=-g\phi\psi_A$ to the Schrödinger equation for a free nucleon.

[5] H. A. Bethe, *Elementary Nuclear Theory* (John Wiley and Sons, Inc., New York, 1947), p. 8.

[6] L. Rosenfeld, *Nuclear Forces* (Interscience Publishers Inc., New York, 1948), p. 193.

[7] We might note, as Schiff also does in reference 2, that in any similar nonlinear meson theory where ϕ^{2n-1} is proportional to ρ, the binding energy will be positive as long as $n>5/2$.

[8] E. Fermi, *Nuclear Physics* (University of Chicago Press, Chicago, 1950), p. 7. The empirical volume energy term is $a_1=0.01507$ mu $=14.03$ Mev.

From (2.7), (2.8), and (2.17), it can be shown that $\phi(R)\approx\frac{3}{4}\phi_0$, so that for $r<R$, we can then substitute $\phi(r)=\phi_0-\psi(r)$ in Eq. (2.18) and neglect terms higher than quadratic in $\psi(r)=\phi_0-\phi(r)$. Integrating Eq. (2.18), we then find

$$\phi(r)\approx\phi_0(1-\tfrac{1}{4}\exp[(3g^4\lambda\phi_0^2/\mu^2)^{\frac{1}{2}}\mu(r-R)]),\quad r<R. \quad (2.19)$$

On the other hand, for $r>R$, $\rho=0$ and (2.18) can be integrated directly. Making use of (2.7) and $\phi(R)\approx\frac{3}{4}\phi_0$, we then obtain

$$\phi(r)\approx\tfrac{3}{4}\phi_0\frac{e^{-\mu(r-R)}}{1+\frac{3}{4}(\frac{1}{2}g^4\lambda\phi_0^2/\mu^2)^{\frac{1}{2}}e^{-\mu(r-R)}\sinh\mu(r-R)},$$

$$r>R. \quad (2.20)$$

Actually (2.20) is too complicated to warrant being treated analytically in an approximate calculation of the type considered here. For the subsequent numerical calculation, we therefore replace (2.20) by

$$\phi(r)=\tfrac{3}{4}\phi_0e^{-\alpha\mu(r-R)}, \quad (2.21)$$

where the constant α is adjusted so that Eqs. (2.20) and (2.21) are equal at the characteristic range of nuclear forces $r-R=1/\mu$. A subsequent graphical analysis of the potential wells formed by (2.20) and (2.21) shows no significant difference in shape for the values used in this paper (see Fig. 1).

If we again calculate the binding energy using $\phi(r)$ in Eq. (2.3), we can determine g by comparing the surface potential energy with the difference between the empirical surface energy and surface kinetic energy.[9] With $\lambda=13.6$, we find that $g^2/\hbar c=40.0$. This corresponds to $(g^4\lambda\phi_0^3)/(\mu^2\phi_0)=32.0$, so that the tentative assumption made in (2.7) is justifiable.

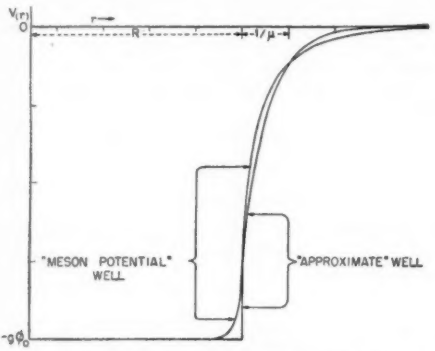

FIG. 1. A comparison of the "approximate" well of Eqs. (3.1) and (3.2) with the "nonlinear meson theory potential" well calculated from Eqs. (2.19) and (2.20) for $R=r_0(200)^{\frac{1}{3}}=8.77\times10^{-13}$ cm, $g\phi_0=34.1$ Mev, and $\alpha=1.83$.

[9] We used the results of E. Feenberg, Phys. Rev. **60**, 204 (1941) to approximate the value of the surface kinetic energy.

3. ENERGY LEVELS AND SHELL STRUCTURE

From Eqs. (2.4), (2.19), and (2.21), we can say that a nucleon moves in an effective potential well

$$V(r)\approx-g\phi_0, \qquad r<R \quad (3.1)$$

$$V(r)\approx=\tfrac{3}{4}g\phi_0e^{-\alpha\mu(r-R)}, \quad r>R \quad (3.2)$$

where we will use the calculated values $g\phi_0=34.1$ Mev and $\alpha=1.83$. In writing Eq. (3.1), we have neglected the exponential term of Eq. (2.19), since this term drops off quite rapidly for $r<R$, the calculated value of the coefficient of $\mu(r-R)$ being 9.8. It will be noted from Fig. 1 that Eqs. (3.1) and (3.2) describe a potential well whose shape is somewhat between a square well and an isotropic oscillator well. The energy levels of neutrons or protons in this well are determined by solving the usual Schrödinger problem for bound states. To be specific, we will assume a heavy nucleus of $A\approx200$.

The solution of the Schrödinger equation for $r<R$ is the well-known solution[10] for a three-dimensional square well of finite depth, namely the spherical Bessel function

$$j_l[(W-\epsilon)^{\frac{1}{2}}r], \quad r<R, \quad (3.3)$$

where l is the orbital momentum quantum number and $W=(2M/\hbar^2)g\phi_0$ so that ϵ is the binding energy of a nucleon in the well in units of $\hbar^2/(2M)$. To solve the Schrödinger equation for $r>R$, we note that any nucleons that spend part of their time outside the nucleus can be expected to be largely confined to a region within a distance of the order of the range of nuclear forces, i.e., $1/\mu$, from the nuclear surface. For a heavy nucleus, r changes comparatively little in this region, so that after making the usual $[u(r)]/r$ substitution in the Schrödinger equation for $r>R$, we can replace $l(l+1)/r^2$ by the constant $l(l+1)/R^2$ and solve for $u(r)$. The solution of the Schrödinger equation for $r>R$ is then found to be approximately

$$(1/r)J_{n(\epsilon,l)}(z), \quad r>R, \quad (3.4)$$

where $J_{n(\epsilon,l)}(z)$, is a Bessel function of the first kind and

$$z=[(3RW^2)^{\frac{1}{2}}(\alpha\mu R)]\exp[-\tfrac{1}{2}\alpha\mu(r-R)], \quad (3.5)$$

$$n(\epsilon,l)=[2/(\alpha\mu R)][l(l+1)+\epsilon R^2]^{\frac{1}{2}}. \quad (3.6)$$

The order of the Bessel function is in general not rational, and hence it is too complicated for numerical computation. However, to determine the energy levels and normalization constants, we need only make use of the value of $J_{n(\epsilon,l)}(z)$ at $r=R$. Here we can use the asymptotic form of the Bessel function to simplify the numerical calculations, since WR^2 is larger than, or at least of the order of, $l(l+1)+\epsilon R^2$.

The energy levels are obtained from the requirement that the logarithmic derivative of the wave function be continuous at $r=R$. These levels are shown on the

[10] L. I. Schiff, *Quantum Mechanics* (McGraw-Hill Book Company, Inc., New York, 1949), p. 76.

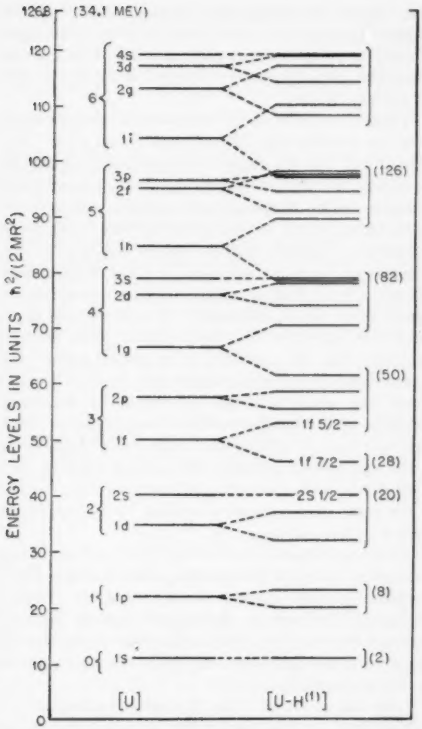

FIG. 2. The splitting of the energy levels of the "approximate" well of Eqs. (3.1) and (3.2) because of the phenomenological spin-orbit coupling $H^{(1)}$. The brackets at the left indicate the levels that are degenerate in the oscillator potential. The numbers at the right are the magic numbers which correspond to the number of neutrons or protons that completely fill all the preceding levels.

left-hand side of Fig. 2, where we have measured the energy $U=WR^2-\epsilon R^2$ in dimensionless units from the bottom of the well. We note that the order of the levels is the same as that originally assumed by Mayer[11] and Haxel *et al.*[12] in their papers on nuclear shell structure. In particular, we note that the critical $1f$, $1g$, $1h$, and $1i$ levels are well separated from their degenerate (in the oscillator potential) neighbors.

To show that the spacing of these levels is such that they can be split according to Mayer's ideas, we assume a phenomenological spin-orbit coupling energy.

$$H^{(1)}=-\beta(\mathbf{L}\cdot\mathbf{S}), \tag{3.7}$$

where $|S_z|=\frac{1}{2}$ and β is a positive constant. We treat $H^{(1)}$ as a simple perturbation energy which is to be added to the energy levels on the left-hand side of Fig. 2. To determine β, we note that the shell corresponding to the magic number 28 apparently consists of a distinct $1f_{7/2}$ level.[11] It then seems reasonable to suppose that this level lies roughly half-way between the $1f_{\frac{1}{2}}$ level above and the $2s_{\frac{1}{2}}$ level below. With this requirement, we obtain $\beta=2$ (i.e., approximately 0.54 Mev) to the nearest integer in the units of Fig. 2. If we now use Eq. (3.7) with $\beta=2$ to calculate the doublet j-splitting, the resulting levels group according to the magic numbers as shown on the right-hand side of Fig. 2. We then see Eqs. (3.1) and (3.2) furnish an example of a potential well that consistently satisfies Mayer's requirements.

4. SHELL STRUCTURE AND NUCLEAR DENSITY

For simplicity and to check the consistency of our original approximation of a constant nuclear density inside the nucleus, let us now neglect the effect of spin-orbit coupling and confine ourselves to the level order obtained for the "approximate nonlinear meson" well described by Eqs. (3.1) and (3.2). The neutron or proton density for completely filled levels is

$$\rho(r)=\textstyle\sum_{\epsilon,l} 2(2l+1)\,|\psi_{\epsilon,l}(r)|^2, \tag{4.1}$$

where $\psi_{\epsilon,l}(r)$ is the wave function of a neutron or proton obtained by properly normalizing (3.3) and (3.4). The weighting factor $2(2l+1)$ is the result of spin and orbital degeneracy. The summation extends up to and including the final level.

In Fig. 3, we have plotted the density $\rho(x)$, where $x=r/R$, in units of the nuclear radius for completely filled levels up to and including $1h$, $2f$, $3p$, and $1i$ levels corresponding respectively to 92, 106, 112, and 138 neutrons or protons in the nucleus. These values are in rough accord with our choice of $A\approx 200$, since the number of neutrons and protons are approximately equal in stable heavy nuclei. From Fig. 3, we then see that $\rho(x)$ is consistent with our original approximation to the extent that it is roughly constant up to a fraction b of the nuclear radius, where approximately $\frac{3}{4}<b<\frac{3}{4}$, but beyond b it decreases continuously to a value of nearly zero at the nuclear surface. For purposes of comparison, we have also plotted $\rho(x)$ using the normalized wave function for a square well potential

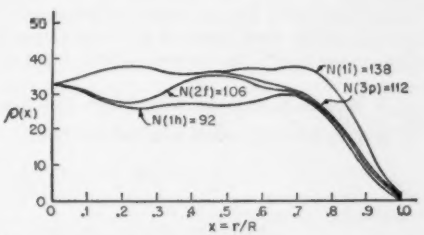

FIG. 3. The neutron or proton density as computed with the wave functions for the "approximate" well according to Eq. (4.1).

[11] M. G. Mayer, Phys. Rev. **78**, 16 (1950).
[12] Haxel, Jensen, and Suess, Z. Physik **128**, 295 (1950).

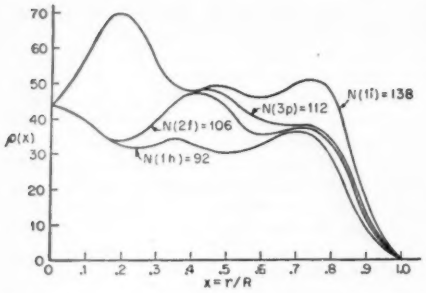

FIG. 4. The neutron or proton density as computed with the wave functions for a potential well with infinite walls according to [Eq. (4.1)].

with infinite walls[13] in Fig. 4. For this potential well, $\rho(x)$ differs noticeably from a constant value in the interior of the nucleus, although a similar "drop off" is indicated for b around $\frac{3}{4}$.

In conjunction with the result obtained in Fig. 3, it is of interest to note that a paper by Yang[14] has appeared, in which correlations between nuclear shell structure and nuclear density are analyzed on the basis of a Thomas-Fermi statistical model of the nucleus. We have essentially repeated his calculations for simple density distributions that resemble Fig. 3. First, for a constant and then linearly decreasing density

$$\begin{aligned} &\rho=\rho_0, && x<b' \\ &\rho=\rho_0[1/(1-b')][1-x], && b'<x<1 \\ &\rho=0, && x>1, \end{aligned} \tag{4.2}$$

where we obtained $b'=0.616$. Secondly, for a constant and then a Gaussian decreasing density (Yang's choice)

$$\begin{aligned} &\rho=\rho_0, && x<b'' \\ &\rho=\rho_0 \exp[-(x-b'')^2/(1-b'')^2], && x>b'' \end{aligned} \tag{4.3}$$

where we obtained $b''=0.691$. These results are in rough quantitative agreement with Fig. 3.

5. DISCUSSION OF RESULTS

It has been shown that a classical nonlinear meson theory will exhibit results that are to a large extent in qualitative and quantitative agreement with our present ideas about an independent particle model of the nucleus. This is to be anticipated to some extent (particularly, in reference to nuclear saturation) in a theory where the potential energy changes more slowly than the nuclear density.

In regard to the model of the potential well obtained, it will be recalled that Mayer[11] and Haxel *et al.*[12] have pointed out that the magic numbers can be explained by adding the doublet j-splitting effect of a relatively strong spin-orbit coupling to the order of energy levels for an independent particle potential well whose shape is somewhat between that of a square well and a three-dimensional isotropic oscillator. It is therefore of some interest to note that an example of such a well was obtained from the consideration of a nonlinear meson theory for heavy nuclei in their ground states, and particularly, that the addition of a rather simple phenomenological spin-orbit coupling was shown to actually group the levels obtained according to the magic numbers. In conjunction with the well shape, we might also note that it represents a reasonable modification of the square well potential for a heavy nucleus, since it effectively adds a potential tail that extends a distance of the order of the range of nuclear forces beyond the surface of the nucleus.

Of course, it remains to further check the consistency and refine the model by repeating the calculations for a modified constant nuclear density, such as exhibited in Fig. 3. However, we note again that the potential energy varies roughly as the cube root of the density, so that not too much of a change in the potential well can be anticipated.

From the point of view of shell structure and the independent particle model, the results of Fig. 3 and Fig. 4 and those of the statistical calculations seem to indicate that our concept of constant nuclear density should be modified to the extent that the nuclear density should begin to decrease somewhere between $\frac{2}{3}$ and $\frac{3}{4}$ of the nuclear radius. In this connection, it should be noted that the comparatively gradual decrease in nuclear density near the nuclear surface is comprehensible from the quantum-mechanical consideration that in order to represent the discontinuous constant particle density distribution of Eq. (2.5), we must be able to extend the sum of Eq. (4.1) over an infinite number of neutron or proton wave functions. This is not possible for a finite nucleus.

The writer would like to express his appreciation to Professor J. Schwinger for his invaluable suggestions and kind encouragement during the course of this work. He is also grateful to Professor V. Weisskopf for his comments.

[12] H. A. Bethe and R. F. Bacher, Revs. Modern Phys. **8**, 82 (1936), Sec. 32(*b*).
[14] L. M. Yang, Proc. Phys. Soc. (London) **64**, 632 (1951).

The Magnetic Moment of K^{40} and the Hyperfine Structure Anomaly of the Potassium Isotopes*

J. T. EISINGER, B. BEDERSON, AND B. T. FELD
Research Laboratory of Electronics and Department of Physics, Massachusetts Institute of Technology, Cambridge, Massachusetts
(Received December 6, 1951)

The nuclear magnetic moment and atomic hyperfine splitting of the rare K^{40} isotope have been measured by the atomic beam magnetic resonance technique. Detection of K^{40} atoms, from a source of normal potassium, was achieved by employing a conventional surface ionization detector as the ion source for a mass spectrometer, and by utilizing an electron multiplier to count the K^{40} ions. By measuring the frequencies of appropriate lines in the Zeeman pattern, the nuclear moment was determined to be $\mu_I = -1.2964 \pm 0.0004$ nuclear magnetons. The hyperfine splitting in the ground state was redetermined, with higher precision than that of previous measurements, to be $\Delta\nu = 1285.790 \pm 0.007$ Mc/sec.

The ratio of the nuclear g factors of K^{39} and K^{40} was measured directly by observing, in the same homogeneous magnetic field, H, the frequencies of two lines (a doublet) in the Zeeman spectrum of each isotope. The doublet separation of these lines is, in each case, proportional to $2g_I\mu_0 H$, so that the ratio of the doublet splittings yielded directly $|g(K^{40})/g(K^{39})| = 1.24346 \pm 0.00024$. From these results and from the previously measured $\Delta\nu(K^{39})$, the hyperfine structure anomaly of these K isotopes is

$$\{[2I(K^{40})+1]g(K^{40})\Delta\nu(K^{39})/[2I(K^{39})+1]g(K^{39})\Delta\nu(K^{40})\}-1 = (0.466 \pm 0.019) \text{ percent.}$$

The theory of the hyperfine structure anomaly, as developed by A. Bohr and V. F. Weisskopf, has been applied to the interpretation of this result. The predictions of a number of specific models, previously suggested to account for the observed nuclear g factors, have been compared with this experiment and with previous results on the anomalies for the Rb and the abundant K isotopes. The "asymmetric core" model of A. Bohr gives the best over-all agreement, mainly on the basis of the $K^{41}-K^{39}$ anomaly. In general, all models which are, in their essential features, based on the independent-particle model with spin-orbit coupling, give predictions in fair qualitative agreement with the experiments. The contribution of K^{40} to the hfs anomaly seems, however, to be (fortuitously) insensitive to the differences between the models investigated.

I. INTRODUCTION

THE interaction of the nuclear magnetic moment with the moment due to the orbital electrons causes the ground state of an atom with electronic angular momentum $J\hbar = \frac{1}{2}\hbar$ to be split into two hyperfine levels characterized by the total angular momentum quantum numbers $F = I \pm \frac{1}{2}$. Fermi and Segrè,[1] assuming the nuclear moment to be a point dipole, calculated the energy separation between these two levels to be

$$h\Delta\nu = \frac{8\pi}{3}\frac{(2I+1)}{I}\mu_I\mu_0^2\frac{m}{M}|\psi(0)|^2, \tag{1}$$

where μ_0 is the Bohr magneton, μ_I is the nuclear magnetic moment in nuclear magnetons (nm), $\psi(0)$ is the normalized electronic wave function at the nucleus, and m/M is the ratio of electron mass to proton mass. If the subscripts 1 and 2 denote two isotopes of the same element, then since $\psi(0)$ will be identical for the two isotopes,[2]

$$\frac{\Delta\nu_1}{\Delta\nu_2} = \frac{(2I_1+1)}{(2I_2+1)}\frac{g_1}{g_2} \tag{2}$$

where $g = \mu_I/I$ is the nuclear g-factor.

Kopferman[3] and Bitter[5] have pointed out that if the finite size of the nucleus is taken into account, $\Delta\nu$ will depend on the spatial distribution of the nuclear magnetic dipole, and the right side of Eq. (1) must be multiplied by a correction factor $1+\epsilon$, where ϵ depends on the magnetic dipole distribution over the nucleus. If this effect is taken into account, Eq. (2) must be replaced by

$$\frac{\Delta\nu_1}{\Delta\nu_2} = \frac{(2I_1+1)}{(2I_2+1)}\frac{g_1}{g_2}(1+\Delta) \tag{3}$$

where $\Delta \cong \epsilon_1 - \epsilon_2$, is a measure of the hfs anomaly and depends on the nuclear structures of isotopes 1 and 2.

Bohr and Weisskopf[4] have shown how the measurement of Δ leads to information about the structures of the nuclei involved. Their theory accounts for the hfs anomaly observed between Rb^{85} and Rb^{87} by Bitter[5] and a similar anomaly for K^{39} and K^{41} reported by Ochs, Logan, and Kusch.[6]

The addition of one neutron to the K^{39} nucleus profoundly affects the static properties of the nucleus; the spin changes from $\frac{3}{2}$ to 4 and the magnetic moment changes from $+0.39$ nm to -1.24 nm. A comparison of the $\Delta\nu$ and g_I values for K^{39} and K^{40} might therefore be expected to reveal a considerable anomaly of the type discussed above. The $\Delta\nu$ of K^{40}, $\Delta\nu$ of K^{39}, and μ_I of K^{39} have previously been measured.[7-9] A direct measurement of $\mu_I(K^{40})$ had, however, never been attempted, owing to the small natural abundance of

* This work has been supported in part by the Signal Corps, Air Materiel Command, and ONR.

[1] E. Fermi and E. G. Segrè, Z. Physik **82**, 729 (1933).

[2] Nuclear mass effects on the hfs are at least an order of magnitude smaller than any of the effects here considered.

[3] H. Kopferman, *Kernmomente* (Akademische Verlagsgesellschaft, M.B.H., Leipzig, 1940), p. 17.

[4] A. Bohr and V. F. Weisskopf, Phys. Rev. **77**, 94 (1950).

[5] F. Bitter, Phys. Rev. **76**, 150 (1949).

[6] Ochs, Logan, and Kusch, Phys. Rev. **78**, 184 (1950).

[7] J. R. Zacharias, Phys. Rev. **61**, 270 (1942); Davis, Nagle, and Zacharias, Phys. Rev. **76**, 1068 (1949).

[8] P. Kusch and H. Taub, Phys. Rev. **75**, 1477 (1949).

[9] T. L. Collins, Phys. Rev. **80**, 103 (1950).

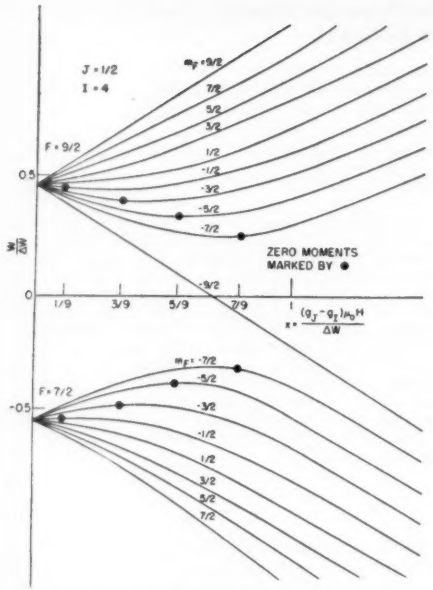

FIG. 1. Energy levels of the K^{40} atom as a function of an external magnetic field.

K^{40} (0.01 percent of ordinary K), which makes the isotope unsuitable for nuclear induction methods. It was therefore decided to measure the ratio $g(K^{40})/g(K^{39})$ by the atomic beam technique. The experiment also includes a direct measurement of $\mu_I(K^{40})$ and a remeasurement of $\Delta\nu(K^{40})$.

II. ENERGY LEVELS

The energy levels $W(F, m_F)$ of an atom with $J=\frac{1}{2}$ in an external magnetic field H are given by the Breit-Rabi formula[10]

$$\frac{1}{h}W(F=I\pm\tfrac{1}{2}, m_F)=-\frac{\Delta\nu}{2(2I+1)}+\frac{g_I\Delta\nu m_F x}{g_J-g_I}\pm\frac{\Delta\nu}{2}\left(1+\frac{4m_F x}{2I+1}+x^2\right)^{\frac{1}{2}}, \quad (4)$$

where $x=[(g_J-g_I)\mu_0 H]/h\Delta\nu$, g_J is the Landé g-factor for the electronic configuration, and g_I is the nuclear Landé g factor.[11] Figure 1 shows the energy levels of a K^{40} atom ($J=\frac{1}{2}$, $I=4$) as a function of an external magnetic field.

The frequencies corresponding to transitions between states $m_F=-5/2$ and $m_F=-7/2$ are readily computed to be

$$\nu_+=\frac{1}{h}\left[W\left(\frac{9}{2},-\frac{5}{2}\right)-W\left(\frac{9}{2},-\frac{7}{2}\right)\right]=\frac{\Delta\nu}{2}\left[\left(1-\frac{10}{9}x+x^2\right)^{\frac{1}{2}}-\left(1-\frac{14}{9}x+x^2\right)^{\frac{1}{2}}\right]+\frac{g_I\Delta\nu x}{g_J-g_I} \quad (5)$$

and

$$\nu_-=\frac{1}{h}\left[W\left(\frac{7}{2},-\frac{5}{2}\right)-W\left(\frac{7}{2},-\frac{7}{2}\right)\right]=\frac{\Delta\nu}{2}\left[\left(1-\frac{10}{9}x+x^2\right)^{\frac{1}{2}}-\left(1-\frac{14}{9}x+x^2\right)^{\frac{1}{2}}\right]-\frac{g_I\Delta\nu x}{g_J-g_I}. \quad (6)$$

Thus, the transitions belonging to $F=I\pm\frac{1}{2}$ are identical except for the last (nuclear) term, which appears with opposite signs in ν_+ and ν_-. The transitions given by Eqs. (5) and (6) therefore constitute a doublet whose separation is

$$\delta\nu=2g_I\Delta\nu x/(g_J-g_I)=2g_I\mu_0 H/h. \quad (7)$$

The $K^{39}(I=\frac{3}{2})$ atom in a magnetic field exhibits a pair of transitions similar to the above, given by

$$\nu_+=\frac{1}{h}[W(2,0)-W(2,-1)]=\frac{\Delta\nu}{2}[(1+x^2)^{\frac{1}{2}}-(1-x+x^2)^{\frac{1}{2}}]+\frac{g_I\Delta\nu x}{g_J-g_I} \quad (5a)$$

and

$$\nu_-=\frac{1}{h}[W(1,0)-W(1,-1)]=\frac{\Delta\nu}{2}[(1+x^2)^{\frac{1}{2}}-(1-x+x^2)^{\frac{1}{2}}]-\frac{g_I\Delta\nu x}{g_J-g_I}. \quad (6a)$$

It is seen from Eq. (7) that if the field is kept constant during the course of a run consisting of measurements of ν_+ and ν_- of both K^{39} and K^{40}, the ratio of the g's can be determined from

$$\delta\nu(K^{40})/\delta\nu(K^{39})=g_I(K^{40})/g_I(K^{39})=g(K^{40})/g(K^{39}). \quad (8)$$

Moreover, if the field at which the transitions characterized by Eqs. (5) and (6) occur is known, the doublet separation will yield the nuclear g-factor of K^{40} directly. The field dependence of these transitions is shown in Figs. 2 and 3.[12]

III. THE OBSERVATION OF TRANSITIONS

The atomic beam apparatus as used in this experiment is a high resolution radiofrequency spectrometer suitable for the observation of the transitions discussed

[10] G. Breit and I. I. Rabi, Phys. Rev. **38**, 2072 (1931).

[11] The nuclear Landé g factor is defined as minus the ratio of the nuclear moment in Bohr magnetons to the nuclear spin, i.e., $g_I=-g(m/M)$.

[12] Note that the constant of proportionality between x and the magnetic field H is different for K^{39} and K^{40}.

in the preceding section. A well-collimated beam of neutral atoms is made to pass through three magnetic fields, the A, C, and B fields, in that order, before being measured by the detection apparatus. The A and B fields have gradients in the same direction which are sufficiently large to produce measurable deflections of atoms whose effective magnetic moments are of the order of 0.1 Bohr magneton. The C field is a homogeneous field on which is superimposed an oscillating perturbing field capable of inducing transitions in the atoms of the beam. If an atom is made to undergo a transition of such a nature that in its new state it has an effective magnetic moment of opposite sign to that which it had in its original state, its deflection in the B field will be opposite to that which it suffered in the A field. Such atoms can be caused to strike the detector and are said to be refocused; the transitions are rendered observable by an increase of the beam intensity at the detector ("flop-in" transitions).

The K^{40} transitions which are of interest in the present experiment occur between the energy levels $(F, -5/2)$ and $(F, -7/2)$. As can be seen from Fig. 1, these energy levels have slopes and therefore effective magnetic moments of the same sign at all fields except between the "zero-moment" fields, for which $x=5/9$ and $x=7/9$.[13] Flop-in transitions can therefore be observed if $x \approx \frac{3}{4}$ for the A and B fields. Alternatively, the deflecting fields can be adjusted to have the value $x=7/9$. K^{40} atoms in the $m_F=-7/2$ state will then not be deflected by the A or B fields. If such an atom is made to undergo a transition to the state $m_F=-5/2$, it will have a finite effective moment in the B field and will be deflected away from the detector ("zero-moment flop-out" transitions).

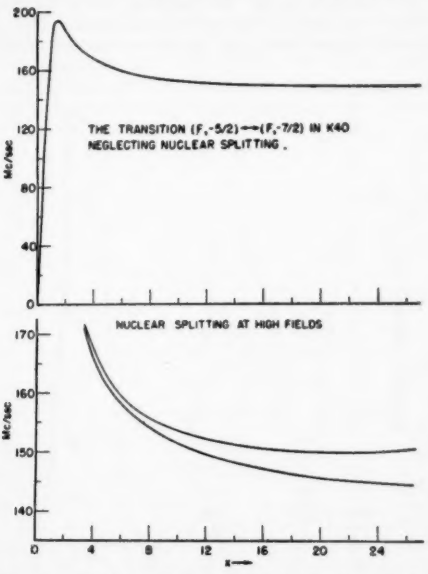

FIG. 2. The field dependence of the K^{40} doublet, the separation of which was measured in order to determine $g(K^{40})$. x is a parameter which is proportional to the external magnetic field.

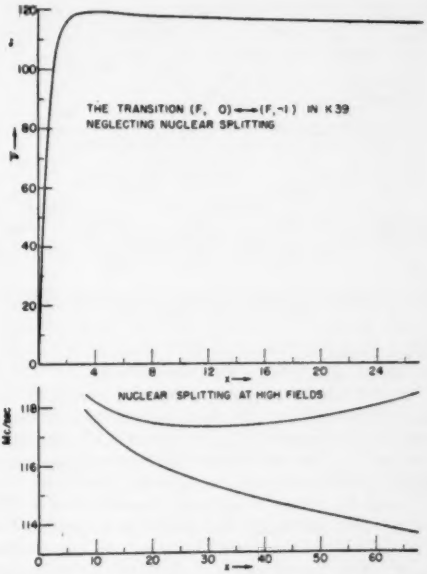

FIG. 3. The field dependence of the K^{39} doublet, the separation of which, when compared to the K^{40} doublet separation, gives $g(K^{40})/g(K^{39})$.

IV. THE APPARATUS

The apparatus[14] on which these experiments were performed has the following characteristics: The vacuum system consists of a brass casting ten feet long and one foot in diameter. The main chamber, which contains the magnets and detection apparatus, is usually at a pressure of 3×10^{-7} mm Hg and is separated from the poorer vacuum of the oven chamber by a partition chamber. The schematic drawing of Fig. 4 indicates the physical arrangement and the pumping system of the apparatus.

The oven for the production of the K beam is $2\frac{1}{2}$ inches high and $\frac{3}{4}$ inch in diameter. It is made of steel and is provided with a slit which is 6 mils wide. A few turns of tungsten wire heat the oven to about 450°C.

[13] It can be readily shown from the Breit-Rabi formula that the effective moment, $\mu_{eff}=-\partial W(F, m_F)/\partial H$ for an atom in the state (F, m_F), vanishes in fields given by $x=-2m_F/(2I+1)$.

[14] This apparatus, including the deflecting magnets and the mass spectrometer, was designed by Dr. Hin Lew while a member of this laboratory.

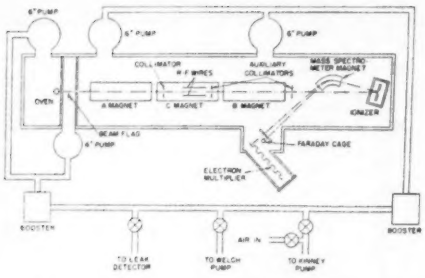

FIG. 4. Schematic diagram to illustrate the atomic beam apparatus used in the present experiment.

When loaded with two grams of K metal, it provided an intense steady beam for about 60 hours.

The A and B magnets, which are essentially the same length (25 and 26 inches, respectively), are single-turn electromagnets; a copper current sheet completely encloses the iron core except for two openings which allow the beam to pass between the pole faces. This construction assures a minimum amount of stray field in the transition region. The gradients are produced in the conventional manner[15] by means of curved pole faces; their magnitudes are given by the expression $|\nabla H| = 1.57H$ gauss cm^{-1}.

The C magnet is 26 inches long, and its gap is $1\frac{1}{2}$ inches high by $\frac{1}{4}$ inch wide. The oscillating field is produced by passing a radiofrequency current through a pair of copper conductors; the beam passes between the conductors. The radiofrequency field so produced is about 15 cm in length. The windings of all magnets are water-cooled and energized by submarine storage batteries.

After passing through the magnets, the K atoms strike a hot tungsten filament and are converted into positive ions at its surface. The ions are accelerated from the filament, which is at a variable positive potential, through a slit held at ground potential and subsequently pass between the pole faces of a 60° mass spectrometer magnet which separates the various isotopes in the ion beam. The intensity of the ion beam corresponding to any particular isotope is then measured by means of a probe connected to the grid of an FP 54-electrometer tube. Very small beam intensities are measured by an electron multiplier[16] connected to a multistage scaler. Figure 5 shows a mass spectrometer curve obtained in the present apparatus. The enrichment factor, defined as the intensity of the K^{39} beam divided by the residual amount of K^{39} beam at the K^{40} position, is about 5×10^{4}. The normal K^{39} beam intensity was of the order of 10^{-10} amp, and the corresponding K^{40} beam gave a count of the order of 600 counts per second.

[15] Rabi, Kellog, and Zacharias, Phys. Rev. **46**, 157 (1934).
[16] H. Lew, Phys. Rev. **76**, 1086 (1949).

The transitions studied in this experiment are only moderately field dependent at high fields (Figs. 2 and 3). As a result, the resonance lines showed no broadening because of inhomogeneities in the C field, and it was possible to achieve resonance curves whose half-widths were equal to the theoretical half-widths as given by the uncertainty principle. For an oven temperature of 800°K, the beam atoms spend an average time of 3×10^{-4} second in the transition region, and the theoretical half-width of a resonance curve is 3 kc/sec. Figure 6 shows a typical resonance curve. The peaks of such curves could be determined to within 1 kc/sec by observing the change in counting rate as the frequency of the oscillating field was varied through the resonance.

The observed frequencies were in the neighborhoods of 115 Mc/sec, 150 Mc/sec, and 190 Mc/sec. Radiofrequency currents of the required stability were produced by mixing an accurately known fixed high frequency (120, 150, and 180 Mc/sec, respectively) with variable low frequencies. The fixed frequencies were obtained by multiplying the signal produced by a 5 Mc/sec crystal which was kept within one cycle per second of the 5 Mc/sec signal transmitted by WWV, so that the accuracy of the fixed frequency was about 2 parts in 10^{7}.

The variable signal was produced by a General Radio 805C signal generator and was measured by a General Radio 620A wave meter. A General Radio

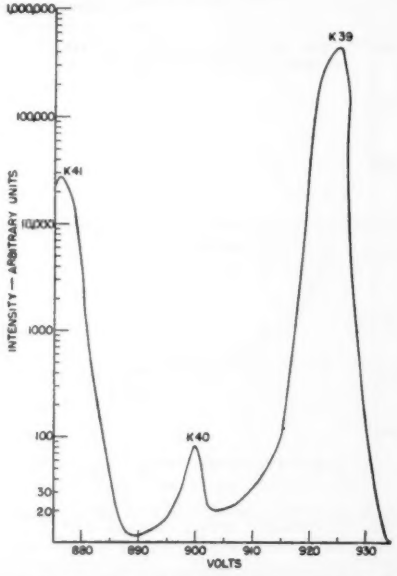

FIG. 5. The curve illustrates the resolution obtained in the mass spectrometer.

724A frequency meter was used to measure frequencies below 2 Mc/sec. Since the tunable frequency was always known to better than 1 kc/sec, this was also the accuracy of the mixed signal. Figure 7 shows a block diagram of the frequency source.

V. EXPERIMENTAL PROCEDURE AND RESULTS

a. The Ratio of the Moments

It was shown in a previous section that the transitions $(9/2, -7/2)\leftrightarrow(9/2, -5/2)$ and $(7/2, -7/2)\leftrightarrow(7/2, -5/2)$ in K^{40} differ in frequency by $2g_I(K^{40})\mu_0 H/h$. Similarly the frequencies of the transitions $(2, -1)\leftrightarrow(2, 0)$ and $(1, -1)\leftrightarrow(1, 0)$ in K^{39} differ by $2g_I(K^{39})\mu_0 H/h$. In order to measure these two doublet separations to sufficiently high precision, the transitions had to be observed at high fields (~9000 gauss) where it was difficult to prevent the C field from drifting during the course of the measurement of the four transitions. The following method of taking data was therefore adopted. The two K^{40} transitions were measured alternately and repeatedly; the time of each observation was recorded. Then the mass spectrometer was retuned, and the two K^{39} transitions were similarly measured. This procedure was repeated several times. The resonance frequencies of the four transitions were then plotted as functions of time and straight lines were drawn through the points belonging to the same transition. All points were less than one kc/sec from the best straight lines, showing that the C field drifted very nearly linearly during the course of a run. The resonance frequencies of all four transitions for particular times, and therefore belonging to the same field, were taken from these curves and are listed in Table I. The average value of $\delta\nu(K^{40})/\delta\nu(K^{39})$ obtained from these data is 1.24350 $\pm$0.00024, where the quoted error is the average deviation from the average of all measurements.

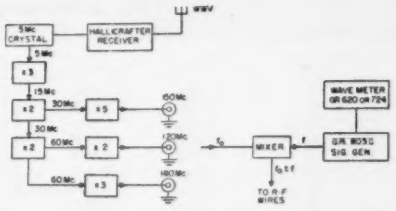

FIG. 7. Block diagram to illustrate the method employed to obtain radiofrequency currents with stable, variable frequencies in the ranges required for the present experiment.

Different A and B fields are required to render the K^{39} and K^{40} transitions observable. It was therefore necessary to determine the effect of stray A and B fields on the C field. This was done by studying a strongly field dependent line $[(2, -2)\leftrightarrow(2, -1)$ in $K^{39}]$ as a function of A and B fields. It was found that the effect on the C field of a change in the deflecting fields, from the values required for K^{39} transition to those used for K^{40} transitions, is only 4 parts in 10^5 at 9000 gauss.

Applying this small correction factor, we obtain $g(K^{40})/g(K^{39}) = -1.24346 \pm 0.00024$.

b. The Measurement of $\mu_I(K^{40})$

The frequencies of the components of the K^{40} doublet corresponding to a particular magnetic field were measured by a method similar to the one mentioned before. From the mean frequency of the doublet, x was calculated by use of the Breit-Rabi formula [Eqs. (5) and (6)]. Knowing x, the doublet separation $\delta\nu(K^{40})$ yields $\mu_I(K^{40})$.

Values of μ_I at different values of H were obtained in this manner. At each field, the C field was allowed to drift for several hours, while the doublet frequencies were repeatedly measured. Figure 8 shows a portion of the data taken during one such run. The values for the moment obtained in the course of each run were averaged to give the values of μ_I quoted in Table II. The weight assigned to each run was determined by the magnitude of x as well as the number of individual measurements made during the run.

The weighted average value for $\mu_I(K^{40})$ is -1.2964 $\pm$0.0004 nm, where the quoted error is the average deviation of the 5 runs. From this, $g(K^{40}) = -0.32410$ $\pm$0.00010. The diamagnetic correction to be applied to potassium is +0.13 percent.[17] Including this correction, $\mu_I(K^{40})$ becomes -1.2982 nm.

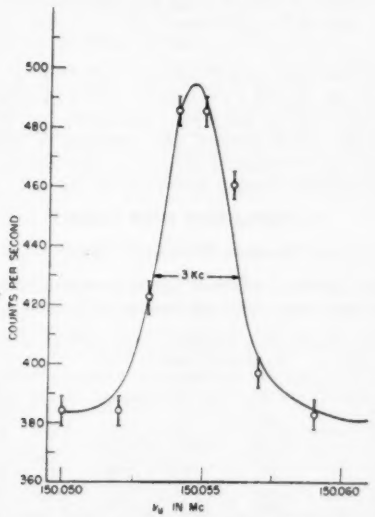

FIG. 6. Resonance curve of the transition $(9/2, -7/2\leftrightarrow 9/2, -5/2)$ in K^{40}. The half-width of the curve is seen to be 3 kc/sec.

[17] W. E. Lamb, Phys. Rev. **60**, 817 (1941).

TABLE I. Data obtained during experiments for measuring $g(K^{40})/g(K^{39})$.

Run	Time	K^{40} ν_+ Mc/sec	K^{40} ν_- Mc/sec	K^{40} $\delta\nu$ Mc/sec	K^{39} δ_+ Mc/sec	K^{39} δ_- Mc/sec	K^{39} $\delta\nu$ Mc/sec	$\frac{\delta\nu(K^{40})}{\delta\nu(K^{39})}$
1	15	150.1530	145.9298	4.2232	117.6686	114.2702	3.3984	1.24270
	20	0.1562	0.9378	4.2184	0.6673	0.2723	3.3950	1.24253
	25	0.1614	0.9450	4.2164	0.6661	0.2745	3.3916	1.24319
	30	0.1654	0.9525	4.2129	0.6648	0.2767	3.3881	1.24344
	35	0.1692	0.9600	4.2092	0.6636	0.2790	3.3846	1.24363
	40	0.1730	0.9677	4.2053	0.6624	0.2811	3.3813	1.24369
	45	0.1763	0.9752	4.2011	0.6611	0.2833	3.3778	1.24374
	50	0.1792	0.9827	4.1965	0.6599	0.2855	3.3744	1.24363
	55	0.1816	0.9900	4.1916	0.6587	0.2877	3.3710	1.24342
2		150.0837	145.7583	4.3254	117.6961	114.2187	3.4774	1.24385
3	15	150.0523	145.6820	4.3703	117.7092	114.1950	3.5142	1.24361
	20	0.0546	0.6875	4.3671	0.7082	0.1967	3.5115	1.24366
	25	0.0567	0.6932	4.3635	0.7072	0.1985	3.5087	1.24362
	30	0.0591	0.6991	4.3600	0.7062	0.2002	3.5060	1.24358
	35	0.0614	0.7054	4.3560	0.7052	0.2021	3.5031	1.24347
	40	0.0639	0.7118	4.3521	0.7042	0.2041	3.5001	1.24342
	45	0.0666	0.7182	4.3484	0.7031	0.2062	3.4969	1.24350
	50	0.0692	0.7242	4.3450	0.7020	0.2083	3.4937	1.24367
	55	0.0719	0.7310	4.3409	0.7007	0.2106	3.4901	1.24377
	60	0.0746	0.7375	4.3371	0.6994	0.2129	3.4865	1.24397
							Average:	1.24350±0.00024

c. The Measurement of $\Delta\nu(K^{40})$

While the measurement of $g(K^{40})/g(K^{39})$ is limited essentially only by the accuracy of the frequency measurement, the value of $\mu_I(K^{40})$, which is obtained by use of the Breit-Rabi formula, depends on g_J and $\Delta\nu$. g_J is known to sufficient accuracy for our purposes (the value used in the present calculations is 2(1.001145)), but the best determination of $\Delta\nu(K^{40})$ to date[7] had an error of 0.050 Mc/sec assigned to it. The resultant uncertainty in μ_I is 0.001 nm, an error greater than the error introduced by the measurement of the two transition frequencies. A redetermination of $\Delta\nu(K^{40})$ was therefore desirable.

The frequencies of both components of the doublet $(F=I\pm\frac{1}{2},\ -7/2)\leftrightarrow(F=I\pm\frac{1}{2},\ -5/2)$ pass through a maximum at $x\approx 1.5$. By observing both these transitions in the neighborhood of this field, the maximum of the mean frequency $\bar{\nu}_{max}$ can be measured. $\bar{\nu}_{max}$ is about 193 Mc/sec. Since $\bar{\nu}=\frac{1}{2}\Delta\nu[(1+x^2)^{\frac{1}{2}}-(1-x+x^2)^{\frac{1}{2}}]$, the value of x corresponding $\bar{\nu}_{max}$ is found by differentiation to be $x_0=1.466037$. $\Delta\nu$ can now be calculated from a knowledge of $\bar{\nu}_{max}$. The percentage error of $\Delta\nu$ is equal to that of $\bar{\nu}_{max}$, which was measured to an accuracy of about 1 part in 200,000. Table III shows the results of two runs of the type described above as well as the results of previous measurements. It is seen that the new value of $\Delta\nu(K^{40})$ overlaps the older results.

d. The Moment of K^{39}

By combining our results for $g(K^{40})/g(K^{39})$ and $\mu_I(K^{40})$, a value of $g(K^{39})$ can be calculated. We obtain $g(K^{39})=0.39097\pm0.00015$ nm. Collins[9] has applied the nuclear induction technique to K^{39}, with a saturated aqueous solution of KNO_2 as a sample. His result is $g(K^{39})/g(H^1)=0.13999\pm0.00002$. With Gardner and Purcell's value for the proton moment,[18] $g(K^{39})=0.391048\pm0.000070$ nm. Our value is in agreement with this result. Since Collins' measurement made no allowance for possible chemical effects on the position of the resonance, we conclude that the chemical corrections are smaller than the experimental uncertainties.

e. The HFS Anomaly

From Eq. (3) the hfs anomaly is given by

$$\Delta=\epsilon(K^{39})-\epsilon(K^{40})=\frac{\Delta\nu(K^{39})}{\Delta\nu(K^{40})}\frac{g(K^{40})}{g(K^{39})}\frac{9}{4}-1.$$

With Kusch and Taub's[8] value for $\Delta\nu(K^{39})$ of 461.723 ±0.010 Mc/sec and the values for $\Delta\nu(K^{40})$ and $g(K^{40})/g(K^{39})$ obtained in the present experiment, we obtain $\Delta=(0.466\pm0.019)$ percent. This experimental value of Δ must now be compared with the Δ's calculated on the basis of different nuclear models for K^{39} and K^{40}.

VI. COMPARISON WITH THEORY

a. The Bohr-Weisskopf Theory[4]

The hyperfine structure anomaly arises from the finite size of the nuclei and from the difference, in the

TABLE II. Results of six runs during which $\mu_I(K^{40})$ was measured at different magnetic fields.

Run	x	$\mu_I(K^{40})$	Weight
1	10.6	−1.2971	2
2	13.8	−1.2964	3
3	18.5	−1.2970	3
4	19.1	−1.2965	3
5	19.3	−1.2957	4
6	19.2	−1.2962	5

[18] J. H. Gardner and E. M. Purcell, Phys. Rev. **76**, 1262 (1949).

two isotopes involved, between the distributions of the nucleon spins and currents which give rise to the nuclear moments. The magnetic hyperfine splitting, resulting from the interaction of the nuclear magnetic moment with the magnetic moment of an S-electron,† is given by the Fermi-Segrè formula, Eq. (1). For a nucleus of finite size, the factor $\mu_I|\psi(0)|^2$ must be averaged over the nuclear volume, and the resulting $\Delta\nu$ depends on the nuclear size, on the nuclear charge, and on the form of the distribution of the magnetic moment in the nucleus.

$$\Delta\nu_{\text{obs}}/\Delta\nu_{\text{pt}}=\langle\mu_I(r)|\psi(r)|^2\rangle_{Av}/\mu_I|\psi(0)|^2=1+\epsilon. \quad (9)$$

In particular, a nuclear moment caused by the intrinsic moments of one or more nucleons will cause a greater anomaly than a moment caused by orbital motion, since the moment arising from a current is strongly concentrated at the center of the nucleus. By a direct computation of the above average, assuming a spherically symmetrical distribution of moments and currents, Bohr and Weisskopf obtained

$$\epsilon=-(\alpha_s+0.62\alpha_L)b(Z,R_0)\langle(R^2/R_0^2)\rangle_{Av}, \quad (10)$$

where α_s and α_L are, respectively, the fractions of the total nuclear magnetic moment as a result of spin and orbit

$$\alpha_s=(g_s/g)[(g-g_L)/(g_s-g_L)], \quad \alpha_L=1-\alpha_s. \quad (11)$$

$b(Z,R_0)$ is a parameter (taken as 0.19 percent for all the K isotopes) tabulated in the paper of Bohr and Weisskopf. Since the value of $|\psi(0)|^2$ cannot, in general, be computed with sufficient accuracy to determine ϵ from measurements on a given isotope, a comparison between experiment and theory can only be obtained from measurements of the ratios of the $\Delta\nu$'s and g_I's for two isotopes of the same element (for which the $|\psi(0)|^2$ are assumed the same), as shown by Eq. (3).

The first set of measurements of the requisite accuracy resulted from the work of Bitter[5] on the Rb isotopes, for which the measurement of the moment ratio, when compared with the previous measurement of the $\Delta\nu$ ratio by Millman and Kusch,[19] showed an anomaly

$$\Delta(\text{Rb})=\epsilon(\text{Rb}^{85})-\epsilon(\text{Rb}^{87})=(0.33\pm0.05)\text{ percent}.$$

Bohr and Weisskopf showed that the computed value of Δ is in satisfactory agreement with the measurements, provided that it is assumed that the nuclear moments result from the odd proton, with $g_s=5.587$ and $g_L=1$; the assumption of $g_L=Z/A$, on the other hand, gives a result in definite disagreement with the experiments.

† Since, for electrons with $L>0$ (p, d, etc.), the electron wave function vanishes at the position of the nucleus, the finite nuclear size and/or distribution of spin and moment in the nucleus has negligible effect on the hyperfine structure. However, due to relativistic effects, the wave function of an electron in a $^2p_{\frac{1}{2}}$ state has, for heavy nuclei, an appreciable $^2s_{\frac{1}{2}}$ component and can, therefore, also give rise to an hfs anomaly.

[19] S. Millman and P. Kusch, Phys. Rev. 58, 438 (1940).

TABLE III. Results of previous and the present measurements of $\Delta\nu(K^{40})$.

		$\Delta\nu(K^{40})$, Mc/sec
Zacharias[a]		1285.7 ±0.1
Davis *et al.*[a]		1285.73±0.05
Present work	Run No. 1	1285.786±0.01
	Run No. 2	1285.794±0.01
	Average	1285.790±0.007

[a] See reference 7.

Another hyperfine structure anomaly measurement was made by Ochs, Logan, and Kusch,[6] who compared the isotopes K^{39} and K^{41} and obtained $\Delta_1(K)=\epsilon(K^{41})-\epsilon(K^{39})=(0.226\pm0.010)$ percent. Assuming, again, the g_s of a free proton, these authors observed that satisfactory agreement with the Bohr-Weisskopf (B–W) theory could only be obtained by assuming $g_L\approx1$. The present experiments give $\Delta_2(K)=\epsilon(K^{39})-\epsilon(K^{40})$.

Although the B–W theory makes no assumption as to the state of the odd proton (or neutron) responsible for the nuclear moment, the result—that $g_L\approx1$ for the odd-proton nuclei investigated—lends support to an independent-particle model. However, the theory makes the assumption that the nucleon responsible for the moment is more or less uniformly (at least symmetrically) distributed throughout the nucleus, which would not be the case for a single-particle orbit. Furthermore,

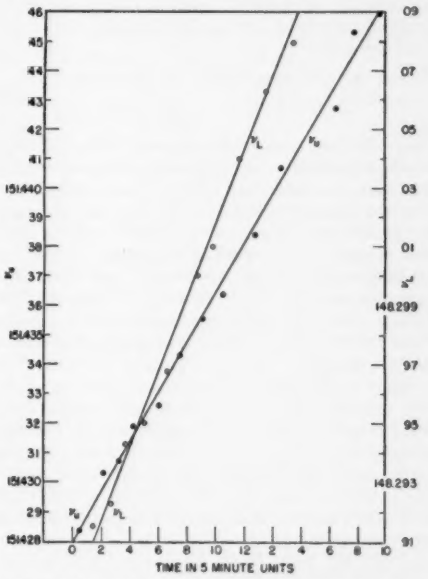

FIG. 8. The graph shows the resonance frequencies of the components of the K^{40} doublet as a function of time while the C field was allowed to drift. The drift of the magnetic field is seen to be nearly linear over a period of two hours.

TABLE IV. Basic data on the spins and moments of the K and Rb isotopes.

Nucleus	I	Odd proton state	Odd neutron state	g(Schmidt)	g(measured)
K^{41}	$\frac{3}{2}$	$d_{\frac{3}{2}}$	···	0.0826	0.14311
K^{39}	$\frac{3}{2}$	$d_{\frac{3}{2}}$	···	0.0826	0.2607
K^{40}	4	$d_{\frac{3}{2}}$	$f_{7/2}$	−0.4209	−0.32412
Rb^{85}	5/2	$f_{5/2}$	···	0.3448	0.5406
Rb^{87}	$\frac{3}{2}$	$p_{\frac{3}{2}}$	···	2.5290	1.8314

the application of the B–W theory to odd-odd nuclei requires at least one further assumption concerning the mechanism of coupling between the neutron and proton spins and their orbital angular momenta in order to obtain the relative contributions to g. The necessary extensions of the theory, permitting its application to specific models, have been given by A. Bohr.

b. The Theory of A. Bohr[20,21]

Bohr has shown that a more accurate theory of the hyperfine structure anomaly leads to the following modification

$$-\epsilon=[(1+0.38\zeta)\alpha_s+0.62\alpha_L]b(Z,R_0)\langle(R^2/R_0^2)\rangle_{Av}. \quad (12)$$

In this expression, α_s and α_L are as previously defined, $b(Z,R_0)$ is the same as in the B–W theory; $\langle(R^2/R_0^2)\rangle_{Av}$ must be computed for the specific model under consideration, as must the constant ζ. In the case of the independent-particle model with spin-orbit coupling,[22] Bohr obtained[21]

$$\begin{aligned}\zeta&=(2I-1)/4(I+1), \quad \text{for} \quad I=L+\tfrac{1}{2}\\ &=(2I+3)/4I, \quad \text{for} \quad I=L-\tfrac{1}{2}.\end{aligned} \quad (13)$$

For models such as those developed by Bohr,[20] in which the single particle is coupled to an asymmetric, rotating core, the expressions for ζ are more complicated.

In the following discussion, we compare the theoretical and experimental values of the hyperfine structure anomalies for a number of specific models; the comparison is shown for the $K^{39}-K^{41}$ and $Rb^{85}-Rb^{87}$ anomalies as well as for the $K^{39}-K^{40}$ anomaly. The data on which the computations are based are given in Table IV. In addition, we use the values $g_p^{free}=5.5870$, $g_n^{free}=-3.8270$.

Model 1a. We assume a strict single-particle model, with the odd nucleon in the state given in Table IV. The intrinsic moment of the odd nucleon is, however, assumed to be different from its free moment; its value is chosen to yield the observed nuclear moment with $g_L=1$. Such a model has been proposed by Bloch,[23] by de Shalit,[24] and by Miyazawa.[25] The modifications of the intrinsic moment could be a result of meson exchange currents in the nucleus.

K^{39} *and* K^{41}: for a $d_{\frac{3}{2}}$ proton, we take

$$g=\frac{\mathbf{S}\cdot\mathbf{I}}{I(I+1)}g_s+\frac{\mathbf{L}\cdot\mathbf{I}}{I(I+1)}g_L=-\frac{g_p^{eff}}{5}+\frac{6}{5}.$$

With g(measured) from Table IV, we obtain $g_p^{eff}(K^{39})=4.6965$ and $g_p^{eff}(K^{41})=5.2845$. Furthermore, for a $d_{\frac{3}{2}}$ proton, $\zeta=1$ and $\langle(R^2/R_0^2)\rangle_{Av}\cong 0.66$; $-\epsilon=(1.38\alpha_s+0.62\alpha_L)(0.19)(0.66)$ percent, with $\alpha_s=-g_p^{eff}/5g$, $\alpha_L=1-\alpha_s$. The results are shown in column 3 of Table V.

K^{40}: Coupling a $d_{\frac{3}{2}}$ proton and an $f_{7/2}$ neutron to give $I=4$ yields

$$g=\frac{\mathbf{I}_p\cdot\mathbf{I}}{I(I+1)}g_p+\frac{\mathbf{I}_n\cdot\mathbf{I}}{I(I+1)}g_n=\frac{g_p(d_{\frac{3}{2}})}{5}+\frac{4g_n(f_{7/2})}{5}.$$

Assuming $g_p(d_{\frac{3}{2}})=g(K^{39})=0.2607$ and $g_L=0$ for the neutron, we compute g_n^{eff} from $g_n(f_{7/2})=g_n^{eff}/7$ and the experimental $g(K^{40})$; $g_n^{eff}=-3.2923$.

For the proton, the constants are as in K^{39}; for the neutron, $\zeta=\frac{1}{4}$ and $\langle(R^2/R_0^2)\rangle_{Av}\cong 0.85$, whence $-\epsilon=(1.38\alpha_{sp}+0.62\alpha_{Lp})(0.19)(0.66)$ percent $+(1.124\alpha_{sn})\times(0.19)(0.85)$ percent with $\alpha_{sp}=-g_p^{eff}(K^{39})/25g$, $\alpha_{Lp}=6/25g$, $\alpha_{sn}=4g_n^{eff}/35g$. The result is shown in column 3 of Table V.

Rb^{85}: for an $f_{5/2}$ proton, $g=-g_p^{eff}/7+8/7$, $\zeta=\frac{3}{5}$, $\langle(R^2/R_0^2)\rangle_{Av}\cong 0.80$; $b=0.58$ percent for Rb. $-\epsilon=(1.304\alpha_s+0.62\alpha_L)(0.58)(0.80)$ percent.

Rb^{87}: for the $p_{\frac{3}{2}}$ proton, $g=g_p^{eff}/3+\frac{2}{3}$, $\zeta=\frac{1}{3}$, $\langle(R^2/R_0^2)\rangle_{Av}\cong 0.49$; $b=0.58$ percent, etc.

The results are given in column 3 of Table V.

Model 1b. The model is the same as 1a, except that we now ascribe the deviations from the Schmidt limits of the magnetic moments to a change in g_L, taking g_p^{free} and g_n^{free} as the intrinsic nucleon moments, and using the measured g to compute g_L^{eff}. (In this model, the neutron also has an effective orbital moment.) From the point of view of a meson theory, this model corresponds to the assumption that the meson currents affect only the orbital angular momenta. The results are shown in columns 5 and 6 of Table V.

Model 2. Feenberg and Davidson[26] have suggested another model which is less extreme in its "independent-particle" character. According to this model, the ground-state nuclear wave function is an admixture of a single-particle wave function (given s, L, and I) and a many-particle wave function, for which the total angular momentum I and the spin s are the same, but for which the orbital angular momentum differs from that of the single particle by one unit. Accordingly, the nuclear moment is made up of two parts (weighted according to the squares of the strengths of the re-

[20] A. Bohr, Phys. Rev. **81**, 134 (1951).
[21] A. Bohr, Phys. Rev. **81**, 331 (1951).
[22] M. G. Mayer, Phys. Rev. **78**, 16, 22 (1950).
[23] F. Bloch, Phys. Rev. **83**, 839 (1951).
[24] A. de Shalit, Helv. Phys. Acta **24**, 296 (1951).
[25] H. Miyazawa, Prog. Theoret. Phys. **6**, 263 (1951).
[26] Private communication. We thank Professor E. Feenberg for illuminating discussions on this problem.

TABLE V. Comparison between theory and experiment of the hfs anomalies of the K and Rb isotopes. All results are given in percent.

	Experiment	Model 1a		Model 1b		Model 2		Model 3	
	Δ	ϵ	Δ	ϵ	Δ	ϵ	Δ	ϵ	Δ
K^{41}	0.226±0.010	0.626	0.360	0.666	0.335	0.632	0.357	0.396	0.231
K^{39}	0.466±0.019	0.266	0.520	0.331	0.611	0.275	0.541	0.165	0.43
K^{40}		−0.254		−0.280		−0.266		−0.26	
Rb^{85}	0.33 ±0.05	0.066	0.325	0.181	0.489	0.085	0.343	0	0.26
Rb^{87}		−0.259		−0.308		−0.258		−0.26	

spective contributions to the wave function). The first is the Schmidt limit corresponding to a single nucleon; the second is the opposite Margenau-Wigner[27] limit ($g_L=Z/A$) for the same I. The proportions of the two types of contribution are chosen to fit the observed nuclear moment. We illustrate by considering K^{39} for which we take $g=ag_{Sch}(d_{\frac{3}{2}})+(1-a)g_{M-W}(p_{\frac{1}{2}})$ with $g_{Sch}(d_{\frac{3}{2}})=0.0826$ and $g_{M-W}(p_{\frac{1}{2}})=2.1790$. Thus, for $g=0.2607$, we obtain $a=0.915$. The computation of the hfs anomaly now proceeds in a straightforward fashion

$$-\epsilon=(1.38\alpha_{s,\,Sch}+0.62\alpha_{L,\,Sch})(0.19)(0.66)\text{ percent}$$
$$+(\alpha_{s,\,M-W}+0.62\alpha_{L,\,M-W})(0.19)(0.60)\text{ percent},$$

where $\alpha_{s,\,Sch}=-ag_p{}^{free}/5g$, etc. In the above, b is (as always) taken to be independent of the model; $\zeta=0$ and $\langle(R^2/L_0^2)\rangle_{Av}\cong 0.60$ for a uniform, spherically symmetrical spin distribution.

In applying the Feenberg model to K^{40}, we have assumed that $g=(1/5)g_p'+(4/5)g_n'$ with

$$g_p'=g(K^{39})=a_pg_{Sch}(d_{\frac{3}{2}})+(1-a_p)g_{M-W}(p_{\frac{1}{2}});$$
$$g_n'=-0.47033=a_ng_{Sch}(f_{7/2})+(1-a_n)g_{M-W}(g_{7/2}).$$

The computation of (K^{40}) then proceeds as outlined above. The results of the application of the Feenberg model to the five nuclei under consideration are given in columns 7 and 8 of Table V.

Model 3. A. Bohr has developed a nuclear model in which the odd nucleon is assumed to be coupled to a symmetric, rotating nuclear core.[20] Depending on the nature of the coupling between the odd nucleon and the core, different values of the nuclear moments can be obtained. In general, the magnetic moments computed by Bohr are in fair agreement with the observed values.

The application of this model to the computation of the hyperfine structure anomaly has been discussed by Bohr[21] for the $K^{39,41}$ and $Rb^{85,87}$ isotopes. The results are reproduced in columns 9 and 10 of Table II. Bohr[28] suggests the following asymmetric model for K^{40}: The nucleus is deformed into an oblate shape (negative quadrupole moment) under the influence of the $f_{7/2}$ neutron. The missing $d_{\frac{3}{2}}$ proton will then prefer to go into a state of $m=\frac{1}{2}$ with respect to the nuclear axis, leading to $I=4$. The resulting g factor turns out to be -0.28, in comparatively good agreement with the observed value (see Table IV). (This is a case of extreme coupling; partial decoupling of L and s for the odd nucleons might lead to even better agreement.) For this model, Bohr has computed $\epsilon(K^{40})=-0.26$ percent, as given in column 9 of Table V.

c. Discussion

Comparison of the computed and measured hfs anomalies in Table V indicates: (1) qualitative agreement for all three models, (2) closest quantitative agreement with the model of Bohr (model 3), and (3) poorest agreement with model 1(b). This last is perhaps not too surprising, since this method of computation (ascribing the deviations of g from the Schmidt limits to an anomalous g_L) leads to values of $g_L{}^{eff}$ that are critically dependent on the nuclear state; the same is not true of model 1a, for which the computed values of $g_s{}^{eff}$ are fairly consistent.

Perhaps the most surprising result is the close agreement between the predictions of models 1a and 2, even for the case of Rb, where the deviations of the moments from the Schmidt limits are not inconsiderable. It is interesting to note, in this respect, that models 1a, 2, and 3 differ appreciably only in their predictions for K^{39} and K^{41}. Indeed, it is only on the basis of the hfs anomaly for these nuclei that it is possible to make any choice between the three models.

The major conclusion, however, is that the available date on the hfs anomalies gives strong support to nuclear models which are, in their essential features, based on the independent-particle model with spin-orbit coupling. The problem of the nature of the coupling between an odd proton and an odd neutron is, however, not particularly elucidated by the K^{40} measurement, since the predicted ϵ for the models employing j-j coupling (1 and 2) and for the model of Bohr (3) are so closely alike. It is to be hoped that measurements on other odd-odd nuclei will shed more light on this question.

The authors gratefully acknowledge the guidance and aid of Professor J. R. Zacharias.

[27] H. Margenau and E. P. Wigner, Phys. Rev. **58**, 103 (1940).
[28] Private communication. We are indebted to Dr. A. Bohr for making these results available to us.

The Average Energy of Beta-Ray Spectra*

RANDALL S. CASWELL†
Radioactivity Center of the Laboratory for Nuclear Science and Engineering, Massachusetts Institute of Technology, Cambridge, Massachusetts

(Received December 14, 1951)

The average beta-energy per disintegration has been measured for P^{32}, Y^{90}, I^{131}, and Ca^{45}. An air-filled water-electrode extrapolation ionization chamber was used for measurement of the rate of emission of energy. The absolute disintegration rate was determined by 4π-counting. Good agreement was found between the measured average energy values and values predicted by the Fermi theory using maximum energy data from the literature. Experimental results obtained were P^{32}, 0.696±0.03 Mev; Y^{90}, 0.895±0.035 Mev; I^{131}, 0.189±0.008 Mev (includes conversion electrons); and Ca^{45}, 0.0746±0.003 Mev.

I. INTRODUCTION

THE ability of a beta-ray emitting radioactive isotope to produce biological effect is determined by the average energy emitted per disintegration. For most isotopes, however, accurate values of only the maximum beta-energies are available. This paper describes a new method of measuring average energies.

If E_m is the rate of energy production per gram by some radioactive material and n is the disintegration rate per gram of the same material, the average energy per disintegration is

$$\bar{E}=E_m/n. \tag{1}$$

The average beta-ray energy per disintegration was first measured by Ellis and Wooster[1] for radium E. The heat produced by the radium E (and therefore E_m) was measured in a very sensitive calorimeter. The disintegration rate n was determined by alpha-counting the growth of the daughter nuclide, radium F. Other calorimeter measurements of average energy have been made for RaE,[2-4] P^{32},[5] and H^3.[6] Disintegration rates were determined for P^{32} with an end-window beta-counter of known efficiency and by H^3 by measuring the growth of the helium daughter.

The calorimetric method and the present method are the only ones which allow a direct determination of the average energy of a beta-ray spectrum without further knowledge of the maximum energy, the type of transition, or its complexity. The spectral energy distribution for a large number of beta-ray emitters has been measured by means of magnetic beta-ray spectrometers. From the experimentally determined energy spectra, Marinelli, Brinckerhoff, and Hine[7] have computed the average energies of many beta-ray emitters. The agreement with the predicted values from the Fermi theory using experimental values for the maximum energy is satisfactory. The accuracy of their average energy determinations is of the order of 10 percent. For many complex spectra, average energies of the individual branches only were reported.

The present work was undertaken to investigate a relatively simple means of determination of average energy for both simple and complex beta-spectra. The ionization produced by a radioisotope is more easily measured than the very small amount of heat produced. For this reason an extrapolation ionization chamber is used in place of the calorimeter. Disintegration rate was determined by the most accurate, generally applicable method, 4π-counting.

II. THE EXTRAPOLATION IONIZATION CHAMBER

A. Theory of Operation

The extrapolation ionization chamber was invented by Failla[8] and has been used in various problems of energy absorption measurement.[9-12] The theory of operation of the extrapolation chamber as used in this experiment is now presented.

In an infinite homogeneous medium with radioactive material distributed uniformly throughout, the energy absorbed per gram of medium just equals the energy produced per gram and is given by $E_m=n\bar{E}$. This energy absorption will likewise hold at the plane interface between two semi-infinite volumes of this same medium. If the radioactivity is removed from one of the volumes, but the material medium is kept the same throughout, the energy absorbed in an infinitesimally thin layer of either volume at the interface is $n\bar{E}/2$. An infinitesimally thin air layer at the interface may be approximated by extrapolating to zero plate separation the curve of ionization per unit volume in a parallel

* This work was supported in part by the joint program of the ONR and AEC.

† Present address: Department of Physics, University of Kentucky, Lexington, Kentucky.

[1] C. D. Ellis and W. A. Wooster, Proc. Roy. Soc. (London) **A117**, 109 (1927).
[2] L. Meitner and W. Orthmann, Z. Physik **60**, 143 (1930).
[3] M. Lecoin and I. Zlotowski, Nature **144**, 440 (1939).
[4] I. Zlotowski, Phys. Rev. **60**, 483 (1941).
[5] Zumwalt, Cannon, Jenks, Peacock, and Gunning, Science **107**, 47 (1948).
[6] Jenks, Ghormley, and Sweeton, Phys. Rev. **75**, 701 (1949).
[7] Marinelli, Brinckerhoff, and Hine, Revs. Modern Phys. **19**, 25 (1947).
[8] G. Failla, Radiology **29**, 202 (1937).
[9] Quimby, Marinelli, and Farrow, Am. J. Roentg. **39**, 799 (1938).
[10] E. H. Quimby and E. F. Focht, Am. J. Roentg. **50**, 653 (1943).
[11] E. H. Quimby and E. F. Focht, Am. J. Roentg. **46**, 376 (1941).
[12] Failla, Rossi, Clark, and Baily, Atomic Energy Commission Declassified Document No. 2142 (1947).

plate, variable plate separation, ionization chamber (extrapolation chamber). To correspond to semi-infinite volumes, the electrodes must be "infinitely thick" to the radiation being studied. The rate of energy absorption may be determined by the Bragg-Gray cavity theorem:[13,14]

$$E_m = J_m \langle W_{air} \cdot \rho_m \rangle_M, \tag{2}$$

where J_m is the number of ion pairs formed per gram of air per second, and E_m is the energy dissipated in the medium Z per gram per second. $\langle W_{air} \cdot \rho_m \rangle_M$ is the mean value of the product of ρ_m, the mass stopping power of the medium relative to air, and W_{air}, the mean energy expended in the production of a pair of ions in the air, averaged over all speeds of particles traversing the cavity. Gray gives

$$\rho_m = \frac{(dE/dx)_{medium}}{(dE/dx)_{air}} = \frac{(n_m)_{medium}}{(n_m)_{air}} f_{\bar{Z}}, \tag{3}$$

where (dE/dx) is the rate of energy loss per g/cm² of path length, n_m is the number of electrons per unit mass, and $f_{\bar{Z}}$ is a function of the mean atomic number of medium Z. The function $f_{\bar{Z}}$ has a value of unity for air, and is taken from the Bethe-Williams theory of the ionization loss by charged particles.[15,16] For the case of beta-rays of about 1-Mev initial energy, $f_{\bar{Z}}$ increases by approximately 1.5 percent per unit increase in Z for Z near that of air.

For the particular case of water source electrode and air cavity (which were used in the average energy measurement), the relative stopping power has been evaluated as a function of energy by Wang,[17] using the theoretical calculations of Bethe[18] for air and of Halpern and Hall[19] for water.

W_{air} may be taken as 32.5±1.0 ev/ion pair for air for all energies above about 8 kev.

After combining Eq. (2) with Eq. (1), and inserting a factor of two because only one medium is radioactive, we have for media of identical composition

$$\bar{E} = 2J_m \langle W_{air} \cdot \rho_m \rangle_M / n. \tag{4}$$

For a backscattering electrode (nonradioactive) not of the same material as the source electrode, the equation may be written

$$\bar{E} = 2J_m \langle W_{air} \cdot \rho_m \rangle_M / nB, \tag{5}$$

where B is called the "backscattering correction factor." Relative values of B have been determined by Baily[20] for a large number of backscatterers, using an extrapolation chamber with P^{32}, Tl^{204}, Sr^{90}, and S^{35} sources in water solution. B is found to be remarkably independent of the beta-energy. For a water source electrode and aluminum backscattering electrode, B is about 1.14 for isotopes above 0.5-Mev maximum energy, decreasing at S^{35} (0.169 Mev) to 1.12.

The ionization per unit volume, J_v, in the extrapolation chamber is observed to decrease linearly with increasing electrode separation. The increased absorption in the air of the cavity and an obliquity effect due to the non-infinite width of the source are believed to account for this. The activity A of beta-radiation observed at an angle θ with the normal to the plane of a source is approximately[21]

$$A = A_0(\cos\theta/\mu x)[1-\exp(-\mu x/\cos\theta)], \tag{6}$$

where μ is the mass absorption coefficient, x is the source thickness, and A_0 is a constant. For an infinitely thick source, A is approximately proportional to $\cos\theta$. From this it may be shown that if the source radius b is large compared to plate separation d, then the ionization per unit volume will fall off linearly with d because of the obliquity effect. More detailed calculations including air absorption also yield a linear decrease in J_v with d. For an ideal infinitely thin source, J_v will become infinite as d approaches zero.

A gamma-ray correction has been calculated, and amounts to 2–3 percent for an isotope emitting equal gamma-ray and beta-ray energy. The expression for the ratio of the gamma-ray energy to the beta-ray energy absorbed in the air volume is

$$\frac{E_{air\gamma}}{E_{air\beta}} = \sum_\gamma \frac{n_\gamma E_\gamma}{n\bar{E}} \left(\frac{\mu_{air\gamma}\mu_{i\beta}}{\mu_{i\gamma}\mu_{air\beta}}\right)\{1-\exp[-\mu_{i\gamma}Y] + \mu_{i\gamma}Y[[-\mathrm{Ei}(-\mu_{i\gamma}Y)]-[-\mathrm{Ei}(-\mu_{i\gamma}b)]]\}, \tag{7}$$

where the summation is over all the gamma-rays in the disintegration scheme of the isotope. $\mu_{i\beta}$ and $\mu_{i\gamma}$ are the beta- and gamma-ray absorption coefficients in the source medium, and $\mu_{air\beta}$ and $\mu_{air\gamma}$ the corresponding coefficients in the air cavity. The thickness of the source is Y, its radius is b, n_γ is the disintegration rate for each gamma-ray, $-\mathrm{Ei}(-y)$ is the exponential integral.

A bremsstrahlung correction of up to 0.5 percent has also been made.[22]

B. Design of the Chamber

An extrapolation chamber was built and modified so that either solid or liquid radioactive materials could be used for one of its plane parallel electrodes. A water solution of a radioactive salt was used for one electrode in the average energy measurements (Failla *et al.*[12]). For the other electrode, the backscattering electrode, alu-

[13] L. H. Gray, Proc. Roy. Soc. (London) **156A**, 578 (1936).
[14] L. H. Gray, Brit. J. Radiol. **22**, 677 (1949).
[15] H. Bethe, Ann. Physik **5**, Folge 5, 325 (1930).
[16] E. J. Williams, Proc. Roy. Soc. (London) **A135**, 108 (1932).
[17] T. J. Wang, Nucleonics **7**, No. 2, 55 (1950).
[18] H. Bethe, *Handbuch der Physik* (Julius Springer, Berlin, 1933), **24/1**, p. 522.
[19] O. Halpern and H. Hall, Phys. Rev. **73**, 477 (1948).
[20] N. Baily, private communication.
[21] Elliott, Engelkemeir, and Rubinson, Plutonium Project Report IXB, 2.1 (1951). (Paper I in *Radiochemical Studies; the Fission Products.*)
[22] R. D. Evans, course notes, M.I.T.

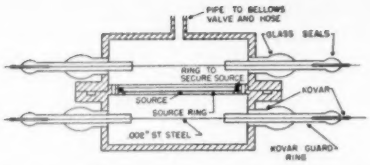

FIG. 1. Schematic diagram of the 4π proportional counter.

minum and water solidified with agar were used. The water-agar electrode was used so that both electrodes could have as nearly identical composition as possible. Spacing between the plane parallel electrodes was adjustable with three micrometers. The absolute value of plate separation was determined by an electrical measurement of the capacity between the guard-ringed collecting electrode and the high voltage electrode. By comparison between the mechanical distance measurement and the electrical capacity measurement, the ionization per unit volume could be measured independent of the area of the collecting electrode. This was important when an agar electrode was used. Ionization current was measured with a vibrating reed electrometer.

III. THE 4π-COUNTER

To determine the disintegration rate n for the solution used as the radioactive electrode, absolute disintegration rate measurements were made with a 4π-counter.

A proportional counter was built in the "pillbox" shape[23] (see Fig. 1). The interior of the counter is $3\frac{1}{4}$ inches in diameter by $2\frac{5}{8}$ inches high. The source is at the center of a collodion film 10–20 $\mu g/cm^2$ thick which is $1\frac{3}{8}$ inches in diameter. To make the source conducting, aluminum may be evaporated on the film yielding a layer about 5 $\mu g/cm^2$ thick. For isotopes with energetic beta-rays, aluminum foil 0.14 mg/cm^2 thick was used. The counter was usually filled to 45-cm pressure with n-butane. Normal operation voltage is about 4100 volts.

The center wires are guard-ringed, with the guard rings at the same high positive potential as the center wire. The brass case of the counter (coated with Aquadag) serves as the cathode and is maintained at a negative high voltage with respect to ground. This connection tends to prevent corona discharge troubles.

The counting rate was independent of pressure between 30 and 60 cm, and the plateau slope against voltage was less than $\frac{1}{2}$ percent in 500 volts. Location of the plateau was taken from the curve of counting rate *vs* pulse-height selector setting.

Disintegration rate comparisons with a P^{32} standard calibrated with a 4π-counter at the National Bureau of Standards, and a coincidence-counted Co^{60} standard of the National Bureau of Standards, checked within the accuracy of those measurements (5 percent and 3 percent). Checks against Na^{24} and Co^{60} standards coincidence counted in this laboratory agreed to within 1 percent, although the expected accuracy of the coincidence counting was taken as ± 5 percent. For Co^{60}, close agreement between 4π-counting and coincidence counting was found for an evaporated source 1 $\mu g/cm^2$ thick, indicating that the intrinsic efficiency of the counter is nearly 100 percent.

The chief loss in counting efficiency is caused by self-absorption in the source. A Ca^{45} sample simply allowed to dry counted 36 percent lower than a properly precipitated thin sample of the same series. A lower limit is placed on the energy of the beta-particles to be counted in a 4π-counter by the source thickness problem.

IV. EXPERIMENTAL RESULTS

Estimated errors for quantities inserted in Eq. (5) were W_{air}, ± 3 percent; B, ± 1 percent (aluminum backscattering electrode); n, ± 2 percent; $J_m \pm 1$ percent (aluminum backscattering electrode), ± 2 percent (agar backscattering electrode). This leads to a probable error in E of about ± 4 percent. W_{air} is taken as 32.5 ev/ion pair.

Wang[17] points out the possibility of large errors in the value of ρ_m. The results for P^{32} below would seem to indicate that no large error of this type is present in these measurements. If improved values of ρ_m are available in the future, then the results below should be corrected accordingly.

A. P^{32}

Results for P^{32} were as follows:

Backscattering electrode	ρ_m	B	$\bar{E}$
Water (agar)	1.11	1.00	0.700 Mev
Aluminum	1.11	1.14[24]	0.692 Mev

We may take the mean as our best value for average energy $\bar{E} = 0.696 \pm 0.03$ Mev. This may be compared with other values reported in the literature[5,7,14,25,26] and collected in Table I.

The beta-spectrum of P^{32} is well known. Since the average energy obtained by the present method is in good agreement with values obtained by independent methods, the present method may be assumed to yield good values for other isotopes.

B. Y^{90}

For Y^{90}, ρ_m was taken as 1.10, a compromise between the values of Wang[17] and Gray[14] for electrons of about 0.9-Mev average energy. B was estimated as 1.14 from the data of Baily.[20] The final result is $\bar{E} = 0.895 \pm 0.035$ Mev. Using $E_{max} = 2.18$ Mev,[27] and the Coulomb correction factor of Nordheim and Yost,[28] numerical

[23] C. J. Borkowski, Conference on Absolute Beta Counting, National Bureau of Standards, July 13, 1949.

[24] Obtained by plotting data from reference 20.
[25] K. Siegbahn, Phys. Rev. **70**, 127 (1946).
[26] G. H. Jenks, private communication.
[27] L. M. Langer and H. C. Price, Jr., Phys. Rev. **76**, 641 (1949).
[28] L. W. Nordheim and F. L. Yost, Phys. Rev. **51**, 942 (1937).

integration of the Fermi spectrum using the forbiddenness factor $[(W_0-W)^2+(W^2-1)]$ yields $\bar{E}=0.90$ Mev. For Y^{90}, one cannot distinguish between the allowed and forbidden shape on the basis of average energy because the theoretically predicted average energies are almost equal ($\bar{E}=0.89$ Mev for the allowed spectrum).

It should be noted here that the relatively low average energy found for RaE is because the correct forbiddenness factor is approximately proportional to $(W_0-W)^2$. For the other isotopes found thus far to have forbidden-shape spectra, the average energy would be little affected by the degree of forbiddenness of the transition.

C. I^{131}

Taking $B=1.14$ and $\rho_m=1.11$ and making a gamma-ray correction of 5.4 percent, we find $\bar{E}=0.189\pm0.008$ Mev. The total electronic energy per disintegration calculated from the decay scheme of Metzger and Deutsch[29] and using the Coulomb correction factor of Longmire and Brown[30] is 0.180 Mev (including 7.3 kev/disintegration of energy because of conversion electrons).

D. Ca^{45}

Ca^{45} of the highest specific cativity obtainable from Oak Ridge was used. A solution of Bentonite, a colloidal mud, was used to precipitate 4π-counter samples of 0.1 mg/cm^2 average thickness. A correction of 1.5 percent for self-absorption in the counter samples was made. Taking $\rho_m=1.11$ and $B=1.13$, four runs with aluminum backscatterer yielded $\bar{E}=0.0748$ Mev. One run with water (agar) backscatterer yielded 0.0738 Mev. Our mean value of $\bar{E}$ is 0.0746 ± 0.003 Mev. The theoretical value using the maximum beta-energy of Macklin *et al.*[31] and the Coulomb correction factor of Longmire and Brown[30] is 0.0761 Mev.

[29] F. Metzger and M. Deutsch, Phys. Rev. **74**, 1640 (1948).
[30] C. Longmire and H. Brown, Phys. Rev. **75**, 267 (1949).
[31] Macklin, Feldman, Lidofsky, and Wu, Phys. Rev. **77**, 137 (1950).

TABLE I. Average energy values for P^{32}.

Method	Value (Mev)	Reference
Spectrometer	0.695±0.02	Marinelli *et al.*[a] using data of Siegbahn[b]
Spectrometer	0.700	Zumwalt *et al.*[c]
Calorimeter	0.68±0.02	Zumwalt *et al.*[c] and Jenks[d]
Ionization chamber	0.63±0.035	Gray[e]
Extrapolation chamber	0.696±0.03	Present measurements

[a] See reference 7. [c] See reference 5. [e] See reference 14.
[b] See reference 25. [d] See reference 26.

V. CONCLUSIONS

The average energy results of this research agree within the accuracy of the experiment with average energy values based on the Fermi theory using the best experimental data in the literature for maximum beta-energy. The method provides a relatively simple means of determining average energy for both simple and complex beta-spectra, provided there is not an overwhelming amount of gamma-radiation. With new tables of the Coulomb correction factor to be published,[32] it should be possible to compute large numbers of very accurate average energy values using published values of maximum beta-energy in the literature.

For isotopes of known average energy, the extrapolation chamber may be used to determine absolute disintegration rate.[12] This should be particularly useful for beta-emitting isotopes of low energy.

The author wishes to thank Professor R. D. Evans for his suggestion of the problem and for his guidance throughout the work. Especially helpful suggestions were made by Professor M. Deutsch and Dr. R. A. Dudley. The author is also greatly indebted to Professor J. W. Irvine, Jr., Dr. G. L. Brownell, Mrs. Jean Caswell, and Mr. W. Kallenbach for help in various phases of the work.

[32] I. Feister, Phys. Rev. **78**, 375 (1950).

Shape of Cosmic-Ray Star-Size Distributions in Nuclear Emulsions*

M. Birnbaum, M. M. Shapiro, B. Stiller, and F. W. O'Dell
Nucleonics Division, Naval Research Laboratory, Washington, D. C.
(Received August 23, 1951)

The occurrence of a break in integral star-size distributions at a prong number of approximately 7, previously observed with nuclear emulsions in the lower atmosphere, has also been found at several stratosphere altitudes under a variety of conditions. This shows that the effect is due mainly to the composition of the nuclear emulsion. Although the shape of the distribution curves is thus strongly influenced by the properties of the detector, the altitude dependence of the nucleonic energy spectrum is clearly reflected in the progressive change in the slopes of these curves.

INTRODUCTION

In reporting on measurements of the star-producing radiation by means of nuclear photoplates, George and Jason[1] and Page[2] have plotted the logarithm of the frequency N of stars with k or more prongs against the prong number k. Their data were obtained on the Jungfraujoch[1,2] at 3450 m, and at sea level.[1] They showed that the integral star-size distribution at mountain altitudes, plotted semilogarithmically, is well represented by two straight lines A and B (similar to those in Fig. 1), which intersect at a prong number of about 7. Subsequently, Barton, George, and Jason considered that this property of the size-frequency distribution must be regarded as fortuitous.[1] Page, on the other hand, had suggested that the break near $k=7$ may be due to the composition of the emulsion which consists of two distinct groups of target nuclei: the light nuclei of C, N, O and the heavy nuclei of Ag and Br.[3] This suggestion implied a simple explanation for the change in slope of the size-frequency curve: large stars ($k>7$ or 8) can be generated only in the heavy nuclei; at prong numbers of ≈ 7 down to 5, a small but increasing fraction of the stars are produced in the light nuclei as well; finally, at 3 and 4 prongs, this fraction becomes considerable.

If this idea is correct, one might expect the break to appear not only in the lower atmosphere but also in the stratosphere, despite the change in the energy spectrum of the N-radiation with altitude. We have accumulated several star collections, in the course of a number of stratosphere investigations,[4] both in air and Pb, which could be used to test this hypothesis. Our integral distributions of star size in the stratosphere show the same break near $k=7$ as those at lower elevations. We have also analyzed similar data from other laboratories which likewise display the same effect. The presence of the break in such varied exposures strongly supports the contention that it reflects a property of the emulsion.

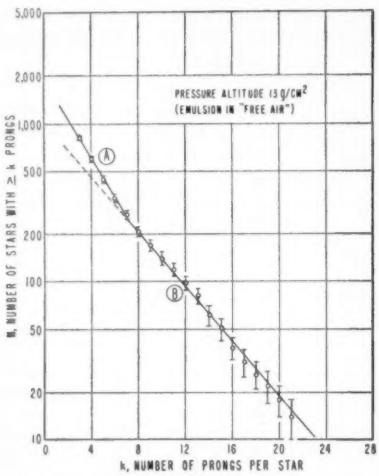

FIG. 1. Integral star-size distribution obtained from flight I with emulsions suspended far from other materials. The slopes of lines A and B are given in Table I. From the extrapolation of B, the frequency of stars produced in Ag and Br nuclei is estimated.

EXPERIMENTAL DETAILS AND RESULTS

Our star data were obtained from three Skyhook balloon flights[5] in Minnesota, at geomagnetic latitude 55°N. Ilford G-5 emulsions, 400μ thick, were used throughout. Flight I attained a maximum altitude of 99,000 ft, and stayed above 90,000 ft for 4 hours, the average pressure altitude during this time being 13 g/cm^2. The "free air" plates exposed in this flight were small (3×2 in.), few in number (6), and surrounded only by a thin aluminum can suspended far from other materials. Figure 1 shows the integral size-frequency

* This work was reported at the Schenectady meeting of the American Physical Society, June 15, 1951 [Phys. Rev. **83**, 874 (1951)].

[1] E. P. George and A. C. Jason, Proc. Phys. Soc. (London) **A62**, 243 (1949); Barton, George, and Jason, Proc. Phys. Soc. (London) **A64**, 175 (1951).

[2] Nora Page, Proc. Phys. Soc. (London) **A63**, 250 (1950).

[3] H is omitted from this list, since the type of stars considered here are not produced in hydrogen.

[4] Shapiro, Stiller, Birnbaum, and O'Dell, Phys. Rev. **83**, 455 (1951).

[5] We appreciate the cooperation of Dr. U. Liddell and Mr. J. Holloway, of ONR, and C. B. Moore, A. T. Bauman, and their staff of the General Mills Aeronautical Research Laboratories in these flights.

TABLE I. Slopes of star-size distributions at various altitudes in air and Pb.

Data	Atmos. depth (g/cm^2)	Slope α_A	Slope α_B	k_t
Balloon flights				
Naval Research Laboratory (NRL) (flight I)	13 ("free air")	0.286±0.012	0.199±0.016	6.2
NRL (flight I)	13 (in Pb)	0.286±0.055	0.188±0.046	7.5
Brookhaven National Laboratory (BNL)[a]	15	0.301±0.044	0.195±0.017	6.9
Chicago[b]	15	0.180	0.137	10
NRL (flight II)	22	0.327±0.018	0.197±0.010	7.3
Bristol[c]	50	0.267±0.004	0.213±0.005	8.0
NRL (flight III)	300	0.412±0.079	0.248±0.059	8.0
Mountain exposures				
London (Birkbeck College)[d]	680	0.48	0.33	8.9
Manchester[e]	680	0.521	0.331	6.3
Bristol[f]	680	0.365±0.085	0.280±0.010	8.2
Sea level exposure				
London[d]	1030	0.48	0.33	8.8

[a] See reference 8.
[b] See reference 11.
[c] See reference 10.
[d] See reference 1.
[e] See reference 2.
[f] See reference 9.

distribution obtained from the free-air emulsions. As an index of star size we adopted the number of "heavy" prongs, i.e., tracks with specific ionization >1.4 times the minimum. It is evident that the data are well represented by two lines which intersect at $6<k<7$. The absolute values α_A and α_B of their least-squares slopes are given in the first line of Table I.[6] Another exposure, of plates buried vertically in a block of Pb 5 cm deep, was made in the same flight. This yielded the same kind of star-size graph, with slopes which agree closely with those for the free-air exposure (see Table I). That the slopes in Pb differ inappreciably from those in air had previously been observed at mountain altitudes.[1]

Plates inside another Pb absorber, 15 cm in height (described more fully elsewhere[4]), were exposed at a somewhat lower altitude in flight II. The balloon reached a maximum altitude of 94,000 ft, and during the 6.5 hours spent above the release point, the mean pressure altitude was 22 g/cm^2. The integral size distribution appears in Fig. 2, and the slopes α_A and α_B are given in Table I. The value 0.327 ± 0.018 of α_A (the slope for $k<7$) is somewhat larger here than either value of the same slope at 13 g/cm^2. Comparing the two Pb exposures, this difference does not lie outside experimental error.[7]

Flight III consisted of an ascent to 92,000 ft, followed directly by descent, the total duration being 2.4 hours. The average pressure altitude (which is, of course, less meaningful in this type of exposure than in a sustained flight at "ceiling") was 300 g/cm^2. The exposure was intended merely to provide a correction for up-and-down accumulation; for this purpose, the collection of a very limited sample of stars (190) sufficed. The meager data have been included because they represent an exposure at a mean atmospheric depth intermediate between 50 and 680 g/cm^2. Again the frequency-size data conform to the 2-slope pattern with a break near $k=7$. The slopes α_A and α_B are intermediate in magnitude between the average values in the upper stratosphere and those at the mountain altitude.

Altogether, the four star distributions from our flights at three different altitudes are alike in shape and in the location of their break. Their slopes agree at a given altitude, and increase with atmospheric depth between the upper stratosphere and 300 g/cm^2.

In Table I our results are compared with those of other stratosphere investigations, three mountain exposures, and one sea-level exposure. For the experiments at the Brookhaven National Laboratory[3] and the H. H. Wills Laboratory in Bristol,[9,10] as well as our own, we had access to the tabulated star-size data and were

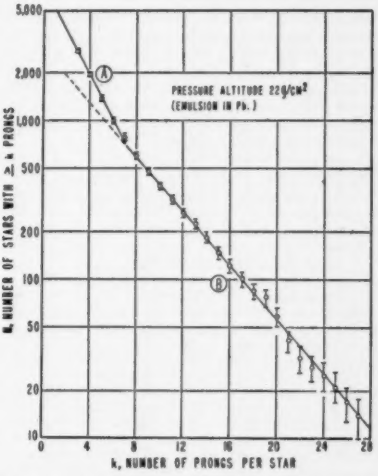

FIG. 2. Integral star-size distribution obtained from emulsions embedded in a Pb block sent aloft in flight II. The break near prong number 7 is characteristic of such distributions regardless of altitude.

[6] All slopes mentioned in this paper are negative. For convenience, the symbols α_A, α_B will be used throughout to denote their absolute values.

[7] We believe, however, that the difference is real, not only because of the lower altitude in flight II, but also because the Pb block used in it was more massive than the other by a factor $\simeq 4$. Both conditions would result in a degraded nucleon spectrum, which would increase the relative number of small stars.

[8] We wish to thank Drs. John Hornbostel and Edward O. Salant for permission to use their unpublished data.

[9] Mountain data: Brown, Camerini, Fowler, Heitler, King, and Powell, Phil. Mag. 40, 862 (1949).

[10] Stratosphere exposure: Camerini, Davies, Fowler, Franzinetti, Lock, Perkins, and Yekutieli, to be published in Phil. Mag. A preprint of this work was forwarded to us by Dr. F. Singer of ONR, London. We are grateful to Professor C. F. Powell's group for making this paper available before publication.

therefore able to compute the slopes by the method of least squares. In these instances, the standard error in each slope, estimated from the differential data as described in the Appendix, is given in the table. For the remaining four experiments, the slopes were deduced graphically (Chicago[11]) or their values were given explicitly by the authors (London[1] and Manchester[2]). The last column in Table I lists the values of k_i, the prong number at the point of intersection of lines A and B, obtained from the integral graphs. All the stratosphere stars were registered in ultrasensitive emulsions, Ilford G-5, Eastman NTB3, or (British) Kodak NT4.[12]

The various star-size distributions show the same basic feature: their semilogarithmic plots are reasonably well represented by two straight lines[13] which intersect near the prong number seven.[14] (The graphs, in fact, resemble Figs. 1 and 2 so closely that we have not reproduced them here.) They strongly support the hypothesis that the break is a consequence of the emulsion composition.

STAR-PRODUCTION RATIO IN HEAVY AND LIGHT NUCLEI

This result can be used for an approximate calculation of the ratio of star production in the heavy and light nuclei of the emulsion. It has been pointed out that line B must be due to stars (with $k \geq 8$) generated in the Ag and Br nuclei alone. We may therefore estimate, as a first approximation, that the total contribution of the Ag and Br disintegrations to the star frequency is given by the extrapolation of line B, shown as a dashed line in Figs. 1 and 2. The ordinate of this line at $k=3$ is then the frequency ν_A of stars with 3 or more prongs produced in the heavy nuclei alone. From the data we obtain directly the frequency ν of all stars with $k \geq 3$ in normal emulsion.

We have computed the ratio ν/ν_A for four of the star collections listed in Table I. The results, given in Table II, can now be compared with values of the same ratio obtained in other ways.

One method is that of Harding,[15] who used the gelatin-sandwich technique. Stars formed in the gelatin[16] can arise only from the disintegration of the light nuclei, C, N, and O. From Harding's results, $\nu/\nu_A = 1.56 \pm 0.2$.[17] Well within experimental error, this value is the same as three of those in Table II, and it is compatible with the fourth (1.3 ± 0.1).

The ratio ν/ν_A can also be calculated from the known composition of the emulsion, if we assume that the cross section for star production is proportional to the geometric one, for all Z, and for all energies of the incident particle. Normalizing the macroscopic cross section per cm^3 of emulsion in the Ag and Br nuclei alone to unity,[18] the cross section for the light elements is found to be 0.36, and for the entire emulsion, 1.36. Thus we expect the ratio ν/ν_A to be 1.36. The results in Table II agree somewhat better with the ratio obtained from Harding's data than with that computed from considerations of geometric cross section. However, the large errors in the experimental values of the ratios preclude a definite choice between the two.[19]

VARIATION OF SLOPES WITH ALTITUDE

Examination of the trend in the slopes as we progress from mountain to stratosphere altitudes shows that α_A and α_B become smaller, indicating an increase in the relative number of large stars. This is expected, for with increasing altitude the spectrum of the star-producing radiation becomes richer in high energy nucleons.

TABLE II. Ratio of stars with ≥ 3 prongs in emulsion to stars in Ag and Br.

Data	Atmos depth g/cm^2	Ratio
Naval Research Laboratory	13	1.5 ± 0.3[a]
Brookhaven National Laboratory	15	1.5 ± 0.4
Bristol	50	1.3 ± 0.1
Bristol	680	1.5 ± 0.2

[a] Errors are standard errors.

It can be seen that the Brookhaven (BNL) values obtained near the top of the atmosphere are the same as ours within experimental error. Lord's slopes for the same altitude are distinctly lower, the difference being more pronounced for α_A. The following may be the explanation: part A of the curve contains the small stars, mainly of 3 and 4 prongs, many of which are readily missed in scanning the emulsions if special precautions are not taken. An underestimate of the fraction missed would result in too low a slope for line

[11] J. J. Lord, Phys. Rev. **81**, 901 (1951).

[12] Additional data on star-size distributions have been reported by M. Addario and S. Tamburino, Phys. Rev. **76**, 983 (1949), and H. L. Bradt and M. F. Kaplon, Phys. Rev. **78**, 680 (1950). Their results, based on 488 and 1000 stars, respectively, were obtained in whole or in part with Ilford C-2 emulsions. The latter are insensitive compared with the electron-sensitive emulsions (in which the tracks of all charged particles are registered) used in our stratosphere studies and those upon which we have drawn for comparison (see references 8, 10, 11, and Table I). Since the total data collected from these balloon flights were quite adequate (>20,000 stars), and since they were gathered independently by four different laboratories, we felt justified in basing our analysis of the stratosphere stars on the studies made with ultrasensitive emulsions exclusively.

[13] There is some indication in the graphs that the distributions might be even better represented by three straight lines, with the second break occurring in the neighborhood of $k=16$. The third line C is steeper than B. However, the statistical data for C, excepting Bristol's at 50 g/cm^2, are too meager for accurate analysis. Therefore, for simplicity, the data for $k>7$ were fitted to a single best line B.

[14] The value $k_i=7$ is an average, rounded off to the nearest integer, of the k_i for all the data treated by least squares, i.e., those for which slope errors appear in Table I (excepting the data at 300 g/cm^2).

[15] J. B. Harding, Nature **163**, 440 (1949).

[16] The breakdown of these stars according to multiplicity helps explain why, contrary to what might be expected from the emulsion composition, there is no abrupt jump in N_k (with decreasing k) at $k \approx 7$, but only a change in slope. Of 26 stars with $k \geq 3$ produced in the C, N, O, Harding found only two with 5 prongs, eight with 4 prongs, and sixteen with 3 prongs. Thus, despite the theoretical possibility of releasing 6 to 8 charged particles from a light nucleus, no stars of this size were observed. Actually, it seems likely that if G-5 emulsions, rather than C-2, had been used in this study, the visibility of more tracks would have enhanced the average multiplicity and yielded one or two stars with 6 or 7 prongs.

[17] The standard error is given here.

[18] The following partial densities of G-5 emulsion components, in g/cm^3, were used in this calculation: Ag, 1.85; Br, 1.36; C, 0.27; N, 0.067; O, 0.27. Minor constituents, and H, were omitted, since they do not affect the present result.

[19] The fact that the dispersion in the ratios is much less than what one would expect from the errors associated with them lends support to our statement in the Appendix that the errors assigned to the slopes (from which the precision of these ratios is deduced), tend to be overestimates.

A. This suggests one of the uses of an integral size-frequency distribution, namely, as an easily obtainable, rough check on the scanning efficiency.

Bristol's slope α_A at 50 g/cm² is somewhat lower than those of both NRL and BNL at greater altitudes, whereas one would expect it to be higher. The reason may be that the results were uncorrected for scanning efficiency.[20] Such corrections, based on extensive cross-checks between the various observers,[21] were applied to our data and to Brookhaven's.

Turning to the mountain experiments, it should first be noted that George and Jason, as well as Page, used Ilford C-2 emulsions; the Bristol group used Kodak NT4 plates. This difference appears to be reflected in the respective results: those of London and Manchester show close agreement, whereas the absolute slopes obtained from the Bristol data are lower. Some of the tracks counted as "gray" prongs in the ultrasensitive emulsions are not visible in the less sensitive C-2 plates. Thus, the average Bristol star size (observed in the NT4 emulsions) must be larger than the others and hence the slopes in the size-distribution curve are smaller. In addition, the relatively low value of α_A could result in part from an underestimate of the small-star frequency, as suggested above for the stratosphere data.

The values assigned to the sea-level slopes in Table I, based on a smaller number of stars, are the same as those obtained from the mountain data of George and Jason. These authors indicate that, within their limits of error, there is no appreciable difference between the two size distributions.

From our discussion of the results in Table I it appears that, although the shape of the size distribution is strongly influenced by the properties of the emulsion, the increasing mean energy with altitude of the star-producing nucleons is reflected in the progressive change in the slopes of the distribution curves. This is especially evident in the slopes α_B.

[20] The recent Bristol investigations have been primarily concerned with meson production processes, and only incidentally with star frequencies.

[21] The actual values are of interest as an indication of the considerable fraction of small stars which may be missed. Our average efficiency in systematic scanning at a magnification of $\approx 150\times$ is 78 percent for 3-prong stars, 88 percent for 4-prong stars, and >99 percent for stars with at least 5 prongs. These figures are of course unlikely to be the same for all emulsions or all observers, but they apply to the data at hand. Moreover, they are probably representative of what can be expected from surveys of stratosphere-exposed plates, as judged from the following: Brookhaven kindly informs us that their over-all efficiency for 3- to 5-prong stars is 85 percent. When our own three values above are weighted by the relative frequencies, we obtain the same efficiency for this group of small stars.

CONCLUSIONS

It has been shown that integral star-size distributions at altitudes ranging from 13 g/cm² down to sea level (over 98 percent of the atmosphere) show a characteristic break near the prong number 7. We conclude that this break is due mainly to the emulsion used to record the stars. Using this result to calculate the ratio of star production in heavy and light nuclei gives fair agreement with values obtained by other methods. Finally, the change with altitude of the energy spectrum of the nucleonic component is reflected in the slopes of the distribution curves.

We thank the following for their help in scanning and computing: Mrs. D. C. Appleby, Mr. E. O. Davis, Miss K. A. DeAngelis, Mrs. N. L. T. Redfearn, and Mrs. H. F. Shapiro. Dr. M. H. Johnson has read the manuscript. It is a pleasure to acknowledge his valuable suggestions. We are especially grateful to Dr. F. N. D. Kurie for his interest and encouragement.

APPENDIX. ERRORS IN THE SLOPES

The values of the slopes of the integral star-size graphs given in Table I were obtained by the method of least squares in those cases in which we had access to the original data in tabular form. α_A was calculated from the 5 points $3 \leq k \leq 7$ and α_B from those with $k \geq 8$.

The statistical errors in the slopes cannot be obtained from the integral data because, contrary to the requirements of least squares theory, these data are not completely independent.[22] Therefore, the errors were calculated from the differential data. If N_k be the number of stars with k or more prongs, and n_k the number with just k prongs, then, according to the graphs,

$$N_k = Ae^{-\alpha k},$$

where A and α are constant for a portion (such as A or B, Fig. 1) of a given star distribution. It follows that

$$n_k = N_k - N_{k+1} = Ae^{-\alpha k}(1-e^{-\alpha}).$$

This function cannot be conveniently treated by the method of least squares. But the approximate function $n_k = Be^{-\alpha k}$ can be so treated. The errors given in Table I are proportional to those obtained by the least squares analysis of the approximate n_k function, the relative error in an integral slope being equated to that in the corresponding differential slope. This approximation for n_k tends to give a conservative estimate of the errors.

[22] The authors are grateful to Mr. John Mandel for an interesting discussion on this point.

Condensations in Expanding Cosmologic Models

AMALKUMAR RAYCHAUDHURI
Physics Laboratory, Asutosh College, Calcutta, India
(Received September 28, 1951)

The consequence of a perturbation in the expanding universe is investigated. It is found that the density gradient decreases with time, while the ratio between the perturbed density and the background density diverges more and more from unity. These results are essentially in agreement with observation and explain why even in "point source" cosmologic models, condensations of extremely high densities are not to be expected at present.

INTRODUCTION

WHILE it is usual to regard the nebulae as condensations out of a homogeneous cosmic fluid, the presence of such condensations offers an interesting and rather intriguing problem. The earlier investigations of Tolman[1] and Sen[2] seemed to show that the Friedman model (i.e., pressureless homogeneous expanding universe) is fundamentally unstable to perturbations either in the distribution of material density or in the rate of expansion; and as such one could expect the formation of condensations as a result of infinitesimal perturbations. Gamow[3] has, however, more recently reported that an expanding universe is stable against small gravitational perturbations, and that in particular a rudimentary condensation is bound to expand and mix up with the rest of the universe. Gravitational influences, alone, cannot thus explain the formation of condensations, and Gamow and his collaborators considered the interaction between radiation and gas particles as a probable causative agent. Later calculations are, however, said to have belied this hope;[4] so that according to the Gamow school the occurrence of these condensations remain an unexplained phenomenon. Gamow has, however, partly used classical nonrelativistic concepts in his considerations, and this throws some doubt on the validity of his conclusions. Lifshitz,[5] too, in considering arbitrary small perturbations of the gravitational field and of the distribution of matter in the expanding universe, has found that these perturbations either decrease with time or increase so slowly that these cannot serve as centers of formation of nebulae.

In view of such conflicting conclusions, and the interest of the problem, it seems appropriate to investigate the problem anew and with a minimum of ad hoc assumptions. Our result seems to show that the difference in conclusion regarding the fate of a rudimentary condensation depends essentially on how one defines the degree of condensation.

Hoyle[6] has recently criticized the ever-expanding relativistic cosmologic models on the ground that "in the early stages of expansion, the material in the general background is unstable against formation of condensations. Thus condensations would be formed in the material with density much higher than the mean densities within the nebulae. No such condensations are observed. Detailed considerations show that this crucial objection cannot be overcome through the action of gas or radiation pressure." We shall see that our results will provide an answer to this criticism as well.

2. BASIC ASSUMPTIONS IN THE PRESENT DISCUSSION

We shall take the line element in the universe to be of the form

$$ds^2=-e^{\mu}(dr^2+r^2d\theta^2+r^2\sin^2\theta d\varphi^2)+e^{\nu}dt^2 \qquad (1)$$

where $\mu=\mu(r,t)$ and $\nu=\nu(r,t)$. The line element of form (1) implies that we are assuming spherical symmetry as well as spatial isotropy. Spatial isotropy has not been assumed by Tolman[1] and Sen,[2] who have taken the line element in the form

$$ds^2=-e^{\lambda}dr^2-e^{\omega}(d\theta^2+\sin^2\theta d\varphi^2)+e^{\nu}dt^2 \qquad (2)$$

where λ, ω, ν are functions of r and t. It is easily seen that the necessary and sufficient condition that the line element (2) can be transformed to the form (1) without destroying the comoving nature of the coordinate system is that $\lambda-\omega$ must be a function of r alone.[7] In the perturbations considered by these authors, the time derivatives of λ and ω are not equal, so that although the unperturbed universe is isotropic, the isotropy is lost afterwards and the radial and cross radial dimensions increase at different rates. We do, however, think that the observable universe does not warrant such non-isotropic perturbations; and that no special loss of generality will result from the assumption of spatial isotropy.

We introduce also the usual assumption that the cosmic material and energy constitute a perfect fluid at

[1] R. C. Tolman, Proc. Nat. Acad. Sci. **20**, 169 (1934).
[2] N. R. Sen, Z. Astrophys. **9**, 215 (1935); **10**, 291 (1936).
[3] G. Gamow, Revs. Modern Phys. **21**, 367 (1949).
[4] R. A. Alpher and R. C. Herman, Revs. Modern Phys. **22**, 153 (1950).
[5] E. Lifshitz, J. Phys. U.S.S.R. **10**, No. 2, 116 (1946); Sci. Abstr. **A50**, No. 190 (1947).
[6] F. Hoyle, Nature **163**, 196 (1949).
[7] See, for example, R. C. Tolman, *Relativity, Thermodynamics, and Cosmology* (Oxford University Press, London, 1934), pages 364–367.

rest in the coordinate system of (1). This means that, besides isotropy, the possibility of a *"co-moving"*[8] coordinate system in which there is no net flux of energy or momentum is assumed. However such a coordinate system exists only under some restrictive conditions, e.g., we can use such a *"co-moving"* coordinate system only if all the different forms of energy existing at a particular point have the same proper macroscopic velocity. If, however, there be different velocities for different forms of energy at the same point, no such *"co-moving"* coordinate system is feasible. Thus, for example, when there is a flow of heat relative to the material contents, the coordinate system in which the matter is at rest will still show a flux of energy corresponding to the flow of heat.

It is clear, therefore, that in these perturbation problems introducing nonhomogeneity, this use of *"co-moving"* coordinate system is not quite justifiable. For instance, if the perturbation consists in a small adiabatic compression of the cosmic fluid in a certain region, there would then be a rise of temperature in this region and a consequent flow of heat away from this region. Similarly, any conversion between matter and radiation in a certain region would cause a change of pressure and a consequent flow of radiation relative to the cosmic mass.

However, in all these cases, if the perturbation be small, the flux of energy will be extremely small compared to the other (static) components of the energy tensor and can perhaps be neglected without introducing sensible error.

3. FATE OF NONHOMOGENEITIES IN EXPANDING UNIVERSE

With the foregoing assumptions, the energy momentum tensor components are $T_1^1=T_2^2=T_3^3=-p$, $T_4^4=\rho$, and $T_\nu^\mu=0$ when $\mu\neq\nu$; p and ρ denoting the pressure and energy density. The gravitational equations then assume the form[9]

$$8\pi p=e^{-\mu}[\tfrac{1}{4}\mu'^2+\tfrac{1}{2}\mu'\nu'+(\mu'+\nu')/r]-e^{-\nu}(\ddot{\mu}+\tfrac{3}{4}\dot{\mu}^2-\tfrac{1}{2}\dot{\mu}\dot{\nu})+\Lambda \quad (3)$$

$$8\pi p=e^{-\mu}[\tfrac{1}{2}(\mu''+\nu'')+\tfrac{1}{4}\nu'^2+(\mu'+\nu')/2r]-e^{-\nu}(\ddot{\mu}+\tfrac{3}{4}\dot{\mu}^2-\tfrac{1}{2}\dot{\mu}\dot{\nu})+\Lambda \quad (4)$$

$$8\pi\rho=-e^{-\mu}(\mu''+\tfrac{1}{4}\mu'^2+2\mu'/r)+\tfrac{3}{4}e^{-\nu}\dot{\mu}^2-\Lambda \quad (5)$$

$$0=2\dot{\mu}'-\dot{\mu}\nu'. \quad (6)$$

In the above expressions, dashes denote differentiation with respect to r and dots with respect to t. The energy momentum tensor satisfies the divergence identities $T_{\mu;\nu}^{\nu}=0$ which gives two nontrivial relations

$$p'=-\tfrac{1}{2}(p+\rho)\nu' \quad (7)$$

$$\dot{\rho}=-\tfrac{3}{2}(p+\rho)\dot{\mu}. \quad (8)$$

These two equations are however not independent of Eqs. (3)–(6) and can be obtained directly from them.

Differentiating (8) with respect to r and substituting for p' from (7) and then eliminating ν' with the help of (6), we get,

$$\dot{\rho}'=-\tfrac{3}{2}\rho'\dot{\mu}. \quad (9)$$

Or,

$$(\partial/\partial t)(\log|\rho'|)=-\tfrac{3}{2}\dot{\mu}. \quad (10)$$

We assume, as seems reasonable, that a small perturbation does not reverse the expanding nature of the space at the point under consideration. This would obviously be true at least at those early stages when the rate of expansion was very large.[10] $\dot{\mu}$ is therefore positive, and Eq. (10) shows that the nonhomogeneity as measured by ρ' would decrease with time. Thus, if one takes the gradient of density (or the difference of density between two points) as a measure of the degree of condensation (or rarefaction), then the condensation (or rarefaction) is smoothed out in an expanding space.

One may, however, define the degree of condensation also by ρ'/ρ, i.e., the percentage rate of change of density.[11] We get using (8) and (9),

$$(\partial/\partial t)(\rho'/\rho)=3\rho'\dot{\mu}p/2\rho^2.$$

Or,

$$(\partial/\partial t)(\log|\rho'/\rho|)=3\dot{\mu}p/2\rho. \quad (11)$$

Equation (11) shows that if ρ'/ρ be taken as a measure of the degree of condensation (or rarefaction), then in expanding space ($\dot{\mu}$ positive) the condensation (or rarefaction) would go on increasing with time.

We can therefore picture the consequence of a perturbation in the following way. In view of (10), the difference of density between any two points will go on decreasing, while (11) shows that the ratio of density at any two points diverges more and more from unity. Thus, consequent to an original perturbation in the early career of the universe, we should have at the present epoch a much smaller difference and a much larger ratio between the densities of the condensations and the background. These conclusions are not inconsistent with observation. For suppose that, when the density was very large, a perturbation in the density actually took place. This perturbation, although very small compared to the then prevailing density, might still conceivably be much larger than the present differences of density between the nebulae and the background. (E.g., a perturbation in density, say, of the order 10^{-12} g/cc, when the background density was of the order 10^6 g/cc, constitutes a small perturbation but is much larger than the present average densities of the nebulae.) The ratio of the perturbed density to the

[8] See reference 7, pages 301–302.
[9] See reference 7, pp. 251–252.

[10] Gamow's semiclassical investigations also confirm this point. See reference 3.
[11] This, in effect, has been done by Tolman and Sen. See references 1 and 2.

background density, while originally very nearly unity, has now a far greater value, in agreement with the requirement of (11).

The limit to the excess of density in the condensations being thus set by the magnitude of the original perturbation (and not the original density), one sees that in spite of condensations occurring in the highly dense cosmic fluid early in the life of the universe, condensations of high densities, as envisaged by Hoyle,[6] cannot be met with at present.

In conclusion, we note that a particularly satisfactory feature of the present investigation is that we have not introduced any assumption regarding the pressure, the pressure gradient, or the mechanism and nature of the original perturbation. We have also not introduced any nongravitational interaction.

PHYSICAL REVIEW VOLUME 86, NUMBER 1 APRIL 1, 1952

Convergence of Intermolecular Force Series*

FRANKLIN C. BROOKS†
Sloane Physics Laboratory, Yale University, New Haven, Connecticut
(Received November 23, 1951)

The commonly used perturbation method of estimating the Van der Waals forces between atoms is shown to lead, when carried to the extreme, to divergent results. The method employs an expansion of the classical electrostatic interaction between the atoms in a series of inverse powers of the internuclear distance. The divergence arises because this expansion is utilized in regions of configuration space where it is not convergent. In this paper, the resulting divergent intermolecular force series are shown to be asymptotic to the true molecular interaction. The divergence is removed in an approximate way and the second-order attractive energy so obtained is added to the first-order exchange energy between the atoms. The method results in an electronic energy curve for H_2^+ in reasonable accord with the exact result of Hylleraas and in a new interaction between helium atoms in good agreement with recent low temperature experiment.

I. INTRODUCTION

THE Van der Waals force between two atoms, at an internuclear distance R, is usually estimated by the use of an expansion of the classical electrostatic interaction between the atoms in a series of inverse powers of R. This expansion is considered as a perturbation upon the combined system of the two atoms and the Schrödinger perturbation theory or the variational method is employed to evaluate the resultant shift in energy levels. The shift is identified with the potential energy of the interatomic force.[1]

The expansion of the electrostatic interaction between the atoms is convergent and meaningful only in a limited region of the configuration space of the combined system. It is, however, commonly employed throughout this configuration space. This paper reports an investigation of the uncertainties arising from this procedure and suggests a method of overcoming them.

Let H_A and H_B be the (unperturbed) Hamiltonians of atoms A and B. The corresponding state functions and energy levels will be designated by $\psi_A^{(s)}$, $E_A^{(s)}$ and $\psi_B^{(t)}$, $E_B^{(t)}$, where s and t are quantum numbers. We shall refer the Hamiltonian and wave functions of each atom to a coordinate system (rectangular or spherical) with origin at its nucleus. The coordinates of charges e_i belonging to atom A are (x_i, y_i, z_i) or (r_i, θ_i, ϕ_i). Those of charges ϵ_j belonging to atom B are (ξ_j, η_j, ζ_j) or $(\rho_j, \omega_j, \chi_j)$. The z and ζ-axes are directed along the internuclear line from A to B.

The intermolecular force results when the electrostatic interaction

$$V=\sum_{i,j} e_i\epsilon_j/r_{ij} \tag{1}$$

between the atoms is taken as a perturbation on the compound system having the Hamiltonian H_A+H_B, state functions $\psi_A^{(s)}\psi_B^{(t)}$ and energy levels $E_A^{(s)}+E_B^{(t)}$.

In carrying out a perturbation or variational calculation (1) is usually expanded in a series of inverse powers of the internuclear distance. Margenau[2,3] has given some of the lower terms in this series:‡

$$\begin{aligned}V'=\cdots&-\frac{1}{R^3}\sum_{i,j} e_i\epsilon_j(2z_i\zeta_j-x_i\xi_j-y_i\eta_j)\\&+\frac{3}{2R^4}\sum_{i,j} e_i\epsilon_j[r_i^2\zeta_j-z_i\rho_j^2\\&+(2x_i\xi_j+2y_i\eta_j-3z_i\zeta_j)(z_i-\zeta_j)]\\&+\frac{3}{4R^5}\sum_{i,j} e_i\epsilon_j[r_i^2\rho_j^2-5z_i^2\rho_j^2-5r_i^2\zeta_j^2-15z_i^2\zeta_j^2\\&\qquad+2(4z_i\zeta_j-x_i\xi_j-y_i\eta_j)^2]+\cdots.\end{aligned} \tag{2}$$

* Part of a dissertation submitted to the Graduate School of Yale University in partial fulfillment of the requirements for the degree of Doctor of Philosophy.

† Now at the Atomic Power Division of the Westinghouse Electric Corporation, Pittsburgh, Pennsylvania.

[1] F. London, Z. Physik **63**, 245 (1930).

[2] H. Margenau, Phys. Rev. **38**, 747 (1931).

[3] H. Margenau, Revs. Modern Phys. **11**, 1 (1939).

‡ The symbol V' is used to denote an expanded form of V.

The terms in the series arise from the interaction of the various electric multipole moments of the two atoms. Those appearing in (2) are, respectively, the dipole-dipole, dipole-quadrupole, and quadrupole-quadrupole terms.

Recently Carlson and Rushbrooke[4] have generalized this result by deriving the following expansion in spherical coordinates:

$$V'=\sum_{i,j} e_i e_j \sum_{\lambda_A=0}^{\infty}\sum_{\lambda_B=0}^{\infty} \frac{r_i^{\lambda_A}\rho_j^{\lambda_B}}{R^{\lambda_A+\lambda_B+1}} Q_{\lambda_A\lambda_B} \times \sum_{\mu=-\lambda_<}^{\mu=+\lambda_<} \frac{Y_{\lambda_A}^{\mu}(\theta_i,\phi_i) Y_{\lambda_B}^{-\mu}(\omega_j,\chi_j)}{[(\lambda_A+\mu)!(\lambda_A-\mu)!(\lambda_B+\mu)!(\lambda_B-\mu)!]^{\frac{1}{2}}};$$

$$Q_{\lambda_A,\lambda_B}=\frac{(-1)^{\lambda_<}4\pi(\lambda_A+\lambda_B)!}{[(2\lambda_A+1)(2\lambda_B+1)]^{\frac{1}{2}}}. \tag{3}$$

In Eq. (3), $\lambda_<$ is the lesser of λ_A and λ_B. $Y_\lambda^\mu(\theta,\phi)$ is a normalized surface spherical harmonic. A term in Eq. (3) with specified values of λ_A and λ_B gives the interaction between the 2^{λ_A}-pole moment of atom A and the 2^{λ_B}-pole moment of B. If the atoms are electrically neutral, the monopole terms vanish when the summations over i and j are performed.

Expansions (2) and (3) are convergent and meaningful only in those regions of the configuration space of the compound system where the charge distributions of the two atoms do not overlap. If the expansions are used for all points of configuration space in the perturbation calculations, the resulting expressions for the interaction energy become the first terms of an infinite series which is divergent for all values of R.

In illustrating and investigating the significance of this fact we shall employ the Schrödinger perturbation theory only as far as the second-order correction. This will falsify those terms in the resulting intermolecular force series depending on R^{-9} and higher inverse powers of R. However, only the terms in R^{-6} and R^{-8} have been found to be of practical importance in calculations of the Van der Waals force between nonpolar molecules.

II. DIVERGENCE OF THE SECOND-ORDER PERTURBATION METHOD. INTERACTING HARMONIC OSCILLATORS

The interaction of simple harmonic oscillators is an example which occurs frequently in the literature of dispersion forces. Margenau,[5] using second-order perturbation theory, has found the dipole-dipole, dipole-quadrupole, and quadrupole-quadrupole interaction energies. We shall compute the complete second-order interaction energy and show that the resulting infinite series is divergent for all R.

For this purpose atoms A and B are taken to be three-dimensional isotropic oscillators of classical frequency ν. The wave functions of such an oscillator, in spherical coordinates, are of the form

$$\psi_{nlm}=S_{nl}(r)Y_l^m(\theta,\phi) \tag{4}$$

where $S_{nl}(r)$ is the normalized radial function. The energy levels are given by

$$E_{nl}=(2n+l+\tfrac{3}{2})h\nu \tag{5}$$

in which n and l are non-negative integers. The single selection rule which we shall have occasion to use is the following: The matrix element $(nlm|r^\lambda Y_\lambda^\mu|000)$ vanishes unless $n=0$, $l=\lambda$, and $m=\mu$.

If the oscillators are in their normal states, as we shall assume, the first-order perturbation caused by (2), or more generally (3), vanishes and the second-order perturbation energy becomes

$$\Delta E_2=-\sum_{\substack{n_A,l_A,m_A\\ n_B,l_B,m_B}}{}' \frac{|(n_Al_Am_A;n_Bl_Bm_B|V'|000;000)|^2}{E_{n_Al_A}+E_{n_Bl_B}-3h\nu}. \tag{6}$$

Taking the perturbing energy as given by Carlson and Rushbrooke, the matrix elements involved in (6) are all of the form

$$(n_Al_Am_A;n_Bl_Bm_B|r^{\lambda_A}\rho^{\lambda_B}Y_{\lambda_A}^{\mu}Y_{\lambda_B}^{-\mu}|000;000) =(n_Al_Am_A|r^{\lambda_A}Y_{\lambda_A}^{\mu}|000)(n_Bl_Bm_B|\rho^{\lambda_B}Y_{\lambda_B}^{-\mu}|000). \tag{7}$$

They vanish by virtue of the selection rule stated above unless $n_A=n_B=0$; $l_A=\lambda_A$, $l_B=\lambda_B$; $m_A=-m_B=\mu$. Therefore

$$(n_Al_Am_A;n_Bl_Bm_B|V'|000;000)=\frac{e^2}{R}\frac{Q_{l_Al_B}}{R^{l_A+l_B}} \times\frac{(0l_Am_A|r^{l_A}Y_{l_A}^{m_A}|000)(0l_Bm_B|\rho^{l_B}Y_{l_B}^{-m_A}|000)}{[(l_A+m_A)!(l_A-m_A)!(l_B+m_A)!(l_B-m_A)!]^{\frac{1}{2}}} \times\delta_{m_B,-m_A}\cdot\delta_{n_A,0}\cdot\delta_{n_B,0}. \tag{8}$$

Employing the selection rule and the rule for matrix multiplication:

$$|(0lm|r^lY_l^m|000)|^2 =\sum_{n\lambda\mu}(00|r^lY_l^{-m}|n\lambda\mu)(n\lambda\mu|r^lY_l^m|000) =(000|r^{2l}Y_l^mY_l^{-m}|000)=(000|r^{2l}|000)/4\pi. \tag{9}$$

The result of incorporating (8) and (9) in (6) is

$$\Delta E_2=-\frac{e^6}{h\nu R^2}\sum_{l_A,l_B,m_A}{}'\frac{(Q_{\lambda_A\lambda_B}/4\pi)^2}{R^{2\lambda_A+2\lambda_B}} \times\frac{(000|r^{2l_A}|000)(000|\rho^{2l_B}|000)}{(l_A+l_B)(l_A+m_A)!(l_A-m_A)!(l_B+m_A)!(l_B-m_A)!}. \tag{10}$$

[4] B. C. Carlson and G. S. Rushbrooke, Proc. Cambridge Phil. Soc. **46**, 626 (1950); see also the discussion in R. J. Buehler and J. O. Hirschfelder, Phys. Rev. **83**, 628 (1951).

[5] H. Margenau, J. Chem. Phys. **6**, 896 (1938).

The summation over m_A may now be performed by means of the relation,

$$\sum_{m_A=-l_<}^{m_A=+l_<}[(l_A+m_A)!(l_A-m_A)!(l_B+m_A)!(l_B-m_A)!]^{-1}=\frac{(2l_A+2l_B)!}{[(l_A+l_B)!]^2(2l_A)!(2l_B)!}, \quad (11)$$

which follows simply from the "addition theorem" for binomial coefficients. Introducing the explicit form of Q_{λ_A,λ_B} in (10), we obtain

$$\Delta E_2=-\frac{e^4}{h\nu R^2}\sum_{l_A,l_B}{}' \times\frac{(2l_A+2l_B)!(000|r^{2l_A}|000)(000|r^{2l_B}|000)}{(2l_A+1)!(2l_B+1)!(l_A+l_B)R^{2l_A+2l_B}}. \quad (12)$$

The ground-state wave function for the oscillator is

$$(000|=(\beta/\pi)^{\frac{3}{4}}\exp(-\tfrac{1}{2}\beta r^2);\quad \beta=e^2/\alpha h\nu \quad (13)$$

where α is the polarizability (classical as well as quantum) of the system. Hence,

$$(000|r^{2l}|000)=\beta^{-l}(2l+1)!/2^{2l}\,l!. \quad (14)$$

Substituting this result in (12) we find

$$\Delta E_2=-\frac{e^4}{h\nu R^2}\sum_{l_A,l_B}\frac{[2l_A+2l_B]!}{2^{2l_A+2l_B}l_A!l_B!(l_A+l_B)} \times\frac{1}{(\sqrt{\beta}R)^{2l_A+2l_B}}, \quad (15)$$

or, in terms of $L=l_A+l_B$,

$$\Delta E_2=-\frac{e^4}{h\nu R^2}\sum_{L=2}^{\infty}\frac{C_L}{(\sqrt{\beta}R)^{2L}};\quad C_L=\frac{(2L)!(2^L-2)}{2^{2L}\cdot L!\cdot L}. \quad (16)$$

When (16) is written out explicitly we obtain

$$\Delta E_2=-\frac{3}{2}\frac{e^4}{R^6}\frac{1}{2h\nu\cdot\beta^2}-\frac{45}{4}\frac{e^4}{R^8}\frac{1}{3h\nu\cdot\beta^3} -\frac{315}{8}\frac{e^4}{R^{10}}\frac{1}{4h\nu\cdot\beta^4}-\frac{4725}{16}\frac{e^4}{R^{12}}\frac{1}{5h\nu\cdot\beta^5} -\frac{322245}{32}\frac{e^4}{R^{14}}\frac{1}{6h\nu\cdot\beta^6}-\cdots. \quad (17)$$

The first three terms of this expansion are identical with those calculated by Margenau who employed them to estimate the magnitude of quadrupole contributions to the dispersion forces between real molecules.

The general term of (16), however, reveals the fact that the infinite series is divergent for all values of R. The behavior is not caused by any inherent divergence in the perturbation theory (because, after all, we have used only the second-order correction formula). Rather, it is caused by the use, in evaluating the matrix elements involved in (6), of the series expansions (2) or (3) in regions of configuration space where they are divergent and meaningless.

We have shown that the divergence occurs in the case of interacting oscillators where the wave function is comparatively "tightly bound," i.e., falls off as $\exp(-r^2)$. It will therefore occur *a fortiori* in a calculation of the interaction of real molecules where the wave functions fall off only as e^{-r}.

Since the divergence is associated with the limited region of validity of expansions (2) and (3), it will also effect a variational calculation which employs these expansions.

III. THE ASYMPTOTIC NATURE OF THE DISPERSION FORCE SERIES

The considerations of Sec. II suggest the following question: What is the relation of a divergent intermolecular force series $\sum C_j/R^j$ to the true atomic interaction $E(R)$? If the coefficients C_j are determined accurately, the series is asymptotic to $E(R)$ in the sense of Poincaré. This will now be proved in a simple manner.

An expansion of the form $\sum C_j/R^j$ is said to be asymptotic to a function $E(R)$ in the sense of Poincaré if, for every positive integral N,

$$\lim_{R\to\infty}R^N\left[E(R)-\sum_{j=0}^{N}C_j/R^j\right]=0, \quad (18)$$

or, equivalently

$$\left[E(R)-\sum_{j=0}^{N}C_j/R^j\right]=O(R^{-N-1}). \quad (19)$$

Such expansions are unique in the sense that a given function $E(R)$ has at most one.[6] They are useful for estimating values of $E(R)$ for large R.

If $\phi(R)$ is the true normalized ground-state function for the compound system of the two atoms and $\mathcal{H}=H_A+H_B+V$, then

$$E(R)=\int\phi^*\mathcal{H}\phi d\tau. \quad (20)$$

Let V_N' represent the series (3) up to and including the terms in R^{-N}. If we use V_N' instead of the true interaction V, we obtain

$$E_N'(R)=\int\phi^*\mathcal{H}_N'\phi d\tau \quad (21)$$

where $\mathcal{H}_N'=H_A+H_B+V_N'$. It is now easy to show that

$$E(R)-E_N'(R)=\int\phi^*[V-V_N']\phi d\tau \quad (22)$$

[6] E. T. Whittaker and G. N. Watson, *Modern Analysis* (Cambridge University Press, London, 1948), p. 153.

is $O(R^{-N-1})$. Within the region Ω of configuration space where the series (2) and (3) are convergent, $V-V_N'$ is $O(R^{-N-1})$ and therefore

$$\int_\Omega \phi^*[V-V_N']\phi d\tau = O(R^{-N-1}). \tag{23}$$

Since the wave function goes to zero exponentially at large distances, the integral over the remainder of configuration space is of the order of $\exp(-pR)$, $p>0$. Moreover,

$$E_N'(R) = T(R) + \sum_{j=0}^{N} C_j/R^j \tag{24}$$

where T is a term of order $\exp(-pR)$. Hence

$$\left[E(R) - \sum_{j=0}^{N} C_j/R^j\right] = O(R^{-N-1}).$$

We conclude that the dispersion force series, although divergent, are asymptotic to $E(R)$, and thus are the best possible representation of the atomic interaction in a series of inverse powers of R.

IV. REMOVAL OF THE DIVERGENCES. RECALCULATION OF THE POLARIZATION ENERGY COMPONENT OF THE PROTON-HYDROGEN ATOM BOND

The divergent, but asymptotic intermolecular force series may legitimately be used to estimate the force at sufficiently large values of R, providing not too many terms of the divergent series are employed. However, at small values of R even the first term in the series greatly overestimates the attractive force. Since the series are the best possible representation of $E(R)$ in a series of inverse powers of R, we must resort to a new form of expression for the interaction energy if the overestimate is to be eliminated.

The significance of these statements can be illustrated simply with reference to the hydrogen-molecule ion. We propose to study the polarization energy which accounts for a part of the strength of the bond in this molecule and which can be estimated mathematically in the same manner as intermolecular force.

Consider a hydrogen atom (A) and a proton (B). The electrostatic interaction V' between these systems may be written

$$V' = -\frac{1}{R}\sum_{\lambda=1}^{\infty}\left(\frac{r}{R}\right)^{\lambda} P_\lambda(\cos\theta), \quad r<R. \tag{25}$$

Atomic units are employed here. [Unit distance$=a$, the Bohr radius; unit energy$=e^2/a=27$ ev.] Expansion (25), to which (3) reduces in this case, is uniformly convergent for $r<R$.

The second-order perturbation caused by (25) is

$$\Delta E_2 = -\sum_j{}' \frac{|(j|V'|0)|^2}{E_j - E_0}. \tag{26}$$

Employing an approximation first used by Unsöld,[7] we replace each denominator in (26) by the constant ϵ, $\frac{3}{8}\leq\epsilon\leq\frac{1}{2}$. Then (26) becomes

$$\Delta E_2 = -(0|V'^2|0)/\epsilon. \tag{27}$$

With the use of the ground-state wave function for hydrogen, $e^{-r}/\sqrt{\pi}$, and the orthogonality property of the Legendre polynomials, the matrix element is found to be

$$(0|V'^2|0) = \frac{1}{R^2}\sum_{\lambda=1}^{\infty}\frac{(0|r^{2\lambda}|0)}{2\lambda+1}R^{-2\lambda}. \tag{28}$$

But

$$(0|r^{2\lambda}|0) = (2\lambda+2)!/2^{2\lambda+1}$$

and, hence,

$$\Delta E_2 = -\frac{1}{\epsilon R^2}\sum_{\lambda=1}^{\infty}\frac{(2\lambda+2)!}{2^{2\lambda+1}(2\lambda+1)}R^{-2\lambda}. \tag{29}$$

We now choose $\epsilon=4/9$ in order to bring the first term of (29) into accord with the known polarizability of the hydrogen atom. The first few terms of this expression then become

$$\Delta E_2 = -9/4R^4 - 81/8R^6 - 405/4R^8 - \cdots. \tag{30}$$

They are the monopole-dipole, monopole-quadrupole, and monopole-octopole terms. Series (29–30) are divergent, as a Cauchy ratio test shows. [This is to be expected since in evaluating the matrix element $(0|V'^2|0)$ we have integrated over all configuration space including regions for which $r>R$ and where V' is divergent and meaningless.]

Coulson[8] has calculated the interaction for this case without resort to Unsöld's approximation or specialization to second-order perturbation theory, but still employing (25) even outside its region of convergence. His ingenious, but laborious, method yields the again apparently divergent expression

$$-9/4R^4 - 15/2R^6 - 213/4R^7 - 7755/64R^8 - \cdots. \tag{31}$$

The H_2^+ case has been selected for consideration here because of the availability of an exact solution of the problem, as well as a reliable calculation of the first-order energy, against which to check the validity of the approximate methods widely in use for estimating Van der Waals forces. The exact interaction curve for the ground state has been computed by Hylleraas.[9] The first-order energy, to which ΔE_2 must be added to obtain an approximate total interaction curve, has been calculated by Pauling.[10] This energy which results from the simplest of molecular structure calculations is

$$\begin{aligned} \Delta E_1 &= (1/R) - (J+K)/(1+\Delta); \\ J &= 1/R - e^{-2R}(1+1/R); \\ K &= e^{-R}(1+R); \\ \Delta &= e^{-R}(1+R+\tfrac{1}{3}R^2). \end{aligned} \tag{32}$$

[7] A. Unsöld, Z. Physik **43**, 563 (1927).
[8] C. A. Coulson, Proc. Roy. Soc. Edinburgh **61**, 20 (1941).
[9] E. A. Hylleraas, Z. Physik **71**, 739 (1931).
[10] L. Pauling, Chem. Rev. **5**, 173 (1928).

TABLE I. H_2^+ electronic energy curve. The exact result of Hylleraas and various approximations. Energy is measured in units of $e^2/a=27$ ev, where $a=$Bohr radius.

$R(a)$	Hylleraas	$\Delta E_1+\Delta E_2$ (2 terms)	$\Delta E_1+\Delta E_2+\Omega$ (2 terms)	$\Delta E_1+\Delta E_2+\Omega$ (1 term)
1	+0.0477	−12.237	−0.028	+0.019
2	−0.1026	− 0.353	−0.123	−0.106
3	−0.0776	− 0.101	−0.084	−0.079
4	−0.041	− 0.051	−0.047	−0.045
5	···	− 0.023	−0.023	−0.023

The Pauling first-order energy ΔE_1 plus the first two terms of Eq. (30), i.e.,

$$\Delta E_1-9/4R^4-81/8R^8, \tag{33}$$

is compared with the Hylleraas energy in Table I. The tremendous overestimate of the polarization energy at small values of R is apparent. If more terms of (30) had been included the results would have been even worse.

The origin of the overestimate has been explained. We now propose to eliminate it in the following simple manner. In evaluating matrix element of V'[12] we shall limit the integration to the region $\Omega(r<R)$ of configuration space in which V' is convergent and entirely neglect contributions to the interaction energy arising from regions outside Ω. This procedure cannot be rigorously justified, although it is certainly more reasonable than the use of V' where it is divergent. (It should be noted that the whole concept of multipole interaction is only meaningful within the region of convergence of V'.)

The effect of this procedure is to replace the matrix elements $(0|r^{2\lambda}|0)$ in (28) by

$$(0|r^{2\lambda}|0)_\Omega=(0|r^{2\lambda}|0)\cdot\Gamma_{2R}(2\lambda+3)/\Gamma_x(2\lambda+3), \tag{34}$$

where

$$\Gamma_x(p+1)=\int_0^x e^{-t}\xi^p d\xi \tag{35}$$

is the incomplete Γ-function. The quotient $\Gamma_x(p+1)/\Gamma_\infty(p+1)=I(x,p)$ has been tabulated by Pearson.[11] It is always between zero and one and approaches unity as x increases, more slowly the larger the value of p. The higher multipole interactions are therefore reduced more by this correction. This is reasonable since these interactions received proportionately larger contributions from the region of configuration space where V' is divergent.

The new polarization force series resulting from the above steps is

$$\Delta E_{2,\Omega}=-\frac{1}{\epsilon R^2}\sum_{\lambda=1}^{\infty}\frac{(2\lambda+2)!}{2^{2\lambda+1}(2\lambda+1)}\frac{I(2R,2\lambda+2)}{R^{2\lambda}}. \tag{36}$$

This series is convergent for $R>0$. The Pauling energy plus the first two terms of $\Delta E_{2,\Omega}$ is tabulated in Table I. A marked improvement in the position of the minimum ($R\cong 2a$) and the depth of the minimum will be noticed, although the curve is still somewhat below that of Hylleraas. If only the first term of (36) is used in conjunction with the Pauling energy (Table I), a surprisingly accurate result is obtained, agreeing with the Hylleraas curve to within 5 percent everywhere around the minimum.

The conclusion to be drawn from these results is that the suggested procedure for removing the divergent behavior of the intermolecular force series greatly improves the quantitative accuracy of the perturbation method of estimating these forces. The uncorrected procedure makes increasingly larger errors in the higher multipole terms.

V. THE INTERACTION BETWEEN HELIUM ATOMS

The helium atom is structurally the simplest chemically saturated atom. The theory of Van der Waals forces thus meets its first important quantitative test in the case of the interaction between two helium atoms.[12]

A number of estimates of the dispersion force in the helium case have been made. Slater and Kirkwood[13] were the first to calculate the dipole-dipole component. They used a variational method. Margenau[2] subsequently recognized the importance of the higher multipole terms and employed second-order perturbation theory to compute the dipole-quadrupole and quadrupole-quadrupole interactions. A later re-examination of the problem by Margenau[14] resulted in the expression

$$E(R)=\{770e^{-4.00R}-560e^{-5.32R}-1.39R^{-6}-3.0R^{-8}\}\times 10^{-12}\text{ erg}. \tag{37}$$

(R in A.) The first term in (37) is the first-order exchange energy computed by Slater.[13] The second term is a small second-order exchange energy. The remaining terms are the dipole-dipole and dipole-quadrupole Van der Waals energies.

We propose to apply a correction of the type described in the preceding section to the Van der Waals force terms in (37).

[11] K. Pearson, ed., *Tables of the Incomplete Γ-function* (H. M. Stationery Office, London, 1922). Pearson actually tabulates $I(u,p)$, where $u=x/(p+1)^{\frac{1}{2}}$.

[12] The problem is complicated by uncertainties affecting the repulsive exchange force. Slater's calculation [Phys. Rev. **32**, 349 (1928)], which uses very accurate state functions, has been regarded as the most satisfactory. N. Rosen [Phys. Rev. **38**, 255 (1931)] in a recomputation has found a weaker repulsive force. Recently, P. Rosen [J. Chem. Phys. **18**, 1182 (1950)] has arrived at a much stronger force than either of the above. The value of this latter work is in its retention of higher exchange integrals which Slater neglects. This advantage may, however, be offset by his use of poorer wave functions. The results of the present paper seem to show that Slater's potential, when modified in accordance with Eq. (37), is essentially correct.

[13] J. C. Slater and J. G. Kirkwood, Phys. Rev. **37**, 682 (1931).

[14] H. Margenau, Phys. Rev. **56**, 1000 (1939).

If orbitals of the Slater type

$$\psi_0=(Z/\pi a^3)^{\frac{1}{2}}e^{-Zr/a}, \quad Z=27/16=1.688, \tag{38}$$

are employed for each electron in the two helium atoms, a straightforward application of second-order perturbation theory in conjunction with (2) or (3) yields for the dipole-dipole and dipole-quadrupole energies, the expression:

$$\Delta E_2=-A(0|r^2|0)^2R^{-6}-B(0|r^2|0)(0|r^4|0)R^{-8}. \tag{39}$$

A and B are constants, as are

$$(0|r^2|0)=\int_0^\infty \psi_0^2 4\pi r^4 dr=1.05a^2 \tag{40}$$

and

$$(0|r^4|0)=\int_0^\infty \psi_0^2 4\pi r^6 dr=2.79a^2. \tag{41}$$

We choose this form for ΔE_2 because it expresses the approximate dependence of the Van der Waals energy on the matrix elements $(0|r^2|0)$ and $(0|r^4|0)$. The integrations involved in these matrix elements extend over all configuration space, and therefore necessarily involve regions in which the dipole-dipole and dipole-quadrupole terms of V' as given by (2) or (3) are incorrect. A minimum region Ω of this space in which V' is convergent and in which these terms are accurate is that where the r for each electron is allowed to range only from 0 to $R/2$.

Therefore in Eq. (39) we replace $(0|r^2|0)$ and $(0|r^4|0)$ by

$$(0|r^2|0)_\Omega=\int_0^{R/2} \psi_0^2 4\pi r^4 dr \tag{42}$$

and

$$(0|r^4|0)_\Omega=\int_0^{R/2} \psi_0^2 4\pi r^6 dr. \tag{43}$$

We then adjust the constants A and B so that as R approaches infinity, the resulting expression agrees with the Van der Waals terms in (37), which is presumed to be accurate for sufficiently large R.

The effect of this procedure is, as before, the introduction of incomplete Γ-functions and (39) becomes

$$\Delta E_{2,\Omega}=\{770e^{-4.60R}-560e^{-5.33R}-1.39R^{-6}[I(x,4)]^2 -3.0R^{-8}[I(x,4)I(x,6)]\}\times 10^{-12}\ \text{erg} \tag{44}$$

with $x=ZR/a=3.191R$(A).

TABLE II. Interaction between helium atoms. Equations (37) and (44). Energy in ergs, R in A.

R(A)	Equation (37) $\Delta E_2\times 10^{16}$	Equation (44) $\Delta E_{2,\Omega}\times 10^{16}$
2.5	+ 7.74	+10.76
2.6	−15.49	− 3.37
2.7	−18.57	−10.60
2.8	−19.01	−13.76
2.9	−18.06	−14.57
3.0	−16.46	−14.13
3.2	···	−11.74
3.4	···	− 9.07

Equation (44) is tabulated in Table II along with Eq. (37). The new curve has a minimum at $R=2.9$A and an energy of -14.6×10^{-16} erg or -9.11×10^{-4} ev. It is in close agreement with low temperature experimental data. Buckingham, Hamilton, and Massey,[15] working with low temperature data, find for the position of the minimum $R_0=2.93$A and for the depth $E_0=-14.2\times 10^{-16}$ erg. Kistemaker and Keesom[16] studying the isotherms of helium from 2.7 to 1.7°K find $-E_0R_0^2=120\times 10^{-32}$ erg-cm^2. Equation (44) yields $-E_0R_0^2=123\times 10^{-32}$ erg-cm^2.

On the other hand, Schneider and Yntema,[17] on the basis of high temperature second virial coefficient measurements (0–1200°C), have recently reported a very much weaker helium atom interaction energy. They find that the values $E_0\cong -11\times 10^{-16}$ erg and $R_0\cong 3$A best fit their experimental data.

I wish to express my thanks to Professor Henry Margenau for directing my attention to the subject of intermolecular forces and for his advice and encouragement during the progress of this investigation. The work was completed under a Sterling Fellowship for which I am very grateful.

[15] Buckingham, Hamilton, and Massey, Proc. Roy. Soc. (London) **A179**, 103 (1941–42).
[16] J. Kistemaker and W. H. Keesom, Physica **12**, 227 (1946).
[17] J. L. Yntema and W. G. Schneider, J. Chem. Phys. **18**, 646 (1950).

The Nuclear Spectrum of Ge^{77}*

ALAN B. SMITH
Physics Department, Indiana University, Bloomington, Indiana
(Received December 3, 1951)

The disintegration of Ge^{77} (12 hour) has been studied with the help of a magnetic lens spectrometer, coincidence counters, and scintillation counters. The beta-ray spectrum consists of three groups of whose end-point energies are 2.196 Mev, 1.379 Mev, and 0.710 Mev. In addition there are 13 gamma-rays appearing in the product nucleus As^{77}, some of which are internally converted. By coincidence counting techniques it has been shown that the beta-ray of energy 2.196 Mev does not go to the ground state but to an excited state 0.264 Mev above the ground state. A disintegration scheme is suggested.

I. INTRODUCTION

EARLY work on germanium activities produced by cyclotron bombardment gave rise to somewhat conflicting results. Among several activities produced, one of approximately 12 hours half-life was assigned[1,2] to Ge^{77}. Work on fission products by Steinberg and Engelkemeir[3] established that Ge^{77} has a half-life of 12 hours and is the parent of a 40-hr As^{77}. They obtained a beta-ray end point by absorption of 2.0 Mev. Arnold and Sugarman[4] showed that in addition to the 12-hr period, there is an isomeric state of Ge^{77} having a half-life of 59 sec. They showed that this state decays, in part, directly to the ground state of As^{77} by the emission of a beta-ray whose end-point energy they determined by absorption to be 2.8 Mev. Finally, Mandeville, Woo, Scherb, Keighton, and Shapiro[5] studied the radiations from the 12-hr Ge^{77} by means of absorption and coincidence counting techniques. The end point of the beta-ray spectrum, which they obtained by absorption in aluminum, was 1.74 Mev. Coincidences were found between beta-rays and a gamma-ray, estimated to have an energy of approximately 0.5 Mev.

A detailed nuclear spectroscopic examination of the radiations from Ge^{77} was undertaken in order to determine its disintegration scheme. The determination of this scheme completes a group at mass number 77 consisting of As^{77}, Se^{77m}, and Br^{77} recently under investigation in this laboratory.

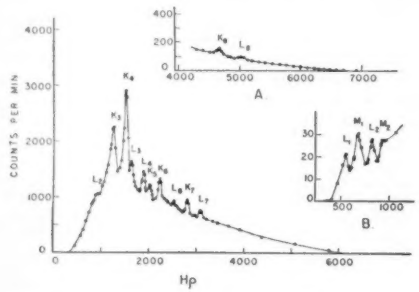

FIG. 1. Photoelectrons ejected by γ-rays of Ge^{77}.

II. METHOD OF PREPARATION OF SOURCES

Sources of the 12-hr Ge^{77} were prepared by bombarding germanium metal with deuterons in the Indiana University cyclotron. The germanium metal was dissolved in aqua regia, and arsenic carrier was added to the solution. The germanium was separated by distilling $GeCl_4$ from the solution in the presence of chlorine gas. The resultant germanium ion was precipitated as sulfide.

Germanium prepared in this manner contains, in addition to Ge^{77}, Ge^{71} (11 days), Ge^{75} (82 minutes), and some As^{77} which grows from the Ge^{77}. Since none of these isotopes except Ge^{77} emit gamma-rays, the material can be used directly to measure the gamma-ray spectrum. In order to investigate the beta-ray spectrum, the source was not separated until 12 hours after bombardment in order to let the Ge^{75} die out. The germanium was then separated from the arsenic and the beta-ray spectrum was measured over short periods of time so that the amount of As^{77} growing from the Ge^{77} would be negligible. Several sources were used in the measurement of the spectrum and a composite of the results prepared.

III. MEASUREMENT OF THE GAMMA-RAYS

The energies of the gamma-rays were determined by measuring the energies of secondary electrons ejected from lead or uranium radiators in a magnetic lens spectrometer. Figure 1 shows the results of a series of measurements taken in this way. The main curve of Fig. 1 was obtained using a lead radiator of surface density 16 mg/cm² and a counter window whose cutoff was about 16 kev. *K*-lines and, in most cases, the accompanying *L*-lines for five gamma-rays are shown on this curve. In addition there is evidence for an *L*-line (L_2) for a gamma-ray of low energy.

* Supported by the joint program of the ONR and AEC.
[1] Seaborg, Livingood, and Friedlander, Phys. Rev. **59**, 320 (1941).
[3] Sagane, Miyamoto, and Ikawa, Phys. Rev. **59**, 904 (1941).
[2] E. P. Steinberg and D. W. Engelkemeir, National Nuclear Energy Series, Plutonium Project Record, Vol. 9, Radiochemical Studies; The Fission Products, Paper No. 54 (McGraw-Hill Book Company, Inc., New York, 1951), p. 566.
[4] J. R. Arnold and N. Sugarman, J. Chem. Phys. **15**, 703 (1947).
[5] Mandeville, Woo, Scherb, Keighton, and Shapiro, Phys. Rev. **75**, 1528 (1949).

In order to investigate the part of the spectrum of low energy a thinner window, supported by a grid, was fitted to the counter. This window transmitted electrons of energy 5 kev or greater. The results of this investigation are shown in Curve *B* of Fig. 1, where it will be seen that *L* and *M* lines were found for gamma-rays having energies of 42 kev (L_1, M_1) and 73 kev (L_2, M_2).

In order to check the energies obtained using the lead radiator and to bring up lines of high energy and low intensity, an experiment was made using a uranium radiator of surface density 90 mg/cm². Curve *A* of Fig. 1 shows the high energy portion of this curve. The *K*- and *L*-lines designated as K_3, L_3 correspond to a gamma-ray of energy 1.105 Mev. In addition, it will be seen that there are Compton electrons for a weak gamma-ray of higher energy extending beyond the photolines for the gamma-ray at 1.105 Mev. The energy of this line, estimated from the energy of the Compton electrons, is 1.75 Mev.

The energies of these gamma-rays, together with some additional gamma-rays appearing as internal conversion lines in the electron spectrum, are shown in Table I. It is difficult to make an estimate of the relative intensities of the lines in a spectrum as complicated as this. Nevertheless, an attempt has been made to do this, using the photoelectric cross sections for lead obtained from Gray's curves. The results serve as a guide in constructing the decay scheme. The strongest line in the spectrum is that at 0.264 Mev. Those at 0.213 and 0.564 Mev are of about equal intensity, and each has an intensity about 0.6 that of the line at 0.264 Mev.

TABLE I. Energies of the gamma-rays from Ge^{77}.

Line No.	Energy[a] (Mev)	Line No.	Energy[a] (Mev)
(a) Lines obtained from measurement of photoelectrons.			
1	0.042	6	0.418
2	0.073	7	0.564
3	0.213	8	1.105
4	0.264	13 from Compton end point	1.75
5	0.368		...
(b) Lines obtained from measurements of internal conversion electrons.			
3	0.209	5	0.366
4	0.268	11	0.408
9	0.300	6	0.425
10	0.327	12	0.466

[a] Energies in this table are averages of all determinations from Pb and U radiations and internal conversion lines.

IV. THE BETA-RAY SPECTRUM

The measurement of the beta-ray spectrum posed a difficult problem. In the method of preparing the source, as mentioned earlier, there is always some Ge^{75} (82 min) produced. In order to get rid of the Ge^{75} activity, the source was allowed to decay for 12 hours after combardment before making a chemical separation. This, of course, decreased the initial activity of the Ge^{77} to one-half. The second difficulty concerns the growth of As^{77} from Ge^{77}. As^{77} is a pure beta-ray emitter having an end-point energy[6] of 0.700 Mev. Measurements on the Ge^{77} beta-spectrum at energies between 0.700 Mev and the end point (2.196 Mev) could therefore be made without interference from the beta-rays of As^{77}. At the lower energies, experiments were made in such a way that only a short time elapsed during the counting period so that the As^{77} did not have time to grow in appreciably. The sources consisted of a slurry of GeS_2 deposited on a thin zapon film.

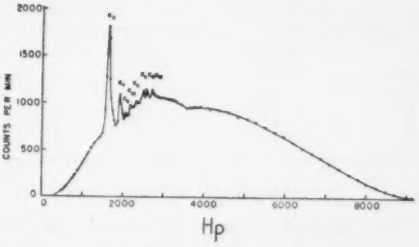

FIG. 2. Beta-spectra of Ge^{77}.

The results are shown in Figs. 2 and 3. Figure 2 is a plot of the beta-ray spectrum together with the internal conversion lines. The most intense internal conversion line corresponds to the gamma-ray of energy 0.213 Mev and the next intense to that of 0.264 Mev. The energies computed from the internal conversion lines are 0.209 and 0.268 Mev, in good agreement with the values obtained from the photoelectron spectrum. Of the remaining lines, those corresponding to gamma-ray energies of 0.366 and 0.425 Mev correspond to the gamma-rays obtained from the photoelectron spectrum with energies of 0.368 and 0.418 Mev. The other lines at 0.300, 0.327, 0.408, and 0.466 Mev were not seen in the photoelectron spectrum, possibly because of overlapping.

The results of a Fermi analysis of the data are shown in Fig. 3. It will be seen that there are three groups of beta-rays whose end-point energies, relative abundances, and log*ft* values are shown in Table II.

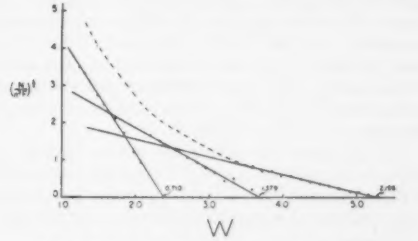

FIG. 3. Fermi analysis of beta-groups from Ge^{77}.

[6] R. Canada and A. C. G. Mitchell, Phys. Rev. **81**, 485 (1951).

TABLE II. Characteristics of the beta-ray spectrum.

Group	End-point energy (Mev)	Relative abundance (percent)	$\log_{10} ft$
1	2.196	42	7.6
2	1.379	35	6.6
3	0.710	23	5.7

V. COINCIDENCE EXPERIMENTS

From the large number of gamma-rays observed it is apparent that the disintegration scheme of Ge^{77} is quite complicated. In order to get a starting point for constructing the scheme, it is necessary to know whether or not the most energetic beta-ray leads to the ground state of As^{77}. In order to determine this, the coincidence experiments of Mandeville *et al.*[6] were repeated under somewhat better controlled conditions. The apparatus and procedures used in this experiment were the conventional ones which have been in use in this laboratory for a number of years.[7,8] A cylindrical lead cathode counter was used for counting gamma-rays and a counter with an end window of mica for counting beta-rays. Since some Ge^{71} was always present in the sources which were used, care had to be taken not to confuse the x-rays from Ge^{71} with the electrons from Ge^{77}. Since it was found[9] in an earlier experiment on Ge^{69} that 0.10-cm aluminum reduced the x-ray count from Ge^{71} to a negligible value, coincidence experiments were made at absorber thicknesses greater than this. A curve showing the number of beta-gamma coincidences ($N_{\beta\gamma}/N_\beta$) against absorber thickness in cm aluminum, from 0.25- to 0.29-cm of aluminum, is shown in Fig. 4. This region corresponds to energies greater than 1.38 Mev, the end point of the middle group, out toward the end point of the highest energy group. It will be seen that beta-gamma coincidences are present and that the number per disintegration is independent of the energy over this region. This shows that the beta-ray group of highest energy does not go the ground state.

VI. DISCUSSION

From the data given in the preceding sections it is possible to construct a decay scheme which gives a good energy fit with the gamma-ray and beta-ray data and is consistent with the relative intensities of the gamma-rays as far as they can be determined. The scheme which results from these considerations is extremely complicated and for this reason must be considered as tentative. It is shown in Fig. 5.

Leaving aside that part of the scheme having to do with the isomeric state of Ge^{77} of half-life 59 sec, which will be discussed later, it has been shown that the beta-ray transition of energy 2.196 Mev does not lead to the ground state. Since the most intense gamma-ray is that whose energy is 0.264 Mev, it probably lies at the bottom of the scheme as shown. This gamma-ray and the highest energy beta-ray fix the energy of the ground state of Ge^{77} at 2.460 Mev. The remaining two beta-rays determine levels in As^{77} at 1.750 and 1.10 Mev from which there are gamma-rays to the ground state. The remaining gamma-rays are placed in the scheme in such a way as to give the best fit energy-wise. The fit is good to about 2 percent in the worst case.

It is surprising that two such low energy gamma-rays as those of energies 0.042 and 0.073 Mev occur so high up in the scheme and in addition are not appreciably internally converted. A test of this scheme would be to show that the 0.073-Mev gamma-ray is in coincidence with those of 0.564-Mev or of 0.213-Mev and 0.264-Mev energy. Such an experiment has been performed for us by Mr. M. M. Miller of this laboratory with two crystal counters in coincidence, and indeed shows that the 0.073-Mev line is in coincidence with those at 0.213 and 0.264 Mev. This experiment is described in the Appendix.

The energy level diagram also shows the energy relation between the 59-sec isomeric state of Ge^{77} and the ground state. Experiments by Arnold and Sugarman[4] have shown that the 59-sec state of Ge^{77} decays to the ground state of As^{77} with the emission of a 2.8-Mev beta-ray. Mitchell and Smith[10] have measured the energy of the gamma-ray transition between 59-sec and 12-hr states of Ge^{77} by means of a scintillation spectrograph and have found a value of 0.380 ± 0.020 Mev. Since the value of $\log ft$ for the 59-sec beta-transition is 4.8, the transition is characterized by no change in parity and $\Delta j = 0, \pm 1$. Since the ground state of As^{77} has the configuration $p_{3/2}$, the 59-sec metastable state has the configuration $p_{1/2}$.

From the results of the present work considered in the light of the shell theory, it is possible to give the configurations of the two lowest states as As^{77} and that of the ground state of Ge^{77}. The ground state of As^{77} is known to have a configuration $p_{3/2}$. From shell model predictions the first excited state of As^{77} would be expected to have the configuration $f_{5/2}$. Ge^{77} has 45 neutrons or 7 neutrons beyond neutron number $N=38$. One would expect the configuration of one of the

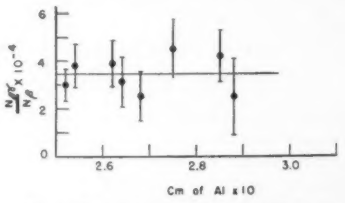

FIG. 4. Beta-gamma coincidences in Ge^{77}.

[7] A. C. G. Mitchell, Revs. Modern Phys. **20**, 296 (1948).
[8] J. L. Meem, Jr., and F. Maienschein, Phys. Rev. **76**, 328 (1949).
[9] C. M. Huddleston and A. B. Smith, Phys. Rev. **84**, 289 (1951).
[10] A. C. G. Mitchell and A. B. Smith, Phys. Rev. **85**, 152 (1952).

isomeric[10,11] states, the lower one in this case, to be $G_{7/2}$ and the other $p_{1/2}$. The present experiments are consistent with this assumption. The beta-ray transition leading from the ground state of Ge^{77} to the first excited state of As^{77} shows a $\log ft = 7.6$ and has an allowed shape, which is consistent with a transition of the type $\Delta j = \pm 1$, yes. If, on the other hand, the ground state of Ge^{77} had the configuration $g_{9/2}$, the beta-ray spectrum would have a forbidden shape ($\Delta j = \pm 2$, yes) and a much larger value of $\log ft$. The present experiments are therefore consistent with the configurations predicted by the shell model and shown in Fig. 5 for the two states of Ge^{77} and the ground and first excited states of As^{77}. It is impossible at the present time to predict the configurations of the many other excited states of As^{77}.

The author wishes to express his thanks to Dr. A. C. G. Mitchell, who suggested this problem, for help and suggestions during the carrying out of the experiments, to Mr. C. M. Huddleston for taking some of the readings, and to Mr. A. E. Lessor for making the chemical separations. He also wishes to thank Dr. M. B. Sampson and the cyclotron crew for making the bombardments. He also wishes to acknowledge that two sources of Ge^{77} irradiated by neutrons in a pile were received, one from the Oak Ridge National Laboratory and one from the Argonne National Laboratory. Unfortunately neither of these sources was strong enough to measure.

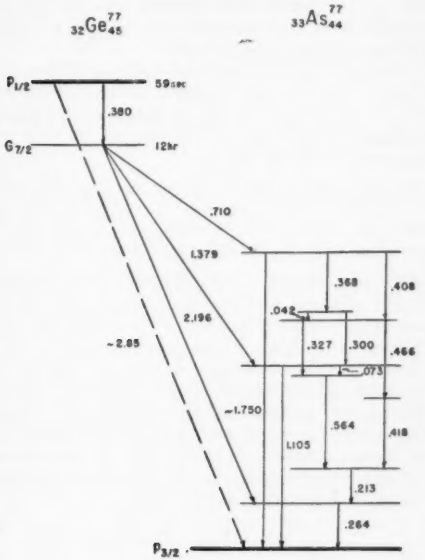

FIG. 5. Tentative decay scheme of Ge^{77}.

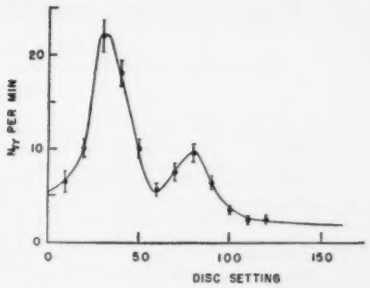

FIG. 6. Gamma-gamma coincidences in Ge^{77} obtained with scintillation counter.

APPENDIX

The proposed disintegration scheme of Ge^{77} assumes that a gamma-ray of energy 0.073 Mev lies high in the disintegration scheme and is in cascade with lines at 0.263 and 0.213 Mev. A test of this part of the scheme would be to show that the 0.073-Mev line is in coincidence with the lines at 0.263 Mev or 0.213 Mev or both.

The apparatus consisted of two scintillation counters with NaI(Tl) crystals and 5819 photomultiplier tubes.[12] The output of each tube was fed through a linear amplifier to a differential pulse-height discriminator and then to either a scalar or a fast coincidence circuit. After a preliminary investigation of the peaks obtained in the singles channels, channel 1 was set on the high side of the peak arising from the 0.263-Mev and 0.213-Mev lines, and the coincidences were measured when channel 2 was run over the spectrum. The result is shown in Fig. 6, in which the number of coincidences per minute is plotted against the dial setting in channel 2. It will be seen that two well-defined peaks occur. The peak at dial setting 30 corresponds to a gamma-ray of approximately 0.070 Mev, while that at dial setting 80 corresponds to a gamma-ray of energy about 0.21 Mev. This shows that the lines at 0.073 Mev and 0.213 Mev are in coincidence with that at 0.263 Mev, as is required by the decay scheme.

[11] M. Goldhaber and A. W. Sunyar, Phys. Rev. **83**, 906 (1951).

[12] For a description of the method see Miller, Pruett, and Wilkinson, Phys. Rev. **84**, 849 (1951).

Positive Ions in the Afterglow of a Low Pressure Helium Discharge*

ARTHUR V. PHELPS† AND SANBORN C. BROWN
Research Laboratory of Electronics, Massachusetts Institute of Technology, Cambridge, Massachusetts
(Received December 26, 1951)

The production and loss of He^+ and He_2^+ ions in the afterglow of a low pressure helium discharge are studied using a mass spectrometer to analyze the positive ions and microwave techniques to determine the electron density. The change of positive ion and electron density with time is explained by considering three dominant processes in the afterglow: the production of He^+ ions and electrons by collisions between pairs of metastable atoms, the ambipolar diffusion of the ions and electrons, and the conversion of He^+ ions to He_2^+ ions by three-body collisions with neutral atoms. The time constants for the decay of the electron density at low pressures yield the ambipolar diffusion coefficient for He^+ ions of 560 cm²/sec and a frequency for the conversion of He^+ ions into He_2^+ ions of 65 sec^{-1}, both at 1 mm pressure and 300°K. The mobility coefficient for He^+ ions in helium obtained from the measured ambipolar diffusion coefficient is 14 cm²/volt-sec at 300°K and 760-mm pressure and agrees satisfactorily with the value of 12 cm²/volt-sec calculated using the quantum-mechanical interaction of the He^+ ion and the neutral helium atom.

I. INTRODUCTION

RECENT measurements of the ambipolar diffusion coefficient[1] and the drift velocity[2] of helium positive ions in helium have yielded respective mobility values of 13.7 and 12 cm²/volt-sec at 300°K and 760 mm. These values are in agreement with the theoretical value of 12 cm²/volt-sec obtained using a quantum mechanical evaluation of the interaction between atomic helium ions and neutral helium atoms.[3] This agreement provides further indirect evidence in favor of the proposal[4] that the molecular helium ion was responsible for the large mobility value of 22 cm²/volt-sec obtained from previous measurements[5] of the drift velocity of helium ions. The experiment to be described in this paper was designed to test this hypothesis by providing for simultaneous measurement of the ambipolar diffusion coefficient and identification of the positive ions which reach the walls of the diffusion vessel. The ambipolar diffusion coefficient is obtained from the rate of decay of the electron density during the afterglow of a pulsed helium discharge. The positive ions which diffuse to the walls are analyzed with a mass spectrometer.

II. THEORY OF AFTERGLOW PROCESSES

The important processes in the afterglow of a low pressure helium discharge appear to be the ambipolar diffusion of the positive ions and electrons, the conversion of the helium atomic ions into molecular ions, and the production of ions and electrons as a result of collisions between pairs of metastable atoms. Recombination between electrons and ions is not included in this discussion, since it was not found to be significant under the conditions of these experiments. We will consider first the ambipolar diffusion of electrons and two types of positive ions and then solve for the time dependence of the metastable, atomic, and molecular ion, and electron concentrations.

The loss of positive ions and electrons to the walls of the discharge vessel is found by solving for the flow of particles under the action of the combined density gradients ∇n and the space charge field $\mathbf{E}$. The particle current densities $\mathbf{\Gamma}$ are

$$\mathbf{\Gamma}_-=-D_-\nabla n_- - \mu_-\mathbf{E}n_-, \quad \mathbf{\Gamma}_1=-D_1\nabla n_1+\mu_1\mathbf{E}n_1,$$
$$\text{and} \quad \mathbf{\Gamma}_2=-D_2\nabla n_2+\mu_2\mathbf{E}n_2, \tag{1}$$

where the subscripts $-$, 1, and 2 refer to the electrons, atomic ions, and molecular ions, respectively. The D's are diffusion coefficients and the μ's are mobility coefficients. In the limit of large densities of charged particles, the difference density required to maintain the space charge field is small; i.e., $n_1+n_2-n_-\ll n_-\approx n_1+n_2$. The particle currents may then be assumed to satisfy the condition of $\mathbf{\Gamma}_1+\mathbf{\Gamma}_2=\mathbf{\Gamma}_-$. If it is also assumed that the spatial distributions of the ions and electrons are the same so that $\nabla n_1/n_1=\nabla n_2/n_2=\nabla n_-/n_-$, the solution for the electric field from Eqs. (1) is

$$\mathbf{E}=\frac{D_1n_1+D_2n_2-D_-n_-}{\mu_1n_1+\mu_2n_2+\mu_-n_-}\frac{\nabla n_-}{n_-}. \tag{2}$$

As the diffusion and mobility coefficients for the positive ions are small compared to those for the electrons, Eq. (2) reduces to

$$\mathbf{E}=-(D_-/\mu_-)(\nabla n_-/n_-). \tag{3}$$

Substitution of Eq. (3) into Eqs. (1) gives

$$\mathbf{\Gamma}_1=-[D_1+\mu_1(D_-/\mu_-)]\nabla n_1=-D_{a1}\nabla n_1$$
$$\text{and} \quad \mathbf{\Gamma}_2=-[D_2+\mu_2(D_-/\mu_-)]\nabla n_2=-D_{a2}\nabla n_2. \tag{4}$$

These equations show that the two types of ions diffuse

* This work has been supported in part by the Signal Corps, the Air Materiel Command, and the ONR.
† Now at Westinghouse Research Laboratories, East Pittsburgh, Pennsylvania.
[1] M. A. Biondi and S. C. Brown, Phys. Rev. **75**, 1700 (1949).
[2] J. A. Hornbeck and G. H. Wannier, Phys. Rev. **82**, 458 (1951).
[3] H. S. W. Massey and C. Mohr, Proc. Roy. Soc. (London) **A144**, 188 (1934).
[4] R. Meyerott, Phys. Rev. **70**, 671 (1946).
[5] A. M. Tyndall and C. F. Powell, Proc. Roy. Soc. (London) **A134**, 125 (1931).

independently of each other with ambipolar diffusion coefficients D_{a1} and D_{a2} which are characteristic of the respective ions. These current equations will be substituted into the continuity equations for the two ions and solutions obtained for the positive ion densities as a function of time. The electron density is found by adding the positive ion densities.

The production of ions and electrons as a result of collisions between pairs of metastable atoms according to the reaction $He^M+He^M \rightarrow He^+ + e + He$ has been studied by Biondi.[6] The observed variation of the electron density with time was found to be consistent with the assumption that the loss of metastables by diffusion to the walls and by some unspecified linear volume loss was large compared to the loss due to metastable-metastable collisions. The rate of increase of the metastable concentration is

$$\partial M/\partial t = D_M \nabla^2 M - GM, \tag{5}$$

where M is the metastable concentration, D_M is the diffusion coefficient, and G is the volume loss coefficient. If the metastable concentration at the walls of a cylindrical cavity of height L and radius R is assumed to be zero, the solution to Eq. (5) is

$$M = M_{00} \exp(-t/T_M) \cos(\pi z/L) J_0(2.4r/R) = M_0 \exp(-t/T_M), \tag{6}$$

where $1/T_M = D_M/\Lambda^2 + G$, $1/\Lambda^2 = (\pi/L)^2 + (2.4/R)^2$, and the high order diffusion modes have been neglected.

The He^+ ions are assumed to be produced by metastable-metastable collisions and lost by diffusion to the walls and conversion to molecular ions[7] He_2^+, according to the reaction $He^+ + 2He \rightarrow He_2^+ + He$. The rate of increase of the atomic ion concentration is then

$$\partial n_1/\partial t = D_{a1} \nabla^2 n_1 - \eta n_1 + \beta M^2. \tag{7}$$

Here η is the frequency of conversion of atomic ions into molecular ions and βM^2 is the rate of He^+ production by metastables. We will solve Eq. (7) under the assumption that the positive ion density has the same distribution in space as the metastable concentration in Eq. (6). An exact solution shows that the changes in the spatial distribution resulting from the M^2 term produce a negligible effect on the time variation of the positive ion currents and the average electron density. The atomic ion concentration is then given by

$$n_1 = (n_{10}+A) \exp(-t/T_1) - A \exp(-2t/T_M), \tag{8}$$

where n_{10} is the initial atomic ion density,

$$A = \beta M_0^2 (2/T_M - 1/T_1)^{-1} \quad \text{and} \quad 1/T_1 = D_{a1}/\Lambda^2 + \eta.$$

The molecular helium ions produced by conversion from the atomic ions are lost by diffusion to the walls. Thus, the rate of increase of the molecular ion density is given by

$$\partial n_2/\partial t = D_{a2} \nabla^2 n_2 + \eta n_1. \tag{9}$$

The solution to Eq. (9) is

$$n_2 = (n_{20} + Bn_{10} + BC) \exp(-t/T_2) - B(n_{10}+A) \exp(-t/T_1) + B(A-C) \exp(-2t/T_M), \tag{10}$$

where n_{20} is the initial molecular ion density,

$$B = \eta (1/T_1 - 1/T_2)^{-1}, \quad C = \beta M_0^2 (2/T_M - 1/T_2)^{-1},$$

and $1/T_2 = D_{a2}/\Lambda^2$. The electron density is found by adding Eqs. (8) and (10) to get

$$n_- = [n_{20} + Bn_{10} + BC] \exp(-t/T_2) + [1-B][n_{10}+A] \exp(-t/T_1) - [(1-B)A + BC] \exp(-2t/T_M). \tag{11}$$

The positive ion current which diffuses to the cavity wall and into the mass spectrometer is found by substituting Eqs. (8) and (10) into Eqs. (4). For the simple spatial distribution assumed above, the positive ion current densities at the mass spectrometer entrance are $D_{a1}\pi/L$ or $D_{a2}\pi/L$ times the respective ion concentrations.

The smooth curves of Fig. 1 show semilogarithmic plots of the time variation of the electron, He^+ and He_2^+ densities predicted by Eqs. (8), (10), and (11) for a pressure of 3 mm. The constants used for this calculation are: $D_{a1}p = 540$ cm²-mm of Hg/sec, as measured by Biondi and Brown;[1] $D_{a2}p = 840$ cm²-mm of Hg/sec, as calculated from the results of Tyndall and

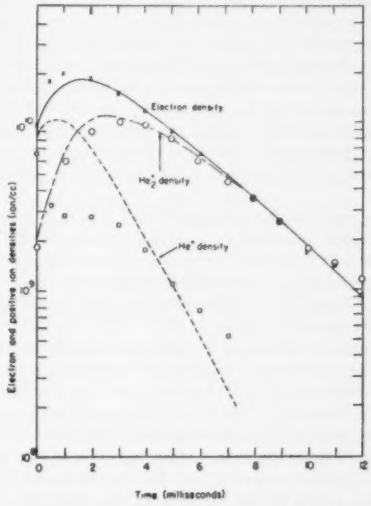

FIG. 1. Theoretical curves and experimental points showing electron, He_2^+, and He^+ densities during the afterglow in helium at 3 mm of Hg pressure.

[6] M. A. Biondi, Phys. Rev. **82**, 453 (1951).
[7] D. R. Bates, Phys. Rev. **77**, 718 (1950).

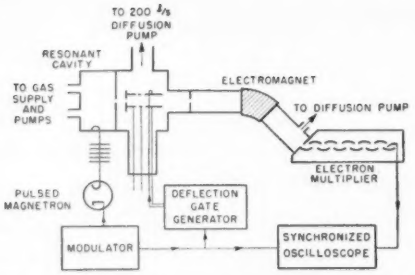

FIG. 2. Block diagram of apparatus used for observing positive ions present during the afterglow.

Powell,[5] $\eta = 65p^2$, as found from these experiments; and $D_M p = 520$ cm²-mm of Hg/sec and $G = 100p$ sec^{-1}, as measured by Biondi.[6] The initial conditions for Fig. 1, $n_{10} = 10^{10}$ ions/cc, $n_{20} = 2\times10^9$ ions/cc, and $C = 2.5\times10^{10}$ cc^{-1}, were chosen to fit the theory to the experimental electron density and molecular ion current curves at $t = 0$ and at times late in the afterglow.

III. EXPERIMENTAL APPARATUS

The electron density during the afterglow of the helium discharge was calculated from measurements of the shift in the resonant frequency of the microwave cavity which contained the discharge. The arrangement of the microwave apparatus was the same as that described by Biondi and Brown[1] except that the cavity resonance was indicated by the maximum in the signal transmitted through the cavity.

The positive ions present during the afterglow were observed with the apparatus outlined in Fig. 2. The helium discharge occurs in a microwave cavity resonant at about 10-cm wavelength. A 4-mil diameter hole in the end of the cavity allows some of the ions which diffuse to the wall to enter the focusing region of the mass spectrometer. The gas which enters the spectrometer is removed by a 200 liter/sec oil diffusion pump.

The positive ions are accelerated first in a uniform field region and then in a three-electrode coaxial lens system which focuses the ions on the entrance slit of the spectrometer. The initial accelerating voltage is only 22.5 volts so as to prevent ionization in the intermediate pressure region. A set of deflecting electrodes is provided so as to align the ion beam with the entrance slit. The spectrometer is of the 60° deflection type and has a resolution of about 1 part in 100. The ions leaving the spectrometer are detected with an Allen type electron multiplier,[8] and the relative amplitude of the ion current is determined from the deflection of the trace of a cathode-ray oscilloscope. The modulator of Fig. 2 supplies pulses to the magnetron, the deflection gate generator, and the synchronized oscilloscope. The output of the deflection gate generator is connected to the deflection electrodes of the spectrometer so that by a suitable adjustment of bias voltages the ion current may be prevented from entering the spectrometer except during the 150-μsec gate. A plot of the height of the deflection of the oscilloscope trace during the gate as a function of time gives the time variation of the ion current.

The gas for these experiments is obtained from two-liter flasks of Air Reduction Sales Company spectroscopically pure helium and is supplied to the cavity through a capillary leak and a liquid helium trap. After a baking at about 270°C for several days, the filling system showed a rate of pressure rise of less than 5×10^{-7} mm Hg per hour. Observation with the mass spectrometer showed that at cavity pressures below 1.5 mm of Hg the positive ion current due to impurities was negligible throughout the afterglow. At the highest usable cavity pressures, about 5 mm, the impurity positive ion current reached as much as 10 percent of the helium ion current at times of the order of 15 milliseconds after the end of the discharge. He_3^+ or other complex helium ions were not observed.

IV. RESULTS

The general features of the theory developed above are confirmed by the measured electron density and ion currents as a function of time. The oscilloscope traces of the ion currents at various pressures as illustrated by the photographs of Fig. 3 show that the dominant ion changes from He^+ to He_2^+ as the pressure is increased from 1 to 5 mm. A more detailed comparison of the theory and experiment is possible when the ion

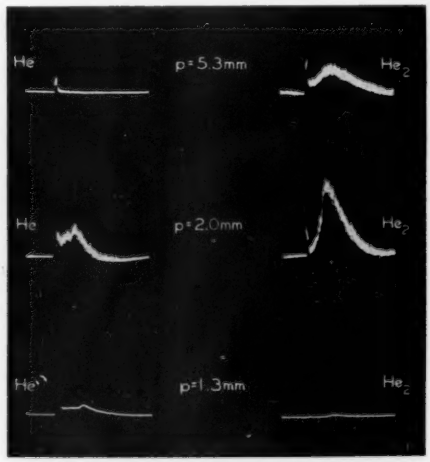

FIG. 3. Oscilloscope traces of helium ion currents as a function of pressure.

[8] J. S. Allen, Proc. Inst. Radio Engrs. **38**, 346 (1950).

current reaching the detector during the deflection gate is plotted along with the electron density measurements. In Fig. 1 the experimental ion current data are fitted to the electron density data at times late in the afterglow. The He^+ ion current readings are increased by the ratio of D_{a2}/D_{a1} so as to give curves of relative ion density rather than relative ion current and to make possible a direct comparison of theory and experiment. The experimental time variation of the electron and molecular ion densities is in general agreement with the theoretical curves. The atomic ion curve differs from the theoretical curve in shape as well as magnitude. Possible sources of the discrepancy in magnitude are differences in the sensitivity of the mass spectrometer and electron multiplier detector for atomic and molecular ions. As yet there is no satisfactory explanation for the discrepancy in the final slope of the He^+ ion current curve.

Equation (11) shows that the final decay of the electron density is determined by the time constant for the slowest loss process. This fact means that the electron density measurements can be used for quantitative determinations of the time constant for the loss of He^+ ions at low pressures where $T_1 > T_2 > T_M/2$. From Eq. (7)

$$1/T_1 = D_{a1}/\Lambda^2 + \eta = (D_{a1}p)/p\Lambda^2 + \zeta p^2, \qquad (12)$$

where $D_{a1}p$ and ζ are independent of pressure. This equation shows that a plot of p/T_1 *vs* p^2 should give a straight line with a slope ζ and intercept $D_{a1}p/\Lambda^2$ at zero pressure. Figure 4 shows such a plot for data taken with cavities for which $\Lambda^2 = 0.31$ cm² and $\Lambda^2 = 0.85$ cm². The average results are $D_{1a}p = 560 \pm 20$ (cm²-mm of Hg)/sec and $\zeta = 65 \pm 15$ sec^{-1} (mm of Hg)$^{-2}$. The ambipolar diffusion coefficient determined by this method is in very good agreement with the value of 540 ± 10 (cm²-mm of Hg)/sec reported by Biondi and Brown.[1] The leveling off of the p/T curves at high pressures indicates that the loss of He_2^+ ions has become slower than the loss of He^+ ions, i.e., $T_2 > T_1$. This transition occurs at very nearly the pressure predicted using the constants given in Sec. II.

If we make use of the fact that the electrons should reach thermal equilibrium with the gas within a few hundred microseconds after the discharge is turned off, the ambipolar diffusion coefficient is related to the positive ion mobility[1] by $D_a = 2D_+$ and $\mu_+ = D_+e/kT$. Here k is Boltzmann's constant and T is the absolute

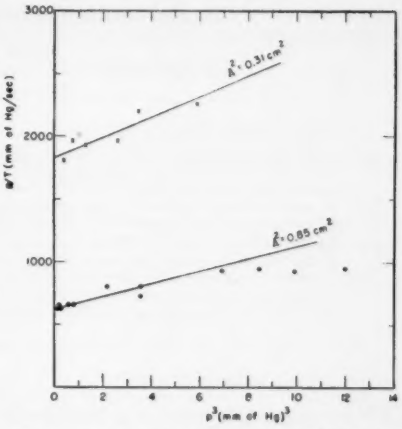

FIG. 4. p/T *vs* p^2 plot for determination of He^+ diffusion and ion conversion rates.

gas temperature. The mobility calculated from the above value of D_a is 14 cm²/volt-sec at 300°K and 760 mm. Thus we conclude that the quantum-mechanical value of 12 cm²/volt-sec for the mobility of the He^+ ion in helium obtained by Massey and Mohr[8] is in satisfactory agreement with experiment. Possible sources of the small discrepancy are the overestimation of the effects of charge transfer and a departure from the ambipolar condition near the walls of the microwave cavity.

The frequency of conversion of the atomic ions into molecular ions is between one-half and one-third the value predicted by Bates.[7] This discrepancy is not considered significant in view of the approximations made in solving this three-body collision problem using the Thomson recombination theory.[9] The measured rate for this reaction is about twice that found[10] for the similar reaction, $3H \rightarrow H_2 + H$. The rate of formation of He_2^+ given above is about five times the value estimated by Johnson, McClure, and Holt[11] from studies of the light output of the helium afterglow at a pressure of 27 mm.

[9] J. J. Thomson, Phil. Mag. **47**, 337 (1924).
[10] I. Amdur, J. Am. Chem. Soc. **60**, 2347 (1938).
[11] Johnson, McClure, and Holt, Phys. Rev. **80**, 376 (1950).

Meson-Nucleon Scattering and Nucleon Isobars*

KEITH A. BRUECKNER
Department of Physics, Indiana University, Bloomington, Indiana
(Received December 17, 1951)

The scattering (including charge exchange) of π^- mesons in hydrogen rises from 18 millibarns at 60 Mev to a broad plateau of about 60 millibarns at 200 Mev, and is smaller than the π^+ scattering at 60 Mev in the ratio of 0.63 ± 0.09. The general features of the π^- scattering, except for the high energy plateau, are given qualitatively by pseudoscalar theory with pseudovector coupling in the weak coupling limit; the ratio of π^- to π^+ scattering predicted by this theory in the weak coupling limit is, however, 1.67, which is much higher than the experimental result. A phenomenological theory of the scattering is developed by using the methods of Wigner and Eisenbud and imposing the restrictions of charge symmetry. By using the qualitative assignment of the resonance levels parameters as given by weak and strong coupling theory, satisfactory agreement with experiment is obtained. It is concluded that the apparently anomalous features of the scattering can be interpreted to be an indication of a resonant meson-nucleon interaction corresponding to a nucleon isobar with spin $\frac{3}{2}$, isotopic spin $\frac{3}{2}$, and with an excitation of 277 Mev.

I. INTRODUCTION

THE scattering[1] of π^- mesons in hydrogen has been studied experimentally by Anderson[2] at Chicago, and of π^- and π^+ mesons in hydrogen and deuterium by Sachs and Steinberger[3] at Columbia. The striking features of the results of these scattering experiments are

(a) the very rapid rise in the π^- total scattering cross section from 18 mb at 60 Mev to a broad plateau of 60 mb at about 200 Mev;

(b) the considerably larger scattering of π^+ than of π^- mesons in hydrogen at 60 Mev;

(c) the equality of the π^+ and π^- scattering in deuterium. The equality of the scattering in deuterium supports the hypothesis of charge symmetry, i.e., the (π^+, D) scattering is charge symmetric to the (π^-, D) scattering since it differs only in the sign of the meson charge. This important result is additional evidence that the neutron and proton are different charge states of a fundamental "nucleon" state. We shall not discuss the deuterium scattering further since it is the subject of a paper (to be published) by Isaacs, Sachs, and Steinberger.

The rapid rise in the π^- scattering cross section in hydrogen can be partially understood from the viewpoint of meson theory. From other experiments it is known that the meson has spin zero and is pseudoscalar; the scattering predicted by this theory with symmetric pseudovector coupling† is[4]

$$\frac{d\sigma}{d\Omega}(p+,p+)=\frac{d\sigma}{d\Omega}(p-,p-)=\frac{g^4k^4}{\omega^2\mu^4},$$
$$\frac{d\sigma}{d\Omega}(n0,p-)=\frac{2g^4k^4}{\omega^2\mu^4}\cos^2\theta, \tag{1}$$

if terms of the order ω/M are dropped; g^2 is the coupling strength, k the meson momentum, ω the meson total energy, and μ the meson mass.[5] These cross sections increase indefinitely with energy, which is of course physically inadmissable. The total cross section for π^- scattering (with the inclusion of charge exchange) is larger than the π^+ scattering in the ratio of 5 to 3, which is also in disagreement with the experimentally observed ratio of 0.63.

The failure of the weak coupling predictions suggests that an explanation of these apparently anomalous scattering phenomena may lie in a theoretical treatment which does not make the weak coupling approximation. One of the most characteristic features of the strong coupling theory of the pseudoscalar meson with pseudovector coupling[6] is the prediction of the existence of spin and charge isobars corresponding to resonant interactions of the meson with the nucleon. It will be shown that the introduction from a phenomenological viewpoint[7] of such resonance phenomena in a form consistent with both weak and strong coupling theory leads to a correct prediction of the general features of the observed scattering.[8]

* Supported in part by the joint program of the ONR and AEC.

[1] The experiments discussed measure only attenuation of a meson beam so that processes other than direct scattering occur, such as, in particular, the charge exchange scattering of π^- mesons in hydrogen.

[2] This work has been reported by H. L. Anderson in an invited paper at the Chicago Physical Society meeting, October 27, 1951, and has been submitted by Nagle, Anderson, Fermi, Long, and Martin in an abstract to the New York Physical Society meeting, January 31–February 2, 1952.

[3] A. Sachs and J. Steinberger, Phys. Rev. **82**, 958 (1951) and post dead-line paper at Chicago Physical Society meeting, October 29, 1951.

† This form of coupling is also called charge independent.

[4] We shall refer to the π^+ and π^- scattering in hydrogen as $\sigma(p+,p+)$ and $\sigma(p-,p-)$, respectively, and to the charge exchange scattering of π^- mesons as $\sigma(n0,p-)$.

[5] We take units such that $\hbar=c=1$.

[6] W. Pauli and S. M. Dancoff, Phys. Rev. **62**, 85 (1942).

[7] A phenomenological analysis of the type made in this paper has also been carried out for low energies by M. L. Goldberger, Phys. Rev. **83**, 239 (1951) and by Yoshio Yamaguchi, Osaka City University (private communication). The author is indebted to Professor Yamaguchi for a copy of his manuscript in advance of publication.

[8] Neutral-photomeson production also can be interpreted to be an indication of the existence of nucleon isobars; see K. A.

II. PHENOMENOLOGICAL DESCRIPTION OF SCATTERING

A. Cross Section for Scattering[9]

When the meson coupling is not weak, the complexity of the meson-nucleon interaction at small distances makes a detailed analysis of the phenomenon very difficult. The considerations of this region can, however, be avoided by substituting boundary conditions on the meson wave function at a radius **a** at which a simpler description is possible.[10] In particular, if this radius is chosen so that the meson-nucleon interaction is negligible in the external region, then the scattering is determined completely by the behavior of the logarithmic derivative of the meson-wave function at the radius **a**.

We shall assume that, as is characteristic of pseudoscalar theory with pseudovector coupling in nonrelativistic approximation, the meson interacts only in P-states of orbital angular momentum. This follows from any gradient coupling of the form given by pseudoscalar theory, $(\sigma\cdot\nabla\varphi)U$ (U the nucleon source density), if the meson wavelength is large compared with the source radius (usually assumed to be about $\hbar/Mc$). In addition, because of the possible coupling of nucleon-spin and meson-orbital momentum, we can in general expect different scattering in states of total angular momentum $J=\frac{1}{2}$ and $J=\frac{3}{2}$.

The states can also be characterized by a total isotopic angular momentum I in charge or isotopic space which is a constant of the system for a symmetric or charge independent theory.[11] We denote the meson-charge states by the eigenfunctions of the meson isotopic angular momentum $\varphi_1{}^M$, where $M=-1, 0, +1$ for positive, neutral, and negative pions, and the nucleon isotopic state by the isotopic spin function $l_{\frac{1}{2}}{}^\alpha$ where $\alpha=+\frac{1}{2}$ for neutrons and $-\frac{1}{2}$ for protons. The meson-nucleon states then are described by the wave functions in isotopic space $\varphi_1{}^M l_{\frac{1}{2}}{}^\alpha$. Expanding these states in the eigenfunctions $I_I{}^{I_z}$ of I and I_z, we have

$$\begin{aligned}
\varphi_1{}^{-1}l_{\frac{1}{2}}{}^{-\frac{1}{2}}&=(\pi^+,\ p)\text{ state}\\
&=I_{\frac{1}{2}}{}^{-\frac{1}{2}},\\
\varphi_1{}^{1}l_{\frac{1}{2}}{}^{-\frac{1}{2}}&=(\pi^-,\ p)\text{ state}\\
&=[I_{\frac{1}{2}}{}^{+\frac{1}{2}}+\sqrt{2}I_{\frac{1}{2}}{}^{\frac{1}{2}}]/\sqrt{3},\\
\varphi_1{}^{0}l_{\frac{1}{2}}{}^{\frac{1}{2}}&=(\pi^0,\ n)\text{ state}\\
&=[\sqrt{2}I_{\frac{1}{2}}{}^{\frac{1}{2}}-I_{\frac{1}{2}}{}^{\frac{1}{2}}]/\sqrt{3}.
\end{aligned}\tag{2}$$

Writing the matrix elements for scattering from the various initial to final states as $(p+|p+)$, $(p-|p-)$, and $(n0|p-)$, we find directly from these wave functions, using the conservation of isotopic angular momentum during the scattering process, the relations

$$\begin{aligned}
(p+|p+)&=(I_{\frac{1}{2}}|I_{\frac{1}{2}}),\\
(p-|p-)&=[(I_{\frac{1}{2}}|I_{\frac{1}{2}})+2(I_{\frac{3}{2}}|I_{\frac{3}{2}})]/3,\\
(n0|p-)&=[(I_{\frac{1}{2}}|I_{\frac{1}{2}})-(I_{\frac{3}{2}}|I_{\frac{3}{2}})]\sqrt{2}/3.
\end{aligned}\tag{3}$$

From these results we obtain the simple relations among the cross sections

$$\begin{aligned}
d\sigma(p+,\ p+)&=d\sigma_{\frac{3}{2}},\\
d\sigma(p-,\ p-)&=(1/9)[d\sigma_{\frac{3}{2}}+4d\sigma_{\frac{1}{2}}+4(d\sigma_{\frac{1}{2}}d\sigma_{\frac{3}{2}})^{\frac{1}{2}}\cos\varphi],\\
d\sigma(n0,\ p-)&=(2/9)[d\sigma_{\frac{3}{2}}+d\sigma_{\frac{1}{2}}-2(d\sigma_{\frac{1}{2}}d\sigma_{\frac{3}{2}})^{\frac{1}{2}}\cos\varphi],
\end{aligned}\tag{4}$$

where we have defined

$$d\sigma_{\frac{1}{2}}=|(I_{\frac{1}{2}}|I_{\frac{1}{2}})|^2,\quad d\sigma_{\frac{3}{2}}=|(I_{\frac{3}{2}}|I_{\frac{3}{2}})|^2,\tag{5}$$

and φ is an undetermined phase factor which may depend on the energy and angles. The combined ordinary and charge exchange scattering for negative mesons, however, is independent of the phase factor, the interference terms cancelling. It is also apparent that the condition of charge independence imposes no condition of equality of the positive and negative pion scattering. The ratio of these cross sections is

$$[d\sigma(p-,\ p-)+d\sigma(n0,\ p-)]/d\sigma(p+,\ p+)=\tfrac{1}{3}+\tfrac{2}{3}d\sigma_{\frac{1}{2}}/d\sigma_{\frac{3}{2}}$$

which can vary from $\frac{1}{3}$ to an arbitrarily large number. Some of this arbitrariness will be eliminated by imposing in the next section some additional restrictions on the cross sections.

We shall now characterize the scattering by the asymptotic phase shifts. Following the above analysis, we can expect separate phase shifts for the four states with $J=\frac{1}{2}, \frac{3}{2}$ and $I=\frac{1}{2}, \frac{3}{2}$. We assign phase shifts to the various states according to the scheme

$$\begin{aligned}
\delta_{++},&\quad J=\tfrac{3}{2},\quad I=\tfrac{3}{2},\\
\delta_{-+},&\quad J=\tfrac{1}{2},\quad I=\tfrac{3}{2},\\
\delta_{+-},&\quad J=\tfrac{3}{2},\quad I=\tfrac{1}{2},\\
\delta_{--},&\quad J=\tfrac{1}{2},\quad I=\tfrac{1}{2}.
\end{aligned}\tag{6}$$

The differential cross section for scattering in the state $I_{\frac{1}{2}}$ then is given by[12]

$$\begin{aligned}
k^2d\sigma_{\frac{1}{2}}/d\Omega=\cos^2\theta|\,&2e^{i\delta_{++}}\sin\delta_{++}+e^{i\delta_{-+}}\sin\delta_{-+}|^2\\
&+\sin^2\theta\sin^2(\delta_{++}-\delta_{-+})^2,
\end{aligned}\tag{7}$$

and a similar expression for scattering in the state $I=\frac{1}{2}$. The total cross sections that are of interest are combinations of the cross sections for scattering in the states $I=\frac{1}{2}$ and $I=\frac{3}{2}$ as given in Eqs. (4).

According to Feshbach, Peaslee, and Weisskopf,[10] the phase shifts (which we denote collectively by δ_λ) are given by the formula

$$\tan\delta_\lambda=\tfrac{1}{2}\Gamma_\lambda/(E_\lambda-E),\tag{8}$$

Brueckner and K. M. Case, Phys. Rev. **83**, 1141 (1951) and Y. Fujimoto and H. Miyazawa, Prog. Theoret. Phys. **5**, 1052L (1950).

[9] The considerations in this section are for scattering in the center-of-mass system.

[10] E. P. Wigner and L. Eisenbud, Phys. Rev. **72**, 29 (1947); Feshbach, Peaslee, and Weisskopf, Phys. Rev. **71**, 145 (1947).

[11] For a more detailed discussion of the theory of charge independence, see the paper of K. M. Watson and K. A. Brueckner, Phys. Rev. **83**, 1 (1951), and in particular of K. M. Watson, Phys. Rev. **85**, 852 (1952).

[12] See C. L. Critchfield and D. C. Dodder, Phys. Rev. **76**, 602 (1949), for a detailed derivative of a similar formula.

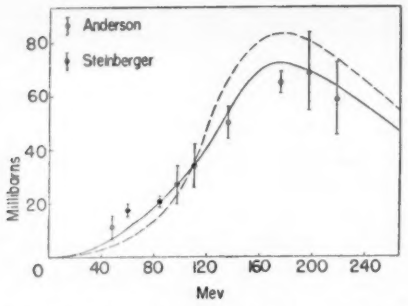

FIG. 1. The scattering of π^- mesons in hydrogen; the experimental points are those of Anderson (see reference 2) and Steinberger (see reference 3). The dashed curve is for $a^2\mu^2=0$, the solid curve for $a^2\mu^2=\frac{1}{2}$.

where

$$\Gamma_\lambda=-2k^3a^3/(1+k^2a^2)\gamma_\lambda, \tag{9}$$

and a is the radius of the boundary of the internal region. The constant γ_λ is determined by the boundary conditions at the radius a. Equations (7), (8), and (9) allow us to express the cross sections in terms of the resonance energies E_λ and the constants γ_λ.

B. Low Energy Limit and the Relation to Meson Theory

At low energies, the meson P-state interaction is weak and the weak coupling predictions for the ratios of the three scattering cross sections might be expected to hold qualitatively. This should also be true if the resonance energies are very large compared with the meson energies which, according to strong coupling theory, is equivalent to letting the coupling constant become very small. Therefore, we shall assume that in this limit the weak coupling prediction is correct and that

$$\begin{aligned} d\sigma(p+,\,p+)&=d\sigma(p-,\,p-),\\ d\sigma(n0,\,p-)&=2d\sigma(p+,\,p+)\cos^2\theta, \end{aligned} \tag{10}$$

and that $\sigma(p+,\,p+)$ is independent of angle. The differential cross section given in Eq. (7) reduces at low energies where, according to Eq. (9), the phase shifts approach zero, to

$$d\sigma_{\frac{1}{2}}/d\Omega=3\delta_{++}(\delta_{++}+2\delta_{-+})\cos^2\theta+(\delta_{++}-\delta_{-+})^2, \tag{11}$$

with a similar expression for $d\sigma_{\frac{1}{2}}/d\Omega$. Comparing this result with Eqs. (4) and (10), we find

$$\delta_{++}=-2\delta_{-+}=-2\delta_{+-}=-\tfrac{1}{2}\delta_{--}. \tag{12}$$

Accordingly, from Eq. (9) relating the phase shifts and resonance parameters, we have

$$\begin{aligned} \Gamma_{++}/E_{++}&=-2\Gamma_{-+}/E_{-+}=-2\Gamma_{+-}/E_{+-}\\ &=-\tfrac{1}{2}\Gamma_{--}/E_{--}\equiv 2\rho\equiv 2\rho_0^{\frac{1}{2}}k^3/[\mu^3(1+k^2a^2)], \end{aligned} \tag{13}$$

where the parameter ρ_0 defined by this equation is independent of the state and of energy. In this limit the low energy cross sections are

$$\frac{d\sigma}{d\Omega}(p+,\,p+)=\frac{9}{4}\frac{\rho_0^2k^4}{\mu^6}, \tag{14}$$

with related expressions for the other cross sections as given by Eq. (10). A comparison of this result with Eq. (1) shows that

$$(9/4)\rho_0^2\simeq g^4, \tag{15}$$

which gives an interesting relation between the resonance parameters and the coupling constant of weak-coupling meson theory. The close connection between meson theory and the more general form of the phenomenological resonance theory is also evident.

Using the restrictions of Eq. (13) on the resonance energies and widths, the total cross sections as a function of energy for meson energies not necessarily near zero are

$$\begin{aligned} \frac{\sigma(p+,\,p+)}{4\pi\lambda^2\rho^2}&=\frac{2}{\rho^2+(E/E_{++}-1)^2}+\frac{1}{\rho^2+4(E/E_{-+}-1)^2},\\ \frac{\sigma(p-,\,p-)+\sigma(n0,\,p-)}{4\pi\lambda^2\rho^2}&=\frac{2/3}{\rho^2+(E/E_{++}-1)^2}\\ &+\frac{1/3}{\rho^2+4(E/E_{-+}-1)^2}+\frac{4/3}{\rho^2+(E/E_{+-}-1)^2}\\ &+\frac{2/3}{\rho^2+(1/4)(E/E_{--}-1)^2}. \end{aligned} \tag{16}$$

To remove the arbitrariness which remains in the choice of the three resonance energies, we turn to strong coupling meson theory for a qualitative assignment of the levels. For symmetric pseudoscalar theory, Pauli and Dancoff give for the resonance energies

$$E_J=\tfrac{3}{2}(\mu^2a_0/g^2)[J(J+1)-\tfrac{3}{4}], \tag{17}$$

where J is the total angular momentum and a_0 is the source radius. The restriction is also imposed that the isotopic angular momentum I be equal to the angular

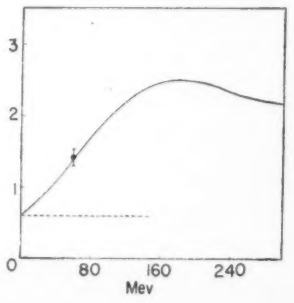

FIG. 2. The ratio of π^+ to π^- scattering, including charge exchange. The experimental point indicated is from the work of Steinberger (see reference 3).

momentum J. An isobar can therefore be excited only by scattering in the $J=\frac{3}{2}$, $I=\frac{3}{2}$ state. For the non-isobaric states, the energy E_λ is chosen to be $-\mu$, corresponding to the absence of isobaric states of the meson-nucleon system. This choice is consistent with the form of the equation given by weak or strong coupling theory. We shall make the assumption that these predictions of the strong coupling theory for the isobar energies are correct and show in the next section that satisfactory agreement with experiment can be obtained.

An additional interesting relation between the phenomenological theory and the weak and strong coupling theories is given by Eqs. (10), (14), (16), and (19) for ρ_0 and E_J. These give

$$\gamma_\lambda = -3a_0/(\mu a^3). \tag{18}$$

Wigner and Eisenbud[10] give for an approximate upper limit on γ_λ

$$-a\gamma_\lambda < (2\mu a)^{-1}. \tag{19}$$

Combining these equations and taking the source radius as the nucleon-Compton wavelength gives the result

$$\mu a > 0.74. \tag{20}$$

This approximate inequality can be satisfied if the boundary radius a is somewhat less than the meson-Compton wavelength, a distance consistent with the phenomenological treatment.

III. COMPARISON WITH EXPERIMENT

With the assignment of the resonance energies made in Sec. II, the total scattering cross sections are[9]

$$\frac{\sigma(p+,p+)}{4\pi\lambda^2\rho^2} = \frac{2}{\rho^2+(E/E_R-1)^2} + \frac{1}{\rho^2+4(\omega/\mu)^2},$$

$$\frac{\sigma(p-,p-)+\sigma(n0,p-)}{4\pi\lambda^2\rho^2} = \frac{2/3}{\rho^2+(E/E_R-1)^2} + \frac{5/3}{\rho^2+4(\omega/\mu)^2} + \frac{2/3}{\rho^2+(1/4)(\omega/\mu)^2}, \tag{21}$$

where E_R is the resonance energy for the $J=\frac{3}{2}$, $I=\frac{3}{2}$ state and $E+\mu=\omega$ is the meson total energy.

The variation of these cross sections with energy is given in Fig. 1, together with the experimental results. The resonance energy has been taken to be 137 Mev, corresponding to 200-Mev mesons in the laboratory system, and the boundary radius a such that $a^2\mu^2=\frac{1}{2}$. The corresponding value of ρ_0 is 0.23, corresponding to $g^2=0.35$ from Eq. (15). The general agreement of the theory with experiment is seen to be excellent except for somewhat too low values of the cross sections at low energies. The ratio of the π^+ to π^- scattering is given in Fig. 2; it is 0.60 at zero energy and then rapidly rises to nearly three at the higher energies. The value at

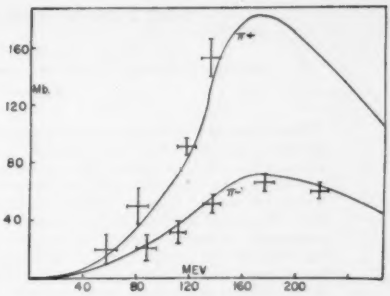

FIG. 3. Total cross sections for scattering of π^+ and π^- mesons in hydrogen (including charge exchange).

60–80 Mev varies from 1.41 to 1.77 which agrees with the ratio of 1.58 ± 0.24 reported by Steinberger for mesons in the energy rrange from 40 to 72 Mev.

IV. CONCLUSIONS

It is found that the steep variation of cross section with energy, the broad plateau suggesting a resonance peak of the π^- scattering at about 200 Mev, and the anomalous ratio of π^+ to π^- scattering can be interpreted to be an indication of the existence of an excited nucleon isobaric state. Assignment of the isobar to the state with total angular momentum $J=\frac{3}{2}$ and total isotopic angular momentum $I=\frac{3}{2}$ gives predictions in excellent agreement with experiment. Although the analysis is made phenomenologically, the parameters in the theory are adjusted to give low energy scattering which agrees with the predictions of symmetric weak-coupling theory and also to give an assignment of isobar energies which is qualitatively in agreement with the predictions of strong coupling charge-symmetric pseudoscalar theory.

The author is indebted to Professor Anderson, Professor Steinberger, and Professor Sachs for information on their experiments and to Professor K. M. Watson for valuable discussions on the theory of charge symmetry.

Note added in proof:—A number of recent measurements of the $(p+, p+)$ cross sections have been made by Anderson, Fermi, and collaborators [reported by H. L. Anderson at the Rochester Conference on Meson Physics, January 11–12, 1952] at Chicago. Their results are given in Fig. 3, together with the theoretical predictions. The charge exchange scattering of π^- mesons has also been measured at 115 Mev [Lundby, Fermi, Anderson, Nagle, and Yodh, Bull. Am. Phys. Soc. **27**, No. 1, 28 (1952)] and found to exceed the direct scattering in the ratio of 2 or 3 to one. The approximate ratios of the observed cross sections above 100 Mev, namely, $\sigma(p+,p+)$: $\sigma(p-,p-)$: $\sigma(n0,p-)=9:1:2$ are seen from Eq. (4) to follow directly from the assumption of predominant scattering in the $I=\frac{3}{2}$ state.

Fast Protons from 270-Mev n–d Collisions*

J. B. CLADIS, J. HADLEY,† AND W. N. HESS
Radiation Laboratory, Physics Department, University of California, Berkeley, California
(Received December 17, 1951)

The differential cross section for production of high energy protons in n-d scattering, using the 270-Mev neutron beam of the 184-in. cyclotron, has been measured at scattering angles between 4° and 58°. For normalization, yields of protons from n-p scattering were measured at each scattering angle. In all cases, only protons above a cut-off energy of 200 Mev $\cos^2\Theta$ were accepted by the counter system. In addition, through the use of a magnetic analyzer, energy distributions of the n-d protons were measured at 4° and 22.5°. The energy distributions closely resembled, in shape, the energy distributions of n-p protons at the same angles, confirming the similarity in nature between collisions of high energy neutrons with free protons and collisions with protons bound in deuterium. Total yield of protons above the cut-off energy is lower for n-d than for n-p collisions, however, the ratio of the two being about 0.7 at all angles observed. Effects of the exclusion principle, of the internal momentum distribution of the deuteron, and of the difference in average potential energy between the dineutron and the deuteron are discussed as possible causes of the lowering of the n-d proton yield below that from n-p scattering.

I. INTRODUCTION

COLLISIONS of protons or neutrons with nuclei have generally been thought of in terms of interaction of the incident particle with the whole struck nucleus. According to this point of view, the incident particle may scatter elastically, without changing the internal energy of the nucleus from which it rebounds, or it may enter the nucleus and expend its energy in raising the nuclear temperature, resulting in the eventual expulsion of particles or quanta in random directions. A transition region covering a rather wide energy interval occurs as bombarding energies are increased, however. Above energies of 100 Mev or so, the wavelength or effective size of the bombarding particle is no longer large with respect to separation distances of nucleons. As the energy of the incident particle increases through this region the particle tends more and more to interact with only one nucleon at a time, and the probability for its interaction with any nucleon decreases so that its mean free path within nuclear matter is large. The result of this transition is seen as a basic change in the nature of nucleon-nuclear collisions: with increasing energy, the collision products take on more and more the character of scattered particles from individual nucleon-nucleon collisions. The role of the struck nucleus passes from that of an integral and closely bound system to that of a cloud of separate scattering centers, each moving with a distribution in momentum determined by its interaction with the rest of the nucleus, but otherwise free to act almost independently. One would expect that in the case of very high bombarding energies, emerging particles would be distributed in energy and angle almost as they are in the case of free nucleon-nucleon collisions. Illustrations of this state of affairs may be seen in recent reports on particles ejected from light elements by 240- and 340-Mev protons[1,2] and by 90-Mev neutrons.[3]

The special case of deuterium struck by high energy particles is of particular interest, because of the simplicity of the deuterium nucleus and the relative ease of theoretical treatment of its behavior in collisions. As suggested by the above remarks, one would expect the deuteron to behave very much as two separate particles when it is struck by neutrons of 200- to 300-Mev energy. It should be possible, in fact, to attribute various kinds of emergent particles to collisions of the incident neutron with either one or the other of the deuteron's components. The total scattering cross section can be expressed as a sum of the n-p cross section, the n-n cross section, and an additional term, probably small, resulting from interference of various kinds.[4–6]

Protons, in particular, resulting from n-d collisions, should fall roughly into two groups. A group at low energies would result partly from n-n collisions which carry away both neutrons, leaving the proton in about the same state of motion that it was in at the time of collision, and partly from n-p collisions in which no charge exchange takes place. The second group, at energies of the order of the bombarding energy and with an angular distribution strongly concentrated in the direction of the incident neutrons, would result from n-p collisions with charge exchange. The purpose of the experiments to be described was an investigation of the distribution in angle and energy of the latter proton group, resulting from bombardment of deuterium with a beam of neutrons of about 270-Mev energy. The quantity best determined was the yield of these protons at a number of angles, integrated over energy. The nearness of approach of this quantity to the differential n-p scattering yield furnishes a measure

* This work was performed under the auspices of the AEC.
† This report is based on a thesis submitted by J. Hadley in partial satisfaction of the requirements for the degree of Doctor of Philosophy at the University of California.

[1] Cladis, Hadley, and Moyer, Phys. Rev. **81**, 649 (1951).
[2] G. M. Temmer, Phys. Rev. **83**, 1067 (1951).
[3] J. Hadley and H. F. York, Phys. Rev. **80**, 345 (1950).
[4] F. de Hoffmann, Phys. Rev. **78**, 216 (1950).
[5] G. F. Chew, Phys. Rev. **80**, 196 (1950).
[6] R. C. Gluckstern and H. A. Bethe, Phys. Rev. **81**, 761 (1951).

of the accuracy of the concepts stated above regarding the nature of high energy n-d collisions; the differences that appear furnish indications of the roles played by effects such as that of the exclusion principle acting on the two neutrons left behind in the collision, and that of the internal momentum distribution of the deuteron. A discussion will be given in the concluding section on such of these factors as appear to influence the measured yield.

II. EXPERIMENTAL PROCEDURE

The experimental procedure chosen consisted of a comparison of the yield of n-d protons in the particular energy and angular interval under consideration with the yield of protons from n-p scattering in the same interval, measurements of the two quantities being alternated during the course of each experimental run. Most of the final data is expressed in the form of ratios of these quantities, not only because of the convenient nature of such ratios, but also because of the elimination of any effect of varying efficiency of the detecting equipment. The detector efficiency at each angle and energy enters as a factor in the determination of each differential yield, and of course cancels out in the ratio.

The experiment was divided into two main sections, the first being concerned with measurements of differential yields as a function of angle and energy, and the second with measurements of yield as a function of angle, integrated over all energies above a certain cut-off value at each angle. The latter measurements contain no information that could not be derived from the former, but were resorted to through necessity. The length of time necessary to carry out a complete set of measurements, at a number of angles, of differential yields of the former sort would have been prohibitively great.

The necessity of the cut-off energy in the latter part of the experiment arises mainly through the spread in energies of the neutrons comprising the incident beam. In measuring yields from n-p scattering in a neutron beam with wide energy spread, it is desired to count just those protons, at each angle, which are produced by neutrons lying within certain energy limits. The energy of scattered protons in n-p collisions varies as $E_n \cos^2\Theta$, E_n being the incident neutron energy and Θ the angle of emergence of the proton, measured in the laboratory frame with respect to the direction of the incident neutron. Consequently, for a fixed neutron energy limit, one must vary the energy limit on scattered protons as $\cos^2\Theta$. The cut-off energy chosen in the present experiments was 200 Mev $\cos^2\Theta$, corresponding to a 200-Mev neutron cut off; the same limit was used in the n-p scattering experiments of Kelly, Leith, Segrè, and Wiegand.[7] The energy limit used in the measurements of n-p yields in the present experiment was chosen to agree with the n-p scattering experiments cited above, to permit direct reference to their values of the n-p differential scattering cross section. The energy limit used in measurement of yields from n-d collisions was also chosen the same for two reasons. First, because the amount of absorber used in setting the cut-off energy affects the efficiency of the counters (nuclear collisions in the absorber material), and it is desirable to keep the counter efficiency the same for both measurements at a given angle, as explained above; and second, because fast protons from high energy n-d collisions should approach a $\cos^2\Theta$ energy dependence, and setting a cut-off energy varying as 200-Mev $\cos^2\Theta$ is almost again equivalent to choosing only those protons produced by neutrons of 200-Mev energy or greater.

[7] Kelly, Leith, Segrè, and Wiegand, Phys. Rev. 79, 96 (1950).

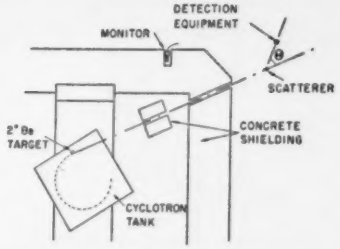

FIG. 1. General experimental arrangement.

The integral measurements were performed with a telescope of counters, arranged so that particles emerging from a scatterer placed in the neutron beam emerging from the 184-in. synchrocyclotron could be observed in any chosen direction. Scattered particles were required to pass through an appropriate thickness of material at each angle, so that only those particles having energy above a fixed lower limit could be counted. During the course of a day's run, measurements of yield at a number of different angles could be made.

Differential measurements were made with a magnetic particle spectrometer, in which particles emerging from the scatterer within a certain small solid angle in a given direction were sorted according to their momentum.

The apparatus was not by itself able to discriminate between protons and deuterons, but theoretical and experimental evidence, which will be discussed later, indicates that practically all of the observed particles were protons, and that no more than a negligible number of elastically scattered deuterons contributed to the observed yields.

Figure 1 shows the over-all experimental arrangement as used in both sections of the experiment.

III. DETAILS OF APPARATUS

A. Neutron Beam

The neutron beam used was produced by placing a 2-inch thick beryllium target in the 350-Mev circulating

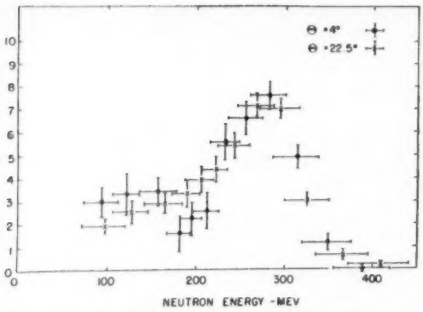

FIG. 2. Energy distribution of neutron beam.

proton beam of the cyclotron. Neutrons emerging in a direction tangent to the path of the proton beam pass through the wall of the cyclotron tank and are collimated in a series of holes through the concrete shielding around the cyclotron before emerging to strike the scatterer.

The distribution in energy of these neutrons has been measured by Kelly *et al.*[7] in connection with n-p scattering experiments and can be determined from particle spectrometer results of the present experiment. Figure 2 shows a spectrum derived from the data described in Sec. IV. It is in agreement with those given by other workers.

B. Monitor

In order to compare yields from various scatterers, it is necessary to have some measure of integrated beam intensity. The monitors used for this purpose consisted of boron-trifluoride filled proportional counters placed in holes in the concrete shielding wall. Fast neutrons entering the shielding produce slow neutrons through elastic scattering and through generation of secondary neutrons in collisions with nuclei. The slow neutrons are captured in large numbers by the boron in the counter, and the α-particles produced through the $B^{10}(n,\alpha)Li^7$ reaction are counted. Variation of the neutron beam intensity showed that the counting rate of such a monitor varied in proportion to the counting rate from a scatterer placed directly in the beam.

C. Magnetic Spectrometer

The magnet used to obtain momentum spectra had a pole gap measuring 2½ inches by 12 inches by 30 inches. The maximum field attainable for any considerable length of time was about 14,000 gauss. Electronic current regulation provided a field constant to about ½ of one percent, corresponding to an energy variation of one percent.

In order to define in the magnet, a path having a certain radius of curvature, one must fix three points along the proposed path. Here, the first consisted of the scatterer; the second consisted of a narrow slit at the entrance end of the magnet; and the third was one of a series of G-M tubes located at the exit end of the magnet. At low energies the slit at the entrance end could be defined by a physical gap in some material, but at high energies this system would not be satisfactory. The particle penetration in the gap walls would (1) render the gap width a function of the particle energy, and (2) would degrade the particle energies, causing the energy spectra to be distorted. Because of these effects, small thin-walled proportional counters were used for the second slit. They were made in cylindrical shape, having diameters of ⅛ inch and ¼ inch. The G-M tubes, which located the final points defining the energy channels, were arranged to intercept all protons of energies above about 20 Mev. In this way a complete energy spectrum could be taken in a single measurement. G-M tubes were used in spite of their long dead time because the associated electronic equipment is simpler than for proportional counters. It was found that usable beam intensity was not seriously limited by the effect of dead time.

The pulses originating in the slit counter were fed into the G-M tube amplifiers in such a way that no count from a G-M tube would be registered unless a count from the slit counter arrived within a time interval of about 2 microseconds around the start of the G-M pulse. To eliminate accidental coincidence counts three additional proportional counters were placed within the magnet pole gap, and connected in electronic coincidence with the slit counter. With this system simultaneous pulses in all four proportional counters were necessary to send a "gating" pulse to the G-M tube amplifiers and permit them to register counts. Figure 3 shows the arrangement of the magnet with associated counters.

Determination of the proton energies corresponding to the various magnet channels, at given field settings, was accomplished through use of a light, flexible wire suspended in the pole gap. When a current is passed through the wire, it assumes the same shape as the trajectory of a proton, and the value of $H\rho$, along the wire is given by the ratio of wire tension to wire current.

The spectrometer provided angular resolution of about 1°.

D. Counter Telescopes

The coincidence counter telescopes used in measurements of integrated scattered intensities as a function of angle, consisted of a series of three or sometimes four particle counters fixed with their centers along a straight line passing through the scatterer. The counter system was capable of rotating as a whole about the scatterer. Copper absorbers of varying thickness were placed between the next to last and last counters to fix the lower limit of proton energies that would be accepted by the telescope at the desired value of 200 Mev$\times\cos^2\Theta$.

Part of the experimental data was obtained using proportional counters in the telescope. It was later found that advantage could be taken of the shorter coincidence resolving time and dead time of anthracene scintillation counters to permit the use of a more intense neutron beam without difficulties from accidental coincidences and loss of counter efficiency through dead time. Thus data could be accumulated at a somewhat faster rate, and the proportional counters were accordingly replaced by scintillation counters.

Angular resolution obtained with the counter telescope was about 3°.

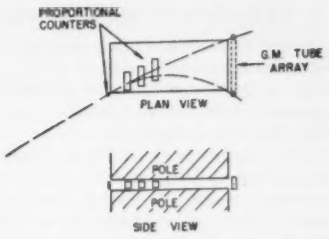

FIG. 3. Schematic diagram of spectrometer.

E. Scatterers

The scatterers used to determine yields of protons from n-p collisions were blocks of carbon and polyethylene (CH_2), the hydrogen yield being obtained by taking the carbon-polyethylene difference. Yields from n-d collisions were obtained through the use of water and of heavy water scatterers, a subtraction eliminating the oxygen effect and giving the difference in D_2 and H_2 yields. The water and heavy water were held in thin-walled containers, a third identical container being left empty for use as a blank. The scatterers were made taller vertically and narrower horizontally than the neutron beam so that the amount of material in the beam was well known and reproducible. The scatterer thicknesses were chosen so that protons of a given energy suffered equal energy loss in passing through the various scatterers.

IV. REDUCTION OF DATA

A. General Treatment of Data

The yield from each scatterer, normalized to yield per incident neutron through division by appropriate monitor values, will be denoted by symbols in brackets: $[H_2O]$, $[D_2O]$, $[CH_2]$, $[C]$, $[B]$, and $[K]$, where B represents the background yield with no scatterer in place, and K represents the yield with the empty can in place.

To obtain actual yield per mole from each scatterer, we must subtract the background and then divide by the number of moles of scatterer intercepted by the beam, e.g.,

$$CH_2=\frac{1}{n(CH_2)}([CH_2]-[B]).$$

The following subtraction then gives the yield per mole resulting from H_2,

$$H_2=CH_2-C=\frac{1}{n(CH_2)}[CH_2]-\frac{1}{n(C)}[C]-\frac{n(C)-n(CH_2)}{n(C)n(CH_2)}[B].$$

Similarly,

$$H_2-D_2=\frac{1}{n(H_2O)}[H_2O]-\frac{1}{n(D_2O)}[D_2O]-\frac{n(D_2O)-n(H_2O)}{n(D_2O)n(H_2O)}[K],$$

and to obtain the deuterium yield,

$$D_2=H_2-(H_2-D_2).$$

The results of the integral measurements made with the counter telescope are always to be expressed in terms of the quantity (D/H), which may be thought of as the ratio of the fast proton component of the n-d cross section to the n-p scattering cross section,

$$\frac{D}{H}=1-\frac{H_2-D_2}{H_2}=\frac{d\sigma_{n-d(p)}/d\Omega}{d\sigma_{n-p}/d\Omega}.$$

The results of measurements made with the magnet are probably most significant when expressed in terms of the relative quantities D_2 or H_2, so that the actual shapes of spectra are shown. The yield measured in each energy channel must be divided by the counting efficiency of that channel to give proper relative yields.

B. Energy Intervals Accepted by Magnet Channels

Each channel of the magnet accepted protons within an energy interval given by a bell-shaped curve whose form could be derived by a folding process combining the energy uncertainties introduced by each of the three slits. Additional spread in the acceptance interval of each channel was caused by the thickness of the scatterer, and a function describing this was combined with the acceptance function of the magnet channels proper. The energies at half-height of the resulting efficiency curve were taken as the upper and lower limits of the energy interval to which the data from each channel refers, and will be indicated in the presentation of the data. Energy intervals corresponding to the scatterer thickness were obtained from the range-energy curves of Aron, Hoffman, and Williams.[8]

[8] Aron, Hoffman, and Williams, Atomic Energy Commission Unclassified Document No. 663 (1949).

C. Efficiencies for Magnet Channels

The efficiencies of the various magnet channels depended primarily on the width of the G-M tubes. The energy intervals corresponding to these widths were determined from the data obtained from flexible wire calibrations of the magnet.

The effective energy interval of each channel varied with the position in the scatterer of the particular volume element where the protons were produced. Therefore, the effective energy intervals were averaged over the scatterer thickness to obtain the relative channel efficiency for a given scatterer. This was done and the effect of the scatterer was found to be quite small but was included in the efficiencies used.

D. Data obtained with Magnet

Data obtained from magnet runs at scattering angles of 4° and 22.5° are presented in Figs. 4 and 5, which show spectral distributions of yields from hydrogen and from deuterium. The vertical scale of each figure is arbitrary and the scale of Fig. 4 bears no relation to that of Fig. 5. The relative heights of the deuterium and hydrogen spectra in each figure do represent actual relative yields, however. The standard deviation resulting from counting statistics and energy interval pertaining to each point is indicated.

Since the scattered particles from n-p collisions have energies that are uniquely determined by the energies of the incident neutrons, it is possible to determine the energy spectrum of a neutron source through a measurement of the energy spectrum from n-p scattering at a given angle. In order to carry out such a determination one must have some knowledge of the form of the differential n-p scattering cross section as a function of energy at the particular scattering angle used. Figure 6 shows a curve representing this cross section for 8° and 45° scattering angles in the center-of-mass system, as a function of energy. Angles of 8° and 45° in the center-of-mass system correspond nonrelativistically to n-p scattering angles of 4° and 22.5° in the laboratory

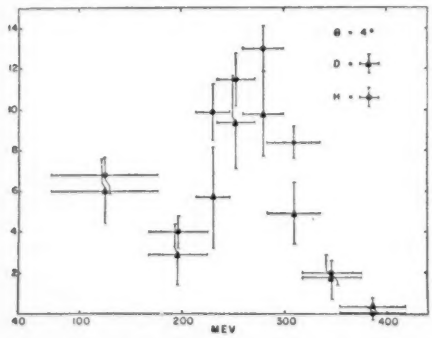

FIG. 4. H and D spectra at 4°.

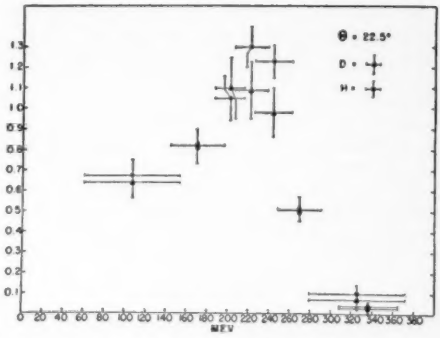

FIG. 5. H and D spectra at 22.5°.

system. Figure 6 was obtained by drawing smooth curves through experimental values of the n-p cross section as obtained by various groups.[9] Figure 2 shows energy spectra obtained from the 4° and 22.5° data through division by cross-section values obtained from Fig. 6 and application of the following additional factors. The cross sections given in Fig. 6 refer to unit solid angle in the center-of-mass system, whereas the solid angle referred to in the course of the experiment was constant in the laboratory system. Consequently the variation of center-of-mass solid angle corresponding to a fixed laboratory solid angle must be determined through the relation

$$d\Omega_{\text{c.m.}}/d\Omega_{\text{lab}}=2(1+\gamma)\cos\Theta/[\cos^2\Theta+\tfrac{1}{2}(1+\gamma)\sin^2\Theta]^2,$$

where Θ = laboratory scattering angle, and $\gamma = 1 +$ neutron energy$/mc^2$.

The second correction factor to be applied arises through the nonlinear relation between neutron and scattered proton energies, causing a variation in neutron energy interval corresponding to unit proton energy interval

$$T_p=\frac{T_n\cos^2\Theta}{1+(T_n/2mc^2)\sin^2\Theta}$$

$$\frac{dT_p}{dT_n}=\frac{\cos^2\Theta}{[1+(T_n/2mc^2)\sin^2\Theta]^2}=\frac{\cos^2\Theta}{[\cos^2\Theta+\tfrac{1}{2}(1+\gamma)\sin^2\Theta]^2}$$

T_n and T_p being the kinetic energies of the incident neutron and scattered proton. The distribution of scattered protons is then related to the distribution of incident neutrons as,

$$\frac{dN_p}{dT_p d\Omega_{\text{lab}}}\propto\frac{dN_n}{dT_n}\cdot\frac{dT_n}{dT_p}\cdot\frac{d\sigma}{d\Omega_{\text{c.m.}}}\cdot\frac{d\Omega_{\text{c.m.}}}{d\Omega_{\text{lab}}},$$

[9] See Hildebrand, Hicks, and Harker, University of California Radiation Laboratory Report No. 1305 (1951); Kelly *et al.*, reference 7; and E. M. Baldwin, Phys. Rev. **83**, 495 (1951) for cross-section values and further references.

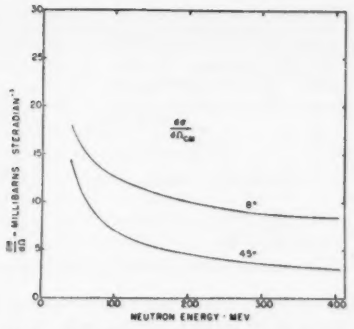

FIG. 6. Values of $d\sigma/d\Omega_{\text{c.m.}}$ used in derivation of neutron beam energy spectrum.

or

$$\frac{dN_n}{dT_n} \propto \frac{dN_p}{dT_p d\Omega_{\text{lab}}} \cdot \frac{dT_p}{dT_n} \cdot \frac{d\Omega_{\text{lab}}}{d\Omega_{\text{c.m.}}} \Big/ \frac{d\sigma}{d\Omega_{\text{c.m.}}}$$

$$= \frac{dN_p}{dT_p d\Omega_{\text{lab}}} \cdot \frac{\cos\Theta}{2(1+\gamma)} \Big/ \frac{d\sigma}{d\Omega_{\text{c.m.}}}.$$

E. Considerations on Presence of Scattered Deuterons

Up to this point the scattered particles have been referred to as protons. There was, however, no provision made for excluding other particles, and it would seem important to try to form an estimate of the number and spectrum of deuterons that might be present among particles emerging from n-d collisions.

First, let us refer to the spectra presented in Figs. 4 and 5. The horizontal scales are labeled in terms of proton energies for convenience, but it must be remembered that the actual sorting is according to momentum rather than energy, as each channel represents a certain fixed value of $H\rho$, or momentum, for particles entering it. In the nonrelativistic limit, which will be a sufficiently close approximation for the time being, protons of a given energy, E, will have the same momentum as deuterons of energy $\frac{1}{2}E$. Consequently, if the energy scale of the figures is divided by a factor of 2, an energy scale appropriate to deuterons will result. It is shown in Figs. 4 and 5 that essentially no particles were counted with momenta corresponding to protons of energy greater than about 350 Mev $\cos^2\Theta$, or to deuterons of energy greater than about 175 Mev $\cos^2\Theta$.

The relation between incident neutron energy and elastically scattered deuteron energy is given by

$$E_d = (8/9)E_n \cos^2\Theta$$

setting an upper limit of $(9/8)\times 175 \cong 200$ Mev on the energy of neutrons producing an appreciable number of deuterons through n-d scattering at angles of 4° and 22.5°. More evidence on this point can be adduced from the data presented in Fig. 7. This figure shows spectra obtained in two different ways from D_2O at an angle of 22.5°. The upper set of points represents a spectrum taken in the normal way, while the lower set represents data taken with a carbon absorber of thickness 24 g cm^{-2} placed between the scatterer and magnet. If the curve for no absorber represented only protons, one would expect its form to be preserved when the carbon absorber was used, as correction for proton energy loss in the carbon was made. No deuterons of energy less than 240 Mev can penetrate a carbon thickness of 24 g cm^{-2}, however, so that any deuterons contributing to the spectrum obtained from D_2O without absorber should not be present in the spectrum taken with absorber. It is seen that the two curves lie roughly parallel at proton energies greater than 225 Mev, but that a sharp break in the lower curve occurs at that point. It is felt that this break, at a deuteron energy of $225/2 = 113$ Mev, marks the upper limit of the spectrum of deuterons present. The corresponding neutron energy is

$$E_n = 9\times 113/8 \cos^2 22.5° \cong 150 \text{ Mev}.$$

The almost constant difference between the two curves at energies above the break is felt to represent attenuation in the carbon absorber because of nuclear scattering and inelastic processes. The attenuation factor is about 1.6 ± 0.3, which would correspond to a cross section of 0.33 ± 0.13 barn per carbon nucleus for removal of scattered protons. This value is certainly within reason.

Neutrons of energy 150 Mev and lower seem to produce deuterons at 22.5° from heavy water; we have no information specifically as to whether the source is in the oxygen or in the deuterium. Thus the figure of 150 Mev represents only an upper limit for production in deuterium. It may be that no appreciable number of deuterons is scattered at 22.5° in n-d collisions by neutrons down to a considerably lower energy.

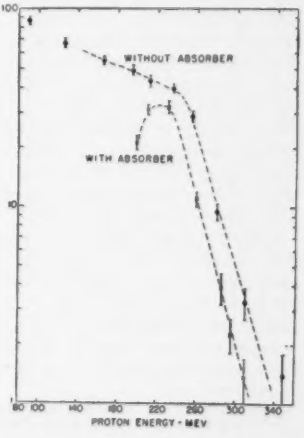

FIG. 7. Effect of carbon absorber on particles from D_2O at 22.5°.

TABLE I. Data from counter telescope runs. Scatterers A: 2.26 g cm^{-2} C equivalent; Scatterers B: 4.02 g cm^{-2} C equivalent.

	Cut-off energy Mev		Proportional counters	D/H values from various runs Scintillation counters			
Θ	A	B	B	A	A	B	Average D/H
4°	195–205	192–209		0.774±0.046		0.704±0.024	0.719±0.201
9°	195–205	191–209	0.670±0.058	0.701±0.066			0.682±0.044
15°	195–205	190–209	0.708±0.063	0.800±0.065			0.752±0.045
22.5°	194–206	189–210	0.697±0.069	0.750±0.086			0.715±0.052
30°	193–207	187–213	0.755±0.108		0.828±0.091	0.926±0.126	0.827±0.061
35°	191–209			0.806±0.113			0.806±0.113
45°	185–215	173–227	0.772±0.128		0.465±0.150		0.643±0.097
55°	169–232			0.513±0.219	0.627±0.142		0.593±0.120
58°	158–243				0.705±0.100		0.705±0.100

Theoretical analysis of n-d elastic scattering[10,11] predicts a weak maximum for deuterons projected forward (pick-up process), and a gradual decrease of cross section with deuteron angle out to well past 60°. This general form is characteristic, regardless of the particular interaction potential used. Consequently, the upper limit of 200 Mev for neutrons producing an appreciable number of scattered deuterons at 4° and 22.5° should hold good for all angles examined in this experiment, the maximum angle at which data was taken being 58°. This fact will be of interest in the next section.

F. Data Obtained with Counter Telescope

Data obtained with the counter telescope was treated in the manner outlined in Sec. IV-A to give values of D/H.

Two separate sets of scatterers were used, one set fairly thin to provide low energy loss by scattered particles in traversing the scatterers, and another set thicker to provide a large quantity of scattering material. The former were used at wide angles, where scattered energies are low, and the latter at small angles, where scattered energies are high and energy loss in the scatterers is of relatively little importance. Particles originating at various depths in the scatterers of course traversed different amounts of material on their way out; the 200 $\cos^2\Theta$ Mev cut-off energy applied only to particles originating in the central plane of the scatterer. As a result the real cutoff took the form of a linear variation in efficiency from 0 to 1 over an energy interval, determined by the scatterer thickness, whose center lay at 200 $\cos^2\Theta$ Mev. Values of lower and upper limits of the cut-off energy interval are tabulated in Table I for both sets of scatterers.

Table I also sets forth values of D/H obtained with each combination of counter type and scatterer size used, together with average values at each angle, which are shown graphically in Fig. 8. Agreement between various sets of data is shown to be good.

Errors tabulated here, as well as with the magnet data, are standard deviations derived from numbers of counts obtained. It is felt that these quantities give a good indication of accuracy of the data, as they are considerably larger than estimated errors likely to have been introduced from other sources.

The absorbers used to provide a proton energy cutoff of 200 $\cos^2\Theta$ Mev also provided a lower energy limit for deuterons accepted, which correspond at each angle to deuterons scattered by neutrons of energy 300 Mev. Since evidence presented in the previous section indicates an upper limit of 200 Mev on neutrons producing a countable number of deuterons at any angle, it is felt safe to assume that the data obtained with the counter telescope refers to scattered protons only.

The integrated D/H value obtained at 22.5° is about 0.7. Comparison with the spectra plotted in Fig. 5 shows that in order to secure agreement, one might assume that part of the D_2 curve results from scattered deuterons. According to this view, and as suggested by the spectra of Fig. 7, one would lower the portion of the D_2 curve lying below 225 Mev by an amount increasing with decreasing energy. The result of such an operation, giving a curve purporting to represent protons alone, might well bring the shape of the D_2 spectrum into close agreement with the shape of the H_2 spectrum. Similar considerations apply to the spectra of Fig. 4.

V. INTERPRETATION OF RESULTS

The experimental results may be described in terms of two main features: first, that the energy spectrum of the fast protons produced at small angles in n-d collisions is a fairly close reproduction, in form, of the energy spectrum of the incident neutrons; and second, that the yield of all protons, of energy greater than 200 $\cos^2\Theta$ Mev, from n-d collisions, bears at each scattering angle the ratio of about 0.7 to the yield of protons, greater than the same cut-off energy, from n-p collisions.

Owing to the wide distribution of incident neutron energies, the first of these features serves merely as a somewhat qualitative demonstration of the similarity of high energy protons from n-d scattering to the protons from n-p scattering. If a more nearly monochromatic neutron beam could be obtained, it would seem well worth while to measure spectra from n-d scattering

[10] G. F. Chew, Phys. Rev. **74**, 809 (1948).
[11] Ta-You Wu and J. Ashkin, Phys. Rev. **73**, 986 (1948).

at wide angles, in order to get information on the effects of the momentum distribution of the deuteron and of the interaction between the two neutrons that are left when a proton is expelled from an n-d collision. The breadth of the present neutron spectrum effectively washes out the detailed features of the expelled proton spectrum, and makes the derivation of any information on the above effects quite undependable. For this reason, and also because of the small number of protons produced at wide angles and consequent difficulty in accumulating good statistics, it was not thought worth while to attempt further spectral measurement at present.

The most interesting feature of the data seems to lie in the distribution in angle of the D/H values obtained with the counter telescope. If the proton bound in a deuteron behaved exactly as a free proton in scattering neutrons, one would expect D/H to have the value 1 at all angles. It will be of interest to examine the various perturbing factors which may be the cause of the low value obtained for D/H.

One of the most evident of these factors is the necessity for satisfaction of the Pauli exclusion principle, which should affect the yield of protons in the forward direction. When a fast proton emerges from an n-d collision in a direction close to that of the incident neutron, the two residual neutrons must be in a state of low relative momentum. There is a high probability in such a case for the two neutrons to be left in an S-state of angular momentum, which will only be possible in the case of antiparallel spins. The consequence is a depression of proton yields at small angles. A different effect must be found which will tend to lower proton yields at wide angles.

Effects which have been proposed as possible causes of the low D/H rate at wide angles are the following: The internal momentum distribution of the deuteron causes, at wide angles, a spread in emerging proton energies, with resultant net displacement of some protons to energies below the cutoff and consequent reduction in measured yield. A second effect of the deuteron's momentum distribution would be of importance if the differential n-p cross section, averaged over the motion of the proton in the deuteron, were different from the cross section referring to a stationary proton.

Finally, one might expect that the energy loss involved in converting the deuteron plus neutron system into a dineutron plus proton system would cause the energy of n-d protons to be lower than the energy of n-p protons at the same angle. The result of this energy shift would be a displacement of part of the proton spectrum below the cut-off energy, with resultant loss

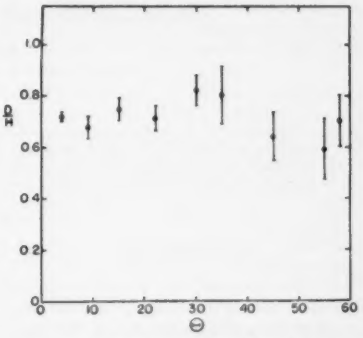

FIG. 8. D/H as a function of angle.

in apparent n-d yield and lowering of the observed D/H ratio.

Professor G. F. Chew has supplied us with the results of some calculations on this subject, made in connection with a forthcoming paper on scattering by light nuclei.[12] He finds that the final effect mentioned above, together with the effect of the exclusion principle, gives a D/H ratio close to that observed, and that the form of the D/H curve indicates a very large probability of spin flip in charge-exchange n-p collisions. He also finds confirmation in the data for the assumption that the triplet-odd p-p force is not attractive.

VI. ACKNOWLEDGMENTS

The authors wish to express their appreciation to the many people who have been of great assistance in the completion of this experiment, and especially to the following: Dr. B. J. Moyer, whose encouragement and suggestions have been of the greatest aid; Dr. G. F. Chew, who suggested the experiment and who has taken an active interest in its interpretation; Dr. Walter Crandall, who worked with the author throughout various preliminary investigations; Dr. Robert Jastrow and Dr. Peter Wolff, who have furnished very helpful discussions regarding interpretation of the experiment; Mr. Boris Ragent, who collaborated in the planning of the spectrometer; Dr. Robert Richardson and Mr. William Ball, who assisted greatly through the loan of scintillation counting equipment; Mr. Hugh Farnsworth and the electronics group under his direction, who designed and maintained the electronics equipment used; and to the crew of the 184-in. cyclotron for their consistent cooperation.

[12] G. F. Chew and G. Placzek (to be published).

Dielectric Constant in Perovskite Type Crystals

JOHN H. BARRETT*
Rice Institute, Houston, Texas
(Received December 26, 1951)

Slater's theory of the dielectric constant in $BaTiO_3$ has been extended by treating the ionic polarizability quantum mechanically instead of classically. This leads to an expression for the dielectric constant which is good at all temperatures and shows a deviation from the Curie-Weiss law at low temperatures. The theory is applied to $SrTiO_3$ and to $KTaO_3$ above its transition at 13.2°K.

INTRODUCTION

SLATER has proposed a theory[1] to explain the dielectric behavior of $BaTiO_3$, at least above its Curie temperature. His model treats the crystal as though the Ba and O ions were fixed in position and as though each Ti ion acted like an independent harmonic oscillator with small additional anharmonic terms. The Ti ion is supposed to be very loosely bound, and the only interaction between these oscillators is through the electric field. The system was then treated by statistical mechanics in a completely classical fashion. It seemed desirable to find also the results of a quantum-mechanical treatment, particularly at low temperatures.

I. DERIVATION OF THE QUANTUM-MECHANICAL FORMULA

Following Slater, let the potential energy of the Ti ion in an electric field be given by

$$\phi=a(x^2+y^2+z^2)+b_1(x^4+y^4+z^4)+2b_2(x^2y^2+x^2z^2+y^2z^2) -q(xE_x+yE_y+zE_z). \quad (1)$$

Let the part of ϕ independent of the b's be called ϕ_1 and the part containing the b's be called ϕ_2. The ϕ_2 will be treated as a perturbation. Using ϕ_1 as the potential energy in the Hamiltonian operator, the problem is just that of a simple harmonic oscillator in an electric field, and the energy levels are given by

$$W_{lmn}{}^0=(l+m+n+\tfrac{3}{2})h\nu-q^2E^2/4a. \quad (2)$$

These energy levels are degenerate, so that the first-order perturbations to the energy levels must be obtained by solving a series of determinants. For any group of levels having the same unperturbed energy, the sum of the energy perturbations is equal to the sum of the diagonal matrix elements. Assuming that the energy perturbations are small with respect to kT, one can use the approximation $\exp(-x)=1-x$ in computing the partition function. The justification of this approximation will be considered in Sec. III. Let the first-order perturbation energies be denoted by $W_{lmn}{}^1$ and the diagonal matrix elements by $(lmn|\phi_2|lmn)$. Then, using the approximation for the exponential given above, it can be seen that the diagonal matrix elements may be used in place of the true first-order energy perturbations to compute the partition function.

The diagonal matrix elements are given by

$$\begin{aligned}(lmn|\phi_2|lmn)&=b_1\{(3/4\beta^2)[(2l^2+2l+1)+(2m^2+2m+1)\\&\quad+(2n^2+2n+1)]+(3q^2/4a^2\beta)[(2l+1)E_x^2\\&\quad+(2m+1)E_y^2+(2n+1)E_z^2]\\&\quad+(q^4/16a^4)[E_x^4+E_y^4+E_z^4]\}\\&\quad+2b_2\{(1/4\beta^2)[(2l+1)(2m+1)+(2l+1)(2n+1)\\&\quad+(2m+1)(2n+1)]+(q^2/8a^2\beta)[(2l+1)(E_y^2+E_z^2)\\&\quad+(2m+1)(E_x^2+E_z^2)+(2n+1)(E_x^2+E_y^2)]\\&\quad+(q^4/16a^4)[E_x^2E_y^2+E_x^2E_z^2+E_y^2E_z^2]\}, \quad (3)\end{aligned}$$

where $\beta=2a/h\nu$. Let z be the partition function for a single oscillator, and let $Z=z^N/N!$ be the partition function for a system of N oscillators. The polarization is given by $P_i=-(\partial A_E/\partial E_i)_T$, where $A_E=-kT\ln Z$. Now one obtains for α_{Ti}', the ionic polarizability resulting from the Ti ion,

$$\alpha_{Ti}'=(1/N)(P_x/E_x)=(q^2/2a)[1-((3b_1+2b_2)h\nu/2a^2) \times\coth(h\nu/2kT)]. \quad (4)$$

It should be noted that this formula is applicable only above the Curie temperature in the unpolarized or nonferroelectric state. The above treatment will reduce to Slater's if $kT\gg h\nu$.

II. APPLICABILITY OF THE QUANTUM-MECHANICAL FORMULA

In order to see how κ depends on $X_{Ti}'=\alpha_{Ti}'/\epsilon_0 v$ for perovskite crystals in general, where v is the volume of the unit cell, one must consider the Lorentz correction as Slater has done in his paper. This will be done here in less specific fashion. Because of the linearity of a set of equations such as his Eqs. (18) and (19) relating the polarization to the field, one will get,

$$\kappa=A+B/(1-DX_{Ti}'). \quad (5)$$

Slater's Eq. (26) is a particular example of this relation for $BaTiO_3$. The values of A, B, and D will depend on the values of the electronic polarizabilities of the various atoms in the lattice and on the geometry of the lattice. The X_{Ti}' will be the only temperature dependent quantity in κ.

* Holder of Gen. Elec. Charles A. Coffin fellowship.
[1] J. C. Slater, Phys. Rev. **78**, 748 (1950).

Combining (4) and (5) and noting that A is negligible,

$$\kappa=\frac{M}{\frac{1}{2}T_1\coth(T_1/2T)-T_0} \tag{6}$$

where

$$T_1=\frac{h\nu}{k},\quad M=\frac{2a^3\epsilon_0 v B}{q^2(3b_1+2b_2)kD},$$

$$T_0=\frac{2a^3\epsilon_0 v}{q^2(3b_1+2b_2)kD}\left(\frac{Dq^2}{2a\epsilon_0 v}-1\right).$$

The behavior of κ as given in Eq. (6) is shown in Fig. 1. For $T\gg T_1$, $\frac{1}{2}T_1\coth(T_1/2T)$ asymptotically approaches T and (6) becomes a Curie-Weiss law. As T approaches 0°K, κ will approach $M/(\frac{1}{2}T_1-T_0)$. Roughly, it may be said that T_1 is the dividing point between the low temperature region where quantum effects are important and κ deviates from a Curie-Weiss law and the high temperature region where a classical approximation and a Curie-Weiss law are good. If a material undergoes a transition to the ferroelectric state at a temperature above T_1, the quantum effect will be unnoticed.

Now we shall see how this theory applies to $BaTiO_3$. Using Slater's value of $a\doteq 7.6n^2$ ev/A$^2=1.2\times10^9n^2$ joules/m^2 and m as the mass of the Ti atom gives $T_1=410n$ degrees absolute, where n is now the number of electronic charges on the Ti ion. Since the Curie-Weiss law holds in $BaTiO_3$ down to the transition temperature at about 390°K, n cannot be much above 1.

Consider the values of the constants in Eq. (6) in the case of $BaTiO_3$. Experimentally $M=1.5\times10^5$, $T_0=390$°K, and Slater has computed[1] $B=1.93$. This gives

$$2a^3\epsilon_0 v/[q^2(3b_1+2b_2)kD]\sim10^5,$$
$$(Dq^2/2a\epsilon_0 v-1)\sim4\times10^{-3}. \tag{7}$$

The last quantity can be said to be zero, so that $a=Dq^2/2\epsilon_0 v$ as Slater has given in his Eq. (29) with $D=5.39$.

Now it seems reasonable that the quantities considered just above, excepting T_0, will be of the same order of magnitude for other compounds of the same structure as $BaTiO_3$. The T_0 can vary quite drastically because it is determined by the difference of two very nearly equal quantities. Nevertheless, it will still be expected that the latter order of magnitude relationship given in (7) will not be exceeded and that a is still given by $a=Dq^2/2\epsilon_0 v$.

In particular $SrTiO_3$ might be expected to behave in the same manner as $BaTiO_3$ with a different T_0. Hulm[2] has reported the dielectric constant of $SrTiO_3$ to follow a Curie-Weiss law down to about 50°K. He found $M=8.4\times10^4$, $T_0=-35$°K. Below 50°K the dielectric constant falls below the Curie-Weiss law and approaches a value of 1300 in the neighborhood of 0°K. A curve of the form (*a*) in Fig. 1 seems to fit these facts quite well. From the value of κ near 0°K, T_1 can be computed to be about 60°K. This explains why the dielectric constant is observed experimentally to begin to deviate from a Curie-Weiss law around 50°K.

Another ferroelectric to which this might be expected to apply is $KTaO_3$ above its transition to the ferroelectric state. Hulm, Matthias, and Long[3] have reported the behavior of the dielectric constant of this compound at low temperatures. The behavior in this case is like that of curve (*c*) in Fig. 1 down to the transition temperature of 13.2°K. The graph given in their article can be fitted fairly well by Eq. (6), but exactly how well cannot be determined merely by taking values from the graph.†

It also seems of interest that the behavior of $LiTlC_4H_4O_6\cdot H_2O$, reported recently by Matthias and Hulm,[4] follows something of the nature of Eq. (6) above its transition to the ferroelectric state. Of course the theory given here could not be expected to fit this case because of the entirely different crystal structure. However, any model having discrete energy levels will cause κ to level off near absolute zero, because the system settles into the ground state and thereby loses its temperature dependence.

III. JUSTIFICATION OF THE APPROXIMATION TO THE EXPONENTIAL

In Sec. I $\exp[(lmn|\phi_2|lmn)/kT]$ was approximated as $1-[(lmn|\phi_2|lmn)/kT]$. The validity of this must be examined after the values of certain constants are determined. Assuming $b_1=b_2=b$ and using the formula

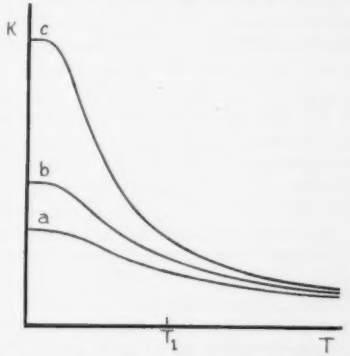

FIG. 1. Curve *a*: $T_0=-0.25T_1$; Curve *b*: $T_0=0$; Curve *c*: $T_0=0.25T_1$.

[1] J. K. Hulm, Proc. Phys. Soc. (London) **A63**, 1184 (1950).

[2] Hulm, Matthias, and Long, Phys. Rev. **79**, 885 (1949).

† *Note added in proof:*—The author has recently obtained by private communication precise measurements of the dielectric constants of $KTaO_3$ from Hulm, Matthias, and Long and of $SrTiO_3$ from J. F. Youngblood. Equation (6) fits the data quite well both for $SrTiO_3$ and for $KTaO_3$ above 13.2°K. The value of T_1 obtained by fitting Youngblood's data is about 100°K. However, this higher value does not appreciably affect any of the results of this paper.

[4] B. T. Matthias and J. K. Hulm, Phys. Rev. **82**, 108 (1951).

for a and the definition of M given below Eq. (6), $b/a^3=B/5Mk$. Now it can be seen from Eq. (3) that the validity of the approximation in question depends on $b/\beta^2kT\ll 1$. Using $h\nu=kT_1$ and $\beta=2a/h\nu$,

$$b/\beta^2kT=(BT_1/20M)(T_1/T). \tag{8}$$

The quantities T_1 and M can be determined experimentally, but B cannot. Slater finds $B=3$ for the simple Lorentz correction and $B=1.93$ for his more involved theory. Since B varies but little for these two quite different situations, it seems safe to assume an upper limit of 10 in general. Now for $SrTiO_3$ at $T_1=60°K$, $b/\beta^2kT=4\times10^{-4}$, and at $T=3°K$, $b/\beta^2kT=8\times10^{-3}$. Somewhat below 3°K, the expansion will fail even for the ground state. However, note that at 3°, $\exp(-h\nu/kT)=\exp(-20)=2\times10^{-9}$. Then at 3°K the system will be practically in its ground state and z will consist of only one term $\exp\{-[W_{000}{}^0+(000|\phi_2|000)/kT]\}$. This will mean that A_E and hence X_{Ti}' and κ will be temperature independent. But at 3°K the formula given for κ is already virtually temperature independent, $d\kappa/dT$ being $-1.7\times10^{-6}°K^{-1}$ and

$$(1/\kappa)(d\kappa/dT)=1.3\times10^{-9}°K^{-1}.$$

Some consideration should also be given to the validity of using the approximation to the exponential at high temperatures. At any given temperature the expansion will fail for sufficiently large l, m, and n. It is necessary to depend on the rapid decrease of $\exp[-(l+m+n)h\nu/kT]$ as l, m, and n increase in order to make the failure of the approximation unimportant. As T increases $h\nu/kT$ will decrease to a point where the exponential factor will no longer decrease rapidly enough with l, m, and n to make failure of the approximation for large quantum numbers unimportant. In order to estimate at what temperature this effect becomes important, a quadratic term was added to the approximation to the exponential and its effect on X_{Ti}' was computed. For $BaTiO_3$ at 500°K the contribution of the quadratic term was about one percent of that from the linear term. As the temperature increases, the ratio of the quadratic contribution to the linear contribution will be proportional to the temperature. Hence, it is felt that the formula for X_{Ti}' is good at all temperatures at which the dielectric constant can be measured.

IV. DISCUSSION

We may expect the quantities involved in the theory —excepting T_0—to be roughly of the same magnitude for other perovskite type crystals as for $BaTiO_3$. This should be particularly true among the titanates. But there is very poor agreement between the value of $T_1=60°K$ obtained for $SrTiO_3$ by fitting the above theory to the experimental data and the value of $T_1=410n$ degrees absolute obtained for $BaTiO_3$ by using the value of a obtained by Slater's theory. Let us examine the factors which influence T_1 as calculated for $BaTiO_3$.

The mass m to be used in calculating ν might be larger than that of the Ti, because of a coupling of the Ti ion to the other ions of the lattice in a normal coordinate vibration. But even using the sum of the masses of all the ions in a unit cell only reduces the value of T_1 by a factor of slightly more than 2. A small value of n would reduce T_1 for $BaTiO_3$, but as Slater has pointed out, experimental data on spontaneous polarization and x-ray data on the ionic displacements rule against a value of $n<1$. The value of a cannot be expected to change enough between the two compounds to account for the difference between the values of T_1.

If the value of D were more nearly the Lorentz value of $\frac{1}{3}$, rather than the value of 5.39 computed by Slater, the a for $BaTiO_3$ would be small enough to reduce T_1 by a factor of 4. However, such a change does not seem possible unless rather large changes are made in the electronic polarizabilities and other quantities used in Slater's work.

In this connection it is interesting to note that the vibration of the Ti ions corresponds to a reststrahlen frequency. Since the binding is supposed to be very loose, the frequency should be unusually low. However, a frequency ν which gives $h\nu/k$ of the order of 400°K is not at all low. It seems that the large Lorentz correction which Slater has computed has made ferroelectricity possible with bindings ordinarily found in crystals. Measurement of the reststrahlen frequencies would provide another means of evaluating the two values of T_1. Without such measurement, there seems to be no explanation of this difference in T_1 between $BaTiO_3$ and $SrTiO_3$.

The author wishes to thank Professor W. V. Houston for suggestion of the problem and for guidance at all stages of its progress. He also wishes to express his gratitude to many other members of the laboratory for helpful discussions.

Letters to the Editor

PUBLICATION of brief reports of important discoveries in physics may be secured by addressing them to this department. The closing date for this department is five weeks prior to the date of issue. No proof will be sent to the authors. The Board of Editors does not hold itself responsible for the opinions expressed by the correspondents. Communications should not exceed 600 words in length.

A Spin-Wave Treatment of the Saturation Magnetization of Ferrites*

HARVEY KAPLAN
Department of Physics, University of California, Berkeley, California
(Received February 15, 1952)

THE semiclassical theory of spin waves[1] is applied here to ferrites containing two types of paramagnetic atoms distributed in tetrahedral (A) and octahedral (B) sites, with nearest-neighbor exchange integrals J_{AA}, J_{BB}, J_{AB}. We determine the temperature dependence of the saturation magnetization.

The exchange Hamiltonian

$$H'=-2\sum_{ns}[J_{AA}\mathbf{A}_i\cdot\mathbf{A}_j+J_{AB}\mathbf{A}_i\cdot\mathbf{B}_j+J_{BB}\mathbf{B}_i\cdot\mathbf{B}_j] \quad (1)$$

leads for a spinel structure to the following equations of motion in the semiclassical approximation

$$\left.\begin{aligned}\hbar\partial\mathbf{A}/\partial t&=2J_{AB}\mathbf{A}\times[12\mathbf{B}+(11/8)a^2\nabla^2\mathbf{B}]+J_{AA}a^2\mathbf{A}\times\nabla^2\mathbf{A};\\ \hbar\partial\mathbf{B}/\partial t&=J_{AB}\mathbf{B}\times[12\mathbf{A}+(11/8)a^2\nabla^2\mathbf{A}]+J_{BB}a^2\mathbf{B}\times\nabla^2\mathbf{B},\end{aligned}\right\} \quad (2)$$

where $2a$ is the lattice parameter. The magnitudes of A and B are average values of the spin for the two types of sites. The right hand terms of Eqs. (2) arise from expressing the sums over nearest-neighbor $\mathbf{A}$ and $\mathbf{B}$ spins in terms of Taylor series to second order around the positions of the given spins. This replacement of discrete spins by a continuum means that we can only treat spin waves with $\lambda\gg a$. In forming the sums over nearest-neighbors of a $\mathbf{B}$ spin, different cross second derivatives appear depending upon the orientation of the coordinate system. In order to make all $\mathbf{B}$ sites mathematically equivalent, the expansion was carried out around each of the four $\mathbf{B}$ sites of a quarter of a unit cell using a single coordinate system and the resulting expressions then averaged. The result was a Laplacian term for both $\mathbf{A}$ and $\mathbf{B}$ neighbors.

We look for solutions of (2) having the form

$$\left.\begin{aligned}\mathbf{A}&=\mathbf{A}_0+\Delta\mathbf{A}\exp[i(\omega t+\mathbf{k}\cdot\mathbf{r})]\\ \mathbf{B}&=\mathbf{B}_0+\Delta\mathbf{B}\exp[i(\omega t+\mathbf{k}\cdot\mathbf{r})],\end{aligned}\right\} \quad (3)$$

Assuming $\mathbf{A}_0$ and $\mathbf{B}_0$ to be in the z direction and neglecting second-order terms, we find the following four equations

$$\left.\begin{aligned}i\omega\Delta A_x&=P\Delta A_y+U\Delta B_y, \quad i\omega\Delta A_y=-P\Delta A_x-U\Delta B_x,\\ i\omega\Delta B_x&=Q\Delta B_y+V\Delta A_y, \quad i\omega\Delta B_y=-Q\Delta B_x-V\Delta A_x,\end{aligned}\right\} \quad (4)$$

where

$$P=(J_{AA}A_0a^2k^2+24J_{AB}B_0)/\hbar, \quad Q=(J_{BB}B_0a^2k^2+12J_{AB}A_0)/\hbar,$$
$$U=[(11/4)a^2k^2-24]J_{AB}A_0/\hbar, \quad V=[(11/8)a^2k^2-12]J_{AB}B_0/\hbar.$$

Solution of the secular equation yields

$$2\omega^2=(P^2+Q^2+2UV)\pm(P+Q)[(P-Q)^2+4UV]^{\frac{1}{2}}. \quad (5)$$

For $ka\ll1$, the region of validity of the approximation, we find that the dispersion curve consists of two branches

$$\left.\begin{aligned}\hbar\omega_1&\cong\frac{|(11/2)J_{AB}A_0B_0+J_{AA}A_0^2+2J_{BB}B_0^2|}{|A_0+2B_0|}(ak)^2\\ \hbar\omega_2&\cong12J_{AB}(A_0+2B_0)\\ &\quad\times\left[\frac{1+\{J_{BB}+2J_{AA}-(11/2)J_{AB}\}A_0B_0}{12J_{AB}(A_0+2B_0)^2}(ak)^2\right],\end{aligned}\right\} \quad (6)$$

where $|A_0+2B_0|$ is the net spin of one molecule.

In applying these formulas to ferrites it is important to note that we assume following Néel[2] that A_0 and B_0 are directed along $+z$ and $-z$, respectively. This is the case when $|J_{AB}|$ is larger than $|J_{AA}|$, $|J_{BB}|$ (all three being negative) and is generally realized for ferrites except when the Zn or Cd content is high.[3] Using other than nearest-neighbor interactions merely modifies the numerical coefficients.

The magnetization at low temperatures ($<0.2T_c$) is obtained by standard spin-wave methods. In the indicated temperature range the contribution of the upper branch ω_2 is negligible. We thus find the magnetization to be given by

$$M_T=M_0\left[1-\frac{0.0587}{|A_0+2B_0|}\times\left\{\frac{kT|A_0+2B_0|}{|(11/2)J_{AB}A_0B_0+J_{AA}A_0^2+J_{BB}B_0^2|}\right\}^{\frac{3}{2}}\right]. \quad (7)$$

It is interesting to note that this result contains information concerning the interactions in ferrites which does not appear in the Néel susceptibility formula derived using a molecular field approach. Accurate experiments in the temperature range $T<0.2T_c$ needed to test the validity of (7) are not presently available.

A NaCl arrangement of A and B atoms was also studied. In the antiferromagnetic case $A_0=-B_0$ and assuming $J_{AA}=J_{BB}$, the dispersion law for small k becomes

$$\hbar\omega=2aA_0[12J_{AB}(J_{AB}-4J_{AA})]^{\frac{1}{2}}k, \quad (8)$$

a generalization of a result of Hulthén[4] and Anderson[5] obtained using a different formalism.

I wish to thank Professor C. Kittel for suggesting this problem and for enlightening discussions during its solution.

* This work was done during the tenure of a James Sutton Fellowship at the University of California and was assisted in part by the ONR.
[1] G. Heller and H. A. Kramers, Proc. Roy. Acad. Amsterdam **37**, 378 (1934); C. Herring and C. Kittel, Phys. Rev. **81**, 869 (1951), Appendix A.
[2] L. Néel, Ann. phys. **3**, 137 (1948).
[3] Y. Yafet and C. Kittel (to be published).
[4] L. Hulthén, Proc. Roy. Acad. Amsterdam **39**, 190 (1936).
[5] P. W. Anderson, Phys. Rev. (to be published). I wish to thank Dr. Anderson for the privilege of seeing his manuscript prior to publication.

Angular Distribution of π^+ Production in n-p Collisions

H. A. BETHE AND N. AUSTERN*
Laboratory of Nuclear Studies, Cornell University, Ithaca, New York
(Received February 11, 1952)

VARIOUS phenomenological explanations have been given for the anisotropy of the π^+ production in p-p collisions. It is interesting to make similar calculations for meson production in n-p collisions, especially as in this case the angular distribution will be very sensitive to the choice of theory.

(I) Chew *et al.*[1] find that the angular distribution which is observed for the process $p+p\to\pi^++d$ can be fitted by a transition matrix of the form $(\{\boldsymbol{\sigma}_1\tau_1^++\boldsymbol{\sigma}_2\tau_2^+\}\cdot\mathbf{q})$, in accord with pseudoscalar theory and the impulse approximation, provided that one takes account of the ${}^3D_1$ admixture in the deuteron. (Here $\mathbf{q}$ is the meson momentum, and τ_j^+ converts the jth proton into a neutron or annihilates the jth neutron.) Their result, however, is so strongly dependent on the details of the nuclear dynamics, that their suggestion may not describe the actual mechanism of production of the anisotropy. (II) An alternative theory by Watson and Brueckner[2] is not so sensitive to the nuclear wave functions, as it ascribes the anisotropy to the addition to the transition matrix of what are, essentially, recoil terms. The simplest such term which has the correct symmetry to describe meson emission into a P state has the form $(\{\boldsymbol{\sigma}_1\tau_1^++\boldsymbol{\sigma}_2\tau_2^+\}\cdot\mathbf{p})(\mathbf{p}\cdot\mathbf{q})$, where $\mathbf{p}$ is the nucleon momentum.

In Theory I the meson momentum is only oriented with respect to the nucleon spins, and the orbital momentum of the nucleons is conserved in the transition. There cannot be any anisotropy

unless the spins are somehow oriented. If the final state is a deuteron, then it is a mixture of S and D states and there can be some spin orientation, the reference direction being provided by the initial D state. This leads the angular distribution of the emitted mesons to be anisotropic. Whether the correct amount of anisotropy is obtained, depends on the fraction of D state in the deuteron, as well as on the details of the transition matrix elements to the high energy S and D states. If the final state is a double neutron, resulting from $n+p\rightarrow 2n+\pi^+$, then at low energy it must be in a $^1S_0$ state; then the initial state can only be $^3S_1$, and an anisotropy can only exist to the extent that the high energy $^3S_1$ state spins are oriented by the tensor force coupling to $^3D_1$. In the notation of Rohrlich and Eisenstein,[3] the resultant average square matrix element becomes

$$[U_\alpha{}^2+(\eta_1{}^\alpha)^2U_\gamma{}^2][1+(\eta_1{}^\alpha)^2]^{-1}+\tfrac{1}{4}(3\cos^2\theta-1)[1+(\eta_1{}^\alpha)^2]^{-1}$$
$$\times\left\{(\eta_1{}^\alpha)^2[U_\alpha{}^2+U_\gamma{}^2-2U_\alpha U_\gamma\cos(\delta_\alpha-\delta_\gamma)]\right.$$
$$-8\left[\eta_1{}^\alpha U_\alpha{}^2+\eta_1{}^\gamma U_\gamma{}^2\left(\frac{1+(\eta_1{}^\alpha)^2}{1+(\eta_1{}^\gamma)^2}\right)^2\right.$$
$$\left.\left.+(\eta_1{}^\alpha+\eta_1{}^\gamma)U_\alpha U_\gamma\cos(\delta_\alpha-\delta_\gamma)\left(\frac{1+(\eta_1{}^\alpha)^2}{1+(\eta_1{}^\gamma)^2}\right)\right]\right\}, \quad (1)$$

where

$$U_{\alpha,\gamma}\equiv\int_0^\infty u_{\alpha,\gamma}u_F dr, \quad \text{and} \quad \eta_1{}^\alpha\eta_1{}^\gamma=-1,$$

and u_F is the "radial" wave function of the low energy ^1S state. The above expression is sensitive to the nuclear dynamics but does not appear to lead to more than about a twenty percent $\cos^2\theta$-term in the angular distribution, if reasonable dynamical guesses are made for the various quantities in it.

For Theory I an almost isotropic distribution must therefore be expected for the charged mesons resulting from an n-p collision, contrary to the distribution observed for p-p collisions. The isotropy will hold particularly for the fastest mesons which can be produced for a given energy of the incident neutron. Fortunately, the energy spectrum of the mesons will have the now-familiar high energy peak. This peak is expected because of the attraction which two low energy neutrons bear for each other and will be reinforced because the meson production matrix element rises with meson energy. The peak itself will not be visible, however, without the use of a fairly monochromatic neutron beam, such as the beam which may be obtained from charge-exchange $p+d$ scattering.[4,5]

In Theory II, the angular distribution of the mesons will be essentially the same for n-p as for p-p production, because here the meson momentum is directly coupled to the nucleon momentum. To take into account both types of coupling let us consider a transition matrix of the form

$$T'=(\{\boldsymbol{\sigma}_1\tau_1{}^+-\boldsymbol{\sigma}_2\tau_2{}^+\}\cdot\mathbf{q})+A(\{\boldsymbol{\sigma}_1\tau_1{}^+-\boldsymbol{\sigma}_2\tau_2{}^+\}\cdot\mathbf{p}/\mu c)(\mathbf{q}\cdot\mathbf{p}/\mu c). \quad (2)$$

Taking the nucleon final state to be the ^1S state and the high energy state to be the plane wave, $e^{i(\mathbf{k}\cdot\mathbf{r})}$, the matrix element is

$$T_{AF'}=(e^{i(\mathbf{k}\cdot\mathbf{r})}\chi_1{}^m, T'u_F\chi_0{}^0)$$
$$=\tfrac{1}{2}(e^{i(\mathbf{k}\cdot\mathbf{r})}\chi_1{}^m, [(\{\boldsymbol{\sigma}_1-\boldsymbol{\sigma}_2\}\cdot\mathbf{q})+A(\hbar/\mu c)^2$$
$$\times(\{\boldsymbol{\sigma}_1-\boldsymbol{\sigma}_2\}\cdot\mathbf{k})(\mathbf{k}\cdot\mathbf{q})]u_F\chi_0{}^0).$$

Then

$$\Sigma_m|T_{AF'}|^2=U^2[1+2A(\hbar k/\mu c)^2\cos^2\theta+A^2(\hbar k/\mu c)^4\cos^2\theta],$$
$$U\equiv\int_0^\infty u_F\sin krdr. \quad (3)$$

While field theory leads to a coefficient A which is small, of the order $(\mu/M)^2$, it is in the spirit of Theory II to treat A as a free parameter. Indeed, if II is the only mechanism responsible for the p-p anisotropy, then the above expression represents an exactly equal n-p anisotropy.

Production of charged mesons by collisions between neutrons and protons thus provides a sensitive test for the type of coupling between meson field and nucleons. Near-isotropy would favor Theory I, while a strong anisotropy would indicate some such theory as II. It would probably be helpful to have an approximately monoenergetic neutron beam and to observe the angular distribution of the high energy mesons.

The total cross section can be estimated from the p-p cross section, in terms of the relative amplitudes which the final state nuclear wave functions have at the origin.

$$\sigma_{np}\approx\int dE_F\,\rho(E_F)\left[\left(\frac{\partial u_F}{\partial r}\right)_{r=0}\Big/\left(\frac{\partial u}{\partial r}\right)_{r=0}\right]^2\sigma_{pp}.$$

For a total kinetic energy of 50 Mev in the final state, the integrated n-p production cross section is about equal to the p-p production cross section. This estimate is probably more satisfactory for Theory I, which does not involve the uncertain nucleon momenta so strongly as does Theory II.

* AEC Postdoctoral Fellow.

[1] Chew, Goldberger, Steinberger, and Yang, Phys. Rev. **84**, 581 (1951).
[2] K. M. Watson and K. A. Brueckner, Phys. Rev. **83**, 1 (1951).
[3] F. Rohrlich and J. Eisenstein, Phys. Rev. **75**, 705 (1949).
[4] R. Gluckstern and H. A. Bethe, Phys. Rev. **81**, 761 (1951).
[5] G. F. Chew, Phys. Rev. **84**, 710 (1951).

Faraday Rotation of Guided Waves

H. Suhl and L. R. Walker
Bell Telephone Laboratories, Murray Hill, New Jersey
(Received January 23, 1952)

RECENTLY several means of causing microwave Faraday rotation (F.R.) have been proposed: (1) the gyromagnetic resonance in ferrites,[1] (2) the cyclotron resonance of electrons in a discharge plasma,[2] and (3) the Hall effect in conductors or semiconductors.[3] Experimental evidence of the rotation is most readily obtained by placing these agents into a circular waveguide carrying the lowest order transverse electric mode (TE_{11}). A steady magnetic field H_0 along the guide axis $0z$ then causes rotation of the field pattern about the guide axis.

However, the standard treatment of F.R. deals with plane waves of infinite extent, hence is inapplicable to guided waves. We have established the natural modes of propagation in a guide filled with any one of the proposed media. These modes are circularly polarized and are never purely transverse electric or magnetic, but can be classified according to whether their limits as $H_0\rightarrow 0$ are TE or TM. Right-circular and left-circular waves proceed down the guide with different propagation constants given by a transcendental equation. For small H_0, and for waves with TE limit, the difference, as in the elementary theory, leads to a rotation of the plane of polarization of an initially plane polarized wave. The rotation in radians per gauss per unit length (Verdet's constant R) equals that in the unbounded medium R_p, times a factor depending on the propagation characteristics of the guide at $H_0=0$. The rotation of TM limit modes varies as a higher power of R_pH_0 for small H_0, so that there is no Verdet's constant in the usual sense.

The permeability in case (1), and the dielectric constant in cases (2) and (3) are tensors of the form

$$\begin{bmatrix}\mu & -i\alpha_H M_0 & 0\\ i\alpha_H M_0 & \mu & 0\\ 0 & 0 & \mu_z\end{bmatrix};\quad\begin{bmatrix}\epsilon & -i\alpha_E H_0 & 0\\ i\alpha_E H_0 & \epsilon & 0\\ 0 & 0 & \epsilon_z\end{bmatrix}$$

respectively. M_0 is the magnetization due to H_0. The μ's, ϵ's and α's may depend on the frequency ω, and except for μ_0, ϵ_z may be function of $|H_0|$. They may have imaginary parts to allow for losses. In case (1), the μ's and α may also depend on sample shape.[4] All these quantities are assumed independent of position.

Verdet's constant for a plane wave in the unbounded medium progressing along $0z$ is given by $R_p=\alpha_H\beta_0M_0/2\mu H_0$ in case (1) and $R_p=\alpha_E\beta_0/2\epsilon$ in cases (2) and (3), where $\beta_0=\omega(\mu\epsilon)^{\frac{1}{2}}$. In general R_p may be field and frequency dependent.

The possible propagation constants β for the modes that vary as $e^{\pm in\varphi-i\beta z}$ with polar angle φ and axial distance z (in cylindrical

polar coordinates) are given in all three cases by an equation of the form

$$\pm(nA/r_0)J_n(\chi_1 r_0)J_n(\chi_2 r_0)=\alpha_2 J_n(\chi_1 r_0)J_n'(\chi_2 r_0) -\alpha_1 J_n(\chi_2 r_0)J_n'(\chi_1 r_0), \quad (1)$$

where in case (1)

$$A=\frac{\beta^2}{\beta_0}\frac{p_2{}^2-p_1{}^2}{\zeta_1\zeta_2}, \quad \alpha_s=\frac{\chi_s}{\zeta_s}[\beta^2-\beta_0{}^2+2\zeta_s R_p H_0-4R_p{}^2H_0{}^2] \quad (s=1,2),$$
$$\delta=(1-\mu_H/\mu), \quad R_p=(\alpha_H\beta_0/2\mu)(M_0/H_0),$$

and in cases (2) and (3)

$$A=(p_1{}^2-p_2{}^2)\beta_0, \quad \alpha_s=\chi_s[(\beta_0{}^2-\beta^2)\zeta_s+2\beta^2R_pH_0] \quad (s=1,2),$$
$$\delta=1-\epsilon_2/\epsilon_1, \quad R_p=\alpha_E\beta_0/2\epsilon,$$

and where for all three cases

$$\zeta_s=[(\beta^2-\beta_0{}^2)\delta-p_s{}^2]/2R_pH_0, \quad \chi_s{}^2=\beta_0{}^2-\beta^2+p_s{}^2 \quad (s=1,2),$$

$$p_{1,2}{}^2=-2R_p{}^2H_0{}^2-\frac{\delta}{2}(\beta_0{}^2-\beta^2)\pm 2R_pH_0 \times\left\{\beta^2-\beta_0{}^2\delta+\frac{1}{4}\left[2R_pH_0+\frac{\delta}{2R_pH_0}(\beta_0{}^2-\beta^2)\right]^2\right\}^{\frac{1}{2}}.$$

Equation (1) gives the β's for both TE limit and TM limit modes. For small H_0, these β's are easily found by expansion. It turns out that the deviations $\Delta\beta_{\pm n;m}$ from the β_{nm} of the TE_{nm} waves due to a small magnetic field H_0 [or to a small magnetization in case (1)] are proportional to H_0. The corresponding rotation $|\Delta\beta_{nm}/\pi|$ can, therefore, be specified by a new Verdet's constant. In case (1)

$$R_{\text{guide}}{}^{(nm)}=2\lambda_0 R_p/[(u_{nm}{}^2-n^2)\lambda_g], \quad (2)$$

and in cases (2) and (3)

$$R_{\text{guide}}{}^{(nm)}=2\lambda_g R_p/[(u_{nm}{}^2-n^2)\lambda_0], \quad (3)$$

where λ_g is the guide wavelength of the TE_{nm} mode at zero H_0, λ_0 the wavelength in the infinite medium, and u_{nm} is the mth zero of $J_n'(x)$.

Formulas (2) and (3) show that the guide causes dispersion in R additional to that of R_p. They have meaning only in the loss free case. When there is loss, the $\Delta\beta_{\pm nm}$ have opposite imaginary parts leading to progressive conversion from linear to circular polarization (accompanied by rotation). Equations (2) and (3) obviously fail very near resonances. The full equation (1) has then to be solved. Formula (3) also fails near cutoff ($\lambda_g=\infty$). These, and other matters are to be discussed in a later paper. The authors are indebted to Dr. C. L. Hogan and Dr. A. D. Perry of these Laboratories for discussion of their work on ferrites, and for acquainting the authors with their theoretical work on transverse H_0.

[1] D. Polder, Phil. Mag. **40**, 99–115 (1949); C. L. Hogan, Bell System Tech. J. **31**, 1 (1952).
[2] Goldstein, Lampert, and Heney, Phys. Rev. **82**, 956 (1951).
[3] E. R. Wicher, J. Appl. Phys. **22**, 1327 (1951).
[4] C. Kittel, Phys. Rev. **71**, 270 (1947); **73**, 155 (1948).

Radiation from an Electron in a Magnetic Field

D. L. Judd, J. V. Lepore, M. Ruderman, and P. Wolff
Radiation Laboratory, Department of Physics, University of California, Berkeley, California
(Received December 10, 1951)

THIS problem was recently considered by Parzen[1] who concluded that quantum corrections to the classical results of Schwinger[2] and Schiff[3] should be appreciable at an electron energy of 200 mc^2 in a field of 10^4 gauss. The form of his correction is such that for this magnetic field the energy loss per turn by radiation would only increase as R^1 with increasing energy, instead of increasing as E^4/R, thus removing the stringent radiation limitation on synchrotron design.

An examination of Parzen's calculation reveals an invalid approximation.[4] More significantly, the assertion that on $l=0$ to $l=0$ transitions are appreciable can be shown to be incorrect by directly summing the series [Eq. (36)]. This yields

$$I(n'l|n0)=\frac{(-\alpha^2/2)^{l/2}}{\sqrt{l!}}I(n'0|n0) \quad (1)$$

in which the important values of $(\alpha^2/2)$ are of order unity. This result may be verified more easily by use of the energy eigenfunctions in Cartesian coordinates,[5] by the use of which the summation over l is implicitly performed.

If one now examines the formula for the power radiated in the orbital plane and makes use of these results, the exponential correction factor in Eqs. (26) cancels out and the classical result is obtained as sketched in the following:

$$I(n'0|n0)=(n'!/n!)^{\frac{1}{2}}(-\alpha^2/2)^{\lambda/2}\exp(-\alpha^2/2)L_{n'}{}^{\lambda}(\alpha^2/2) \quad (2a)$$
$$=\frac{(-1)^{\lambda/2}}{(n!n'!)^{\frac{1}{2}}}\int_0^{\infty}d\mathcal{E}\,e^{-\mathcal{E}}\mathcal{E}^{n'+\lambda/2}J_\lambda(\alpha(2\mathcal{E})^{\frac{1}{2}}). \quad (2b)$$

Combining Eq. (2b) with the relation[6]

$$J_\lambda(\alpha(2\mathcal{E})^{\frac{1}{2}})=(1+\tau/n)^{\lambda/2}\sum_{m=0}^{\infty}\frac{(-\alpha\tau)^m}{(2n)^{m/2}m!}J_{\lambda+m}(\alpha(2n)^{\frac{1}{2}}), \quad (3)$$

where $t=n+\tau$, one obtains

$$I(n'0|n0)\simeq\frac{(-1)^{\lambda/2}}{(2\pi n)^{\frac{1}{2}}}\exp(-\lambda^2/4n')\int_{-\infty}^{\infty}d\tau\exp(-\tau^2/2n) \times\sum_{m=0}^{\infty}\frac{(-\alpha\tau)^m}{(2n)^{m/2}m!}J_{\lambda+m}(\alpha(2n)^{\frac{1}{2}}). \quad (4)$$

The major contribution to this integral comes in the region $|\tau|<(2n)^{\frac{1}{2}}$. Also, $\alpha(2n)^{\frac{1}{2}}=\lambda\beta$ in the orbital plane. In the summation, only about α-terms contribute so that the relevant values of m are of order $\alpha=\lambda\beta/(2n)^{\frac{1}{2}}\ll\lambda$. For these m, $J_{\lambda+m}(\lambda\beta)=J_\lambda(\lambda\beta)$ for $1-\beta^2\ll 1$, so that (4) becomes

$$\frac{(-1)^{\lambda/2}J_\lambda(\lambda\beta)\exp(-\lambda^2/4n')}{(2\pi n)^{\frac{1}{2}}}\int_{-\infty}^{\infty}\exp[-(\tau^2/2n)-\alpha\tau/(2n)^{\frac{1}{2}}]d\tau \simeq\exp(-\alpha^2/4)J_\lambda(\lambda\beta).$$

The power radiated in the orbital plane is proportional to the sum

$$\sum_{l=0}^{\infty}|I(n'l|n+1,0)+I(n'l|n-1,0)|^2,$$

which may now be evaluated using Eq. (1) to give $[2J_\lambda'(\lambda\beta)]^2$, the classical result.

It is a pleasure to acknowledge helpful discussions with Professor E. M. McMillan, who brought this matter to our attention. We also wish to thank Professor L. I. Schiff for sending us his wave packet arguments[7] which confirms Schwinger's criterion for validity of the classical approximation.

[1] G. Parzen, Phys. Rev. **84**, 235 (1951).
[2] J. Schwinger, Phys. Rev. **75**, 1912 (1949).
[3] L. I. Schiff, Rev. Sci. Instr. **17**, 8 (1946).
[4] Following his Eq. (23), we should have $[(n+\lambda)!/n!]^{\frac{1}{2}}\simeq n^{\frac{1}{2}\lambda}\exp(\lambda^2/4n)$, from the Stirling approximation; terms of order $\lambda^2/n^{\frac{1}{2}}\simeq\alpha^2/n^{\frac{1}{2}}$ are neglected since $n\sim 10^{12}$.
[5] M. H. Johnson and B. A. Lippman, Phys. Rev. **76**, 828 (1949), Eq. (43).
[6] G. N. Watson, *Theory of Bessel Functions* (Macmillan Company, New York, 1944), p. 141, Eq. 5.
[7] L. I. Schiff, Am. J. Phys. (to be published).

Radiation Loss of Electrons in the Synchrotron

H. Olsen and H. Wergeland
Fysisk Institutt, Norges Tekniske Høgskole, Trondheim, Norway
(Received January 14, 1952)

IN a recent paper of Parzen,[1] the radiation of electrons in uniform circular motion was calculated by means of the exact wave functions in a homogeneous magnetic field.

The result would seem to indicate a total radiation loss considerably smaller than to be expected on classical theory.[2,3]

This is very surprising since the main loss is due to the soft quanta, i.e., emissions which cause a relatively small change of the enormous quantum numbers involved in an orbit of macroscopic size at these energies. By the correspondence principle it is

then hard to understand how the classically computed intensity could be much off.

Let us therefore inspect the classical and quantum-mechanical results: On classical theory the energy radiated per unit solid angle and second, with wave number vector $\mathbf{k}$, is

$$P_{\mathrm{cl}}=\frac{c}{2\pi}\left|\frac{\omega}{2\pi}\int_0^{2\pi/\omega}dt[e\boldsymbol{\beta}\times\mathbf{k}]\exp\{i[kct-\mathbf{k}\cdot\mathbf{R}(t)]\}\right|^2$$
$$=\frac{ce^2k^2}{2\pi}\{\cot^2\Theta J_N^2(N\beta\sin\Theta)+\beta^2J_N'^2(N\beta\sin\Theta)\},\quad(1)$$

where $\beta=$ velocity/c, $\omega=$ mechanical frequency, and $N=ck/\omega$.

This is then to be compared with the quantum-mechanical expectation value for the number of photons of frequency ck emitted per second, multiplied by their energy, $\hbar ck$. But that is just the quantity obtained in the first approximation of the conventional perturbation theory, *viz.*,

$$P_{\mathrm{q.m.}}=\hbar ck(2\pi/\hbar)\Sigma|\mathcal{H}_{FA}'|^2\rho(E_F)\quad(2)$$

where $\mathcal{H}_{FA}'$ is the matrix element of single photon emission. To get the total intensity the sum must be taken, not only over the polarizations of the quantum, but also over all the final electron states of the same energy.

In the notation of Parzen's paper[1] the matrix element is

$$\mathcal{H}_{FA}'=e\omega b\left(\frac{\pi\hbar}{ckL^3}\right)^{\frac{1}{2}}\{\epsilon_{k\lambda}^{-}(n+1)^{\frac{1}{2}}I(n',l'|n+1,l)$$
$$+\epsilon_{k\lambda}^{+}n^{\frac{1}{2}}I(n',l'|n-1,l)\}$$

where

$$b^2=\hbar/m\omega_0=\hbar c/eH,$$
$$I(n'l'|nl)=\int u_{n'l'}^{*}\exp(-ik\rho\sin\Theta\cos\varphi)u_{nl}\rho d\rho d\varphi,$$
$$u_{nl}=\left(\frac{l!}{2\pi b^2n!}\right)^{\frac{1}{2}}\cdot\exp(-\rho^2/4b^2)(\rho^2/2b^2)^{\frac{1}{2}(n-l)}$$
$$\cdot L_l^{n-l}(\rho^2/2b^2)\cdot\exp[i(n-l)\varphi].$$

u_{nl} are the wave functions of the electron in the magnetic field, corresponding to circular orbits of radius $R_n=(2n+1)^{\frac{1}{2}}b$ whose centers lie on a circle of radius $(2l+1)^{\frac{1}{2}}b$. The energy eigenvalues

$$E_n=c[p_z^2+m^2c^2+m\hbar\omega_0(2n\pm1+1)]^{\frac{1}{2}}$$

are independent of the quantum number l.

Putting aside for the moment the question of whether the narrowest possible location of the orbit center is a proper representation of the experimental situation, we shall only consider the initial state, $l=0$, treated by Parzen, although the general case is also tractable.[2]

The integral $I(n'l'|n0)$ can be evaluated in closed form:

$$I(n'l'|n0)=\left(\frac{n'!}{n!l'!}\right)^{\frac{1}{2}}\cdot i^{n-n'-l'}\cdot\left(\frac{\alpha^2}{2}\right)^{\frac{1}{2}(n-n'-l')}$$
$$\cdot\exp(-\alpha^2/2)L_{n'}^{n-n'}(\alpha^2/2),$$
$$\alpha=kb\sin\Theta=(n-n')(\hbar\omega/c)b\sin\Theta.$$

Now we need the products and squares of such integrals summed over the quantum numbers l' of the final state. True enough, the term $l'=0$ which was the only one taken into account by Parzen, is the largest, but the others cannot be neglected:

$$\sum_{l'=0}^{n'}|I(n'l'|n0)|^2\approx\sum_0^{\infty}$$
$$=\frac{n'!}{n!}\left[\left(\frac{\alpha^2}{2}\right)^{\frac{1}{2}(n-n')}\cdot\exp(-\alpha^2/4)L_{n'}^{n-n'}(\alpha^2/2)\right]^2.$$

Introducing the harmonic number $N=n-n'$ and a mean velocity $\bar{\beta}=(\omega/c)[(R_n^2+R_{n'}^2)/2]^{\frac{1}{2}}$, it is easy to show[4] that for large n, n' and $N\ll n$, n' the sum is

$$\Sigma|I|^2=J_N(N\bar{\beta}\sin\Theta)+(\alpha^2/2)^{N/4}\cdot O(n'^{-\frac{1}{2}}).$$

Insertion of such expressions in (2) gives the classical result (1), with an error which is certainly negligible in the most important region of angle and frequency. This conclusion can also be shown to hold for an initial state compounded of various l's, but the analysis is then more laborious.[3]

We would like to thank Professor Dyson for calling our attention to the importance of this question for synchrotron design and also for suggesting the probable cause of the discrepancy between Parzen's result and the previous ones, which is indeed chiefly due to the terms $l'>0$.

[1] G. Parzen, Phys. Rev. **84**, 235 (1951).
[2] J. Schwinger, Phys. Rev. **75**, 1912 (1949).
[3] H. Olsen and H. Wergeland, Kgl. Norske Videnskab. Selskab. Forh. **XXIII**, 91 (1950); H. Olsen, Thesis, Trondheim (to be mimeographed).
[4] G. Szegö, *Orthogonal Polynomials* (American Mathematical Society, New York, 1939), p. 193.

Electrical Properties of the Sodium Tungsten Bronzes

HELLMUT J. JURETSCHKE
Polytechnic Institute of Brooklyn, Brooklyn, New York
(Received November 29, 1951)

RECENTLY Brown and Banks[1] have determined the resistivity of the sodium tungsten bronzes (Na_xWO_3, $x<1$) as a function of x and of the temperature. They confirmed the metallic nature of the conduction proposed earlier on the basis of resistance-temperature[2] and magnetic susceptibility[3,4] measurements, and ascribed conduction primarily to the free electrons contributed by Na. However, their results disagree quantitatively with those to be expected for pure sodium.

It is the purpose of this note to indicate that their results are not inconsistent with those to be expected for pure Na, distributed uniformly in a cubic mesh within the WO_3, under high (positive or negative) pressure. The same model accounts for the values of the Hall coefficient (Huibregtse, Barker, and Danielson[2]) and of the magnetic susceptibility (Stubbin and Mellor[3]) obtained for these bronzes.

It is often noted that many properties of the alkali metals depend primarily on the atomic volume, and much less on crystal structure. The recently established continuity of the compressibility of liquid and solid sodium[5] is an example of this behavior. Let us assume that pure Na occupies a fraction α of the total volume of the bronze crystal. The volume available to Na in the cubic WO_3 is roughly the difference between the total volume and the ionic volume of the constituents. In the perovskite structure it is very likely that the tungsten completely fills the space between its six surrounding oxygens. Using the linear increase in lattice dimensions with x[6] and an average ionic radius $r(O^{--})=1.37$A one finds the volume per Na atom $v(\mathrm{Na})=19.6/x+2.9$A^3, assuming the ionic volume to be relatively independent of x. The fraction of the total volume occupied by Na is nearly independent of x: $\alpha=0.36$. The value $x=0.55$ corresponds to the normal density of metallic Na. If sodium has its normal properties in the volume it occupies in the lattice, the volume susceptibility of the bronze for $x=0.55$ should differ from that for pure Na by a factor α. Kupka and Sienko[4] found the volume susceptibility of the bronze ($x=0.55$) to be 0.25×10^{-6} cgs. Using $\chi=0.63\times10^{-6}$ cgs for pure sodium, the above considerations would lead to a value $\chi=0.23\times10^{-6}$ cgs for this bronze.

The resistivity minimum of the bronze for $x=0.70$ found by Brown and Banks corresponds to a pressure of 24,000 kg/cm^3, assuming the normal properties of metallic sodium ($\Delta v/v_0=-0.19$). At its minimum the resistivity is 0.57 of its value at $x=0.55$ (0°C). Since the pressure value depends on the ionic volume assumed, only its general magnitude is significant. Bridgman[7] has predicted the resistivity minimum for pure Na at a pressure of 28,000 kg/cm^2. He expects the minimum resistivity to be 0.44 of its normal value. Furthermore, the specific temperature coefficient of resistivity $(1/\rho)(d\rho/dT)$ of pure sodium is independent of pressure. This is in good agreement with the values of this coefficient as a function of x.[8]

The measured values of the electrical properties of the sodium bronzes must now be reinterpreted on the basis that sodium has its normal properties in the volume it occupies in the lattice.

TABLE I. Electrical properties of Na_xWO_3 and normal metallic Na. Corrected values for the bronze are based on the actual atomic density of Na in WO_3.

	Resistivity 10^3 ohm-cm	Temp. coeff. of res. 10^6 ohm-cm/°C	Hall coeff. 10^4 cm³/coul.	Magn. susc. 10^6 cgs
Measured (indicated x)	5.3 (0.55)	15.7 (0.55)	−5.1 (0.66)	0.20 (0.65)
Adjusted (to $x=0.55$)	5.3	15.7	−6.1	0.19
Corrected	0.80	2.4	−2.2	0.53
Pure Na	0.52	2.3	−2.5	0.63

In an elementary way the sodium can be thought of as distributed in a cubic framework of tubes of uniform diameter. If α is the fraction of the total volume which is conducting, the ratio of the resistivity of the conducting material to the measured resistivity is slightly larger than $\alpha/3$ (using the exact relation between cross-sectional and volume fraction for a cubic mesh), while the true and measured Hall coefficients differ by a factor α. Table I lists the measured and corrected values of these quantities ($\alpha=0.36$) and compares them with those of sodium metal (25°C). Wherever necessary, the measured values have been adjusted to the normal density ($x=0.55$) by free electron gas density corrections. Values for the original x and after this adjustment are listed.

The table includes the temperature independent magnetic susceptibility measured by Stubbin and Mellor. It should be noted that the distance between neighboring sodium sites in the bronze lattice (3.80A) is very close to the nearest neighbor distance in metallic sodium, and that at the concentration of interest 0.82 of all sites in one direction are occupied. Thus, both the volume available to the sodium and the nearest neighbor distance in the bronze are comparable to those in the bulk metal.

I would like to thank Dr. Banks for a valuable discussion on the properties of these bronzes.

[1] B. W. Brown and E. Banks, Phys. Rev. **84**, 609 (1951).
[2] Huibregtse, Barker, and Danielson, Phys. Rev. **84**, 142 (1951).
[3] P. M. Stubbin and D. P. Mellor, Proc. Roy. Soc. N.S. Wales **82**, 225 (1948).
[4] F. Kupka and M. J. Sienko, J. Chem. Phys. **18**, 1296 (1950).
[5] T. E. Pochapsky, Phys. Rev. **84**, 553 (1951).
[6] B. W. Brown, M.S. thesis, Brooklyn Polytechnic Institute (1951), unpublished.
[7] P. W. Bridgman, *The Physics of High Pressures* (G. Bell and Sons, London, England, 1931), p. 283.
[8] See reference 1, Table I.

Photodisintegration by Meson Reabsorption

ROBERT R. WILSON
Cornell University, Ithaca, New York
(Received February 12, 1952)

THE production of high energy protons when synchrotron bremsstrahlung are incident on nuclei has been measured by Silverman and Leventhal[1] and by Keck[2] using counters, and by Walker,[3] Miller,[4] and Kikuchi,[5] using photographic techniques. It is observed that the high energy protons are strongly peaked in the forward direction, that the cross section is nearly proportional to Z, that the energy of the protons cuts off at about half the photon energy and that the cross sections are large, i.e., about $Z\times10^{-28}$ cm² per "Q" for protons above 70 Mev produced by 300-Mev bremsstrahlung.

Levinger[6] was able to show fair agreement with the angular distribution assuming an electromagnetic interaction of the photon with two closely interacting nucleons, i.e., a "deuteron," in the nucleus. Basic to his theory were the calculations of Schiff on the disintegration of the deuteron. On the other hand, Levinger's theory gave too low values for the absolute cross section. Kikuchi and Miller measured the number of stars as a function of photon energy. The remarkable increase in the cross section beginning at the meson threshold led them to suggest meson emission and reabsorption in the same nucleus as the mechanism of the disintegration. An objection to this picture was raised, however, because it would predict a more nearly isotropic distribution of the protons inasmuch as the mesons are formed principally at large angles. Kikuchi pointed out that most of the high energy protons were associated with stars and that the absolute cross section was consistent with the assumption of meson emission and reabsorption. Thus, this theory explains the large cross section but fails to explain the angular distribution, while Levinger's theory explains the angular distribution but not the cross section.

The discrepancy between the two theories is resolved if the emitted meson is reabsorbed by the system consisting of the parent nucleon and its nearest neighbor. These two nucleons will usually be a neutron and a proton, in which case the meson production and reabsorption will be indistinguishable from the electromagnetic deuteron disintegration process. The system will retain the momentum of the photon, so that the angular distribution will now be given essentially by Levinger's calculation.

We must now show that most of the mesons are reabsorbed by the parent nucleons. Consider first the case of a deuteron. One can assume, after Fermi,[7] that if the two nucleons and the meson are all produced within a volume of radius $\hbar/\mu c$, then they will all interact and come into equilibrium so that the resulting particles will be given by their statistical weights. The most probable result will be the emission from the system of just two nucleons, the probability of re-emission of the meson being ten percent or smaller. Thus, the above process will look exactly like the photoelectric disintegration of the deuteron. From the known wave function of the deuteron, one can calculate the probability of the two nucleons being within a radius of $\hbar/\mu c$. This is roughly 0.2 for the Hulthén wave function. Then, if the meson is also within this radius at the time of production, as it is at these high energies (meson energy >70 Mev), we need take roughly 0.2 times the known meson production cross section for the neutron and proton to find the cross section for photodisintegration of the deuteron. For 300-Mev photons, the total charged and neutral meson production cross section per nucleon is about $2.\times10^{-28}$ cm², and hence, the photodisintegration cross section at this energy should be about 0.8×10^{-28} cm²—more than an order of magnitude greater than Schiff's extrapolated values would indicate. Except for the effects of virtual mesons, the cross section should parallel the variation of the meson production cross section with energy. Benedict,[8] Kikuchi,[5] and Gilbert[11] have observed anomalously large cross sections, as this treatment would indicate.

One could sharpen the above argument considerably using detailed balancing to determine the probability of reabsorption, but this has not been done because it is felt that virtual mesons will also contribute considerably to the cross section, especially for photon energies near meson threshold. It is difficult in the above process of meson production and reabsorption to see how the nucleons can tell the difference between a meson that is to be real or one that is virtual. Roughly speaking, meson production can be considered in two stages—as are nuclear reactions. First, the photon is absorbed to form an "excited nucleon," which then decays by meson emission or alternatively by re-emission of the photon depending on the available energy, statistical weights, etc. The excited nucleon may consist of a virtually produced meson raised to a different energy state. Then, presumably, this meson is available to be absorbed by the two nucleon system exactly as was discussed above for real mesons. Thus, we would expect the "meson part" of the photodisintegration cross section to parallel the cross section for formation of the excited nucleon and to extend even below the meson threshold.

Now in nuclear matter the probability of a given nucleon having a neighboring nucleon with $\hbar/\mu c$ is much greater than in the simple deuteron. In fact, since the average spacing between nucleons is about $\hbar/\mu c$, the probability will be close to unity. This means that mesons are not essentially produced in the interior of the nucleus, for most of the mesons are reabsorbed directly on production. Furthermore, those mesons which leave the nucleons must have been produced at the surface. This is in agreement

with the observed $A^{\frac{1}{3}}$ variation of the meson production cross section, which extends even to light nuclei—a variation difficult to understand on the basis of the known mean free path for absorption of mesons.

Levinger's calculations could now be remade on the basis of the present model. The changes would be to replace his $\sin^2\theta$ angular distribution of the deuteron disintegration by an isotropic distribution and to change the absolute cross section and its variations with energy. All of these changes would be in the direction to bring his results in better conformity with experiment. The actual calculations should await accurate measurements of the deuteron disintegration, which should be forthcoming shortly. Occasionally three nucleons and a meson will be within the interaction volume. This will happen in nuclear matter about one-third of the time, but it too should be included in the calculation. The probability of re-emission of the meson from the two nucleon system increases roughly as the square of the energy, and hence, this process too becomes important at higher energies.

[1] C. Levinthal and A. Silverman, Phys. Rev. **82**, 822 (1951).
[2] J. Keck, Phys. Rev. **85**, 410 (1952).
[3] D. Walker, Phys. Rev. **81**, 634 (1951).
[4] R. Miller, Phys. Rev. **82**, 260 (1951).
[5] S. Kikuchi, Phys. Rev. **81**, 1060 (1950).
[6] J. Levinger, Phys. Rev. **84**, 43 (1951).
[7] L. Schiff, Phys. Rev. **78**, 733 (1950); L. Marshall and E. Guth, Phys. Rev. **78**, 738 (1950).
[8] E. Fermi, Prog. Theoret. Phys. **5**, 570 (1950).
[9] T. Benedict and W. Woodward, Bull. Am. Phys. Soc. **27**, No. 1, 54 (1952).
[10] S. Kikuchi, Bull. Am. Phys. Soc. **26**, No. 8, 5 (1951).
[11] W. Gilbert and J. Rose, Bull. Am. Phys. Soc. **26**, No. 8, 18 (1951).

The Condensation Phenomenon of an Ideal Einstein-Bose Gas

OTTO HALPERN
University of Southern California, Los Angeles, California
(Received February 18, 1952)

THE well-known statistical conclusions concerning the "condensation phenomenon" of an ideal Einstein-Bose gas are not only of independent theoretical interest, but have gained additional importance through attempts to base on them explanations for the superfluidity effects observed with He II.[1]

The ideal E.-B. gas below the "condensation temperature" is looked upon as being composed of essentially two phases, both of which fill the accessible volume uniformly; one phase is thought to consist essentially of gas particles of zero energy, while the other behaves similarly to an E.-B. gas above the condensation temperature. The equilibrium shifts very rapidly in favor of the first-mentioned condensed phase if below the condensation temperature, density is increased or temperature lowered. To distinguish from ordinary condensation one talks about condensation in the momentum space.

A renewed investigation of these statistical results leads to a revision of some accepted views. It can be shown that by proper introduction of the energy levels occurring in an ideal gas one arrives, on account of the zero point energy, at a distribution law over the various states of momentum which is not the same as that given in reference 1. This, by itself, constitutes only a quantitative change which otherwise does not affect the general conclusions.

One encounters, on the other hand, essential modifications in the study of an ideal E.-B. gas in the earth's gravitational field, hereby approaching real conditions more closely. Again, we find a separation into two phases as described before. But now the condensed phase no longer occupies the total accessible volume; it is essentially confined to a very thin layer at the bottom of the vessel. To fix ideas: 2×10^{22} atoms of He, looked upon for the moment as constituting an ideal gas at 2°K and contained in a cube of 1 cm³ volume, would form a film on the bottom about 10^{-3}-cm thick. Analytically, the ratio determining the "barometer formula" of the ideal condensed phase is no longer mgz/kT but mgz/ϵ_i, where ϵ_i denotes the energy of the quantum state under consideration; in the present case this will be essentially the zero point energy in the gravitational field.

The density of such an ideal "condensed" He gas reaches values of the order of 100 g/cm³. Experience shows that liquid He is formed by the interatomic forces at densities of the order of 10^{-1} g/cm³; the interatomic distance in the ideal "condensed" gas phase would be about as small as the Bohr radius of He. Obviously, such an ideal condensed gas could never be realized; long before the conditions for its existence are satisfied the interatomic forces will become predominant and make the gas strongly nonideal.

The ideal condensed gas is still described by eigenfunctions corresponding to the lowest momentum state in the plane perpendicular to the gravitational field. This condition obviously cannot be preserved in the presence of interatomic forces; how far it persists approximately can only be decided with the aid of a theory of the liquid state.

The difference in the behavior of He^3 and He^4 strongly suggests that E.-B. statistics play a fundamental roll as far as superfluidity is concerned. Still, care seems indicated in the use of analogies based on effects occurring in ideal E.-B. gases, since the interatomic forces apparently influence the phenomena qualitatively.

A more detailed paper will follow.

[1] F. London, Phys. Rev. **54**, 947 (1938). This paper contains a review of the historical development of the much discussed problem of "condensation" as well as inferences concerning the phenomena of superfluidity.

The Photodissociation of the Helium Nucleus by High Energy Gamma-Rays

SEISHI KIKUCHI*
Radiation Laboratory, Department of Physics, University of California, Berkeley, California
(Received February 18, 1952)

THE photodissociation of alpha-particles by high energy synchrotron gamma-rays of a maximum energy of 320 Mev was studied by the previously reported[1] method used in the study of the photodissociation of the deuteron. The analysis was made on the proton tracks found in photographic emulsion exposed to the secondary particles emitted from a gas target of helium. The exposure had been made originally by Jakobsen *et al.*,[2] to investigate the photomeson production in the helium nucleus. Because of the fairly large experimental error, the conclusions are not entirely free from ambiguities. It seems, however, difficult to get more accurate results before the intensity of the synchrotron beam

TABLE I. Energy spectra of the protons in the photodissociation of the deuteron and the α-particle, at emission angles of 45°, 90°, and 135°.

	Energy (Mev)	Deuteron	α-particle		Energy (Mev)	Deuteron	α-particle
45°	78		26.2±2.9	90°	68		11.7±1.7
	80	18.7±1.7			72	5.2±0.8	
	87	15.6±1.6			80	4.1±0.8	
	93	9.0±1.4	17.7±2.0		86	3.9±0.8	7.3±1.1
	99	12.3±2.5			93	4.8±1.0	
	103	8.6±1.5	17.4±2.1		99	6.3±1.3	9.0±1.6
	116	6.8±1.2			108	5.9±1.6	6.5±1.2
	126	7.3±1.3			117	5.7±1.7	6.0±1.3
	141	5.8±1.3			125	3.7±1.4	
	154		6.4±1.3		132	2.4±1.2	3.9±0.9
	165		5.5±1.4		143	2.1±0.7	
	177	6.7±1.6			161	0.67±0.47	
	189	8.5±1.6			172		1.3±0.4
	205	3.5±1.8	6.4±1.4		182	1.2±0.7	
	216	2.3±1.6	2.8±1.2				
	241		3.3±1.5	135°	84		4.5±0.9
	258		1.9±1.1		86	3.7±0.8	3.5±0.8
	320	2.6±1.1			92	3.4±0.8	3.5±0.8
					98	2.7±0.8	5.6±1.0
					103	2.8±0.9	3.6±1.2
					116	0.6±0.4	2.9±0.8
					122		2.2±0.7
					127		1.6±0.6
					134		1.3±0.6
					140	1.7±0.7	1.1±0.4

is improved considerably. Therefore, it was considered worthwhile to present the results in spite of their lack of completeness.

The energy spectra of the protons at the emission angles of 45°, 90°, and 135° are shown in Table I together with the previously reported[1] data for the deuteron. The values are corrected for the nuclear absorption of protons in the absorbing material. To make the numbers comparable in the deuteron and alpha-particle cases, they are normalized to the number of protons in the nucleus concerned. The data available in the helium case are less complete than those in the deuteron case.

In the 45° case, there seems to be a fairly well-defined cutoff at energy almost equal to the cutoff energy of the deuteron, which is approximately 200 Mev. The yield corresponding to a proton energy of about 160 Mev is nearly equal in both cases. In the case of helium, the yield of protons below 140 Mev increases more steeply with decreasing energy than in the case of the deuteron, indicating the existence of more low energy protons.

In the 90° case, the cutoff energy is again nearly the same in both cases. The energy distribution curve below the cutoff energy in the helium case shows a steady increase of the number of protons with decreasing energy, leaving no plateau below the cutoff, indicating again the larger number of protons below about 140 Mev.

In the 135° case, the energy spectrum extends up to about 130 Mev, which is higher than the cutoff energy of the deuteron case.

The conclusions one can draw from these data might be as follows. The fact that the cutoff energies of the spectra of protons at 45° and 90° are approximately the same as in the case of the deuteron, seems to indicate that the high energy protons, at least in the 45° case, are produced by the absorption of a photon in a two-nucleon system. The existence of protons of energy higher than the cutoff energy of the deuteron in the 135° case might be due to an absorption process in which the energy and momentum of a photon is taken up by three or four nucleons. The fact that there are more protons below, say, 140 Mev at the emission angles of 45° and 90° in the helium case than in the deuterium case, might also be explained by the three- or four-nucleon process mentioned above. The lack of protons above the cutoff energy for the two-nucleon process in the 45° and 90° cases and the lack of protons of energy above about 130 Mev in the 135° case, seem to indicate that the cross section for a process such as $He+\gamma\rightarrow T+p$ is small compared to the two-nucleon process. They also indicate the small probability for a process such as $He+\gamma\rightarrow 2p+2n$ or $He+\gamma\rightarrow D+p+n$, in which the proton gets more energy than allowed by the two-nucleon process.

The present results, together with the previous results on the deuteron, should help to provide a fundamental basis for interpreting the photodissociation of nuclei in general by high energy gamma-rays.

The author thanks Professors McMillan and Helmholz and members of the synchrotron group for helpful discussions as well as for their generosity in placing the plates at the author's disposal.

[1] S. Kikuchi, Bull. Am. Phys. Soc. **26**, No. 8, 5 (1951).
[2] M. J. Jakobsen *et al.*, Bull. Am. Phys. Soc. **26**, No. 8, 24 (1951).

V^0 Particles and Isotopic Spin*

D. C. Peaslee
Columbia University, New York, New York
(Received February 12, 1952)

RECENT experiments and interpretations on the scattering of mesons by protons[1,2] have suggested that the isotopic spin T is a good quantum number for meson-nucleon systems. It is therefore of interest to consider the implications of this quantum number for the unstable cosmic-ray particles. As an example the V^0 will be considered as a nucleon in an excited state, a generic term that includes any heavy fermion. Similar considerations are applicable to bosons without essential novelty.

The most remarkable feature of the V^0 particle is its stability against decay by π- and γ-emission. As a first approximation, we inquire under what conditions it could be absolutely stable. Let $\mathbf{t}$, $\boldsymbol{\tau}$, and $\mathbf{T}$ be the respective isotopic spin vectors of the nucleon, π-meson, and total system. The interaction energy is $H_0\sim(\mathbf{t}\cdot\boldsymbol{\tau})$, with corresponding selections rules for single meson emission

$$\Delta t,\ \Delta t_z=0,\pm 1, \tag{1a}$$
$$\Delta T,\ \Delta T_z=0. \tag{1b}$$

The emission of a real meson requires at least 140 Mev, so that by (1) an excited nucleon will be stable against π-decay to its ground state ($t=\frac{1}{2}$) if its excitation energy E and isotopic spin satisfy the relation

$$E<(t-\tfrac{1}{2})\ 140\ \text{Mev}. \tag{2}$$

Since the V^0 ultimately emits one π-meson, it must have $E>140$ Mev, which is charge forbidden only if $t>\frac{3}{2}$. The simplest choice is $t=5/2$, $140<E\lesssim 280$ Mev, with an eventual Q value for π-emission of $0<Q\lesssim 140$ Mev. There is of course no difficulty about the production of states with large t values in a high energy nuclear event where many particles are present in strong interaction.

This stability against π-emission is independent of the magnitude of H_0, which is not true of the stability against γ-emission. In the isotopic spin formalism the photon interaction term is of the form $H\sim a+bt'$, where t' is the isotopic spin of whatever particle is involved. The selection rule accordingly depends on whether the V^0 is in a single-nucleon state or a virtual state of nucleon plus meson,

$$\text{single-nucleon}\quad H_\gamma\sim A+BT_z,\quad \Delta T=\Delta T_z=0 \tag{3a}$$
$$\text{nucleon+meson}\quad H_\gamma\sim a+\alpha+bt_z+\beta\tau_z,\ \Delta T_z=0,\ \Delta T=0,\pm 1. \tag{3b}$$

The rule (3b) requires $b\neq\beta$, which is generally true; it is this type of process that occurs in the decay of a π^0 meson ($T=1$) into two photons, each of isotopic spin $T=0$.

If isotopic spin is to be made the basis of γ-stability, (3a) indicates that the V^0 must have $t>\frac{1}{2}$. On the other hand, (3b) shows that the V^0 must also be stable against virtual π-meson emission, for otherwise it could decay rapidly by emitting $(t-\frac{1}{2})$ photons and one π. Thus isotopic spin considerations alone cannot account for both π- and γ-stability but only for one of the two: If γ-emission can be "turned off," π-stability can be achieved, or if some external postulate ($e^2/\hbar c\sim 10^{-15}$) is introduced to give π-stability, isotopic spin restrictions can provide equally good γ-stability without additional assumptions.

Therefore, if isotopic spin is to help account for V^0 stability, a model must be chosen in which $t\geq\frac{3}{2}$ for the V^0. This would imply the existence of a number of companion particles, including at least V^- and V^{++}, which decay in a similar fashion to $n+\pi^-$ and $p+\pi^+$. The V^+ particles would exist for any value of t, and their modes of decay should provide some information on t of the initial state. For $\pi-V$ coupling of the type H_0 the relative frequencies of decay $(V^+\rightarrow n+\pi^+):(V^+\rightarrow p+\pi^0)=2:1$ or $1:2$ according as $t=\frac{1}{2}$ or $\frac{3}{2}$. For higher values of t, $(t-\frac{1}{2})$ quanta must accompany the π-decay if the $\pi-V$ coupling is of type H_0; if it is of type H_γ, the decay will divide in comparable proportion among processes accompanied by $(t-\frac{1}{2})$, $(t-\frac{3}{2})$, $(t-5/2)$ quanta. The decay lifetime increases by order $1/\alpha\sim 10^2$ per quantum.

Thus the following conclusions are reached: The apparent failure to observe V^{++} and other companion particles with frequencies comparable to V^0 suggests that the V-particle wave functions have some (or all, if T is a good quantum number) components with $t<\frac{3}{2}$. This would mean that independent principles must be found to explain both the π- and γ-stability of these particles without help from isotopic spin considerations, which could have eliminated one type of instability. A direct check of t for the V^+ particles is in principle possible from a determination of the $(n+\pi^+):(p+\pi^0)$ ratio. The presence of V^- particles in the face

* Now at Osaka University, Osaka, Japan.

of an established absence of corresponding V^{++} would suggest failure of T as a good quantum number.

The stimulating discussions of Professors R. Serber and H. Yukawa are acknowledged with pleasure.

* This research was supported by the research program of the AEC.

[1] Lundby, Fermi, Anderson, Nagle, and Yodh, Bull. Am. Phys. Soc. **27**, No. 1, 28 (1952). Nagle, Anderson, Fermi, Long, and Martin, Bull. Am. Phys. Soc. **27**, No. 1, 28 (1952).

[2] K. A. Brueckner, Bull. Am. Phys. Soc. **27**, No. 1, 51 (1952).

The Absorption Rate of Cosmic-Ray Neutrons Producing C^{14} in the Atmosphere

RUDOLF LADENBURG
Palmer Physical Laboratory, Princeton University, Princeton, New Jersey

(Received February 8, 1952)

ANDERSON and Libby,[1] who determined the average number of disintegrating C^{14} atoms per cm³ of the earth surface, found an approximate agreement of this number with the average integrated absorption rate of atmospheric neutrons computed from Yuan's measurements.[2] Since Yuan's more recently published value of this absorption rate[3] is nearly twice as large and since improved neutron cross sections have been published in the meantime,[4] a recalculation seems necessary.

The measurements of Yuan on January 8, 1949, integrated over the atmosphere up to 102,000 feet at Princeton's geomagnetic latitude (51° 46′ N), give for the tin-shielded boron counter $I_t = \int n_t d\rho = 834$ counts-g/cm³-sec and for the cadmium-shielded boron counter $I_{cd} = \int n_{cd} d\rho = 394$ counts-g/cm³-sec. By taking the difference of these values one can eliminate the background of "secondary" counts b due to stars produced in the shields or to recoils etc.; and by multiplying this difference by the ratio A/Σ_c, where $A = 0.0545$ cm²/g is the absorption of one gram of air and $\Sigma_c = 12.5$ cm² is the effective absorption cross section of the counter,[5] both for thermal neutrons, one obtains as the total number of absorbed neutrons up to 0.4 ev (the cut-off energy of the cadmium-shield) $(I_t - I_{cd})A/\Sigma_c = 1.92$/cm²-sec. An upper limit for the absorption rate up to 0.4 Mev is $I_t A/\Sigma_c = 3.64$/cm²-sec, since I_t is uncorrected for the unknown background effect $I_b = \int b d\rho$ and since the cross sections for nitrogen and for boron follow the $1/v$ law; but above 0.4 Mev nitrogen has some resonance absorptions for the (n, p) as well as for the (n, α) reaction. On the other hand, the corrected neutron absorption rate can be obtained approximately from the cadmium-difference counts by using the "slowing-down theory" of neutrons.[6] If $q(E)$ is the "slowing down density past the energy E," then

$$q(E_2)/q(E_1) = \exp\left[-\frac{1}{\xi}\int_{E_2}^{E_1}\frac{\sigma_a}{\sigma_0+\sigma_s}\frac{dE}{E}\right] = S(E_2, E_1).$$

With $E_1 = 0.4$ Mev and $E_2 = 0.4$ ev, $\xi = 6/(3A+2) = 0.132$ one obtains by numerical integration

$$q(0.4\text{ ev})/q(0.4\text{ Mev}) = (I_t - I_{cd})/(I_t - I_b) = 1/1.77;$$

therefore,

$$(I_t - I_b)A/\Sigma_c = (I_t - I_{cd})A/\Sigma_c \times S(E_1, E_2) = 3.4/\text{cm}^2\text{-sec}$$

is the absorption rate up to 0.4 Mev neutrons.[7] To compute the absorption rate of neutrons of higher energy, the energy distribution $f(E_p)$ of the neutrons as they are "evaporated" from cosmic-ray stars has to be taken into account. The integrated number of all neutrons absorbed by the $N(n, p)C$ reaction in the atmosphere at 52°N will then be

$$Q = q(E_1)\int_0^\infty f(E_p)dE_p \Big/ \int_{E_1}^\infty f(E_p)\times S(E_1, E_p)dE_p,$$

with $E_1 = 0.4$ Mev and $E_p > E_1$. The cross section $\sigma_a(n, p)$ is measured up to 3.6 Mev where it is only 1/100 barn, and is approximately known[8] at 14 Mev. Using the function[9] $f(E_p) = E_p \times \exp(-E_p/3)$ one obtains Q (up to 14 Mev) $= 3.4 \times 1.2 = 4.2$/cm²-sec. But this result should be taken as tentative, inasmuch as the function $f(E_p)$ and some of the cross sections (including that of the counter) are somewhat uncertain and as the neutron flux at high latitudes fluctuates due to changes of the activity of the sun.[10] On account of the strong latitude dependence of atmospheric neutrons[11] one obtains finally for the averaged value over the earth's surface[12] (including neutron energies up to 14 Mev) $\bar{Q} = 0.58 \times 4.2 = 2.4$/cm²-sec. Anderson and Libby's value for the average number of disintegrating carbon atoms is 2.23/cm²-sec. Their conclusion, that apparently no considerable change in the cosmic-ray intensity has occurred over the past several thousand years is, therefore, corroborated so far by the present recalculations.

I am very grateful to my colleagues of the cosmic-ray group, especially to Dr. Kouts and Dr. Yuan, now at Brookhaven, and ot Dr. M. C. Edlund for many helpful discussions.

[1] E. C. Anderson and W. F. Libby, Phys. Rev. **81**, 64 (1951).

[2] L. C. L. Yuan, Phys. Rev. **76**, 1267, 1268 (1949); **77**, 728 (1950); R. Ladenburg and L. C. L. Yuan, *Cosmic Radiation*, The Colston Papers, Buttersworth Scientific Publications, London, England (1949), p. 35.

[3] L. C. L. Yuan, Phys. Rev. **81**, 175 (1951). The reason for the discrepancy is discussed by H. J. Kouts and L. C. L. Yuan, following letter, Phys. Rev. **86**, 128 (1952).

[4] Brockelmann, Miller, Adair, and Barschall, Phys. Rev. **84**, 70 (1951); Johnson, Petree, and Adair, Phys. Rev. **84**, 775 (1951); W. Bollmann and W. Zuenti, Helv. Phys. Acta **24**, 517 (1951).

[5] Obtained by calibration of the counter with neutrons from the Argonne pile and with a standardized neutron source. For the thermal cross section of the $N^{14}(n, p)C^{14}$ reaction the value 1.68 barns was used in the present calculations (August 1951 edition of the AEC Cross-Section Committee Report).

[6] See, e.g., H. Soodak and E. C. Campbell, *Elementary Pile Theory* (John Wiley and Sons, Inc., New York, 1950); also see reference 1 and the references given there.

[7] The "true cadmium ratio" $(I_t - I_b)/(I_{cd} - I_b) = R_0 = 1/[1 - S(E_2, E_1)] = 2.3$, so that with $R = I_t/I_{cd} = 2.12$ the relative background $I_b/I_t = [(R_0/R) - 1]/(R_0 - 1)$ was only 7 percent in the present case.

[8] According to private information from T. W. Bonner, Dr. A. Lillie found, at 14 Mev, $\sigma_H = 0.040$b (disintegration of N into H^1, H^2, and H^3); and according to information from E. O. Salant σ_{total} at 14 Mev is (1.7±0.1)b for N and (1.64±0.04) for O.

[9] See S. Fluegge, *Cosmic Radiation* (John Wiley and Sons, Inc., New York, 1946), p. 154. The rather different energy distribution of neutrons found by D. M. Skyrme and W. S. C. Williams [Phil. Mag. **42**, 1187 (1951)] when bombarding carbon with 171-Mev protons gives essentially the same result.

[10] Simpson, Fonger, and Wilcox, Phys. Rev. **85**, 366 (1952), but no special solar activity has been recorded on the day of Yuan's measurements (January 8, 1949).

[11] J. A. Simpson, Phys. Rev. **83**, 1175 (1951).

[12] Anderson and Libby (see reference 1) obtained $S(E_2, E_1) = 1/2.20$ (using $\xi = 0.124$ and Melkonian's nitrogen cross sections) and $\bar{Q} = 2.6$/cm²-sec without including neutron absorption above 2 Mev.

The Production Rate of Cosmic-Ray Neutrons and C^{14}†

HERBERT J. KOUTS AND LUKE C. L. YUAN, *Brookhaven National Laboratory, Upton, New York*

(Received February 21, 1952)

A REPORT of measurements made by one of us,[1] and containing references to calculations made by the other, deduced the low energy capture rate of cosmic-ray neutrons to be 7.1 per second per square centimeter of the earth's surface at Princeton. These results were based on the assumption of what seemed at the time to be the best values of the scattering and absorption cross sections of nitrogen and oxygen. Now, the predicted experimental cadmium ratio of the $1/v$ detectors used depends strongly upon the values of the cross sections assumed (actually, upon the average value of their ratio in the energy region where most of the capture occurs). This can be seen from the approximate theoretical expression for this ratio:

$$R = 1 - \exp[-2B/(\sigma_s \xi \sqrt{E_0})], \quad (1)$$

where ξ is the logarithmic decrement of the energy for neutrons in air, σ_s is the mean scattering cross section of air, the capture cross section of an air atom is $B/(E)^{\frac{1}{2}}$, and E_0 is the cadmium cutoff of the counters used.

We have decided that, because the cross sections used were not correct, it would be wise to review the conclusions of (1), so that a

better determination of the absolute production rate may be deduced. The way we shall proceed is to choose a value of $2B/\xi\sigma_a$ which fits the observed cadmium ratio, and to determine the capture rate from this choice. A further problem is the theoretical derivation of this quantity, which depends upon low-energy molecular effects on scattering, and the fact that the air has a finite (non zero) temperature. This theoretical treatment is being carried out by one of us.

The weighted average of the observed cadmium ratios reported in (1) is 2.13. One can match this observed cadmium ratio theoretically by assuming $2B/\xi\sigma_a=0.425$. In this event, the computed low energy (n, p) capture rate by nitrogen of cosmic ray neutrons is 3.50 per cm² sec at Princeton. This is, therefore, the production rate of C^{14} by capture of these neutrons. There is also capture leading to C^{14} production in the resonance region of nitrogen; use of the data of Johnson and Barschall[2] leads to the conclusion that the total production rate of C^{14} is 4.13 per cm² sec at Princeton.

Correcting the calculations made by Anderson and Libby[3] by this factor, we find the predicted disintegration rate of carbon due to C^{14} to be 17.6 disintegrations per minute per gram. This moderate agreement with the observed value[3] is certainly reasonable, because the counters used in the slow neutron measurements (1) were probably calibrated to no greater accuracy than about twenty percent.[4] This inaccuracy, higher than that mentioned in reference (1), is caused by uncertainty in flux values in the Argonne standard pile, used to calibrate the foils which were used in turn to calibrate the counters. Thus, the uncertainty is carried over to the counter calibration.

Moreover, the cadmium ratio given above is probably not correct because, as stated in reference (1), the counters used may have registered production of stars and showers.

Ladenburg[5] has considered the experimental data bearing on the true cadmium ratio (that obtained without stars, etc.), and has determined the best values between which the C^{14} production rate may be expected to lie. His results are in substantial agreement with ours. Similar considerations based on the true cadmium ratio were also made by Anderson.[6]

Pfotzer[7] also analyzed and compared various results on the neutron production rate derived by different authors and obtained a conclusion which agrees well with our present values.

† Work supported in part by the AEC.
[1] Luke C. L. Yuan, Phys. Rev. **81**, 175 (1951).
[2] See R. K. Adair, Revs. Modern Phys. **22**, 249 (1950).
[3] E. C. Anderson and W. F. Libby, Phys. Rev. **81**, 64 (1951).
[4] D. J. Hughes, private communication.
[5] R. Ladenburg, preceding Letter [Phys. Rev. **86**, 128 (1952)]. We are indebted to Dr. Ladenburg for discussions and for allowing us to see his manuscript before publication.
[6] E. C. Anderson, private communication.
[7] G. Pfotzer (to be published). We are deeply grateful to Dr. Pfotzer for sending us his manuscript entitled "Über den Absolutwert der Ergeugung β-aktiven Kohlenstoffes in der Atmosphare durch die Neutronen der Ultrastrahlung" prior to publication.

A Search for New Mesons by Means of a Cloud Chamber

M. Inoki, T. Yasaki, and Y. Matsukawa
Physics Institute, Yamanashi University, Kofu, Japan
(Received December 10, 1951)

FOR the purpose of studying whether new mesons stable against β-decay exist or not, we have measured the β-decay probability of slow mesons in the soft component of the cosmic rays at 300 meters altitude, using a cloud chamber containing a thin carbon plate as stopping material. The cloud chamber is controlled by two proportional counters which are set inside and over the chamber, respectively, as shown in Fig. 1. The use of proportional counters has the advantage of giving selective expansions of the cloud chamber for the slow particles among the cosmic rays. The pulse sizes are recorded on photographic films, using a cathode ray tube. Stereoscopic cloud chamber photographs are taken with two cameras.

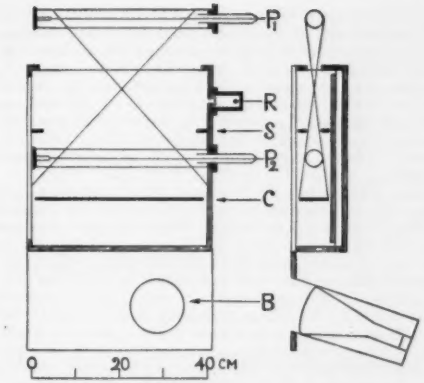

FIG. 1. A schematic diagram of the apparatus showing the cloud chamber, the two proportional counters (P_1, P_2), the slit (S), the carbon plate (C), the RaE (R), and the cathode ray tube (B).

We have obtained 27 particles stopped in the 2-mm carbon plate during an effective working period of 261 hours. We have examined their rates of ionization by means of the recorded pulse sizes and by comparison of their photographic track densities with the track density of slow β-rays from RaE, injected into the chamber at the time of coincidence of the proportional counters. Among these particles there are 16 having rates of ionization between 3 and 6 times the minimum rate as measured with pulse sizes, and also having track densities comparable to that of slow

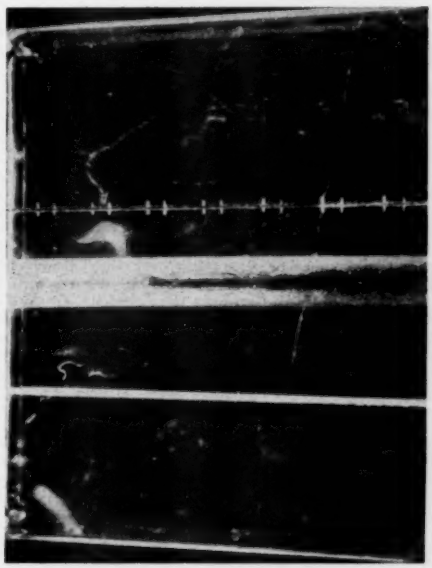

FIG. 2. A typical cloud chamber photograph taken with the side camera, showing a slow meson stopped in a 2-mm carbon plate without emitting a decay electron, and β-rays including one stopped in the gas.

β-rays with ranges of 1 to 5 cm. One of them is shown in Fig. 2. Their masses should be between those of an electron and a proton, because protons stopped in a 2-mm carbon plate, corresponding to a 1.2-mm aluminum plate, ionize at more than 12 times the minimum rate, and electrons which can penetrate the counter tube, whose wall is made of 0.3-mm aluminum foil, ionize at the minimum rate inside the counter tube. Therefore they should be mesons. It is uncertain whether the remaining 11 particles are mesons or protons, within the accuracy of our ionization measurements.

Decay electrons from the 16 mesons and 11 unidentified particles were not observed, except for two obscure thin tracks emerging from each of two mesons. If we count them as decay electrons, the β-decay probability of these mesons is 0.16, taking the mean detection efficiency for fast electrons emerging isotropically from any point in the carbon plate to be 0.79. We have calculated the statistical probability of occurrence of a measured value of 0.16 for the β-decay probability assuming that all the particles are negative μ-mesons whose β-decay probability is 0.89 in carbon,[1] and have obtained a value of 0.00001. We surmise, therefore, that they are new mesons stable against β-decay assuming that μ-mesons have no mode of decay unknown hitherto. An apparatus designed for determination of their masses is under construction, but if we estimate their masses from the data outlined above, they should be lighter than μ-mesons.[2] The range of μ-mesons ionizing at 3 times the minimum rate is 7 mm in carbon. The probability for the emergence of decay electrons from a 7-mm carbon plate, therefore, is about 3.5 times that from a 2-mm plate. We have tested this and obtained 4-decay electrons which are observed clearly during an effective working period of 90 hours.

In addition to the above results, we have obtained 9 particles stopped by the wall of the proportional counter facing the carbon plate, during an effective working period of 351 hours. They are again distinguished from protons and electrons by the method discussed above. If they were μ-mesons, we should observe many more μ-mesons stopped in the carbon plate and their decay electrons. We surmise, therefore, that they also are mesons of the kind mentioned above.

[1] John A. Wheeler, Revs. Modern Phys. **21**, 133 (1949).
[2] M. Inoki, J. Phys. Soc. (Japan) **6**, 398 (1951).

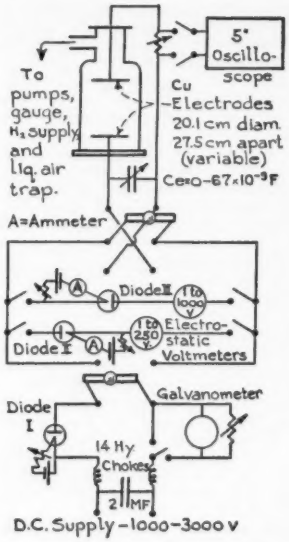

FIG. 1. Experimental arrangement.

The Dark Current in the Intermittent Glow Discharge in Hydrogen

HERMAN RITOW
Highland Park, Illinois
(Received September 24, 1951)

MEASUREMENTS of the intermittent glow discharge were made by a number of investigators.[1-3] In the writer's experiments the striking and extinction potentials, V_s and V_0, the flash frequency f, the external capacity C_e and the supply current I_s were recorded. The circuit used is shown in Fig. 1. The current supplied by the generator is limited to the desired constant value by a diode. The flash current or its rate of change can be observed on the oscilloscope and the period, $T=1/f$, can be measured.

For each period the charge supplied is I_sT. The amount of charge leaving the condenser during a flash is $C_e(V_s-V_0)=C_e\Delta V$. The difference between the supply charge I_sT and the condenser loss $C_e\Delta V$ was found to be a linear function of the period T when the current I_s is kept constant and the external capacity, C_e, is varied. Thus,

$$I_sT-C_e\Delta V=Q_0+I_dT. \quad (1)$$

This equation describes the graph shown in Fig. 2.

The intermittent glow consists of a series of flashes with dark intervals between them. The dark current, I_d, occurs during the intervals. The straight line drawn closest to the plotted points crosses the charge axis at Q_0, which is interpreted to be the net charge leaving the electrodes with each flash. The slope of the line, $\Delta Q/\Delta T=I_d$, is taken to be the measure of the average current passing between the electrodes during the period, T.

Often at low pressures the charge I_sT, supplied by the current I_s during the period T, is less than the condenser loss $C_e\Delta V$. Thus, in Fig. 3, the points plotted are for an experimental series in which $I_sT-C_e\Delta V$ is negative for all but one point. The pressure was 0.16 mm Hg and the current was kept constant at 29.1×10^{-6} amp. The slope of the line I_d is -16.6×10^{-6} amp or -54 percent of I_s. In this case, then, the dark current is reversed in direction

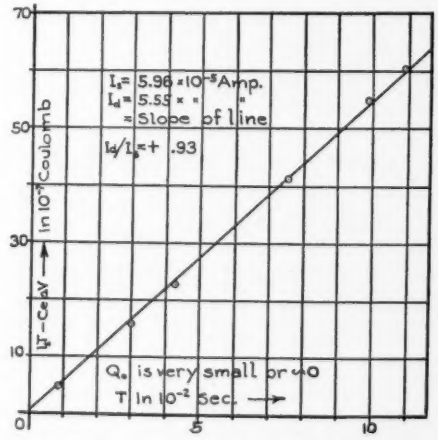

FIG. 2. $(I_sT-C_e\Delta V)$ *vs* T. Pressure = 1.38 mm Hg; D = 275 mm; gas H_2; electrodes: Cu disks 20.1 cm in diameter.

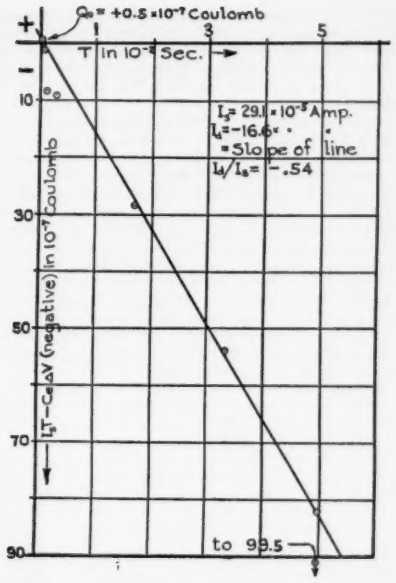

FIG. 3. $(I_3T - C_3\Delta V)$ *vs* T. Pressure = 0.16 mm Hg; D = 275 mm; gas H_2; electrodes: Cu disks 20.1 cm in diameter.

relative to the supply current and aids in the recharging of the condensers.

For still lower pressures, I_4 was many times $-I_3$. A large number of experiments were made at various pressures, and the ratios I_4/I_3 were plotted against $\log P$. Figure 4 shows the results. Thus, at higher pressures I_4/I_3 approaches unity. At lower pressures I_4/I_3 may be -5, -20, or even more negative.

From the fact that the dark current is reversed at low pressures and the further fact that just before a flash the potential difference must be in the normal direction, it is believed that the dark current at low pressure undergoes one back and forth relaxation oscillation each period. On that assumption the intermittent glow discharge at low pressures may be interpreted as consisting of a series of current pulses of rapidly oscillating electrons separated by intervals during which the current through the gas probably oscillates once.

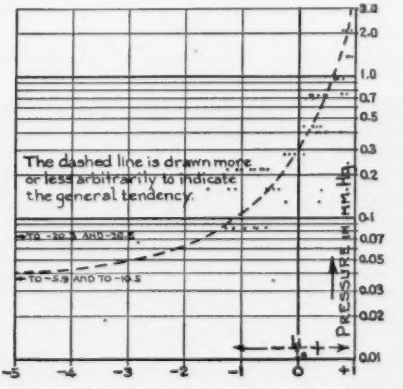

FIG. 4. Dark to charging current ratio *vs* gas pressure. Gas H_2; D = 275 mm; electrodes: Cu disks 20.1 cm in diameter.

So far as the writer knows, there is no mention in the literature of the relatively high magnitude of the dark current nor of its reversal of direction.

The writer wishes to acknowledge his indebtedness to the Department of Physics, Northwestern University, for making available to him the experimental facilities used for these measurements.

[1] E. W. B. Gill, Phil. Mag. **8**, 955 (1929).
[2] S. K. Mitra, Phil. Mag. **14**, 616 (1932).
[3] D. E. Clark, unpublished studies at Northwestern University (1935).

The Dispersion of Permittivity and Conductivity of Semiconductors

R. E. BURGESS
Radio Research Station, Slough, Bucks, England
(Received February 7, 1952)

IN the recent paper by the late C. G. Koops[1] on the dispersion of permittivity and resistivity of nickel-zinc ferrites, use is made of the two-layer model of the dielectric medium in which one layer represents the grains of the ferrite and the other the insulating intergranular material which may owe its low conductivity to a physical barrier layer or to chemical differences from the grain material.

In the paper the validity of this model was tested by attempting to find the best fit to the curves of resistivity, permittivity, and loss tangent (as functions of frequency) using the theoretical dependence of these quantities on frequency. The goodness of the fit so obtained is not very satisfactory, as may be seen from the tanδ curves in which the calculated values reach a maximum considerably higher than the experimental observations. It is, therefore, relevant to examine the applicability of the two-layer model to these observations, and to determine in some unequivocal manner the parameters defining the model which best fit the data.

A simple general method for such an analysis of dispersion in semiconductors is as follows: The permittivity ϵ and conductivity σ of a dielectric conforming to the two-layer model are given by equations of the Debye type:

$$\epsilon = \epsilon_\infty + \frac{\epsilon_0 - \epsilon_\infty}{1+\omega^2\tau^2} \quad \text{and} \quad \sigma = \sigma_\infty - \frac{\sigma_\infty - \sigma_0}{1+\omega^2\tau^2} \tag{1}$$

where $\omega = 2\pi \times$ frequency, τ = relaxation time, and the suffixes denote the values at zero and infinite frequency. Furthermore

$$\tau = \frac{1}{4\pi}\frac{\epsilon_0 - \epsilon_\infty}{\sigma_\infty - \sigma_0}. \tag{2}$$

Thus, if ϵ is plotted against σ (with frequency as parameter) a straight line of slope $-(\epsilon_0-\epsilon_\infty)/(\sigma_\infty-\sigma_0) = -4\pi\tau$ should be obtained. Hence the degree of linearity of the ϵ, σ plot is a measure of the closeness with which the two-layer model in fact accounts for the observed data, and the best straight line which can be drawn through the experimental points enables the relaxation time τ to be determined directly.

This method is illustrated by Fig. 1, in which the data from Table I of Koops's paper have been replotted on an ϵ, σ basis. The plot is quite curved, thus showing that the simple model is not very closely obeyed, especially at the higher frequencies.

From Eq. (2) the value of τ fitting the over-all range of permittivity and conductivity values is 1.1×10^{-4} sec. However, for the lower frequencies a higher value is clearly appropriate in view of the slope of the ϵ, σ curve, while at the higher frequencies a lower value of τ is inferred.

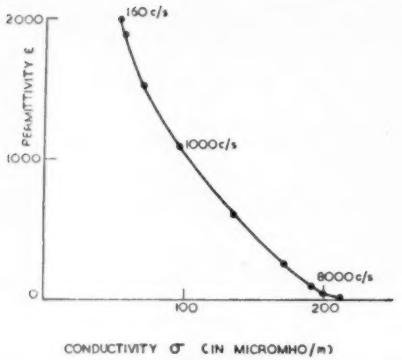

FIG. 1. Replot of Koops' data from Table I.

The loss tangent for the model is given by

$$\tan\delta \equiv \frac{4\pi\sigma}{\omega\epsilon} = \frac{4\pi}{\omega}\,\frac{\sigma_0+\omega^2\tau^2\sigma_\infty}{\epsilon_0+\omega^2\tau^2\epsilon_\infty}.$$

For the materials under discussion, $\epsilon_0/\epsilon_\infty \gg \sigma_0/\sigma_\infty$, and $\tan\delta$ then has minimum and maximum values of

$$\tan\delta_{\min} = 2(\sigma_0\sigma_\infty)^{\frac{1}{2}}/(\sigma_\infty-\sigma_0) \quad \text{at} \quad \omega\tau = (\sigma_0/\sigma_\infty)^{\frac{1}{2}},$$
$$\tan\delta_{\max} = (\epsilon_0-\epsilon_\infty)/[2(\epsilon_0\epsilon_\infty)^{\frac{1}{2}}] \quad \text{at} \quad \omega\tau = (\epsilon_0/\epsilon_\infty)^{\frac{1}{2}}.$$

From Koops' data $\sigma_\infty/\sigma_0 \approx 4$, whence $\tan\delta_{\min} = 1.3$ and $\epsilon_0/\epsilon_\infty \approx 130$ giving $\tan\delta_{\max} = 5.7$; these values lie close to the experimental ones of 1.4 and 6.7.

[1] C. G. Koops, Phys. Rev. **83**, 121 (1951).

The Inelastic Scattering of Fast Neutrons from Iron*

P. H. STELSON AND W. M. PRESTON
Laboratory for Nuclear Science and Engineering, Massachusetts Institute of Technology, Cambridge, Massachusetts
(Received February 13, 1952)

WITH adequate resolution and at moderate energies, the energy distribution of inelastically scattered neutrons should exhibit a "line spectrum." The theory has been given by Feld and others.[1] Experimental difficulties, particularly the low efficiency of high-resolution fast-neutron spectrometers, have thus far prevented the direct detection of separated neutron groups. Their existence has been inferred by Feld[1] from the poor-geometry experiments of Barschall *et al.*,[2] in the case of 2–3 Mev neutrons scattered from iron, and for a number of elements by Grace *et al.*[3] by the detection of the γ-rays emitted from the low excited states in which the target nucleus is left, following inelastic scattering.

We have carried out a straightforward experiment as illustrated in Fig. 1. The neutron source, at T, was an evaporated layer of lithium having roughly 100-kev stopping power for protons at the bombarding energy of 3.61 Mev. The neutron energy distribution was, therefore, fairly uniform, from 1.82 to 1.92 Mev. The neutron beam passed through a tapered hole in the paraffin shield to the scatterer S, a cylinder of iron 2 cm in diameter and 2 cm long. Scattered neutrons were detected by the tracks of recoil protons in Eastman NTB emulsions of 200 micron thickness. The plates were placed at P, at right angles to the beam. The acceptance angle for tracks was ± 12 degrees. Exposures were for about 40 μa-hours, at an average proton current of 5 μa, but the actual monitoring was done with a BF_3 "long counter." Additional shields around the target and the plates served to reduce background from the walls of the room.

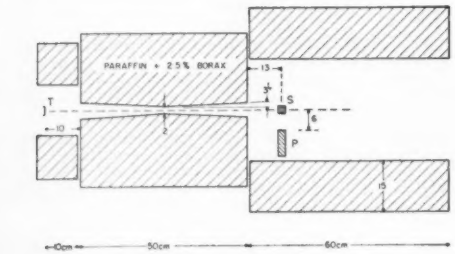

FIG. 1. Experiment arrangement for inelastic scattering of fast neutrons.

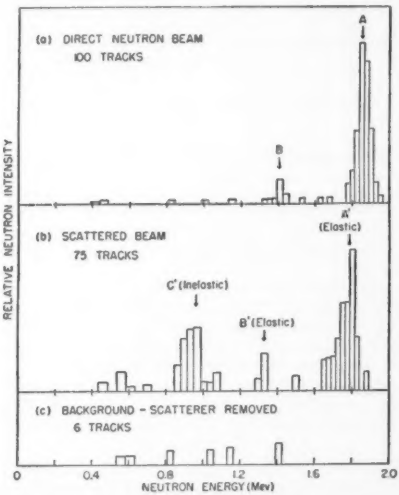

FIG. 2. Histograms of relative neutron intensity *vs* neutron energy derived from recoil proton track length distributions in nuclear track plates.

The results are shown in Fig. 2. Histogram (a) is the energy spectrum of the incident neutron beam determined by exposing plates at the position of the scatterer, S. Peaks A and B are the familiar primary and secondary neutron groups from the Li(p, n) reaction. The intensity of neutrons other than those in peaks A and B is low, showing that the arrangement produces a reasonably monoenergetic neutron beam at the position of the scatterer.

Histogram (b) is the neutron energy spectrum obtained by exposing plates at position P with the scatterer in place. Histogram (c) is the result of a similar exposure but with the scatterer removed to obtain a background measurement. The two histograms are normalized with respect to exposure time and area of emulsion measured. Corrections were applied to convert the track length distributions to relative neutron intensities.[4]

A new group of neutrons, C', is observed in the scattered neutrons shown in (b). Therefore, in addition to the elastic scattering shown by peaks A' and B', there is considerable inelastic scattering

of the primary group A to the lower energy of group C'. Neutrons of 1.87 Mev elastically scattered through 90° by iron nuclei lose 65 kev. Peak A' is ~90 kev below peak A. The somewhat larger shift is probably the result of the finite angle subtended by the scatterer at the position of the plates.

The energy of group C' indicates that a level at 850±50 kev is being excited by inelastic neutron scattering. This agrees with the result of Grace *et al.*[3] on the gamma-ray measurements. The decay schemes of Mn^{55} and Co^{55} both indicate a level at 845 kev in Fe^{55},[4] the principal iron isotope (91.5 percent). The ratio of the differential cross section for inelastic scattering to the 850-kev level, $d\sigma_{in}/d\Omega$, to the elastic scattering, $d\sigma_s/d\Omega$, at 90° for neutrons of energy 1.82 to 1.92 Mev is 0.55±0.15, as determined from the ratio of the intensity of the peak C' to A'. The consideration of track densities and exposure times for the histograms (a) and (b) gives the values $d\sigma_s/d\Omega=0.112\pm0.023$ and $d\sigma_{in}/d\Omega=0.062\pm0.015$ barn/steradian at 90° in the laboratory system. The errors indicated are the statistical errors only. The assumption of isotropic scattering gives 1.40 and 0.82 barns for σ_s and σ_{in}.

The measured total cross section of iron is about 2.8 barns at this energy, of which a large fraction should be "potential scattering" concentrated largely in the forward direction. In consequence, our rather rough determinations of absolute differential cross sections seem high. This could be the result of systematic errors.

It appears that by this method it is practical to measure elastic and inelastic differential scattering cross sections as a function of angle and incident neutron energy, with fair accuracy and resolution adequate to separate many low-lying levels in intermediate weight nuclei. It is a tedious method because of the low track densities involved, although the neutron exposure can be increased readily by a factor of ten over that used in this experiment.

We would like to thank Mrs. Gertrude Lurie for her assistance.

* This work was jointly supported by the Bureau of Ships and the ONR.
[1] B. T. Feld, Phys. Rev. **72**, 881 (1947); also AEC Technical Report NYO-636, Jan. 31, 1951.
[2] Barschall, Battat, Bright, Graves, Jorgensen, and Manley, Phys. Rev. **72**, 881 (1947).
[3] Grace, Beghian, Preston, and Halban, Phys. Rev. **82**, 969 (1951).
[4] P. H. Stelson and W. M. Preston, Phys. Rev. **82**, 655 (1951).
[5] L. G. Elliott and M. Deutsch, Phys. Rev. **63**, 321 (1943).

Domain Patterns on FeSi Crystals*

C. F. Ying, S. Levy, and R. Truell
Metals Research Laboratory, Brown University, Providence, Rhode Island
(Received January 23, 1952)

IN the course of our present investigation of the effect of magnetic history on the domain patterns of 3.8 percent Si Fe-Si crystals, several interesting patterns have been observed. The sample, approximately 2.0 cm×1.5 cm×0.5 cm was grown from the melt and oriented so that its surfaces are parallel to the crystallographic planes. The domain patterns were observed by the concentrated colloid technique[1] which forms striations normal to the flux direction. These patterns reveal relatively large domains some of which have a structure. The "subdomains," whose basic pattern is of the same type as that of the main domains, can be thought of as lying within a large domain and oriented normal to it, giving rise to two types of patterns. The first pattern occurs when the fluxes in the larger domains adjacent to the substructure are parallel, Fig. 1, and the second when the fluxes in these regions are antiparallel, Fig. 2. These are easily distinguished by their respective alternating or opposing domains of closure. An explanation of Fig. 1 is given in Fig. 3 where the flux is indicated by the arrows. A similar explanation applies to Fig. 2. Long irregular chains of much smaller domains of the types shown in Figs. 1 and 2 have also been recorded. These chains were previously observed

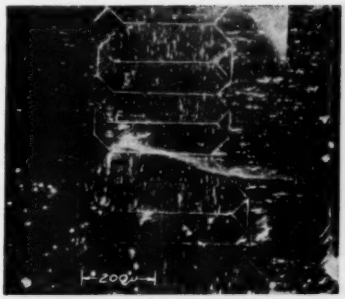

FIG. 2. Subdomain structure, type II.

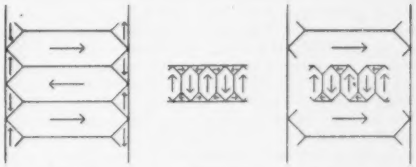

FIG. 3. Explanation of the structure of Fig. 1.

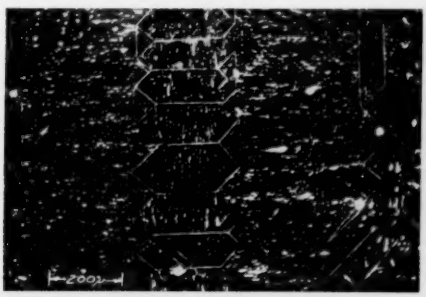

FIG. 1. Subdomain structure, type I.

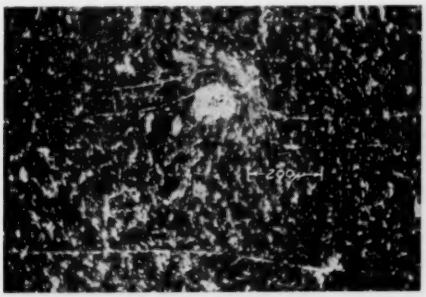

FIG. 4. Bending of a domain about an inclusion.

by Williams.[2] Whether this domain behavior is due to stress-free distortion or stress concentrations has not been determined.

Another pattern showing the bending of a thin domain around an inclusion is given in Fig. 4.

* The work described here was supported by the Research Corporation of New York and by the Office of Air Research.
[1] Williams, Bozorth, and Shockley, Phys. Rev. **75**, 155 (1949).
[2] Private communication from H. J. Williams.

Formative Time Lags of Positive Point Corona in Air*

M. Menes and L. H. Fisher
College of Engineering, New York University, University Heights 53, New York
(Received February 15, 1952)

AMONG the motivating facts leading to the streamer theory of spark breakdown in air were the extremely short breakdown times in uniform fields (at high overvoltages), and the filamentary streamers observed in the positive point corona.[1] However, recent experiments with uniform fields in air close to threshold have revealed formative lags too long ($\sim 10^{-4}$ sec) to be in accord with the streamer theory.[2] An investigation of the formative lags of the positive point to plane corona in air near threshold was undertaken to determine whether this corona has a slow build-up process near threshold similar to the uniform field breakdown.

Studies were made in dry air at pressures ranging from atmospheric to a few centimeters of mercury; tungsten points with radii of curvature of 0.007, 0.02, and 0.03 cm were used with electrode separations of 0.5, 1.0, and 1.5 cm. Ultraviolet illumination of the cathode provided a continuous supply of initiating electrons. The time lag of the discharge current pulse was measured oscillographically from the time of application of the full voltage to the gap. Twenty-five observations of the time lag were made for each set of conditions at a number of overvoltages; a standard statistical analysis was used to separate the formative time lag from the statistical scatter. In addition, a photomultiplier tube was used to observe the light output of the discharge, the signal being displayed on the same time base as the discharge current pulse. The photomultiplier tube was arranged so that it "saw" any desired part of the gap.

Near atmospheric pressure, the formative lags are too short (upper limit estimated as 10^{-7} sec) to be resolved from the statistical scatter, but with decreasing pressure the formative lags become resolvable. Figure 1 compares the formative lags of the positive point corona with those obtained for a plane parallel gap[3] for a comparable pressure and electrode separation. The corona formative lags are short even at threshold and vary little with overvoltage. This is in marked contrast with the behavior of uniform field formative lags. Thus no long build-up process is associated with the formation of the pulsed positive point corona; the cathode can therefore play no role in this formation. The corona formative lags (where they were resolvable) are too long to be ascribed to the transit time of the initiating avalanche across the high field region of the gap; these results therefore do not preclude a fast (up to 1 μsec at low pressures) secondary process in the gas preceding streamer formation. Steady-state current voltage characteristics measured in connection with this study indicate the presence of a secondary mechanism below threshold. The corona results shown in Fig. 1 are typical of all other gap geometries and a wide range of pressures. The intensity of ultraviolet illumination has no appreciable effect on the formative lag.

Visual observation of the discharge shows a difference in behavior between the pulsed and steady-state conditions. Under steady voltages the corona often develops as a glow close to the point[3] (filamentary streamers were seen for only one gap geometry out of nine). Under pulsed conditions, however, a filamentary streamer appears. The photomultiplier tube showed that light

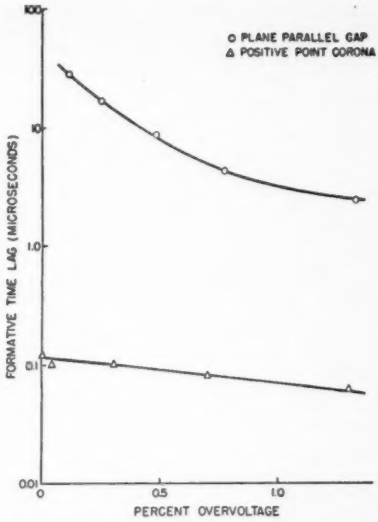

FIG. 1. Formative time lag *vs* percent overvoltage in dry air. Plane parallel gap: electrode separation 1 cm, pressure 422 mm Hg, static breakdown ~17.5 kv. Positive point corona: electrode separation 1.5 cm, point radius 0.03 cm, pressure 500 mm Hg, onset voltage ~4.9 kv.

issuing from the streamer both near and far from the point is coincident (within 10^{-7} sec) with the current pulse. The formative lags observed are thus to be associated with the filamentary streamer.

* Supported by the ONR and the Research Corporation.
[1] L. B. Loeb and J. M. Meek, *The Mechanism of the Electric Spark* (Stanford University, California, 1941).
[2] L. H. Fisher and B. Bederson, Phys. Rev. **81**, 109 (1951).
[3] Analogous results have recently been found in the dc corona by H. W. Bandel, Phys. Rev. **84**, 92 (1951).

Behavior of the Heat Capacity of Superconducting Niobium below 4.5°K

A. Brown, M. W. Zemansky,* and H. A. Boorse†
Pupin Physics Laboratories, Columbia University,‡ New York, New York
(Received February 8, 1952)

ALTHOUGH the critical magnetic field *vs* temperature curve for niobium has been measured by various investigators,[1-3] the results are not in agreement, and thus the derived specific heats are uncertain. In order to resolve the uncertainties we have directly measured the heat capacity of this metal from 2.5°K to 20°K in both the normal and superconducting phases.

The measurements were made on a cylindrical sample (about a half mole) suspended in an adiabatic vacuum calorimeter. Specimen temperatures were determined to better than 0.001° (at low temperatures) by means of a special carbon composition resistor[4] embedded in the metal. Accurately measured amounts of heat were added electrically to the specimen by means of a coil wrapped about the exterior. The thermometer resistance and energy input were determined by Leeds and Northrup Type K-2 and Wenner potentiometers. To determine a heat capacity, measurements were made before, during, and after heating so that compensation could be made for the small unavoidable heat leak. To determine heat capacities in the normal phase below the superconducting transition temperature, measurements were made in the presence of a constant magnetic field of about 6000 gauss.

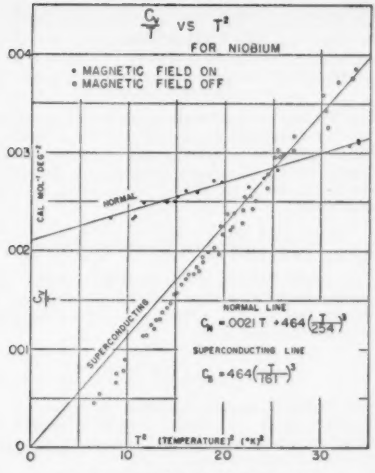

FIG. 1. Heat capacity of niobium below 6°K.

A C_v/T *vs* T^2 plot of the experimental data for the superconducting phase at the lowest temperatures is shown in Fig. 1 (open circles). The solid line through the origin gives the best fit for a T^3 specific heat dependence with no linear term, i.e., $C_s = 464(T/\theta_s)^3$, with $\theta_s = 161°$. (Superconducting data at higher temperatures are shown in Fig. 2.) It will be noted that below 4.5°K the data lie below the solid line, the departure being definitely greater than the estimated experimental error. It thus appears that for niobium the superconducting specific heat below 4.5°K falls off more rapidly than a T^3 law would allow. It would be of considerable theoretical interest to know whether a departure of this kind is a general property of the superconducting phase at very low temperatures or whether this behavior is peculiar to niobium, or to take a more pessimistic point of view, only to the present specimen. There is not enough information on low temperature heat capacities to choose among these possibilities. In the published papers on low temperature heat capacities this effect either has not been noticed or the data have too much scatter to determine if it is present.

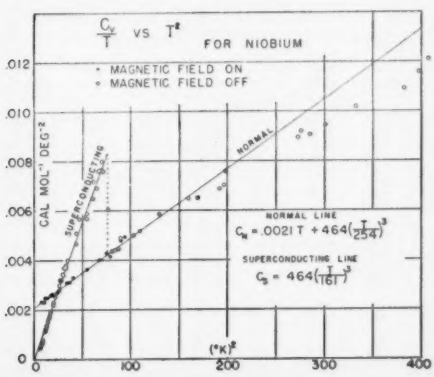

FIG. 2. Heat capacity of niobium below 20°K.

In contrast with the behavior of the specific heat in the superconducting phase, the specific heat in the normal phase follows the usual relation $C_n = \gamma T + 464(T/\theta_n)^3$, where in this case the constants θ_n and γ are 254° and 21.0×10^{-4} cal/mol-deg^4. The specific heat expressed in this way fits the data from the lowest measured temperature to about 12°K, above which the experimental points fall below those predicted by the equation (see Fig. 2). This is interpreted as indicating that the Debye characteristic temperature changes, a value of 268° being appropriate to 20°K. This behavior was expected since earlier determinations of the specific heat made in this laboratory at liquid nitrogen temperatures gave a value for θ_n of about 280°.

If we assume an ideal case for which the superconductor follows the parabolic relation, $H = H_0(1-T^2/T_0^2)$, between the critical magnetic field, H, and the absolute temperature, and also for which the superconductor has thermodynamically reversible transitions between the normal and superconducting phases, then a number of well-known relations[5] hold among the following quantities, H_0, $(dH/dT)_{T=T_0}$, γ, T_0, $TC_n = C_s$, $(\Delta C)_{T=T_0}$. (The last four of these were determined independently in this experiment.) With the aid of these relations, any pair of experimental values, except the pair T_0 and $TC_n = C_s$, serves to determine all the other quantities. When H_0 is chosen to be 1960 gauss (a value considerably lower than any previously reported), complete consistency was found between the theoretical relations and the experimental data. In other words, the heat capacity data reported here correspond to the behavior of a sample of niobium which undergoes reversible transitions and which follows the parabolic relation with the constants $H_0 = 1960$ gauss, $T_0 = 8.7$°K.

* City College of New York, New York, New York.
† Barnard College, Columbia University, New York, New York.
‡ Assisted by the ONR and Linde Air Products Company.
[i] J. G. Daunt and K. Mendelssohn, Proc. Roy. Soc. (London) **A160**, 127 (1937).
[ii] Cook, Zemansky, and Boorse, Phys. Rev. **80**, 737 (1950).
[iii] L. C. Jackson and H. Preston-Thomas, Phil. Mag. **41**, 1284 (1950).
[iv] Brown, Zemansky, and Boorse, Phys. Rev. **84**, 1050 (1951).
[v] M. W. Zemansky, *Heat and Thermodynamics* (McGraw-Hill Book Company, Inc., New York, 1951), third edition, p. 369.

Total Collision Cross Sections of Negative Atomic Iodine Ions in Nitrogen and Argon

FRANK L. MCCRACKIN
National Bureau of Standards, Washington, D. C.
(Received February 14, 1952)

THE total collision cross sections of positive ions in gases have been measured for several cases,[1] but no previous measurements have been reported for negative ions. A convenient instrument for measuring these cross sections is a Bennett radio-frequency mass spectrometer.[2]

The source of negative atomic iodine ions was an oxide-coated cathode that had been previously exposed to iodine fumes. The iodine poisoned the cathode so that it emitted negative iodine ions but no electrons when heated. These ions were accelerated and passed through the mass spectrometer, and a fraction of them was detected at the plate of the spectrometer. If I_0 is the current due to the iodine ions at the plate of the spectrometer with a high vacuum in the spectrometer tube, the ion current I, when gas at a pressure p is introduced in the path of the ions, is

$$I = I_0 e^{-\sigma p L/kT},$$

where σ is the cross section for collisions between the ions and gas molecules which prevent the ions from reaching the plate, L is the distance the ions travel in the gas, k is Boltzmann's constant, and T is the temperature of the gas. The value of σ can be calculated from the slope of the straight line obtained by plotting ln I against p. Some typical curves are shown in Fig. 1.

The Bennett mass spectrometer does not require that the ions be formed in a narrow beam, so a measurable ion current is more easily obtained than in a magnetic type of spectrometer. Measurements were made at pressures from 10^{-5} to 6×10^{-4} mm of Hg.

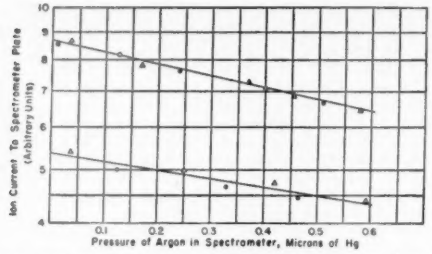

FIG. 1. Typical curves used to calculate the total cross section of ions of 400-volts energy in argon. The readings indicated by triangles were taken as the pressure was increased, and then the readings indicated by circles were taken as the pressure was reduced.

These pressures were measured on an ionization gauge calibrated for each gas. A weak magnetic field applied across the ion beam swept out stray electrons.

Considerable scattering of the measured cross sections was observed, which was partially a result of variations in emission from the cathode during a particular run. This variation can be seen in Fig. 2. The gases used should not react chemically with the cathode and did not appear to affect the ion yield. The temperature of the cathode was measured by means of a thermocouple but was found not to vary appreciably with the gas pressure or variations in the heater current. Therefore the variation in emission was not mainly caused by variation in the temperature of the cathode or gas pressure.

The types of collisions that are expected are elastic collisions, de-ionization of the iodine ion by a neutral molecule, and inelastic collisions. Charge transfer is not possible, as the gases used do not form negative ions. De-ionization of a negative ion produces a neutral atom which will not be detected. The energy selection of the spectrometer prevents all ions slowed down by more than one volt from reaching the plate. Therefore, all ionizing and nearly all inelastic collisions are included in the measured cross section. Elastic collisions prevent the ions from reaching the plate if the decrease in the velocity along the axis of the tube corresponds to more than one volt. For ions of 20 volts energy this corresponds to scattering of more than 6° and for ions of 400 volts, more than 1.4° from conservation of energy and momentum.

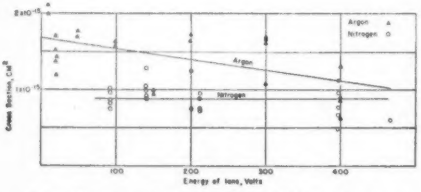

FIG. 2. The measured cross sections for collisions of negative iodine ions in argon and nitrogen.

The average value of the measured cross section in nitrogen was 9×10^{-16} cm². The measured cross section was constant within the accuracy of the measurements from 100 to 400 volts. The average value of the measured cross section in argon was 14×10^{-16} cm². The measured cross section appeared to decrease slightly from 10 to 400 volts, and the decrease was on the borderline of experimental error. The accuracy of both averages is estimated to be $\pm3\times10^{-16}$ cm².

[1] For example, R. B. Kennard, Phys. Rev. **31**, 423 (1928); A. J. Dempster, Phil. Mag. **3**, 115 (1927); G. P. Thomson, Phil. Mag. **2**, 1076 (1926); C. Ramsauer and O. Beeck, Ann. Physik **87**, 1 (1928); J. S. Thompson, Phys. Rev. **35**, 1196 (1930).

[2] W. H. Bennett, J. Appl. Phys. **21**, 143 (1950).

Diffusion of Donor and Acceptor Elements into Germanium*

CALVIN S. FULLER
Bell Telephone Laboratories, Murray Hill, New Jersey
(Received January 25, 1952)

WHEN donor or acceptor elements diffuse into p-type or n-type germanium, respectively, pn barriers are formed. By determining the distance of these barriers for two specimens of different but known original conductivities, the diffusion constant, D, as well as the surface concentration, C_0, can be determined from

$$\frac{\sigma_1}{q\mu}=C_0\,\mathrm{erfc}\left[\frac{x_1}{2(Dt)^{\frac{1}{2}}}\right],\quad \frac{\sigma_2}{q\mu}=C_0\,\mathrm{erfc}\left[\frac{x_2}{2(Dt)^{\frac{1}{2}}}\right],\qquad(1)$$

where σ_1, σ_2 are the original conductivities in ohm^{-1} cm^{-1}; q=elementary charge, 1.6×10^{-19} coulombs; μ=carrier mobility, 3600 cm²/volt sec for n type, 1700 cm²/volt sec for p-type; erfc=error function complement,

$$1-\frac{2}{\sqrt{\pi}}\int_{-x/2(Dt)^{\frac{1}{2}}}^{\infty}\exp(-\beta^2)d\beta;$$

x_1, x_2=corresponding diffusion distances of barriers in cm; D=diffusion constant in cm²/sec; t=time in seconds, and C_0=the surface concentration in cm^{-3}, assumed to be constant and the same for both specimens.

In Eq. (1) the quantity $\sigma/q\mu$ is the concentration of the carriers in the original germanium. This at the boundary is equal to the concentration of diffusing atoms if we assume each atom supplies one electron to the conduction band or one hole to the filled band.

Thus, in a given experiment, Eq. (1) allows D to be calculated from the ratio of the conductivities (p or n) of two specimens exposed to the same surface concentration of donor or acceptor element, respectively, from the relation

$$\mathrm{erfc}\left[\frac{x_1}{2(Dt)^{\frac{1}{2}}}\right]\Big/\mathrm{erfc}\left[\frac{x_2}{2(Dt)^{\frac{1}{2}}}\right]=\frac{\sigma_1}{\sigma_2}.\qquad(2)$$

When D is known, C_0 is obtainable from (1).

Specimens of single crystal[1] p-type germanium containing gallium have been subjected to both arsenic and antimony diffusion. Similar specimens of n-type germanium have been diffused with indium. The barrier positions were determined by means of a "cold" tungsten probe employing contact rectification as an indicator and by means of a "hot" tungsten probe connected to a galvanometer to measure the sign of the thermoelectric voltage. The hot probe method in most instances gave somewhat lower values for the barrier distances. Values of D

TABLE I. Data for antimony and arsenic diffusion into germanium.

T (°C)	(Time)$^{\frac{1}{2}}$ (sec)$^{\frac{1}{2}}$	σ_1 (ohm^{-1} cm^{-1})	σ_2 (ohm^{-1} cm^{-1})	x_1 (cm)	x_2 (cm)	$D\times10^{10}$ cm²/sec	C_0 (cm^{-3})
			Antimony				
710	778	14.5	1.12	0.0038	0.0045	0.03	2.0×10^{20}
755	761	11.1	0.50	0.0084	0.0123	0.13	3.2×10^{19}
810	564	32.3	1.08	0.0152	0.0229	0.76	1.8×10^{18}
850	922	52.6	1.25	0.0350	0.0399	0.37	1.0×10^{22}
850	704	52.6	1.25	0.0186	0.0265	0.51	2.9×10^{19}
850	481	13.5	1.30	0.0166	0.0217	0.96	4.4×10^{18}
850	481	13.5	1.30	0.0180	0.0227	0.96	7.0×10^{18}
905	408	32.3	1.08	0.0154	0.0263	2.3	7.2×10^{17}
			Arsenic				
710	778	13.5	1.12	0.0064	0.0075	0.01	1.0×10^{20}
750	831	11.1	1.30	0.0127	0.0138	0.05	1.0×10^{20}[a]
						(0.09)[a]	
755	761	11.1	0.50	0.0150	0.0164	0.04	1.0×10^{20}[a]
						(0.14)[a]	
800	613	16.7	5.6	0.0112	0.0133	0.36	3.0×10^{18}
800	487	16.7	8.3	0.0038	0.0052	0.36	3.0×10^{17}
850	701	76.9	12.5	0.0183	0.0350	1.2	1.5×10^{18}
850	920	76.9	12.5	0.0169	0.0355	0.79	2.2×10^{18}
905	701	14.3	1.08	0.0222	0.0333	1.4	1.0×10^{18}

[a] These values of D are calculated assuming $C_0=1.0\times10^{20}$.

calculated by both methods, however, agree fairly well. Table I and Fig. 1 show the results at different temperatures for the cold probe method. The straight line of Fig. 1, plotted by least squares, gives an activation energy of 51,000 calories. This value provides the following tentative diffusion equation which applies within experimental error to both arsenic and antimony,

$D_{As} = D_{Sb} = 0.71 \exp(-51{,}000/RT)$ where $R = 1.98$ calories.

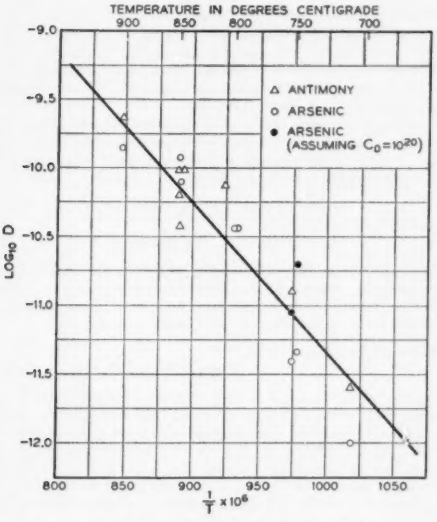

FIG. 1. Diffusion constants of antimony and arsenic as a function of temperature.

Because germanium when heated above 500°C tends toward p-type, all specimens were equilibrated at 500°C for 40 hours before measurement. Figure 2 shows plots of barrier distance (cold probe method) against square root of time for arsenic and antimony diffusions. The linear trend of these plots indicates that, for the surface concentrations employed, ideal behavior is approximated.

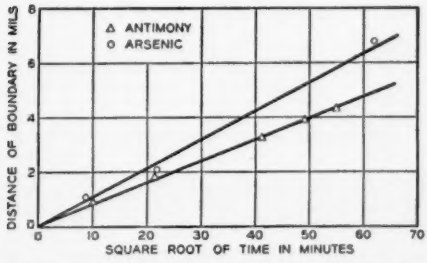

FIG. 2. Diffusion distance versus time for antimony and arsenic.

The diffusion constants for indium and zinc determined by this same method are 0.9×10^{-12} and 2.3×10^{-12} cm² per sec (775°C), 4.0×10^{-12} and 1.0×10^{-11} cm² per sec (845°C), respectively. The activation energies are approximately 50,000 calories for both elements.

The writer is indebted to W. Van Roosbroeck for formulations of Eqs. (1) and (2) and to J. A. Ditzenberger for assistance with the experimental work.

* Work very similar to that described here has just been reported by W. C. Dunlap, Jr. [Bull. Am. Phys. Soc. 27, No. 1, 40 (1952)]. See the accompanying Letter by McAfee, Shockley, and Sparks, Phys. Rev., this issue.

[1] Teal, Sparks, and Buehler, Phys. Rev. 81, 637 (1951).

Measurement of Diffusion in Semiconductors by a Capacitance Method

K. B. McAFEE, W. SHOCKLEY, AND M. SPARKS
Bell Telephone Laboratories, Murray Hill, New Jersey
(Received February 15, 1952)

SHOCKLEY[1] has derived a relationship between the capacitance of a p-n junction biased in the reverse direction and the gradient a of the difference between the concentrations of donors and acceptors in the transition region. If one of the impurities is present uniformly throughout, a junction can be made by introducing a larger concentration of the opposite type impurity into one end of the sample. In such a junction a will be just the gradient of the nonuniform impurity. At high

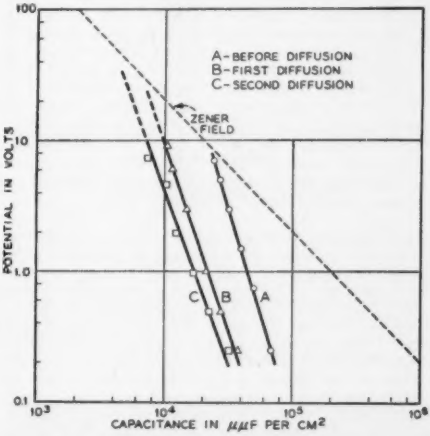

FIG. 1. Change in capacitance of a p-n junction with heat treatment. A dielectric constant of 16 is assumed for germanium.

temperatures the nonuniformly distributed impurity will diffuse into the material. Measurement of the capacitance of the junction before and after one or more heat treatments thus determines the change of the gradient of one impurity. From this and a knowledge of the limiting concentrations of donors and acceptors immediately adjacent to the transition region, a diffusion constant may be calculated for the nonuniform impurity by solution of the diffusion equation.

Experiments have been performed with single crystals of germanium in which gallium was the uniformly distributed acceptor, and arsenic was the nonuniform donor. The capacitance data for one junction are shown in Fig. 1, and the deduced concentrations of these two impurities in the region of the junction are shown in Fig. 2. Ten similar junctions were studied at temperatures between 600 and 925°C. Heat treatments were about 50 hours each. The calculated diffusion constant for arsenic in

germanium at 800°C, where several measurements were taken, fell between 1×10^{-13} and 5×10^{-13} cm²/sec. This value is several orders of magnitude smaller than that reported by Fuller in the accompanying letter and by Dunlap.[2] The activation energy for the process, which is calculated from the temperature dependence of the diffusion rate, is about 3.0 electron volts.

The limiting concentrations were calculated from conductivity measurements made locally on each side of the junction. The calculation employs the mobility of holes and electrons, and we have used Hall effect data obtained from Pearson and Debye[3] which include most of the range of impurity concentration in the junctions studied.

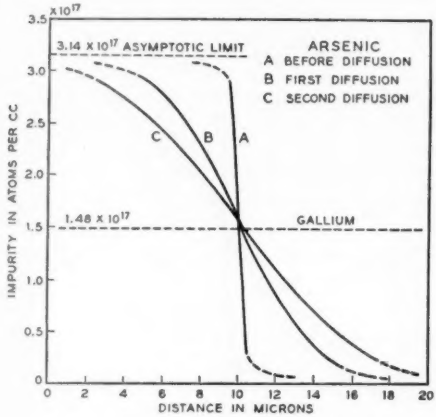

FIG. 2. Impurity concentration gradients in the region of the p-n junction as deduced from Fig. 1.

For all junctions the capacitance was found to be proportional to the inverse cube root of the bias voltage. This relationship is expected for junctions in which the gradient is constant across the transition region.[1] For one junction it was possible to observe a sharp Zener break[4] in the current-voltage curve at each step throughout the heat treatments. The concentration gradients obtained from the critical Zener voltages agreed to within 20 percent with those obtained from the capacitance measurements.

There are two features of the technique which make it particularly suitable for measurement of diffusion. First, it permits the significant measurement of very small diffusion distances and very low concentrations of impurities. Second, and perhaps more important, diffusion may be studied from a gradient which is established in the crystal at the time it is grown. In the usual techniques for measurement of diffusion in solids, the impurity atoms are introduced at the surface. Their concentration here is difficult to determine since it may be influenced by adsorption and chemical reactions. If the surface concentration builds up sufficiently, it may reach a composition which will melt at the temperature under investigation. In the method described here there is no reservoir of the impurity and no mechanism for its concentration to increase beyond that built into the crystal when it is grown.

We wish to acknowledge the assistance of Mr. R. M. Mikulyak in growing the crystals and of Miss C. J. Peffer in taking many of the measurements. Mr. W. van Roosbroeck obtained the particular solutions of the diffusion equation.

[1] W. Shockley, Bell System Tech. J. **28**, 335 (1949).
[2] W. C. Dunlap, Jr., Bull. Am. Phys. Soc. **27**, No. 1 (1952).
[3] G. L. Pearson and P. P. Debye, private communication.
[4] McAfee, Ryder, Shockley, and Sparks, Phys. Rev. **83**, 650 (1951).

Pressure Broadening of Absorption Lines*

GILBERT N. PLASS AND DOUGLAS WARNER
The Johns Hopkins University, Baltimore, Maryland
(Received January 21, 1952)

SPITZER[1] has shown that the familiar Lorentz formula for the absorption coefficient

$$k(\nu)=(S\alpha/\pi)[(\nu-\nu_0)^2+\alpha^2]^{-1} \tag{1}$$

is valid when $|\nu-\nu_0|<3M^{-1}$, where α is the half-width of the line, ν is expressed in wave numbers, S is the total intensity of the line, $M=27.8(c/v)^{6/5}b^{1/5}$, and b is the constant in the frequency perturbation $\nu_p(t)=br^{-6}$. Although the following calculations can be easily extended to perturbations varying as r^{-n}, we give only the results for Van der Waals forces.

Holstein[2] has shown that $k(\nu)$ derived from statistical theories is valid at moderate pressures and for nondegenerate levels when $|\nu-\nu_0|>3M^{-1}$. In this range of frequencies the Lindholm[3] equations are valid in the wings of the line

$$k(\nu)=(0.933)(M^2S\alpha/\pi)[M(\nu_0-\nu)]^{-3/2} \tag{2a}$$

and

$$k(\nu)=(0.638)(M^2S\alpha/\pi)[M(\nu-\nu_0)]^{-7/2}. \tag{2b}$$

In the usual case Eqs. (2a, b) apply to the red and violet wings, respectively. Instead of the discontinuous rectangular pulses used by Lindholm, Holstein,[4] using an inverse power frequency perturbation, obtains Eq. (2a) for the red wing and

$$k(\nu)=(16.6)(M^2S\alpha/\pi)(\nu-\nu_0)^{-7/3}\times\exp\{-(0.474)[M(\nu-\nu_0)]^{3/2}\} \tag{2c}$$

for the violet wing. All of the calculations reported here have been made using both Eqs. (2b) and (2c). Although the latter equation is based on more reasonable physical assumptions, we find that the difference in the results calculated from these two equations does not differ by more than a few percent within the range of validity of the statistical theory. This is because the absorption from the red wing dominates the violet. Since Lindholm's equations are easier to integrate and give the same answers as Holstein's, we report below only on calculations made with Eqs. (2a, b).

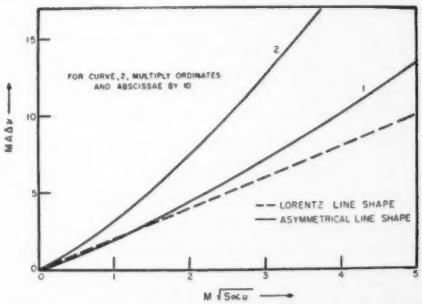

FIG. 1. Absorption of a single line as a function of $M(S\alpha u)^{\frac{1}{2}}$ [Eqs. (3) and (4)]. The dashed and solid lines show the absorption with the Lorentz and asymmetrical line shapes, respectively. Both the ordinates and abscissae of curve 2 should be multiplied by ten.

The fractional absorption, A, by a single line is given by the familiar square root law

$$A\Delta\nu=2(S\alpha u)^{1/2}, \tag{3}$$

when the radiation is completely absorbed at the center of the line, where u is the optical thickness of the absorbing gas. If $k(\nu)\sim|\nu-\nu_0|^{-n}$ in the wings of the line, by the usual derivation $A\sim(S\alpha u)^{1/n}$. For $n=2$, this agrees with Eq. (3). If $k(\nu)$ is given

by Eqs. (2a, b), then

$$A\Delta\nu M=(1.19)(M^2S\alpha u)^{2/3}+(0.789)(M^2S\alpha u)^{1/2}. \quad (4)$$

Equation (3) is valid when there is little absorption from the beam for wave numbers $|\nu-\nu_0|>3M^{-1}$. Equation (4) is valid when the beam is largely absorbed for all $|\nu-\nu_0|<3M^{-1}$. When neither of these conditions is satisfied, the value of A is intermediate between that given by Eqs. (3) and (4). In Fig. 1, where these equations are plotted, it is seen that the actual absorption curve in this range is always concave upwards and thus could not be confused experimentally with the concave downwards curve that begins when the lines in a band begin to overlap. The stronger absorption from Eq. (4) than from (3) for large $M^2S\alpha u$ is due entirely to the larger $k(\nu)$ in the red wing.

We have also calculated the transmission of an idealized band of equally spaced, equally intense lines with $k(\nu)$ given by Eqs. (2a, b) by the same procedure used by Elsasser[6] for the Lorentz shape. In our case the calculations have to be performed numerically. The results are given in Fig. 2. The region of validity

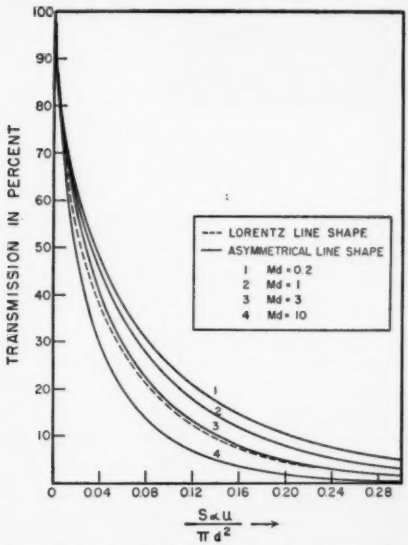

FIG. 2. Transmission of an idealized band as a function of $S\alpha u/\pi d^2$, where d is the separation between line centers in the band.

of these curves is determined by considerations similar to those for a single line. The curves for $Md\leqq 1$ should be modified by using $k(\nu)$ from Eq. (1) for nearby lines and Eqs. (2a, b) for more distant lines.

An experimental measurement of the line shape in the wings by accurate measurement of the absorption of a single line would be desirable in view of the importance of this subject for band absorption and for considerations of heat transfer in the atmosphere.[8] A paper discussing these applications in detail will appear shortly in another journal.

* This work was supported by the ONR.

[1] L. Spitzer, Jr., Phys. Rev. **58**, 348 (1940).
[2] T. Holstein, Phys. Rev. **79**, 744 (1950).
[3] E. Lindholm, Arkiv Mat. Astron. Fysik **32**, No. 17 (1946).
[4] T. Holstein, private communication.
[5] W. M. Elsasser, Phys. Rev. **54**, 126 (1938).
[6] J. Strong and G. N. Plass, Astrophys. J. **112**, 365 (1950); L. D. Kaplan, J. Met. (to be published).

Interferometric Measurements of the Hyperfine Structure of the Mercury Green Line*

JOHN STERNER
Baird Associates, Inc., Cambridge, Massachusetts
(Received January 7, 1952)

IN his classic work on the subject, Schüler[1] did not include accurate wavelength measurements of the six normally unresolved components which make up the main part of the green line of mercury. He did, however, from theoretical considerations predict accurately all the components which have been found, including an analysis of their separations.

Gehrcke and Lau,[2] followed by Burger and Van Cittert[3] using quite different techniques, measured all components. The values given by these authors checked reasonably well with Schüler's earlier measurements of the resolved components and predictions of the unresolved.

Recently, Breit[4] has pointed out the importance, for a better understanding of intranuclear forces, of more accurate measurements of hyperfine structure components. Mercury hyperfine structure has a particular significance in this respect because it has five even isotopes and two odd, thus offering an array of nuclear levels for studying and evaluating anomalous behavior.

In the present work previous measurements of the hyperfine structure of the green line of mercury have been refined by application of a novel Fabry-Perot interferometer which permits photographing of patterns rapidly and with high resolution. Each interferometer plate consists of a multilayer film formed by the alternate deposition of layers of two dissimilar dielectrics. The resultant film is similar to that which is deposited in the fabrication of the presently available commercial interference filters.[5] In this way a resolving power of nearly three million has been obtained using spacers of only 37 mm in a standard Fabry-Perot interferometer. Since absorption in a multilayer film is very much lower than that inherent in a silver film, transmission is considerably higher for equivalent reflecting power. Indeed, it has been possible to make high resolution interferograms in a matter of minutes, so quickly that only the crudest temperature regulation is required.

A typical interferogram is shown in Fig. 1. This was made by using an enriched isotope sample furnished by the Isotopes Division of the U. S. Atomic Energy Commission. The sample illustrated contains nearly equivalent amounts of Hg^{198}, Hg^{200}, Hg^{202}, and Hg^{204}. The components shown are approximately 0.03 cm^{-1} apart.

In Table I are given measurements of the central components

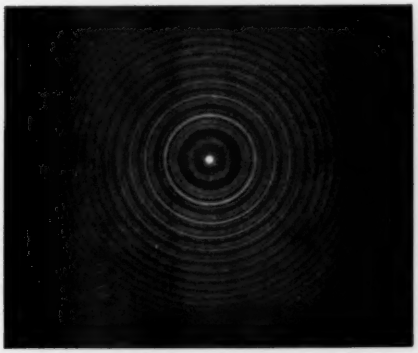

FIG. 1. A typical interferogram of the mercury green line, using an enriched isotope sample.

TABLE I. Hg hyperfine structure 5461A, comparative data (units 10^{-3} cm^{-1}).

Isotope	201(c, e)*	198	200	199(B)*	202	204
Sch[1]	−93	−64	−37	···	0	20
G&L[3]	−90	−60	−36	···	0	30
B&V.C.[2]	−89	−60	−31	···	0	28
J.S.	−86.9	−56.6	−32.6	0.4	0	29.8

* Designation according to Schüler.

obtained by using a number of enriched samples excited by electrodeless discharge. Precision of measurement is ±0.0005 cm^{-1}. The value given for component B of Hg^{199} was made using an enriched sample containing practically no Hg^{202}. This is believed to be the first reported measurement of this particular component. The present measurement of the Hg^{198} component is seen to differ markedly from previous ones. This was the most difficult component for earlier researchers to measure in ordinary mercury because of its relatively low concentration. It was not possible to measure the component of Hg^{196} because of its close coincidence with two strong components of Hg^{201} and the fact that it has not been possible so far to obtain a sufficiently enriched sample.

It seems very certain that the even component frequencies of 5461A do not lie in a sequence according to atomic weights as has been reported for other mercury lines.[6]

TABLE II. Odd-even staggering (isotopic units).

	Hg^{199}	Hg^{201}
$5461 - 6^3P_2 - 7^3S_1$	0.87	0.34
$2537 - 6^1S_0 - 6^3P_1$	0.9	0.3
$6072 - 7^3S_1 - 8^3P_1$	0.6	0.6
$6716 - 7^1S_0 - 8^1P_1$	0.8	0.6
$5676 - 7^3S_1 - 9^1P_1$	0.8	0.8

Utilizing the definitions of Breit,[4] staggering values were calculated for Hg^{199} and Hg^{201} of the green line. These are shown in Table II compared with approximate values for other lines taken from a diagram of Schüler[7] and Keyston. It is interesting to note that the values obtained for 5461A in the present research are in good agreement with those of Schüler for 2537A, which can be measured with about five times less available resolution.

The author wishes to acknowledge the contributions made by Dean G. R. Harrison of the Massachusetts Institute of Technology under whose supervision this research was prosecuted.

* Based on part of a thesis submitted for degree of D.Sc. from the Department of Physics, Massachusetts Institute of Technology.

[1] H. Schüler, Z. Physik **98**, 239 (1935).
[2] E. Gehrcke, Physik. Z. **31**, 373 (1930).
[3] H. C. Burger, Physica **5**, 239 (1938).
[4] G. Breit, Phys. Rev. **78**, 390 (1950).
[5] B. H. Billings, Phot. Eng. **2**, 45 (1951).
[6] K. Murakawa, Phys. Rev. **78**, 480 (1950).
[7] H. Schüler, Z. Physik **72**, 423 (1931).

THE AMERICAN INSTITUTE OF PHYSICS

INCORPORATED

57 East 55 Street New York 22, N.Y.

MEMBER SOCIETIES:

American Physical Society
KARL K. DARROW, *Secretary*, Columbia University, New York 27, New York.

Optical Society of America
ARTHUR C. HARDY, *Secretary*, Massachusetts Institute of Technology, Cambridge 39, Massachusetts.

Acoustical Society of America
WALLACE WATERMAN, *Secretary*, 57 East 55th Street, New York 22, New York.

Society of Rheology
G. J. DIENES, *Secretary*, Brookhaven National Laboratory, Upton, Long Island, New York.

American Association of Physics Teachers
R. F. PAUL, *Secretary*, University of Illinois, Urbana, Illinois.

AFFILIATED SOCIETIES:

American Crystallographic Association
Electron Microscope Society of America
Physical Society of Pittsburgh
Physics Club of Chicago
Physics Club of Philadelphia
Cleveland Physics Society
Physics Club of the Lehigh Valley
Sigma Pi Sigma

ASSOCIATES:

Over seventy-five leading industrial enterprises and other institutions which contribute to the support of the Institute.

JOURNALS:

The Physical Review
S. A. GOUDSMIT, *Editor*, Brookhaven National Laboratory, Upton, Long Island, New York.

Reviews of Modern Physics
J. W. BUCHTA, *Editor*, University of Minnesota, Minneapolis, Minnesota.

Journal of the Optical Society of America
WALLACE R. BRODE, *Editor*, National Bureau of Standards, Washington 25, D. C.

The Journal of the Acoustical Society of America
FLOYD A. FIRESTONE, *Editor*, 57 East 55th Street, New York 22, New York.

American Journal of Physics
THOMAS H. OSGOOD, *Editor*, Michigan State College, East Lansing, Michigan.

The Review of Scientific Instruments
GAYLORD P. HARNWELL, *Editor*, Randal Morgan Laboratory of Physics, University of Pennsylvania, Philadelphia, Pennsylvania.

The Journal of Chemical Physics
JOSEPH E. MAYER, *Editor*, Institute for Nuclear Studies, University of Chicago, Chicago 37, Illinois.

Journal of Applied Physics
ELMER HOUSTON, *Editor*, Case Institute of Technology, Cleveland 6, Ohio.

Physics Today
GAYLORD P. HARNWELL, *Editorial Director*; RALPH E. DANIEL, *Managing Editor*, American Institute of Physics, 57 East 55 Street, New York 22, New York.

OFFICERS

GAYLORD P. HARNWELL, *Chairman*
Massachusetts Institute of Technology

GEORGE B. PEGRAM, *Treasurer*
Columbia University

GOVERNING BOARD

KARL K. DARROW
G. J. DIENES
S. A. GOUDSMIT
G. P. HARNWELL
GEORGE R. HARRISON
F. V. HUNT
RUDOLPH KOMPFNER
HUGH S. KNOWLES
C. C. LAURITSEN
F. W. LOOMIS
WILLIAM F. MEGGERS
GEORGE B. PEGRAM
I. I. RABI
DUANE ROLLER
FREDERICK SEITZ
FRANCIS G. SLACK
JOHN C. STEINBERG
RICHARD T. SUTTON
MARK W. ZEMANSKY

Consultant on Publications
MELVIN LOOS

ADMINISTRATIVE STAFF

HENRY A. BARTON, *Director*

WALLACE WATERMAN
Executive Secretary

THEODORE VOSBURGH
Advertising Manager

RUTH F. BRYANT
Publications Manager

BETTY H. GOODFRIEND
Assistant Secretary

EILEEN B. NEUSTADT
Circulation Manager

KATHRYN SEIDL
Assistant Treasurer

THE American Institute of Physics was founded in 1931 as a federation of leading societies in the field of Physics. It combines into one operating agency those functions on behalf of physics which can best be done by the Societies jointly. Its purpose is the advancement and diffusion of physics and its applications to human welfare. To this end it publishes for itself or the Societies the nine journals listed on this page; promotes unity and effectiveness of effort among all who are interested in physics; renders numerous direct services to physicists and to the public; and cooperates with government agencies, national associations, educational institutions, technical industries, and others in such manner as to realize the opportunities and fulfill the responsibilities of physics as an important and constructive human activity.

CONTENTS

The Previous Issues iii

Forward Scattering of Light by Colloidal Gold 1
Small Angle Scattering of Light by Macromolecules 11
Scattering and Absorption of Light by Turbid Media 17
Spontaneous Nucleus 27
Nuclear Bhabha Scattering of High Energy Protons 35
Nuclear Photodisintegration by High Energy Cosmic Gamma-Rays 43
Nature of Weak-Scattering 51
High Energy Electron-Electron Scattering 61
Spin-Forbidden Beta-Decay Matrix Elements 67
Nonlinear Meson Theory for Heavy Nuclei 73
Magnetic Moment of H^3 and the Hyperfine Structure Anomaly 77
Average Energy of Beta-Ray Spectra 83
Shape of Cosmic-Ray Size-Spectra for Nuclear Interactions 91
Condensation in Expanding Cosmological Models 99
Convergence of Iteration-Time Series 101
Nuclear Spectrum of Cs^{137} 105
Positive Ions in the Atmosphere at Low Pressures 111
Meson-Nucleon Scattering 117
Fast Protons from $^{37}Cl(n,p)^{37}S$ and Collisions 121
Dielectric Constant in Ferroelectric Type Crystals 125

Letters to the Editor:

Spin-Wave Transformation for Ferromagnetism 131
Angular Distribution of the Protons in np Capture 133
Parity Relation of Hyperon Decay 135
Radiation from an Electron in a Magnetic Field 137
Radiation Loss of Electrons in the Synchrotron 139
Electrical Properties of the Sodium Chloride Crystal 141
Photodisintegration of Nuclei by γ-Rays 143
Condensation Phenomena of an Ideal Bose-Einstein Gas 145
Photodissociation of the Deuteron Nucleus by High Energy γ-Rays 147
π^0 Particles and Isotopic Spin 149
Absorption Rate of Cosmic-Ray Neutrons 151
Production Rate of Cosmic-Ray Neutrons and C^{14} 153
Search for New Mesons by Scattering of Cosmic Gamma-Rays 155
Dark Current in the Scintillation-Counter Photocell 157
Dispersion of Reactivity and Stochasticity of Fission 159
Inelastic Scattering of Fast Neutrons from Iron 161
Periodic Potential on Hall Coefficient 163
Penetrative Time Rate of Positive Ions in Gases 165
Behavior of the Hall Effect in Ferromagnetic Substances 167
Rapid Collision Cross Sections of Negative Atomic Ions 169
Diffusion of Boron and Arsenic Impurities into Germanium 171
Measurement of Neutrons in Radiation by a Counting Method 173
Neutron Interaction 175
Scintillometric Measurement of Fast Neutron Flux 177

LANCASTER PRESS, INC., LANCASTER, PA.